## *The Wind Tunnel Simulation and Effect of Turbulent Air flow on Automotive Aerodynamics*

MANKOWSKI, OLIVER,ANDREW

**The Wind Tunnel Simulation and Effect of Turbulent Air flow on Automotive Aerodynamics**
**Oliver Mankowski**

## Abstract

This thesis presents the research completed to design, commission and evaluate a turbulence generation system for Durham University's 2m wind tunnel and the development of a method to simulate on-road turbulence and measure its effects on a vehicle. The objective was to develop a test approach for simulating and analysing a vehicle's response to unsteady airflows. This approach focussed on simulating the overlap of the range of turbulence frequencies which exist both at significant energy in the on-road environment and the frequencies at which a significant vehicle response is seen. The frequency range where both conditions exist was seen to be between 1 – 10Hz. Confirmation of this transient frequency range was through the use of an admittance technique developed in this thesis which compares unsteady effects to quasi-steady effects. The technique was also developed to account for the component of unsteady pressure self-excitedness that exists, effectively the noise component in an admittance analysis. The approach concluded with the operation of a new turbulence generation system (TGS), which simulates the wind characteristics experienced by vehicles as they move through the on-road wind environment. The design was informed both by previous works and an on-road investigation of environment and vehicle response.

An on-road study consisting of 8,800-seconds of on-road measurements was completed to record incoming flow velocities and passenger sideglass static pressures (a region noted in studies to show a notable response to yawed flow). The on-road environment was shown to have significant energy in the 0.1 - 10Hz range (reduced frequency K = 0.1 - 10 for a vehicle driving at highway speeds). Yaw angles ranged between ±20$^{o}$, but with the vast majority within ±6$^{o}$. Correspondingly, the turbulence intensity range was 0.5 - 15%, but with the majority below 8%.

The challenges of generating turbulent length scales in the order of size of a vehicle's length, whilst also at reasonable turbulent intensities were assessed to be beyond the capability of a passive device. Through a series of iterative CFD tests, an active "lift-based" TGS was designed, based around two oscillating yaw aerofoils, which also encompassed additional inlet and outlets controlled by shutter panels. These ensured that the jet shear layer did not interact with the test model and helped to achieve higher peak yaw angles and good flow uniformity. A full aerodynamic design of the TGS was completed from the CFD studies, from which a high-level mechanical design was specified including target aerofoil displacement and acceleration rates, control system requirements and the linkage design. The construction and installation of the TGS was undertaken by an external contractor. Due to its numerous

configurable control parameters, a significant commissioning project was required and completed to determine the system's optimum configuration. The system is capable of operating up to 10Hz at ±10$^{o}$ flow yaw angle and in a programmed arbitrary mode. The system also has the capability to generate pitch and longitudinal turbulence effects (Cooper et al (1989)).

A 40% scaled model of the vehicle studied on the road was placed into the wind tunnel and a range of cases were generated including wind conditions previously recorded on-road. The results showed that the technique of using both a roof-mounted probe and the TGS system are able to take on-road flow conditions and accurately recreate their effects on vehicles in a wind tunnel.

Multiple aspects of the work (on-road, CFD and wind tunnel) showed that below $K = 0.3$ pressure fluctuations behaved in a quasi-steady manner. Admittance greater than unity was observed near the A-pillar, but admittance was generally below unity and reduced progressively for $K > 1$. Self-excitedness was seen to decrease in unsteady tests (in comparison to quasi-steady) tests in the A-pillar region, but increase between unsteady to quasi-steady tests in the mirror wake region.


**Thesis Submission**

***of***

# The Wind Tunnel Simulation and Effect of Turbulent Air flow on Automotive Aerodynamics

***Volume 1 of 1***

**Oliver Mankowski**

***for***

**The Degree of Doctorate of Philosophy**

***Supervisors***

**David Sims-Williams**

**Robert Dominy**

***Department of Engineering and Computer Sciences - Durham University***

**2013**

## i. Table of Contents

## ii. Figures

## iii. Tables

# iv. Nomenclature

## Acronyms and Notations

| | |
|---|---|
| a | - Acceleration |
| A | - Vehicle frontal area at zero yaw |
| $A_g$ | - Gust amplitude |
| ABL | - Atmospheric Boundary Layer |
| AC | - Auto-correlation (turbulence length scale) |
| C | - Aerodynamic coefficient |
| $C_D$ | - Drag coefficient |
| CFD | - Computational Fluid Dynamics |
| $C_N$, $C_{YAW}$ | - Yawing moment coefficient |
| Cp | - Pressure coefficient |
| $Cp_{dyn}$ | - Dynamic pressure coefficient |
| $Cp_o$ | - Total pressure coefficient |
| $Cp_s$ | - Static pressure coefficient |
| $C_y$, $C_{SIDE}$ | - Sideforce coefficient |
| $C_z$, $C_L$ | - Lift coefficient |
| d | - Diameter |
| f | - Characteristic frequency |
| $F_X$ | - Force in longitudinal (x) direction |
| $F_{Y,}$ $F_S$ | - Force in lateral (y) direction, sideforce |
| h | - Model height |
| I | - Turbulence Intensity |
| l | - Model \ characteristic length |
| L | - Turbulence length scale |
| k, $k_m$ | - Reduced frequency |
| n | - Frequency |
| P(f), PDF | - Probability density function *of function 'f'* |
| $p_{1-5}$ | - Individual hole pressures (five hole probe calibration) |
| $p_{DYN}$ | - Dynamic Pressure |

$p_o$, $p_T$ - Total pressure

$p_{o\_ref}$ - Reference total pressure

$p_s$ - Static Pressure

$p_{s\_ref}$ - Reference static pressure

r - Corner radius

Re - Reynolds number

$R_t$ - Auto-correlation magnitude

S - Spectral Density

Sr - Strouhal number

t - Time

$T_u$ \ TI - Turbulence intensity

$t_r$ - Grid spacing

TF - Transfer function

TGS - Turbulence Generation System

TLS - Turbulence Length Scale

UAV - Unmanned aerial vehicle

$U_X$, $U_Y$, $U_Z$ - Component Velocities

u - Axial, longitudinal (x) direction velocity

u', ∂u - Local / time variant axial velocity

$u_{ref}$ - Reference axial (x) velocity

u∞, U - Freestream velocity

$\overline{U}$ - Average turbulence value

U(t) - Fluctuating velocity magnitude *($\overline{U}$ + u(t))*

v - Cross-stream, lateral (y) velocity

VK - von Karman (turbulence length scale)

VR - Variable resolution Region (Powerflow)

w - Model width

x - Axial (stream-wise), longitudinal direction

y - Cross-stream, lateral direction

z - Vertical direction

## Greek Symbols

α - Foil angle

| | |
|---|---|
| $\beta$ | - Yaw angle |
| $\mu$ | - Air dynamic viscosity |
| $\xi$ | - Vorticity |
| $\Theta$ | - Foil Angle |
| $\omega_R$ | - Reduced frequency |
| $\pi$ | - Pi |
| $\rho$ | - Air density, probability density function |
| $\sigma$ | - Standard deviation |
| $\tau$ | - Autocorrelation time index |
| $\psi$ | - Yaw angle |
| $\nu$ | - Air kinematic viscosity |
| $\chi$ | - Admittance / Aerodynamic magnitude |
| $\Delta$ | - Change / delta |

## Subscripts and Superscripts

| | |
|---|---|
| $x'$ | - Fluctuating component of X |
| $\overline{x}$ | - Mean of X |
| $x_{min}$ | - Minimum of X |

Frequently in this thesis velocities, forces and moments are expressed in tri-axis component form, defined as shown below. These detail how the x, y and z (and u, v, w) axes are composed relative to a vehicle's orientation, as presented in Oettle (2012).

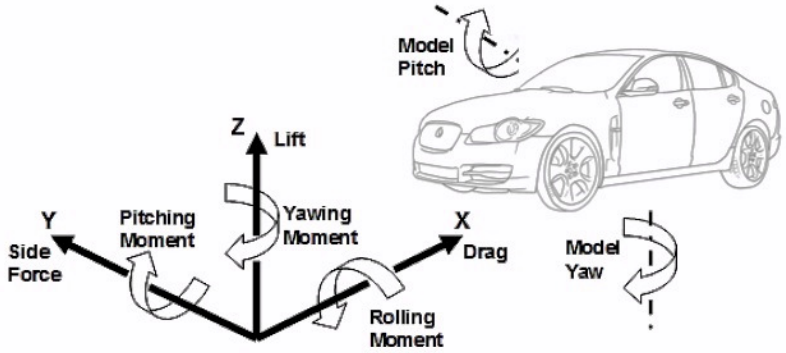


Additionally, the terms longitudinal, lateral and vertical are used throughout this thesis to express force, velocity or turbulence axial components. Longitudinal refers to components aligned with the X-axis, lateral refers to components aligned with the Y-axis and vertical refers to components aligned to the Z-axis. These co-ordinates are always expressed as aligned to the referred body in question (i.e. magnitude or resultant airflow or vehicle vector).

**Declaration**

The work contained in this thesis has not been submitted elsewhere for any other degree or qualification, and unless otherwise acknowledged, it is the author's own work.

**Acknowledgements**

I am most grateful for the guidance and encouragement provided by my supervisors, Dr. David Sims-Williams and Dr. Robert Dominy, throughout the duration of this work.

Guidance and assistance was also received from many other members of the Engineering Department, both academic and technical, who are too many to name, but their help has not been forgotten.

I would also like to thank Exa Corporation for their CFD support and assistance, JLR for access to CFD facilities and cooperation in using the XF model and to the ECS Engineering Workshop for continual support throughout the project in manufacturing the TGS, Rover 40% model and numerous other jobs.

The PhD would not have been achieved without the generous financial support that I received through SCAST, the School's Competition Act Settlement Trust, who funded the 3-years of my research and also to the Durham Universities Centre for Doctoral Training, Durham Energy Institute, who funded my final 6-months.

Finally, I would like to thank my family, without whose continued support none of this would have been achieved.

# 1. Introduction

## 1.1 Background and Overview

This thesis aims to create and evaluate a device to simulate real-world wind turbulence in Durham University's $2m^2$ wind tunnel. As such, the unsteady air flow in the on-road environment was researched and generated in order to replicate the unsteadiness of air flow that a vehicle experiences as it passes through the on-road environment. Such air flows can be a combination of spatially steady and unsteady air flows, but are perceived as temporally variant due to the vehicle's motion. The turbulence generation system's focus is that of automotive research, but due to the wide variety of devices and vehicles (i.e. from wind-turbines to UAV's) tested in Durham University's wind tunnel, the TGS requires the necessary control and adjustment to generate a relatively wide range of length scales and turbulence. The successful creation of this unsteady air flow, in a manner simulating those experienced in real-world air flows will allow further aerodynamic optimisation of wind turbines, cars, trains, aircraft and the like.

At present, almost all wind tunnels are designed for low turbulence inlet conditions, which offer an appropriate and repeatable datum for test-work. However, as our understanding of the field of vehicle aerodynamics progresses, the discrepancies in measurements between on-road and tunnel based tests are becoming of greater interest and relevance. Simulation of these on-road conditions, especially in a controlled yet repeatable environment, will assist explaining these measurement differences. For road vehicles, aerodynamic efficiency, reduction in cabin noise and the optimisation of a vehicle's stability and handling are all important fields of research. Trains and aircraft also experience a temporally variant unsteady flow field and the aerodynamic development of both is central to energy saving and vehicle stability.

This thesis focuses on automotive aerodynamics. The unsteadiness experienced by vehicles is complicated to replicate due to the variety of terrains and the pronounced effect that wind has on a moving vehicle and its aerodynamic efficiency. One of the major factors in considering turbulence simulation is the effect that the varying turbulence length scales and intensities have on a vehicle's operation. As further detailed in the literature review, it has been found that turbulence length scales in the order of a vehicle's length generate a notable vehicle response in terms of drag and sideforce loads on vehicles when compared to steady-state measurements, and have sufficient spectral energy in the on-road environment to be of significance. Recent research has quantified the nature of the turbulence scales that vehicles experience whilst in motion, as well as characterising new devices that

can generate controlled turbulence spectra not previously achieved, thereby offering the potential for real development in this field of research. Unsteady turbulence can be important for a vehicle's fuel economy, handling and aero-acoustics. The development of a wind tunnel simulation device combined with a model's and full-size vehicle's response to turbulence will offer a valuable insight at the design stage of a vehicle.

## 1.2 Thesis Outline

The thesis focuses on reviewing the nature, effects and simulation in a wind tunnel of on-road air flow turbulence.

Chapter 2 starts by presenting our current understanding of the on-road air flow environment. The quantifying of on-road turbulence then allows potential simulation devices to be assessed, with a review of both active and passive devices. The effects of turbulent air flow upon a vehicle are then discussed with a particular emphasis on forces. The chapter then covers the computational and real-world methods of simulation and considers the development of a test method and simulation approach for investigating transient air flow.

Chapter 3 describes a 2D CFD simulation of a simplified vehicle shape which experiences a range of harmonic frequencies. This test is then proposed to be scaled-up to a full 3D model. However, as the on-road environment offered a readily achievable test case, the 3D simulation was used only to validate the on-road probe location and measurement system.

Chapter 4 presents a comprehensive on-road study using a mid-sized European hatchback vehicle, with incoming flow yaw angles correlated with sideglass surface pressures. This furthered the understanding of the frequencies and scales of turbulence that affect the air flow around a vehicle and the resultant pressure variations that occur.

In Chapter 5, 2D and 3D CFD simulation studies are presented detailing a wide variety of proposals to design a turbulence generation system suitable for Durham University's 2m wind tunnel. In Chapter 6 and 7 a final design is developed that uses a combination of oscillating aerofoils and additional inlets and outlets to generate controlled length scales and intensities of turbulence.

The generation system was then installed and Chapter 8 presents a full commissioning process that captured the major variables that affect the system's aerodynamic operation, with note particularly given to the hugely multi-variant nature of the system's potential operation and the need to gain a

complete understanding through a broad range of experiments, finishing with a study assessing several 'real-world' simulation test modes.

Chapter 9 presents a study of a Rover 200 wind tunnel model's response to ranges of static, harmonic and arbitrary turbulence simulation modes, in terms of sideglass pressures and force balance readings, correlated with the earlier on-road study. The chapter concludes the thesis suggesting that the method proposed of using roof-mounted probes with on-road vehicles can be used to capture the real-world air flow environment, and through other methods proposed in this thesis, those air flows can be replicated in a wind tunnel and a reasonably accurate model response can be predicted.

# 2. Literature Review

This chapter covers measurement methods of turbulence, on-road turbulence characteristics, passive and active turbulence generation systems and summaries of a vehicle's response to transient air flow.

## 2.1 On-road Turbulence Characteristics

### 2.1.1 Overview, Metrics and Methodology

It is typical for a vehicle to experience varying air flow yaw angles and velocities as it moves (as shown in Figure 1). The actually wind velocity may be constant at specific locations, but as the vehicle translates through a domain, it experiences varying flow angles and velocities in terms of time (i.e. crosswinds). In addition, air flow which may enter the road-side environment in a steady manner can have induced unsteadiness due to roadside furniture. Therefore the variation in air flow experienced by a vehicle is a combination of the spatially variant flow fields (which a vehicle perceives temporally) and also flow unsteadiness.

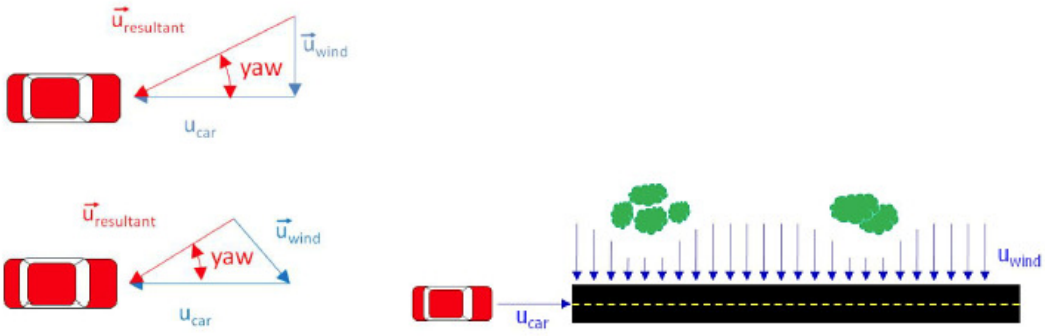


Figure 1 - Definition of yawed flow for roadside conditions - Sims-Williams (2010)

The turbulence intensity is defined as the root-mean-square of the turbulent velocity fluctuations (u') over the mean velocity ($\overline{U}$) as:

$$TI = \frac{u'}{\overline{U}} \quad [1]$$

Turbulence length scale is the time taken for a yaw to vary between peaks (i.e. oscillating period temporal length or flow eddy size).

The resultant flow velocity is a combination of the vehicle speed and the variation in wind velocity in time and space, as defined in the following equation. The variation in vehicle velocity is predominantly of interest for racing cars where the vehicle's velocity is highly significant and varies rapidly. Therefore

the latter two components of the resultant velocity equation are most of interest, that is the variation in wind over time and the spatial variations in wind as the vehicle covers ground (from Sims-Williams (2011)).

$$\frac{D\vec{u}_{resultant}}{Dt} = \frac{\partial \vec{u}_{car}}{\partial t} + \frac{\partial \vec{u}_{wind}}{\partial t} + u_{car}\frac{\partial \vec{u}_{wind}}{\partial x} \quad [2]$$

The incoming flow yaw angle will vary in time (due to a vehicle's motion through a spatial domain). The variation in yaw angle will adopt a probability density function that will be influenced by environmental factors, but typically is as shown in Figure 2, where the majority of yaw exists in the ±10° range.

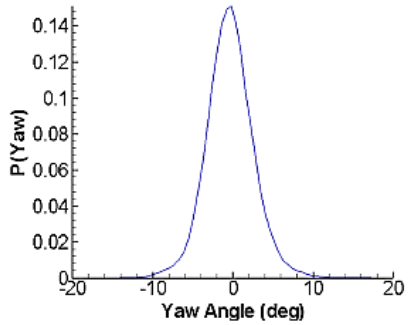


Figure 2 - Typical yaw probability density function - Wordley et al (2009)

Further, a typical 3D probability distribution of this is shown in Figure 3, from Oettle et al (2012). The test vehicle speed was constant at 35.8ms$^{-1}$ (80mph), showing wind velocity variations experienced up to ±5ms$^{-1}$ (i.e. 10 - 15% of vehicle speed) with yaw ranges of ψ±10° being typical.

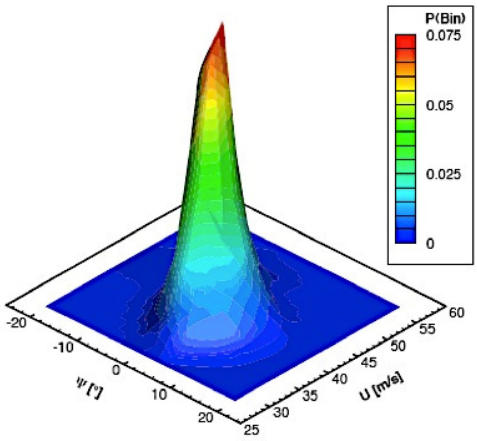


Figure 3 - Probability density distribution of velocity by yaw - Oettle et al (2012)

Additionally, as vehicle speed varies the effect of head or tailwind also varies. Oettle et al (2010) reviewed the aerodynamic response to transient air flows through on-road measurements and demonstrated that this is significant and variant with flow yaw angle, as shown in Figure 4.

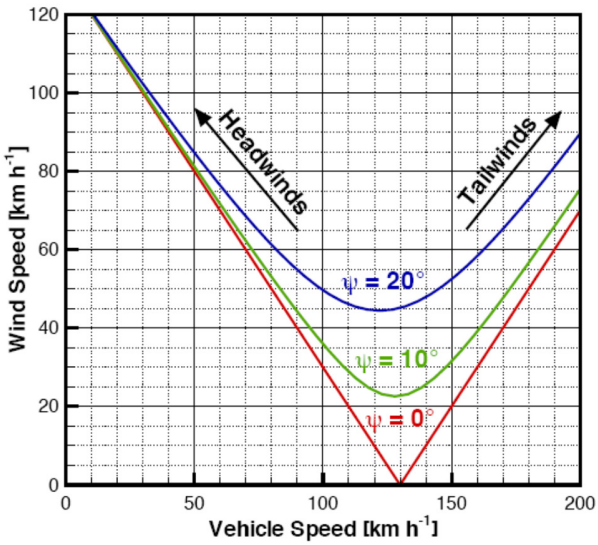


Figure 4 - Head and tailwinds on vehicle speed - Oettle et al (2010)

Before reviewing results covering on-road turbulence, it is of value to present the background to stationary and the moving reference frame measurements of air flow and to analytically define turbulence length scale and intensity. ESDU74030 (1974) noted that in measuring turbulence there is usually some interrelation between measurements of a gust component at a point taken at different time intervals and also between the gust components measured at two points in space. This interrelation, which can be correlated, deceases as the time lag (or separation) increases.

Real turbulence properties are often defined using a Gaussian probability density function (ESDU74030 (1974)), which is defined using a third and fourth order metric that are skewness and kurtosis values. This function denotes the distribution of velocities for all axes. The turbulence intensity defines the amplitude of the flow, with covariance and correlation functions used to quantify the flow. The covariance function can be at a single or multiple points in space, with the former defining the gust in time and the latter showing the flow characteristic in different regions of a turbulent flow field both spatially and in time.

A function defining the auto-covariance of the flow ($\tau$) measures the correlation between gust components (i.e. amplitude variation). It can be stated that when $\tau$ is much larger than a typical time scale of turbulence, that the correlation between gust components will be insignificant. This is to say

that if the time scale momentarily exists which is much greater than the mean air flow speed, the gust will not greatly affect the overall effect of the flow unsteadiness. As results were measured at multiple points in space, (ESDU 74030 (1974)) demonstrates tri-axis flow variance. It was found that isotropic turbulence (i.e. same velocity in 3 axes) rarely exists and that all the correlation functions are different and must be computed.

Flay (ESDU 74030 (1974)) further noted that Taylor's hypothesis (Wyngaard et al (1977)) suggests that if a velocity is much greater than u(t) (i.e. the flow over a period of time) then the unsteadiness can be evaluated as to be frozen in space and convected past a point location. This means that the flow's velocity can be resolved from only one measurement location, suggested valid for turbulence length scales (TLS's) less than 300m. As such for the Taylor hypothesis to hold, it is required that the mean velocity be much greater than the fluctuating component.

Further, Flay (ESDU 74030 (1974)) commented that it is important to review the whole frequency spectrum due to the highly distributed and variant nature of turbulence. Spectral density functions should therefore be used as they can show the dynamic loading of, and response to, a body immersed in flow. Figure 5 is included as it shows the relationships of these measurements systems.

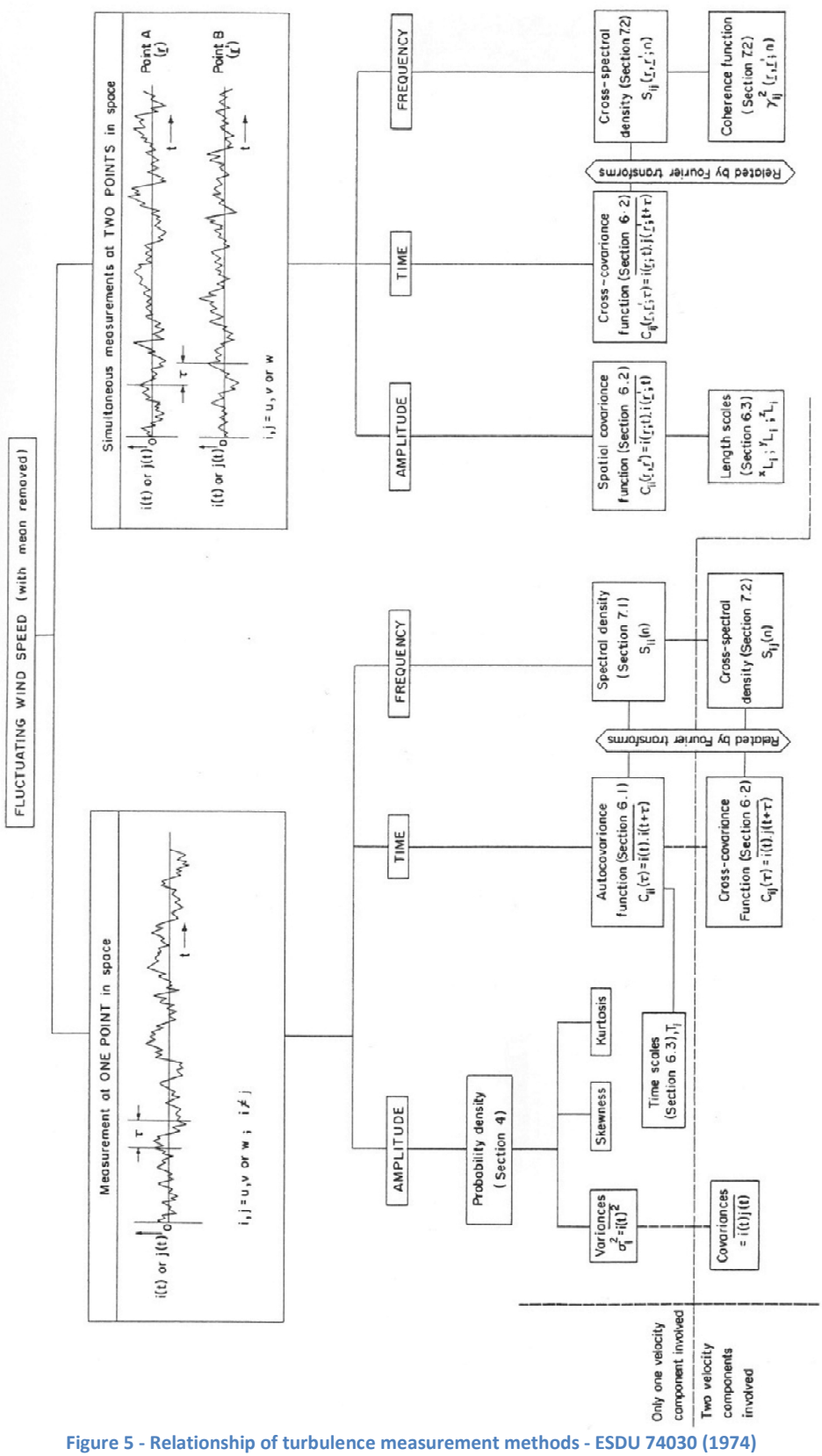


**Figure 5 - Relationship of turbulence measurement methods - ESDU 74030 (1974)**

Methods for finding TLS are auto-correlation and the von Karman spectral model. The auto-correlation method finds correlation between points separated by time, as given in ESDU 74030 (1974) and 85020 (1985). Watkins et al (1990) discussed the auto-correlation system, which is used extensively in this thesis. The form to be used is the simplified equations as they avoid the need to re-evaluate the Bessel functions and that the variation of the sub functions can be assumed to be small, such that the simplified forms can be produced, as per ESDU 74030 (1974). In order to undertake the calculations required, the auto-correlation is to be defined as in ESDU 74030 (1974) (where ρ is the probability density function of the flow, L is length scale, and U is velocity):

$$\begin{aligned} &\rho_{UU} = f = \frac{1}{2}\left(f_1 + f_1^{\,2}\right) \\ &where\ f_1 = \exp\left(-0.822F_f^{0.77}\right) \\ &where\ F_f = {}^{\tau U_Z}\!\!\diagup_{X} L_U = {}^{\Delta X}\!\!\diagup_{X} L_U \end{aligned} \qquad [3]$$

For the i = v or w component :

$$\begin{aligned} &\rho_U = g = \frac{1}{2}\left(g_1 + g_1^{\,2}\right) \\ &where\ g_1 = \exp\left(-1.230F_g^{0.85}\right) \\ &where\ \mathrm{F}_g = {}^{\tau U_Z}\!\!\diagup_{2^X} L_i \end{aligned} \qquad [4]$$

Significantly, therefore, the method shown for evaluating auto-correlation is based upon timescale, not explicitly on length scales. This method also uses the mean bulk velocity multiplied by component timescales to give lateral velocity and length scales rather than using axial velocity, which can understate potential yaw angle measurements.

A practical application of the method detailed in the ESDU datasheet was given alongside tests undertaken by Lindener et al (2007) at Audi and Pininfarina. The tests were to quantify the turbulent environment on the road and in a wind tunnel from an aeroacoustic perspective to present definitions of length scale and intensity. As the definition of length scale is important to this thesis, and was referenced from works of Saunders et al (2006) and Wordley et al (2009), it is reproduced here in detail. The longitudinal velocity of the flow is comprised of three velocity components in (u, v and w) of which the longitudinal component can be defined as:

$$U(t) = \overline{U} + u(t) \qquad [5]$$

Where $\overline{U}$ is the average turbulence value and u(t) is the longitudinal turbulence component, with similar formulas for lateral (v) and vertical (w) flow components. The average velocity is used to evaluate the turbulence intensity of the flow, that is the variation in yaw or pitch angle, which is defined as the ratio of the standard deviation of each varying velocity component from the mean:

$$I_i = \sigma_i / \overline{U} \text{ and } i = u, v, w \quad [6]$$

This parameter offers a sufficient description of turbulence such that it can be evaluated in the frequency domain by a Fourier Transform to derive the Power Spectral Density Function ($S_{UU}(n)$, $S_{VV}(n)$, $S_{WW}(n)$) for the energy at each frequency f. The turbulence length scale, $L_U$, evaluated using the auto-correlation function, denoted by u(t), is defined as:

$$R(t) = \frac{\int_{-\infty}^{\infty} u(\tau) \cdot u(\tau + t)\, d\tau}{\sigma_u^2} \text{ and the respective inverse, } R^{'} = \int_0^{t_0} R(t)\, dt \quad [7]$$

Where $t_0$ is the first value of *t* such that $R(t_0) = 0$, which determines the time-scale and is the time interval where *u* is in maximum correlation with itself (i.e. auto-correlated). Further, Taylor's hypothesis is used, which states that a turbulent eddy current which is measured at one spatial location in time can be considered to represent an instantaneous snapshot, such that it can be viewed as having been measured as one temporal period and therefore can be used to convert between the time scale and spatial scale ($L_U$), as shown by the formula:

$$L_U = \overline{U} \cdot R^{'} \quad [8]$$

Data recorded in this form is therefore, over a particular period of time, defined by a critical reduced frequency, and is subsequently spectrally viewed for a time period. However, the singular length scale and intensity is time-averaged over the same period.

The 'Durham University Software for Windtunnels' program, Sims-Williams (2012), that evaluates auto-correlation length scales has a few key parameters which, though in line with the theoretical and practical examples presented in this section, should nevertheless be stated. The two major points are that when the correlation coefficient passes below zero for the first time the measure is then truncated, as it is assumed that the sum of the coefficient variances thereafter will sum to zero. Secondly, the bulk velocity is used in the generation of the length scales as opposed to axial velocity, as consistency can remain when lateral and vertical length scales and intensities are evaluated. In this way the intensities and length scales quoted are all in terms of their own respective axis. Also note that

the length of a recording sample (e.g. 4.0 seconds) acts as a high-pass filter and the logging frequency acts as a low pass filter in terms of the range of length scales measureable. It should also be stated that when compared to the von Karman method of analysis, with the correct filtering, an auto-correlation analysis is comparable to the von Karman method.

Assessments of the simulation of length scales has greater validity if the proper non-dimensional elements are included in the final metric, hence reduced frequency is used to define frequencies analysed in tests conducted in this thesis. Of particular interest is the assessment of the critical range of turbulence frequencies (length scales) in the onset air flow, namely in terms of the body's aerodynamic response. The focus is on yaw angle variation as these are, arguably, the most important in the on-road environment. This compliments work of Theissen et al (2010). A direct outcome will be to determine the quasi-steady reduced frequency limit of 0.1 to 1.0 as discussed by Corin et al (2008) and to further define the significant inlet flow frequency range as proposed by Wordley et al (2009). Reduced frequency (also denoted as K) is defined as:

$$\omega_R = \frac{2\pi L}{U} \quad [9]$$

Where L is a characteristic dimension (vehicle length is used here) and U is driving velocity, which gives a quasi-steady frequency threshold around 0.11Hz:

$$f = \frac{\omega_R U}{2\pi L} \approx 0.11\text{Hz} \quad [10]$$

A key focus in vehicle aerodynamic research is determining the frequency range that is most significant to the drag force and stability of vehicles. Wordley et al (2009) was successful at defining the range of frequencies and intensities that characterise ground-level air flow, with a view to guiding the wind tunnel simulation of turbulent conditions for road vehicles. Wordley et al (2009) recognised that generating the full range of conditions experienced by a vehicle on-road is problematic and that it would be attractive to only simulate a subset of the full range. Wordley et al (2009) suggested that length scales from 0.5 - 15m are key, though recent work by Theissen et al (2010) has suggested that the relevant upper limit could be as high as 30 - 90m. Determination of the relevant range would assist the development and operation of such turbulence generation systems. The development of systems to reproduce the full range of appropriate length scales is as yet unsolved and inevitably intricate. The simulation of length scales down to 3m is achievable with lift devices such as in Schröck et al (2009)

and scales below 0.5m can be simulated with passive devices, such as in Newnham et al (2006) and in Newnham et al (2008), but it is the intermediate scales that provide the greatest challenges (i.e. Knebel et al (2010)).

It is expected, as proposed by Corin et al (2008) and Sims-Williams (2010), that the effect of inlet turbulence on vehicle drag and stability will be curtailed by a quasi-steady limit, which this report will define. The use of idealised vehicle models, such as by Ryan (2000) and Docton (1996), allows a wide range of frequencies to be analysed with regard to the effect of delayed or encouraged separation and other consequential flow features that are apparent with simple geometries. Finally, the ability to assess a range of factors (i.e. corner radii, width, viscosity) in numerical simulations will focus and encourage future simulation analysis.

### 2.1.2 On-road Measurements

Understanding the flow characteristics experienced by a vehicle needs to consider both the natural wind environment (i.e. varying in component flow speeds) at differing heights and also the variation of wind along a road (i.e. which the vehicle experiences as it drives along a road). This section will initially present works covering wind measurements (static mast data) and on-vehicle recordings. Then numerous other sources will be added to show a variety of measurements recorded statically and on a vehicle at varying heights and build a picture of how height and vehicle motion affect vehicle perceived flow characteristics. Plots combining all of the presented results into one view are presented relating turbulence length scales and intensities with measurement height location.

As an aside for the presentation of turbulence results, when on-road results are shown there are occasions where the probability density functions are presented with peaks in excess of unity. Unlike probabilities, this is due to the nature of a continuous probability density function, where the essential criteria are that the area sums to unity and therefore, over short widths, the peak can correctly be greater than unity.

A initial review of the length scales of interest is based upon the works of Knebel et al (2010) and Wordley et al (2009) who both undertook wind measurements (Knebel statically, Wordley using a vehicle mounted probe) and offer an insight into the frequency and power spectrum of unsteady air flow characteristics. These results will then be compared and numerous other sources also presented. Graphs at the end of this chapter summarise this catalogue of flow measurement results and combine all the results into a graphs of turbulence intensity and length scales against measurement height location.

Knebel et al (2010), undertook an initial analysis by determining the desirable wind characteristics to measure. Knebel suggested that the Weibull distribution (Boettcher et al (2007)) would be a good fit for velocity fluctuations denoted as turbulence intensity. Knebel represented the probability distribution of flow velocities by a function based upon the duration of a velocity perturbation (which was termed the 'flatness' function). A 6-standard deviation (σ) of velocity variation from the mean was used as a filter since it captured a significant proportion of a population data sample. 6σ of velocity variation corresponds to a variation of $10ms^{-1}$ within a measurement window of 2.5s, which is a relatively common occurrence (certainly within 24-hours of recording), and therefore such a wide probability distribution is necessary.

Flow was captured over 10-minute samples for an anemometer placed at a height of 20m. Such a height for an anemometer is relatively high for the flow to be considered to be the same as that which an on-road vehicle would experience, and as such the flow distribution does differ from that of Wordley, but offers an insight into the distribution of velocity variations and a measurement approach. Knebel's flow distribution (see Figure 6) shows variation in velocity variation (i.e. turbulence intensity) for differing sampling intervals, and the probability drop for a mean wind speed is symmetric about the mean. It is important to note the several orders of decreasing magnitude of the wind power as the velocity varies from the mean. Note that in the Figure 6, 'u' is the wind speed, and 'τ' denotes the duration window over which a velocity perturbation was measured (e.g. 1.25s).

As such the Y-axis shows the probability of the magnitude of variation of wind speed over a certain time period and the X-axis denotes the number of standard deviations that the velocity perturbation is from the mean. This shows that short time period velocity perturbations are far more common than long period oscillations but that a wide variation of velocities are recorded (several standard deviations from the mean). Corresponding time intervals increase in the traces plotted from top to bottom.

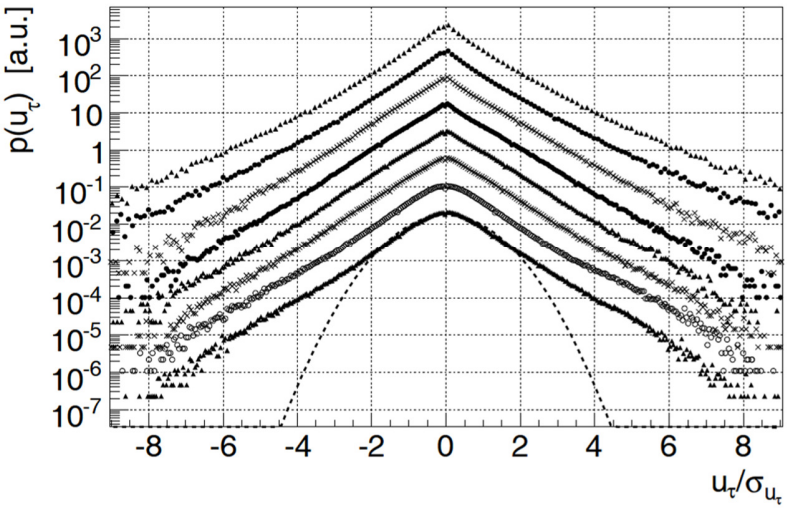


Figure 6 - Probability distributions of velocity variation of wind data at z=20m - Knebel et al (2010)

Recorded at 4Hz. Distributions shifted in the Y-axis for clarity. Corresponding time intervals from top to bottom: 1.25s, 2.5s, 25s, 2min 5s, 4min 10s, 20min, 40min

Wordley et al (2009) took on-road flow velocity measurements with an ahead of vehicle, car-mounted probe as in Figure 7.

Figure 7 - Wordley probe mounting - Wordley et al (2009)

Wordley reviewed road turbulence flows, with an overview of the data collection given in Figure 8, and found that the von Karman (VK, typically around half in size of those reported by the auto-correlation method) longitudinal and lateral length scales measured were bounded from 14m length scale at 2% intensity (top left of the greyed box) to 0.2m at 14% intensity (bottom right of the greyed box) for

smooth terrain, with the peak length scale decreasing to around 8m where road-side obstacles (RSO) were present.

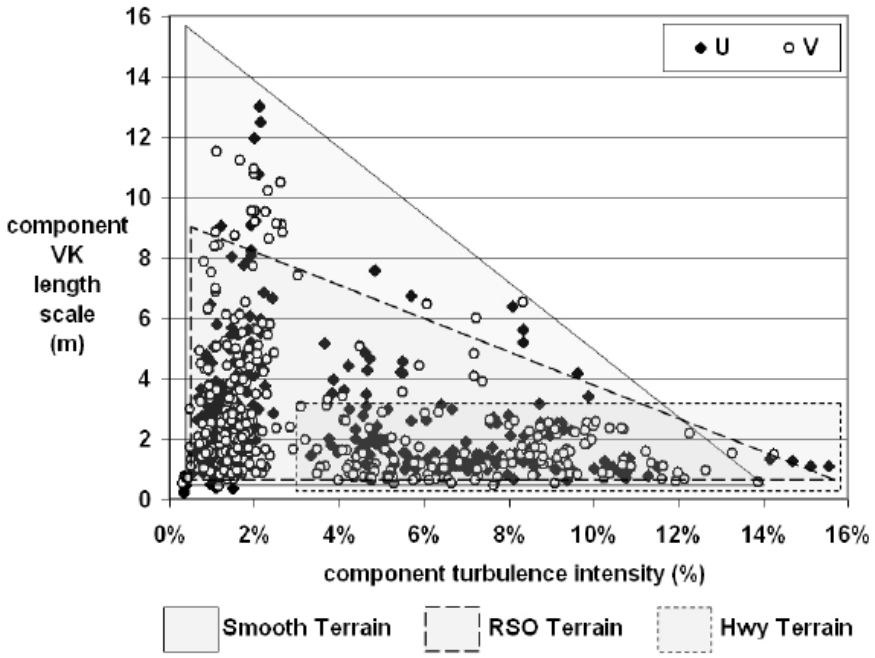


Figure 8 - Measured turbulence length scales - Wordley et al (2009)

Figure 9 shows a more detailed summary of von Karman (VK) length scales against turbulence intensity measured by Wordley et al (2009) for 4 different road environments of varying road-side furniture. The regions have been bounded in differing grey boxes, with Freeway traffic experiencing far larger turbulence intensities at lower turbulence length scales in comparison to City Canyon traffic, which saw low intensities at much larger length scale, mainly due to the more open road environment and large fetch areas creating long length scales. The longitudinal (U) and lateral (V) marks are plotted in close clusters, suggesting comparable isotropic turbulence in these axes, but the 'W' marks (crosses) are mainly at notably shorter length scales (mainly as vertical scales are confined due to the ground).

Figure 10 shows the power spectral curve for lateral velocities measured on the road, in the Monash wind tunnel and suggested TGS capabilities. Note the reduction in on-road spectral energy above around 10Hz.

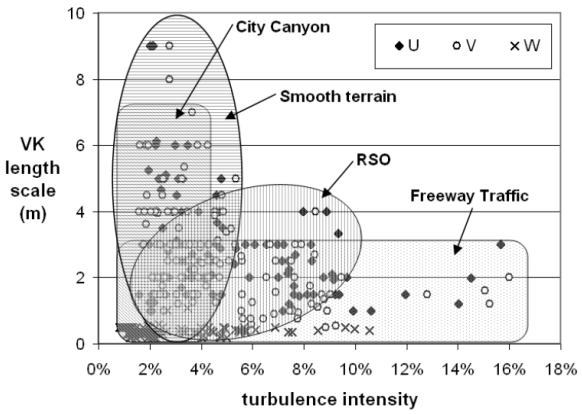


Figure 9 - Summary of the results from Wordley et al (2009), for a variety of road environments

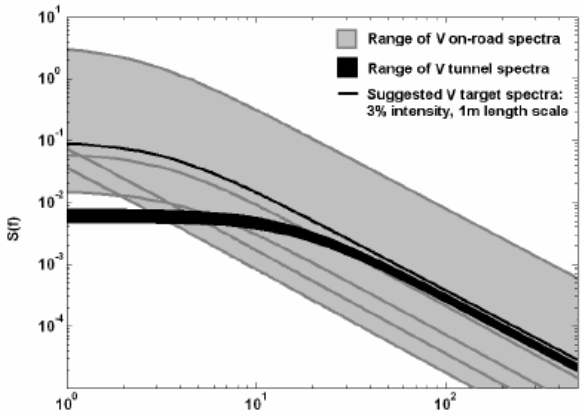


Figure 10 - Comparison of dimensional, wind component power spectra ranges - Wordley et al (2009)

Range of all on-road spectra (grey), range of Monash wind tunnel spectra (black), suggested interim target spectra (black lines)

Flay, ESDU 85020 (1985) complied numerous flow characteristic results in a datasheet including surface roughness measurements (i.e. large, open fetch terrain to environments with numerous road-side obstacles). Results presented in the datasheet showed that for heights less than 1m, turbulence intensities are around 1%, depending on terrain roughness, increasing to 1.1 - 3.6%, for city centres and forests. Auto-correlation turbulence length scales were shown to be around 10 - 100m at 3m heights, again for a smooth terrain, decreasing to a TLS of around 10m at 1m heights. Therefore reducing the measured height location from 3 to 1m would cause TLS drop of around 90%. For heights below 3.5m, Watkins et al (1995), recorded wind speeds in the range of 1.7ms$^{-1}$ to 9.4ms$^{-1}$, resulting in the suggestion of an average of a TLS of 3m at a height of 2m, with intensities found to be between 10 - 34% at a height of 5m from ESDU 85020 (1985).

In comparing Knebel, Wordley and ESDU 85020 results, Knebel's flow distribution (Figure 6) is more suitable for wind turbines, which operate higher above the ground. Further, work by Newnham et al (2006) and ESDU85020 (1985), suggested large length scale and intensity variations occur between heights of 3 to 20m (the lower height of presented results, further changes could occur below this height), as recorded length scales increase from around 10m to around 100m as the measurement height increases over this range and intensities decrease from around a maximum of 12% to a maximum of 7% with a similar height increase. Therefore, though the Knebel's velocity profile is similar to that of Wordley, the ESDU85020 (1985) datasheet does suggest that the differences between them are likely to be due to the height of the measurement location.

Tests undertaken by Lindener et al (2007) at Audi and Pininfarina looked to quantify the turbulent environment on the road and in a wind tunnel from an aeroacoustic perspective. Two Cobra probes were mounted close to the front bumper and the second at the intersection of the cowl and the right side A-pillar. Road tests were conducted on a variety of German A roads at speeds of 140 – 160kmh$^{-1}$, with the wind tunnel testing being conducted in both a smooth and turbulent inlet condition, using Pininfarina's turbulence generation system. Results for a variety of on-road environments are included in Figure 11 showing decay in spectral energy with log frequency, with a clear drop off of spectral energy around 10Hz and significant reductions above 100Hz.

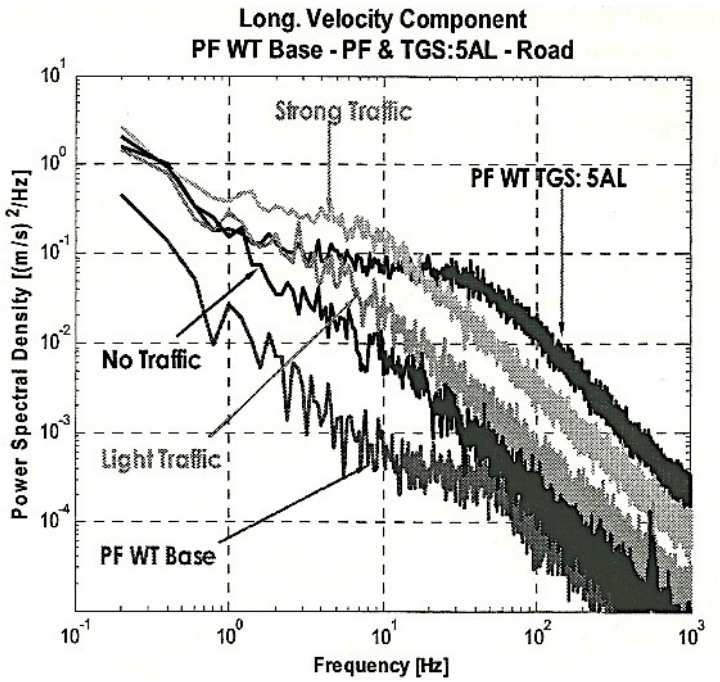


Figure 11 - Comparison between different road test condition and Pininfarina wind tunnel - Lindener et al (2007)

Additional results of turbulence intensity and length scale for a variety of environments were derived as shown in Figure 12. It can be seen that length scale is generally below 8m and intensity below 8%, with the vast majority of data points lying under 6m and 7%, though the turbulence length scales generated by the Pininfarina TGS (denoted PFWT) were much shorter but had comparable intensities.

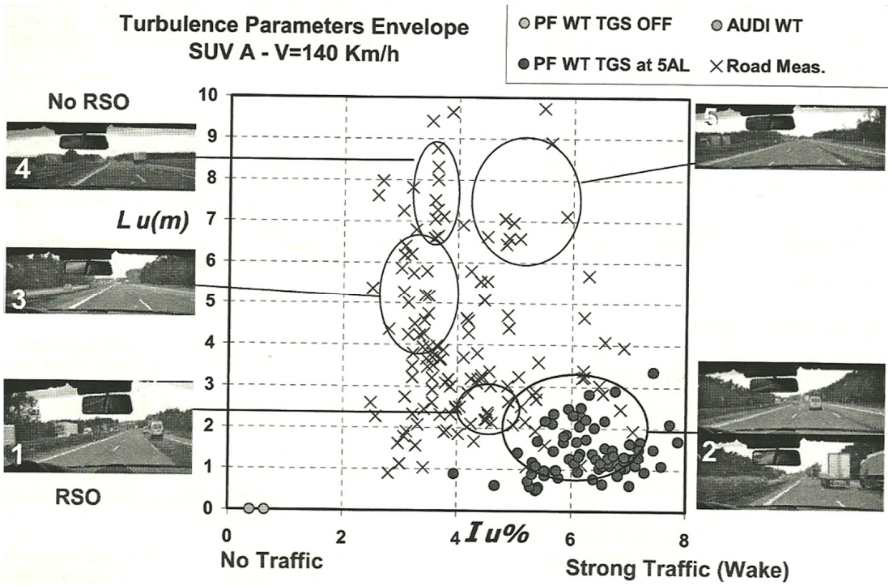


Figure 12 - $L_U$ (m) vs. $I_V$ (%) for road and wind tunnel results for a SUV vehicle in various road conditions - Lindener et al (2009)

A presentation of on-road and wind tunnel TGS measurements by Pininfarina is given in Figure 13 and Figure 14, showing that the TGS system generates higher intensity turbulence relative to the on-road environment, and at much shorter length scales. Note that the TGS configurations that seem to be most similar to the road conditions are the 3BL and 5AL. Length scales are seen to reside in the sub 6m region, with the majority under 2m, with turbulence intensities in the 2 - 8% range.

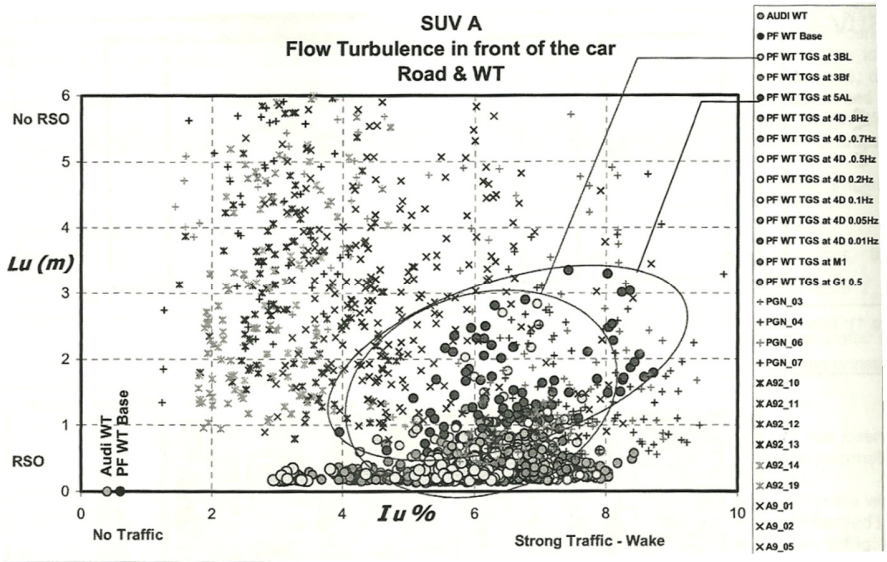


Figure 13 - $L_V$ (m) vs. $I_U$ (%). Road and Pininfarina wind tunnel results for various TGS set-ups on a SUV vehicle - Lindener et al (2009)

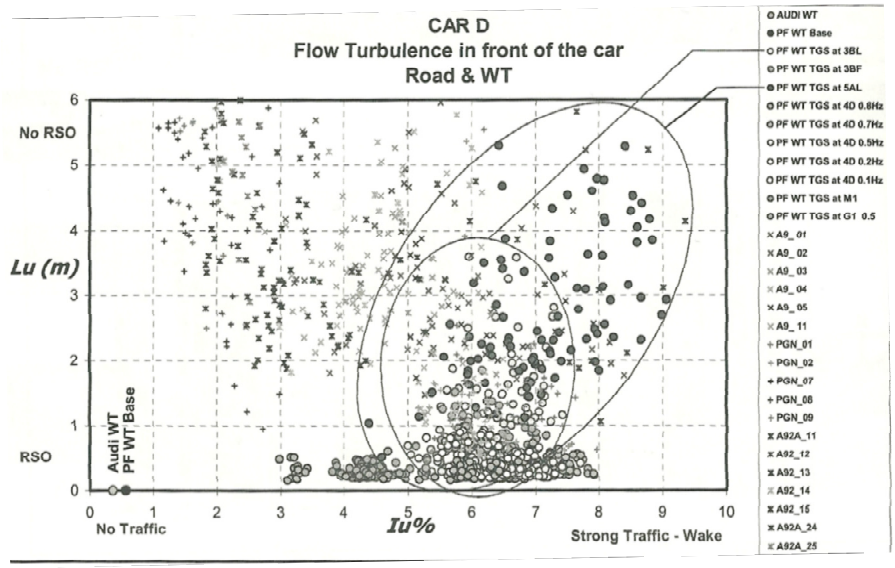


**Figure 14 - $L_V$ (m) vs. $I_U$ (%). Road and Pininfarina wind tunnel results for various TGS set-ups on the CAR-D model - Lindener et al (2009)**

Hopkins et al (2007) performed anemometer velocity measurements in the height range of 2.1 - 10.3m, which were adjusted by superimposing a longitudinal vehicle velocity of 31.5ms$^{-1}$ at the yaw angle determined from the angle experienced by the anemometer under test. The purpose was to adjust statically recorded velocity measurements such that they could be compared to and considered as on-road measurements for analysis, as the effect of the vehicle's speed significantly changes the resultant measured yaw angle from the vehicle's perspective relative to the actual flow angle. It should be re-iterated at this stage that a vehicle experiences varying onset flow due to its movement spatially through a domain, thus it experiences spatial flow variations temporally, therefore by superimposing a vehicle's speed on to the static measurements, the comparison could be made of whether the on-road wind flow characteristics are due to wind unsteadiness (i.e. time-variant at a single location) or also, or mainly, due to spatial variation (i.e. steady or unsteady single point air flows that vary from location to location).

From the anemometer readings, a mean lateral component of 0.01ms$^{-1}$ was recorded, suggesting that indeed lateral gusts do, over a few seconds, cancel themselves out. Measured velocities were between 2.8 and 5.2ms$^{-1}$ were recorded, with average longitudinal intensities range from 10 - 35% with lateral intensities ranging from 13 - 34%, with ratios found to be within a few per cent of being isotropic when recorded from a stationary point. Mast data also recorded by Hopkins et al (2007), again with superimposed vehicle velocity, returned intensities from 1.0 - 5.5%, with the average length scales

around 6 - 8m. TLS's were recorded between 16 - 28m at higher heights, with variations in height being far less significant than variations in time.

Data from Lawson et al (2007) also recorded mast-based measurements and on-road recordings. The on-road recordings were conducted using a 3-hole probe on a car's roof at a height of 1.42m. The on-road measurements showed yaw angles varying around ±14°, with infrequent peaks at ±28°. For a vehicle velocity of 28 - 36ms$^{-1}$, lateral component averages ranged from 1.5 - 3.6ms$^{-1}$, with the average longitudinal velocity being 31.8ms$^{-1}$, resolving to a 0.3ms$^{-1}$ average velocity increase above the 31.5ms$^{-1}$ vehicle speed (i.e. nominal probe speed). Longitudinal intensities were around 4.2 - 7.0%, and lateral intensities at 3.9 - 6.7%, giving a ratio of 1.0 : 0.93 ($L_U$ : $L_V$). Length scales were around 3.5 - 5.0m longitudinally and laterally at 2.4 - 5.6m, again giving a ratio of 1.0 : 0.87 ($L_U$ : $L_V$). Comparing results overall of mast with a superimposed longitudinal 'vehicle speed' of 31.5ms$^{-1}$ and car data, they correlated well with longitudinal and lateral wind speeds in or around 34ms$^{-1}$ and 4ms$^{-1}$ respectively, and intensities around 3% in both axes. TLS's were recorded between around 4 - 22m (though the 22m case is superimposed mast data, so arguably of lower validity).

Static, mast-based flow measurements showed that turbulence intensity varied between 2 - 6% over a height range of 2 - 10m, though cars would generally fall below or at the 2m threshold, thus being at the lower of these result ranges. TLS increases from 1 - 4m as height increases from 2 - 9m, with flow mainly isotropic in nature (i.e. within a couple of per cent of intensity). Watkins suggested a longitudinal TLS of 4m, which is smaller than those recorded by ESDU 85020, though readings reported in the datasheet were at higher wind speeds. This suggests a rough rule that TLS ranges from 4 - 20m for a windspeed of 3 - 10ms$^{-1}$. Work by Flay (1985) resulted in a graph of turbulence intensity for given road environments and heights, giving intensities at in u, v, w of 9.0%, 14.4% and 7.0% respectively at a 3.3m height, for a vehicle speed of 27.8ms$^{-1}$.

In terms of velocity distribution, the Lawson et al (2007) data, using mast data with a superimposed car velocity of 31.5ms$^{-1}$, recorded a Gaussian curve from ±20°, though the peak probability (of around 0.10) was at ±4.5°, and at this yaw longitudinal length scales were much larger than lateral scales. The Lawson data suggested intensities much lower than those for the mast, in the range of 0.7 - 2.4%, with variations between heights more significant than variations in time, with again relatively isotropic turbulence, at a ratio of 1.0 : 0.91.

Summaries of these results from Hopkins et al (2007), would suggest longitudinal scale ranges of 2 - 5m, and lateral ranges of 2 - 6m, and therefore relatively isotropic turbulence, which correlate well

with results of mast data for longitudinal scales around 2.6m and 2.8m for lateral values, and with Lawson's data of 4.3m for longitudinal TLS and 3.0m for lateral TLS. It was found that turbulence intensity generally gets higher as the wind speed falls as only small component velocity changes are required to greatly change the flow's yaw angle. It was also found that the lateral component of turbulence intensity is increased for a car exposed to the atmospheric wind.

Saunders et al (2000) performed on-road tests recording TLS's around 1.4 - 17.0m with an average of 6.5m. The power spectral density function showed a low frequency peak close to 1Hz and the majority of the energy before 10Hz, with the von Karman curve correlating well with the measured results between 1 and 20Hz.

A review by Swalwell (2005) covering Sacre et al (1987) found intensities did not vary that greatly with height (<30m) with longitudinal intensities of 0.10 - 0.17% and TLS between 20 - 40m.

Watkins et al (1990) also reviewed commercial vehicle drag including the analysis of unsteadiness. Watkins' findings showed a wide range of intensities and length scales for all three axes, from 1 - 15%, at length scales 2 - 30m, suggesting that due to such a wide range of values that reviewing the power spectra is to be more advantageous. Watkins suggested that for approximately 98% of the day time the natural wind will be less than $10ms^{-1}$ at 2m, this gives turbulence intensities in u, v and w of 0 - 11%, 0 - 8% and 0 - 4% respectively, for a vehicle speed of 62mph and winds up to $10ms^{-1}$ for various orientations to the road.

Watkins noted that American highways have an average windspeed of $3.11ms^{-1}$, giving u, v and w turbulence intensities of 1.5 - 2.5%, 1.5 - 2.2% and 0.7 - 0.9% respectively. Watkins comments that the length scales do vary according to windspeed, with the highest intensities being for sub $1ms^{-1}$ winds. Stronger winds (those around $8ms^{-1}$) gave lower intensities and for smooth upstream fetches, longitudinal intensities of 13% and lateral intensities of 11% being typical. Roadside obstacles notably increased turbulence intensities for a given windspeed, with lateral intensities shown to be able to double in magnitude and longitudinal intensities increasing by 10% (Cogotti et al (2003)). Additionally it was shown that the wake of a car produces approximately 8% turbulence intensity.

Finally a coast-down technique experiment by Bischof et al (2008) was conducted to see varying aerodynamic loads in real-world conditions on BMW's test track. A deceleration plot from 160 - $120kmh^{-1}$ was shown, with a recorded longitudinal intensity of 0.96 - 1.54%. A frequency of recorded turbulence showed a peak response at 1.25Hz (as per previous sources, supporting that the

range from 1 - 10Hz being critical, but in this experiment the range from 0.2 - 2Hz was of the highest importance). The author also highlighted a noticeable response corresponding to a TLS of 30m.

The key result from the numerous sources shown is that the flow characteristics greatly vary with height location, and therefore measured intensities and length scales need to be assessed based upon their measurement height, and as such measurements close to vehicle height should be seen as dominant. In comparing on-vehicle to statically recorded measurements, length scales and intensity differences exist (i.e. Wordley to Lawson). This is mainly because the flow characteristics that a vehicle experiences are significantly the net result of a vehicle's motion through both steady and unsteady flows. Therefore on-vehicle data (i.e. Wordley) offers the best insight into true on-road flow conditions as it is recorded at vehicle height and is a measurement of flows experienced under vehicle motion.

All of the on-road environment sources reviewed are summarised in Figure 15 and Figure 16. Figure 15, a display of turbulence intensity with measurement height, shows a general trend of a decrease in intensity as height increases. At vehicle height, around 1.5m, turbulence intensities are ranging from 1 - 15%, with measurements taken at higher heights resulting in turbulence intensities from 1 - 23%. The results also show that on-vehicle measurements tend to show lower intensities than stationary measurements, for comparable measurement heights. The linear lines of best fit are shown to give a simple trend of the effect of increasing height on turbulence intensity, though of course they cover a variety of measurement methods (i.e. on-road and static) and therefore are only for illustration purposes.

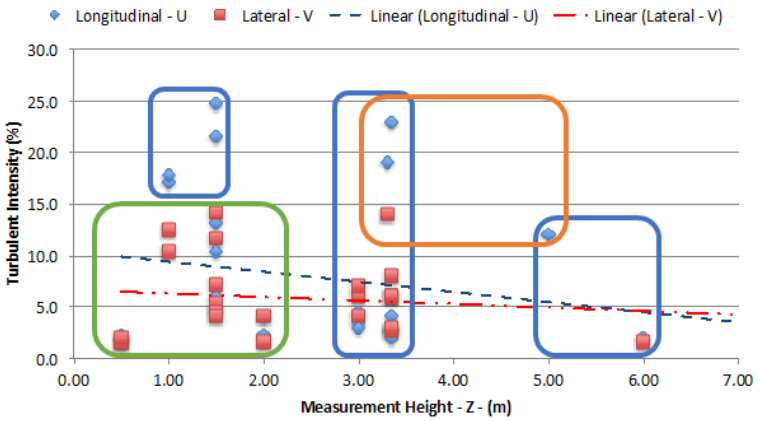


| Key | Environment | Sources |
|---|---|---|
| | On-Road On-Vehicle | ESDU 85020 - Flay et al (1985)<br>Watkins et al (1990)<br>Lawson et al (2007)<br>Lindener et al (2007)<br>Bischof et al (2008)<br>Wordley et al (2009) |
| | On-Road Stationary | ESDU 85020 - Flay et al (1985)<br>Hopkins et al (2007) |
| | Stationary | Hopkins et al (2007) |

Figure 15 - Summary plot of longitudinal and lateral turbulence intensities plotted against height of measurement probe

Figure 16 shows a gradual increase in turbulence length scale with measurement height (presented in their reported form, evaluated by auto-correlation for all results). The linear lines of best fit are shown to give a simple trend of the effect of increasing height on turbulence length scale, though of course they cover a variety of measurement methods (i.e. on-road and static) and therefore are only for illustration purposes. The result show that a TLS of 2 - 15m is typical in the vehicle height region (i.e. Z ≈ 1.5m), with turbulence length scales increasing with height location. The results also show that on-vehicle length scale measurements tend to be shorter than those taken at a stationary source, primarily due to a vehicle's velocity causing a turbulence yaw variation to occur over a shorter time period.

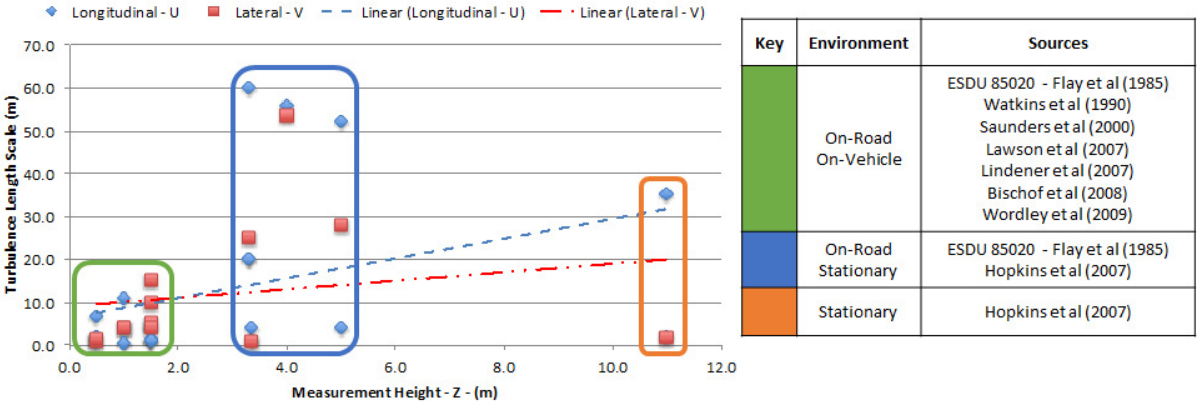


| Key | Environment | Sources |
|---|---|---|
| | On-Road On-Vehicle | ESDU 85020 - Flay et al (1985)<br>Watkins et al (1990)<br>Saunders et al (2000)<br>Lawson et al (2007)<br>Lindener et al (2007)<br>Bischof et al (2008)<br>Wordley et al (2009) |
| | On-Road Stationary | ESDU 85020 - Flay et al (1985)<br>Hopkins et al (2007) |
| | Stationary | Hopkins et al (2007) |

**Figure 16 - Summary plot of longitudinal and lateral turbulence length scale plotted against height of measurement probe**

Finally, Figure 17 is a plot of TLS against intensity for a range of measurements reviewed. It can be seen that TLS and Intensity for longitudinal waveforms remain rather proportional regardless of the intensity, such that all intensities (up to a limit) can be expected at a respective length scale. With lateral turbulence, there is however, a greater correlation showing that a proportional increase with length scale will show an increase in intensity, which is slightly contradictory to Wordley et al (2009) who showed a linearly decreasing correlation of intensity with length scale.

Turbulence length scales at the height of a vehicle tend to be relatively shorter in length (i.e. 14m), but with a relatively wide range of turbulence intensities (i.e. 0.5 - 9.0%). Stationary measurements tend to report greater length scales, though comparable turbulence intensity measurements to those taken on a moving vehicle.

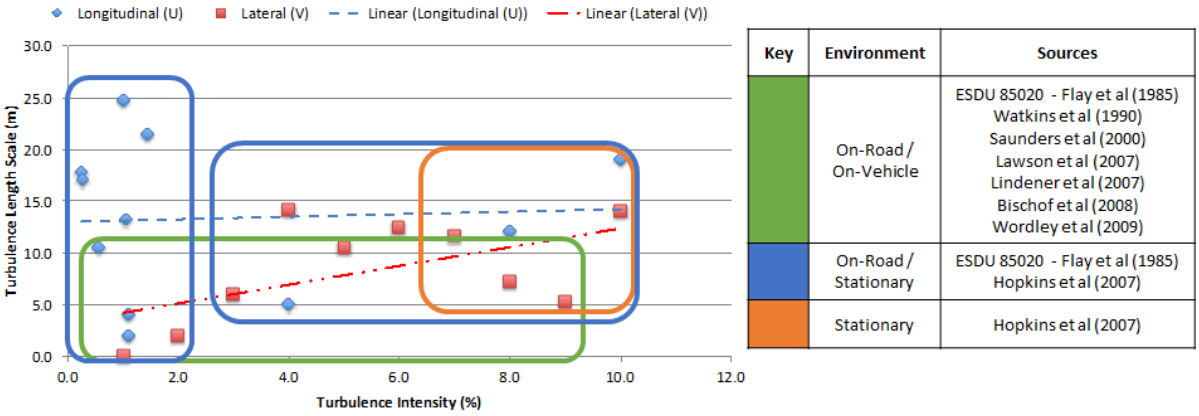


| Key | Environment | Sources |
|---|---|---|
| | On-Road / On-Vehicle | ESDU 85020 - Flay et al (1985)<br>Watkins et al (1990)<br>Saunders et al (2000)<br>Lawson et al (2007)<br>Lindener et al (2007)<br>Bischof et al (2008)<br>Wordley et al (2009) |
| | On-Road / Stationary | ESDU 85020 - Flay et al (1985)<br>Hopkins et al (2007) |
| | Stationary | Hopkins et al (2007) |

Figure 17 - Summary plot of longitudinal and lateral turbulence intensities plotted against length scale

## 2.2 Physical Simulation of Turbulence - Passive Methods

This section reviews a variety of approaches made for passive turbulence generation. Such systems generate flow unsteadiness by creating drag, such as plates, grids or bars. None of the systems discussed in this section vary or move in their operation. The generation of unsteadiness is simply due to the creation of wake turbulence by placing an object into the flow that has a downstream diffusion angle that is too great for flow to remain attached and therefore trailing vortices are generated. Length scales generated are typically in order of the size of the frontal geometry of the object, though plates and square bars, due to their sharp edges, can generate much shorter length scales than their widths. Due to the nature of the turbulence (i.e. wake generated), the turbulence typically decays rapidly and at a rate in proportion to the size of the vortices and therefore the distance between grid and model location needs to carefully consider tunnel speed and grid spacing. Furthermore, it takes time for the turbulence to become uniform and isotropic, again varying on grid spacing and tunnel speed.

Many tests have been conducted where mesh grids, of either rods or flat plates have been constructed and placed upstream in a wind tunnel and then the length scales and intensities measured at various locations downstream. Tunnels reviewed range between 0.5 - 2.0m in cross-sectional area, operating between about 10 - 20ms$^{-1}$. The first set of reviewed tests were conducted by Bearman et al (1994) and Aynsley et al (1977), who both took grid meshes varying from 90 - 25mm diameters (with one test at 180mm diameter) and assessed the length scales generated. They found that the frequencies generated increased with turbulence intensity, for a range of grids placed into the tunnel nozzle, ranging from 180 - 25mm rod diameter measured at a location 3.7m downstream from the tunnel's nozzle. Generated ranges of intensity from 1.7 to 12.0% (large intensities only at very large spacing where the flow was still non-uniform at the measurement location) and length scales from 0.07 to

0.19m were found. These results are compiled in Figure 18, which shows a general increase in flow intensity against bar diameter, a variation of bar diameter from a few millimetres to 40mm only varied the intensity by a few per cent. The results also suggest that the upper limit of intensity generated is constrained by the size of the tunnel. For example, as the generation of 10% intensities is desired, bars of 200mm width would be required of which only a few would fit into a nozzle's width, thus greatly limiting the actual achievable length scale. Additionally, it was noted (Bearman et al (1994) and Aynsley et al (1977)) that distances in the order of 10 - 20 times the grid spacing are required for the turbulence to become uniform, requiring a very long test section (especially as the grids need to be placed downstream of any contraction otherwise the length scales and intensities are reduce as the flow is funnelled).

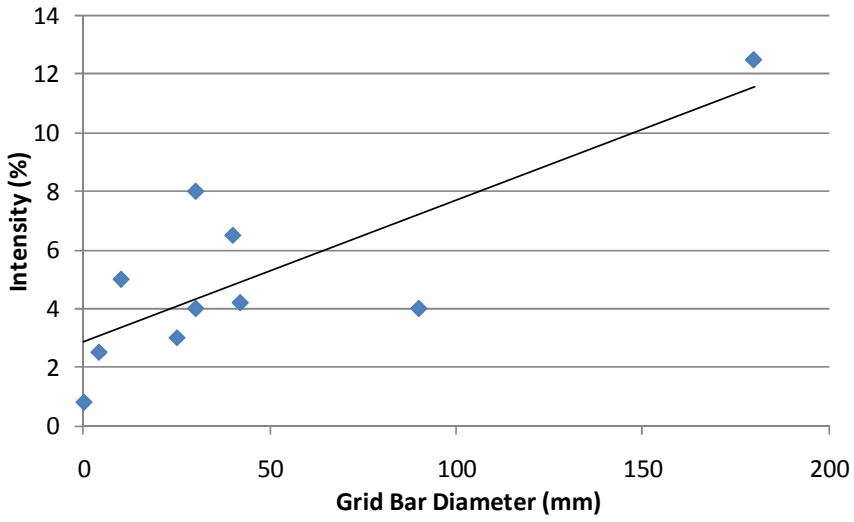


Figure 18 - Summary of results; Grid bar diameter against turbulence intensity - Bearman et al (1994) and Aynsley et al (1977)

Swalwell (2005) reviewed grid based turbulence generation, including work by Liu (1992), Bearman et al (1983) and Stack (1931) with square grid meshes. These tests generated intensities between 8% and 20%, with isotropic turbulence found and the unsteady air flow decaying rapidly. Jancauskas (1983), Mish (2001) and Devinant et al (2002), repeating Stack's experiment, generated intensities between 3.8% and 17.1%. However Huang et al (1999) generated much smaller intensities, as low as 0.45%, and length scales from 0.13 to 0.02m, and Neff et al (1985) with similar tests, resolved values in the middle of this length scale range. Swalwell performed tests with mesh grids, ranging from 0.04 to 0.30m, finding intensities from 2 - 13% and length scales from 0.03 - 0.13m, with the larger scales and intensities coming from the larger grid meshes. These were measured using a von Karman analysis (as

per Iyengar et al (2001)). The important conclusion from this wide range of tests is that no length scales were generated greater than the size of the mesh rod diameter or the mesh spacing. A summary of these results can be seen in Figure 19 where it is evident that increasing the grid spacing increases both length scale and intensity (but this is limited by tunnel dimensions) and that turbulence length scales increase slightly with distance downstream whereas turbulent intensity gradually decays, as shown in Figure 20.

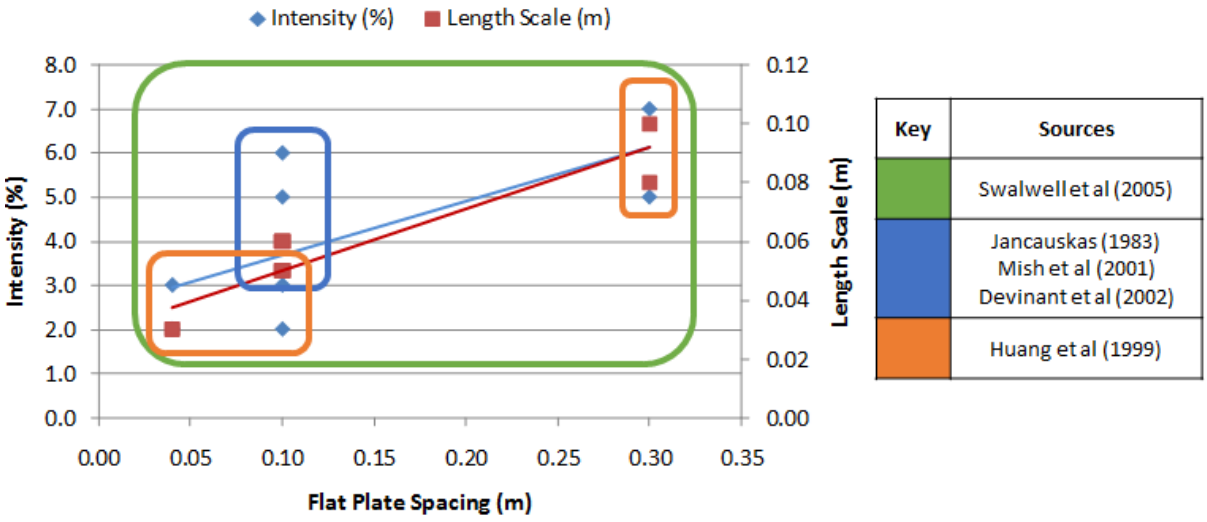


Figure 19 - Variation of length scale and intensity with downstream location (0.00 - 0.35m) and plate spacing interval

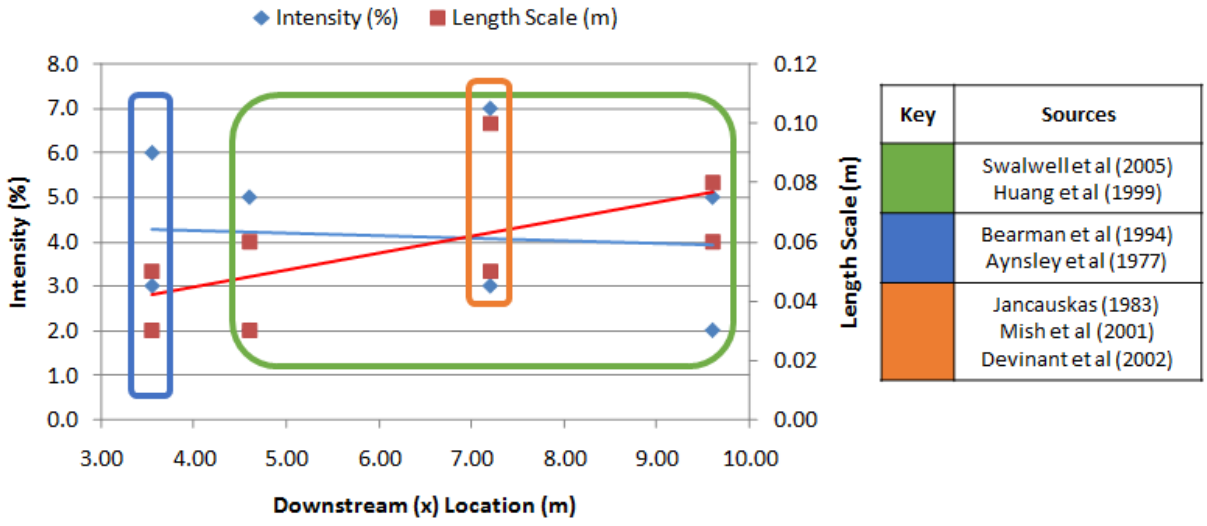


Figure 20 - Variation of length scale and intensity with downstream location (3 - 10m) and plate spacing interval

Several simulation techniques were reviewed by Watkins (2007), including Simmons et al (1934), Corrsin et al (1966) and Batchelor et al (1948). These experiments commented on how the turbulence from passive grids takes 2 - 3 grid spacing in downstream distance to fully generate, and then decays,

with an optimum generation location of around 35-mesh grid widths downstream. Isotropic turbulence was generally found and the longitudinal length scales being slightly larger than the other component length scales. TLS's being generated were typically smaller than the grid spacing (i.e. very short,) with flat plates and square bars proving better than rounded bars as they has little or no Reynolds's number dependence. This suggests that the importance of distance between the TGS location and turntable centre (TTC) is significant for correct TLS generation using grids.

Newnham et al (2006) and Watkins and Saunders (1998) using 50mm spacing static mesh wire grids of 3mm diameter to generate turbulence of up to 5% intensity and with diameters of 10mm to generate intensities around 1.5% and TLS's around 15mm. The experiment was continued with flat plates, in order to increase the plate width of blockage and blockage ratio, with length scales increasing in scale with the width increase, at larger intensities, but still less than 5%. Newnham et al (2006), then moved to a larger tunnel, with correspondingly wider flat plate grids, and naturally the length scales increased, again in proportion to the plate width, with length scales as high as 0.17m, but still with intensities under 5%. Hopkins (2007) and Garry et al (1986) performed similar larger scale tunnel experiments, but successfully creating intensities up to 16%. Watkins (1990), undertook analysis of the effects of unsteady flow on commercial vehicle drag using grids, similar to Newnham et al (2006), but this time with only horizontal bars (to see if single-axis wakes would generate differing length scales and intensities). Intensities around 2 - 5% were created, with the test set-up as shown in Figure 21. These series of tests all highlight that even with large wind tunnels and wide widths of plate and bar, the TLS generated are still far too small for automotive test work and that the intensity cannot be reliably controlled.

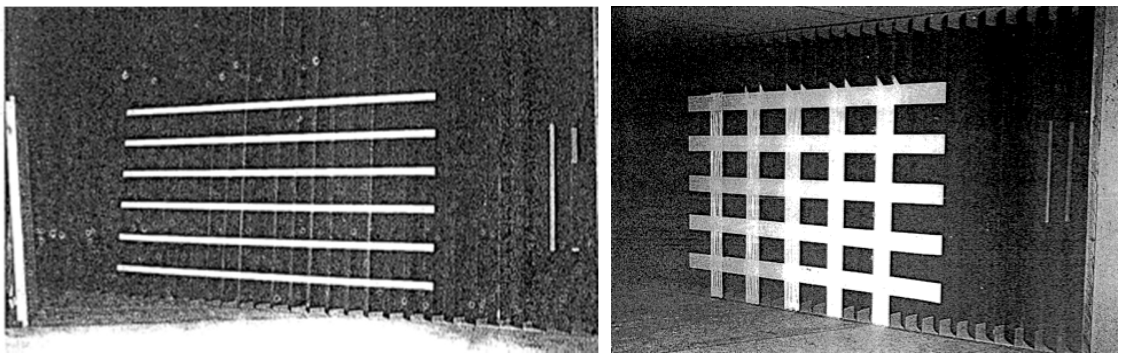

Figure 21 - Grids used to generate turbulence - Watkins (1990)

One noteworthy result, as mentioned earlier but detailed by Watkins, was the good flow uniformity possible from these grid systems. This is shown in Figure 22, where, for almost all of the range of grids

tested, it can be seen that the intensity is uniform over the tunnel height. Table 1 shows the codes, G1 - G5, which represent the grid widths (with NG representing a no-grid configuration):

Table 1 - Grid size and spacing configurations - Watkins (1990)

| Grid Number | Horizontal Width (mm) | Vertical Width (mm) | Horizontal Spacing (mm) | Vertical Spacing (mm) |
|---|---|---|---|---|
| G1 | N/A | 50.8 | N/A | 152.4 |
| G2 | N/A | 50.8 | N/A | 304.8 |
| G3 | N/A | 177.8 | N/A | 939.8 |
| G4 | 177.8 | 177.8 | 533.4 | 939.8 |
| G5 | 177.8 | 177.8 | 533.4 | 469.9 |

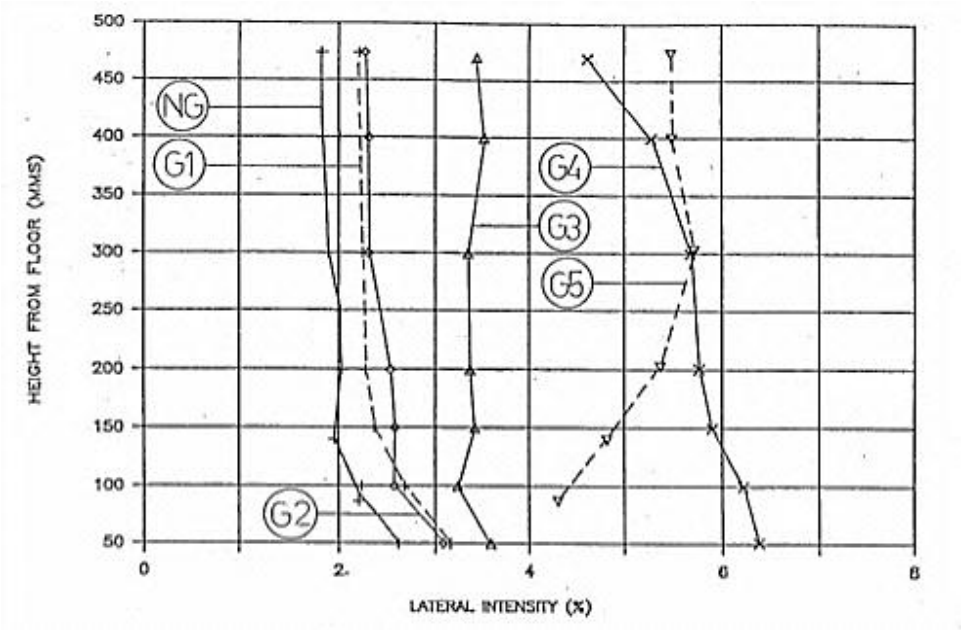


Figure 22 - Grid test results - Watkins (1990)

An area of passive turbulence generation that has been gaining recent attention is that of fractal grids. A fractal grid is a grid where the width and spacing varies throughout the grid structure, as opposed to wire or plate mesh grids where the spacing and width are constant throughout the structure. Typically the overall fractal grid is composed of multiple similar grids at different levels of magnification. Fractal grids generate small scale, high frequency turbulence with a greatly reduced decay rate of turbulence length scale and intensity, thereby making them more favourable for test work in comparison to square grids. The reduced decay rate of turbulence with fractal grids is due to their differing spacing and widths throughout the structure generating a broader spectrum of length scales and intensities.

Nagata et al (2008) undertook a series of tests of fractal grids using CFD. Like square-grid generated

turbulence, the turbulence was found to be homogenous and intensities around 10% were created (depending on tunnel speed, scale of grid and geometric arrangement, see Figure 23 which is an example of a fractal grid from Nagata et al (2008)), where 'd' represents the spacing between bars within the grid and 'M' represents the distance between similar structures within the overall structure.

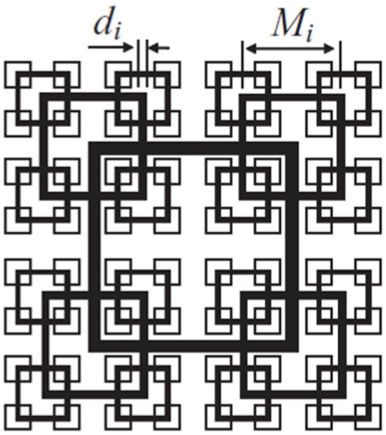


**Figure 23 - A typical fractal grid, with dimensions d=0.3 - 3.0mm and M=0.5 – 2.0mm - Nagata et al (2008)**

The test results for the fractal grid in Figure 23 are shown in Figure 24, which compare the $TLS^2$ (measure of width variance, used to represent TLS) against proportion downstream location over test section longitudinal location ($^x/_{L_X}$). The results show turbulence length scales around 0.1m were generated and good consistency of turbulence length scales and intensity down the length of the tunnel, with relatively high intensities created for a passive turbulence generation system. The improved turbulence consistency is due to the differing spacing and bar diameters occurring throughout the grid mesh causing a broader spectrum of length scales to be generated. This reduces the energy dissipation rate of the vortices in the flow, particularly due to the presence of higher length scales which typically dissipate over a greater downstream distance, resulting in the overall turbulence structure that is sustained for a greater downstream distance.

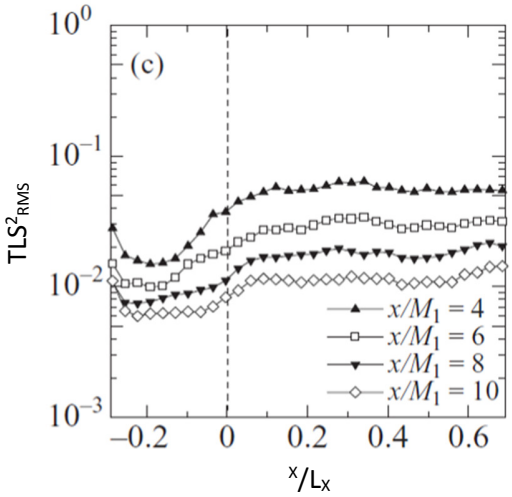


Figure 24 - Flow intensity for test section location - Nagata et al (2008)

An analysis of the decay rate of fractal grid generated turbulence was undertaken by Hurst et al (2007), which found that fractal grids generate turbulence with much higher intensities than square grids. The turbulence length scales did not significantly decay throughout the length of the test section. A plot of a variety of grids tested is shown in Figure 25, with the key result being the turbulence intensity (plotted as variation in local velocity of freestream, $^u/U$) being consistent over the downstream tunnel length. As explained earlier, the reduction in turbulence decay rate is due to the broader spectrum of length scales in the flow (the $\beta_L$ value represents the size scaling between each of the fractals meshes in one grid, so a larger number is a greater spacing).

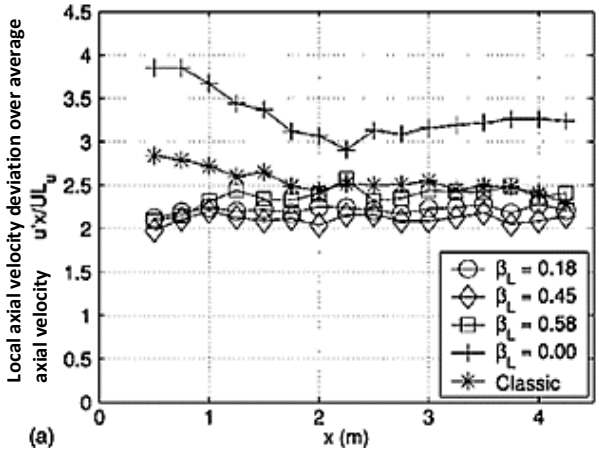


Figure 25 - Results from the testing of fractal grids - Hurst et al (2007)

When a comparison of lateral flow homogeneity was reviewed by Hurst et al (2007), as seen in Figure 26 in terms of local velocity variation ($u'$) over average flow velocity (U), fractal grids showed no benefit over square grids. The lines in Figure 26 plotted from top to bottom are ordered in terms of a decrease

in the number of bars in the grid for a fixed overall size of grid, and hence a decrease in net blockage.

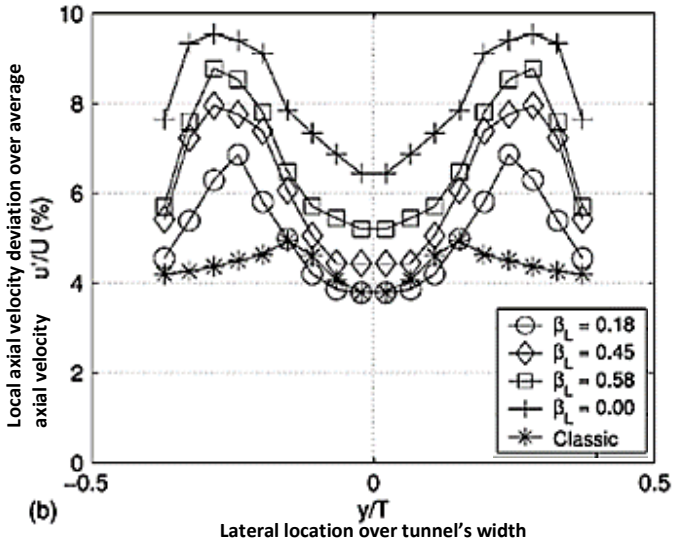


Figure 26 - Flow lateral homogeneity - Hurst et al (2007)

Figure 27 shows the variation of longitudinal to lateral length scales for tunnel downstream distance, with the flow structure taking around 0.5m of tunnel downstream distance to settle. The $t_r$ value represents the range of grid spacing in the fractal grid, with the $t_r$=2.5 being a grid bar diameter range of 9.5 - 3.8mm to $t_r$=17.0 being a grid bar diameter range of 25.8 - 1.5mm.

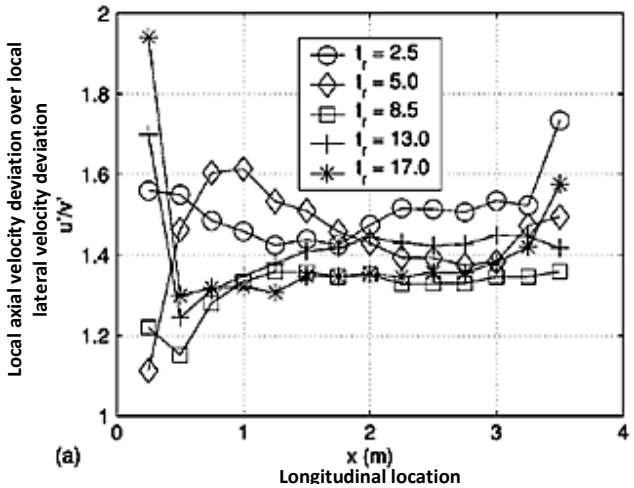


Figure 27 - Flow longitudinal homogeneity - Hurst et al (2007)

In summary, passive turbulence generation systems, whether wire grids, flat plates or fractal grids, all show the ability to generate turbulence, with a range of intensities up to 16% and with some flow structure consistency. However, none of the passive methods are able to generate turbulence length scales that are found to be dominant in the on-road wind environment.

## 2.3 Physical Simulation of Turbulence - Active Methods

The variety of methods that can be used to generated turbulence actively was reviewed. This section is split between drag and lift devices and also reviews papers that used other powered methods. Active devices have their geometry or orientation vary whilst in operation, and generally generate longer length scales than passive devices (that are static at all times). Hence, for the length scales desired, active devices are more suitable for automotive turbulence generation. Drag devices use vortex shedding as their main generation method, whereas lift devices change the angle of the flow rapidly and powered devices vary the local or freestream velocity of the flow. With active devices, their rate of variation or movement generally controls the length scales generated, whereas their peak amplitude determines the turbulence intensity (e.g. Cogotti (2003)).

### 2.3.1 Drag Devices

The Pininfarina wind tunnel uses a dynamic system with vanes oscillating between 0 - 1Hz, with phase control. Cogotti (2003) noted that the TGS at Pininfarina aimed to replicate the general wind frequency and intensity spectrum, not just individual gusts (i.e. $U_{WIND} < 10\ ms^{-1}$). The TGS was placed upstream of the contraction, with measured turbulence intensities of 8% for a TLS of up to 2.0m. The Pininfarina system generates 2 - 4° flow yaw at 0.2 - 0.8Hz, and hence operates just below the quasi-steady limit (based upon reduced frequency, which is discussed in detail later on p.40, but is considered to be around 0.76Hz). The device is also able to simulate the flow of following vehicles (i.e. overtaking manoeuvres), with up-wash or downwash configurable and the vortex magnitude and position determined by set-up.

Figure 28 shows the TGS vanes, which are located upstream of the nozzle and can each be controlled independently.

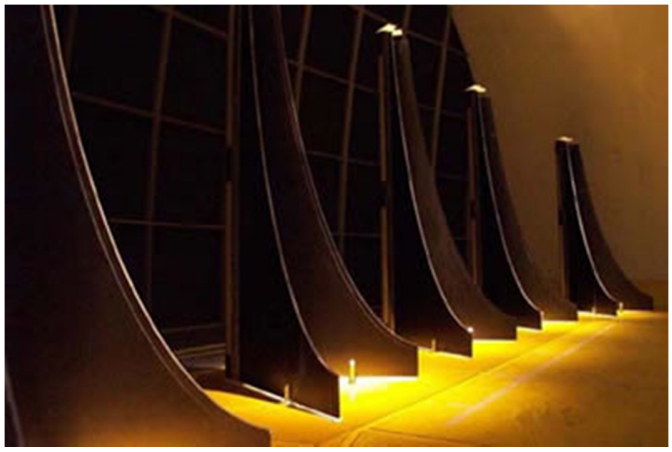

Figure 28 - Pininfarina TGS vanes - Cogotti et al (2007)

Holdsworth (2005) designed a TGS which comprised of a removable set of vertically mounted vanes. The modes of operation varied frequency, amplitude and phasing of the vanes to control downstream flow conditions. A range of tests were undertaken, operating at a variety of modes, which showed dynamic peaks shown due to the forced excitation of the air, with intensities around 2% and length scales around 10m. It was found that increasing the amplitude only increased the turbulence intensity to an extent and clearly this is a limit with drag devices, whereas lift devices should create proportionally greater intensity for greater peak amplitude.

The device generated isotropic turbulence by flapping large vanes creating trailing vortices at the edges of the blades, introducing additional low TLS's. The largest lateral turbulence intensities were created using the smallest phase shift between vanes ($45^{o}$). A recommendation for higher TGS oscillating frequencies was made for future designs, which would create more vane movement, creating larger lateral intensities and hence better tri-axis ratios. This device was therefore effective at turbulence generation, but due to being a drag device created additional high frequency components, which are undesirable as their skew the spectral energy distribution relative to the on-road environment.

Cooper (1989) developed an oscillating grid of orthogonal plates that were laid out to create a 'V' shape, with the apex orientated in to the wind. These could each be operated at different frequencies and phases creating a range of length scales and intensities. The TGS created a power spectrum (see Figure 29) comparable to the on-road environment with potentially greater length scales possible for larger tunnels. The spectrum demonstrates that the system was able to generate meaningful levels of intensity for relatively large turbulent length scales (i.e. approximately 4m), and even though drag TGS

systems can cause excessive high frequency turbulence, the higher frequency components were not overly prominent in this design.

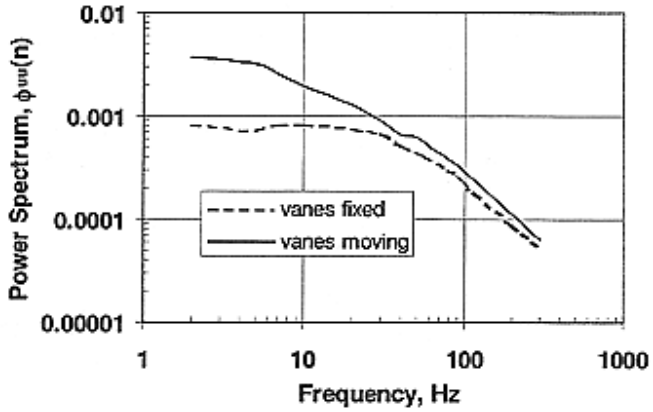


Figure 29 - Power spectra from of an oscillating grid - Cooper (1989)

Wasco (2003) conducted a swinging pendulum rig test at RMIT, though static grids, which were placed upstream, were more significant in generating turbulence. The pendulum swung in the settling chamber upstream of a contraction, pivoted from the roof. The rig generated around 0.5% intensity and 0.33m TLS, with maximum scales generated being between 0.8 - 0.9m, around 3-times greater than the width of the pendulum, peaking at an oscillation rate of 0.46Hz, with intensities peaking at 3.3%. Though the vortex shedding from the bluff nature of the pendulum was more significant in the turbulence generation, as the TLS and intensities were frequency dependent, it is reasonable that the oscillation was important in the characteristics of the turbulence created. However the energy spectrum created too little energy at low frequencies and too high energy at high frequencies.

Bienkiewicz et al (1983) demonstrated how grid turbulence could be modified by active control, namely using a pulsating grid. He showed that for static grids, once the grid bar diameter or plate width has become too large, flow instabilities occur (i.e. large regions of recirculation or inconsistent vortex shedding) and hence a TLS limit is reached, typically 10 - 13% of tunnel test section width. Two grids were used, oscillating 180$^{o}$ out of phase, with the pulsations increasing the TLS by approximately ten-fold, but with still relatively short TLS for automotive test work. By careful modification of the geometry of the grid's input signal, the oscillating grids could produce the same spectrum shape as static grids, but with controllable intensity and TLS. The maximum length scale generated exceeded the width of the tunnel (i.e. 0.91m). The pulsating bars had intensities at 4 - 17% at 0.8 - 1.2m TLS (comparable with 0.1m TLS when static), with good flow uniformity across the tunnel's cross-section.

Kobayashi et al (1992) used an array of 12-plates, arranged horizontally, consisting of some fixed and some driving plates. The array also had 16-aerofoils, chord 0.1m, and to reduce the turbulence from the plate vortices, a separate array of plates and meshes were installed as in Figure 30. Flow was measured with intensities around 5% for up to 20$^{o}$ of incidence (up from 1 - 2% when static). Using a means-of-least-squared analysis returned a longitudinal scale of 1.07m and an auto-correlation TLS of 1.24m, with good flow uniformity found laterally and horizontally, but less so vertically. This TGS, like that of Knebel et al (2010) (to be reviewed later in this chapter) showed good intensities for the intermediate range length scales that would be difficult to achieve with lift devices. Such oscillating plates could be used in conjunction with any lift system to compensate and adjust spectral energy components.

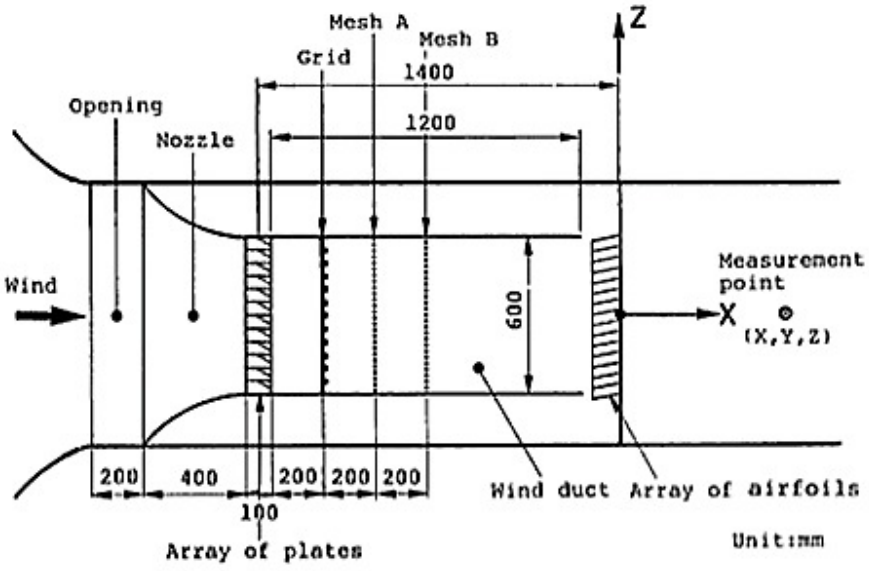


Figure 30 - Experimental set-up - Kobayashi et al (1992)

An experimental study of wind turbine aerofoil aerodynamics in high turbulence by Devinant et al (2002) was undertaken and a flow turbulence generator was made, operating between 0.5 - 16.0% intensity to create an environment for turbine blade testing in 'real-world' conditions.

Square tubes were placed at the nozzle exit, upstream of the test section, with varying tube width and spacing, as in Figure 31. The length scales were found to be very short, with poor flow uniformity, and therefore not suitable for automotive turbulence generation.

Figure 31 - Square grid set-up - Devinant et al (2002)

Knebel et al (2010) focussed on generating 'real-world' length scales for smaller wind tunnels. Knebel noted that the length scales generated by passive devices are limited to the size of the tunnel, which in itself limits the separation size between components in a passive generation device of which the small scales generated then decay with test section length. Knebel suggested that since an active device can dynamically vary the blockage of a tunnel, they are of greater capability for controlling the objective length scale. The final design of their TGS is shown in Figure 32.

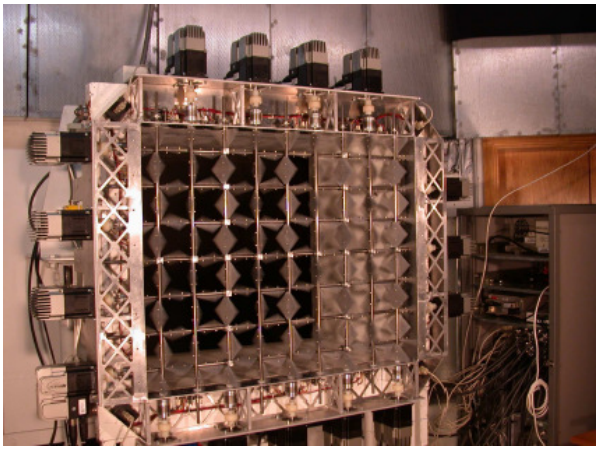

Figure 32 - Active diamond grid - Knebel et al (2010)

The active grid used is a 7 x 9 set of 0.1 x 0.1m diamonds, with 0.11m separations between the diamonds. Each axis is driven by stepper motors, with the input fluctuation pattern being based on 10ms stepped movements. Figure 33 is a plot of the power spectrum distribution for varying plate angles (α). This spectrum is surprisingly similar to that suggested by Wordley for a static mode, with high power spectral density for sub-10Hz frequencies, but with length scales around 0.05m and peak

intensities around 13%, with a noteworthy result being that the peak intensity was reached at 80°, rather than the expected 90°, plate incidence angle.

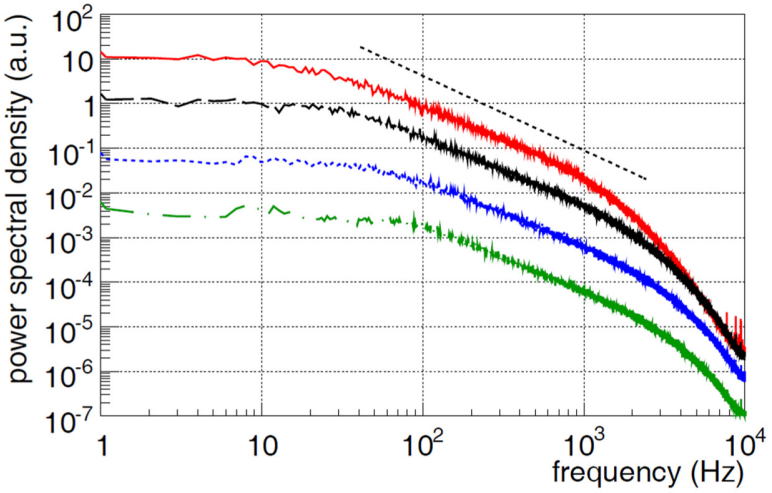


Figure 33 - Power spectra for four different stationary angle positions (passive mode) - Knebel et al (2010)

The power spectra are shifted by one decade against each other for clarity. The power spectra correspond to α=60°, 40°, 20° and 0° from top to bottom. Dotted Line indicates $-5/3$-power law. Measurements were taken 12-mesh widths behind the grid for a reference velocity of 18.4ms$^{-1}$

The movement of the diamonds was controlled using a probabilistic method and several modes of operation were designed with each successive movement being an increase in the random allowable deviation of angular movement. The operation was then tested in an active mode, with the results in Figure 34, showing a similar capability as seen in and describe from Figure 33.

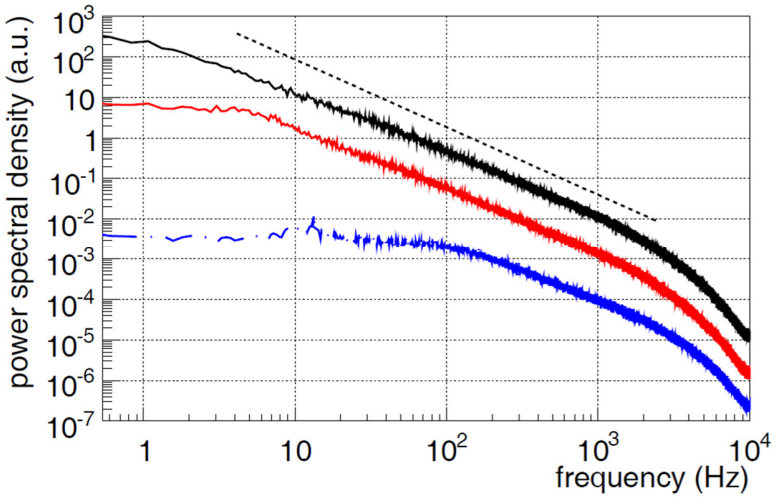


Figure 34 - Power spectral density for the active and passive mode of the grid - Knebel et al (2010)

Results shifted by one decade with respect to each other in vertical direction for clarity. From top to bottom: 2nd type, 1st type, passive mode (the dotted line marks the $^{-5}/_{3}$ law)

The length scales generated were in the region of 0.36 - 1.20m. For an approximately 1m$^2$ tunnel, or 20% model scale, this gives 'real-world' scales in the region of 1.5 - 6.0m. This is a very significant breakthrough as length scales below 10m (full-scale) are hard to generate using aerofoils and scales greater than 0.6 - 0.7m are hard to generate with passive grids. Though not fully achieving the desired power spectrum for automotive test work, the intensities are still very suitable when compared to distribution by Wordley and hence could form an integral part of a full-range TGS system. Such a device can run more slowly (i.e. quasi-statically) to generate other atmospheric wind conditions.

Cekli et al (2009) conducted tests to generate homogenous and shear turbulence using a 2D-grid of diamonds with the 2D-axes controlled individually using stepper motors, as depicted in Figure 35. The aim was to generate a real-world wind velocity profile much earlier in a test section than could be generated by either requiring a long test-section or through passive methods (which also demand a long test-section). The grid used by Cekli consisted of 7 x 10 diamonds with a mesh size of 0.1m and measurements were taken 4.6m down from the grid (with no contraction). Precise control of all of the diamonds created an accurate real-world wind velocity profile, with the factors for exact axes determined from trial and error. It was found that increasing the tunnel floor roughness made the accurate generation of the velocity profile much harder.

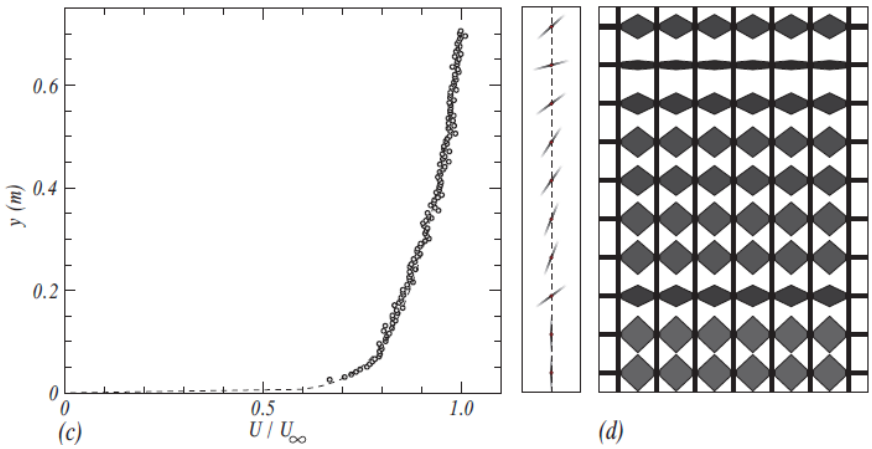


Figure 35 - ABL generated from an active grid. $V_{REF}$=9.8ms$^{-1}$, frequency 6Hz at 7.2° plate angle - Cekli et al (2009)

A review of active methods by Watkins (2007) showed that moving grids have successfully created turbulent length scales greater than grid bar separation distances. This conclusion was developed from reviewing work by Ling et al (1972), Sato et al (1974) and Makita et al (1991). No length scales or

intensities were described, but it is reasonable to assume that they would be in the order of the other devices described in this section, which are of low intensity with TLS not much greater than the separation distance between the bars. Though some devices have been shown to create reasonable spectra, especially that of Knebel's, one major problem of drag devices (active or otherwise) is the high frequency vortex shedding that propagates over a model, potentially corrupting pressure and force measurements over a test model, which could be avoided with lift devices.

### 2.3.2 Lift Devices

Lift devices aim to generate their turbulence through turning the air flow as opposed to merely deflecting or relying on the trailing vortices or a sharp edge. An example of this is the simulation of gusts by Bearman et al (1994) where turbulence was generated using flapping vanes, with TLS ranging from 1 - 10m operating at angles up to ±8°. A pair of vertical, pivoted, symmetric aerofoils was connected to an electric actuator, which oscillated the aerofoils in phase. The aerofoils were part of a resonant system in order to minimise power demands, driven at their natural frequency. The aerofoils had a chord of 0.2m, separation of 0.4m and placed 0.7m upstream of the model, with a maximum operating frequency of 25Hz corresponding to around 20ms$^{-1}$ freestream, with maximum air flow deflection at 15° incidence. The peak flow angle achieved was equal to about $^{2}/_{3}$ of the peak aerofoil angle - described as the non-dimensional gust amplitude. Good flow uniformity of the transverse gust was achieved across the width of the model. To improve flow, a much smaller and in-phase amplitude intensity component at double the aerofoil frequency was introduced, which itself had turbulence intensities around 3 - 8% with TLS around 20% of model length.

At the FKFS facility at the University of Stuttgart, as discussed in Schröck et al (2009), a TGS was constructed (Figure 36) and tested that uses a series of vertically aligned aerofoils, just downstream of the nozzle operating on a 1.65m$^2$ tunnel at 80ms$^{-1}$. Length scales in the order of several vehicle lengths (at 20% scale) were generated, with intensities up to 7%. Though a crosswind test facility, their approach is to generate turbulence in the axial freestream direction and independently control vehicle yaw, hence using separate TGS and vehicle yaw devices. Crosswinds of significance are generally greater than one vehicle length (i.e. Wordley et al (2009), Sims-Williams (2011)), hence the focus of FKFS's system. Four aerofoils were used, each around 1.5 times the height of the test model. An auto-correlation TLS of 0.8m was determined (at scaled size) representing a 4m length scale at full scale, with flow yaw for 90% of the time being within ±5°. The tunnel generated an accurate von Karman curve up to 15Hz. 15Hz x TLS / 80 = 0.2 → TLS $L_V$ = 1.06m which equates to 5.2m full scale,

which was their cut-off of the von Karman spectral curve, though lateral scales down to 4m were robustly recreated.

Figure 36 - FKFS TGS facility - Schröck et al (2009)

In general, the use of lift devices has been under-explored, and the results from the works of Bearman and Schröck suggest that this area has great potential assuming suitable frequencies can be generated (i.e. mechanically that the aerofoils can oscillate at sufficiently a high frequency).

Figure 37 shows a yaw angle against time trace generated using the FKFS TGS system, a 5-second random flow trace with peak yaw angles within ±10°. Figure 38 is the lateral velocity spectrum of the generated flow with the theoretical von Karman curve included for comparison, showing a robust correlation up to 15Hz.

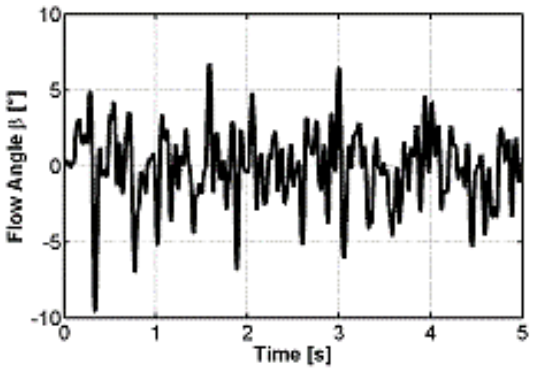


Figure 37 - Frequency distribution of lateral velocity component - Schröck et al (2009)

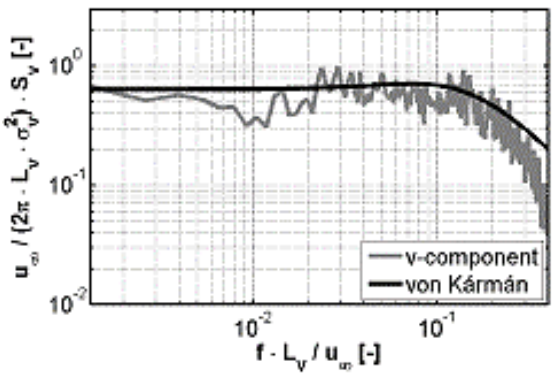


Figure 38 - Dimensionless lateral velocity component spectrum - Schröck et al (2009)

Passmore et al (2001) undertook an investigation using a gust generator, which uses a set of 0.3m chord NACA0015 aerofoils of 1m in height (first presented in Mullarkey (1990), as shown in Figure 39, using the same technique as Bearman et al (1994)). These were installed in the upstream part of a closed section wind tunnel, which has a working section of 1.6m wide by 1.0m high and 4.7m in length. The aerofoils can oscillate up to 18Hz, creating a waveform for a $^1/_6$ scale model of around 2 vehicle

lengths at 22ms$^{-1}$, relating to an upper frequency Strouhal number of 0.23. The gust generator calibration trend is shown in Figure 40, with the x-axis given in reduced frequency, defined as:

$$k_m = \omega_R = \frac{\pi f l}{U} \quad [11]$$

where f is frequency (in Hz), l the characteristic length being the vehicle length in metres and U the freestream airspeed (in ms$^{-1}$). The gust amplitude (y-axis) is defined as:

$$A_g = \frac{U_V}{(u+U)A_0} \quad [12]$$

where $U_V$ is the lateral velocity (in ms$^{-1}$), u is the longitudinal oscillation flow component (in ms$^{-1}$), U is the tunnel freestream speed (in ms$^{-1}$) and $A_0$ is the maximum aerofoil angle (in radians). The resultant plot shows the ability to generate significant crosswind gusts at rates reaching to around 9Hz (i.e. 2.0m TLS) at significant amplitudes.

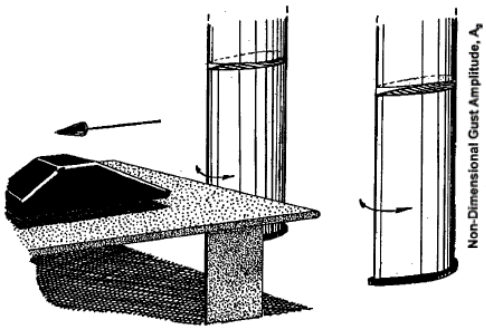

Figure 39 - Gust generator set-up - Passmore et al (2001)

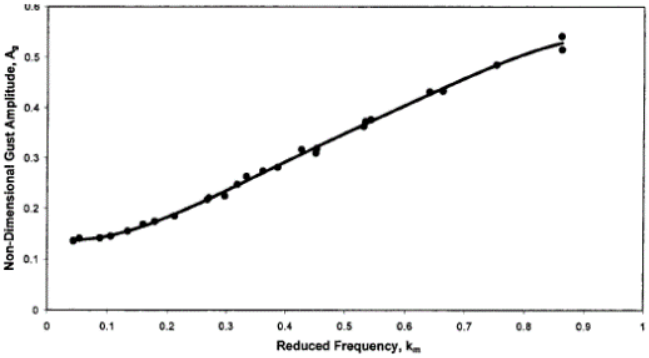


Figure 40 - Gust generator calibration - Passmore et al (2001)

### 2.3.3 Thrust Devices

Thrust generated turbulence are those methods that use fans, jets or similar to rapidly vary the freestream or local velocities and in this way generate pulsations or energy variations that simulate a turbulent wave. Examples of these include jets employed by Gad-el-Hak et al (1974), pulsing banks of fans by Ozono et al (2006), and using a set of rotating shaft winglets by Kang et al (1990), all of which generated length scales in the order of the height of the tunnel. Wind engineering organisations have also evaluated active systems more recently, namely Cooper (1989), Kobayashi et al (1992), Bienkiewicz et al (1983) and Cooper (1989), again with similar turbulence length scales limited to the heights of the wind tunnel, which are too short for automotive test work.

Carr (1994), using crosswind generators, defined the effects of gusts as the vehicle's response to the applied force and the driver's correcting actions. The facility generated a uniform sharp edged gust around 15ms$^{-1}$ over a distance of 4 vehicle lengths, creating a vertical velocity profile.

Multiple fans were used to create controlled turbulence in an experiment by Nishi et al (1995). A 2D-tunnel had 11-fans arranged vertically, and a 3D-tunnel had 6-horizontal rows of the 2D tunnel configuration, making 66-fans in total. The fan speeds were controllable from 0 - 11ms$^{-1}$, with turbulence created by driving the odd fans around 30% faster (i.e. 3.5ms$^{-1}$ vs. 5.0ms$^{-1}$) than the even fans. At the exit from each channel a honeycomb core was installed with the boundary layer reduced by placing 12mm diameter cylindrical bars just after the honeycomb core. Measurements were made 3m downstream of the test-section entrance, with results showing that a uniform flow giving around 0.3m TLS and 8% turbulence intensity being generated, as shown in Figure 41. A flow boundary layer of about 0.25m showed that the flow velocity varied from 5 - 7ms$^{-1}$, which would be a problem for automotive test work unless under floor suction or a rolling-road was used to reduce this boundary layer. Further, vibrating blades were also added, but only a nominal change was noticed. The complexity of the device to achieve the resultant flow structure does not warrant this design as suitable for further TGS research, as the intensities created for the length scales are well within a passive device's generation region.

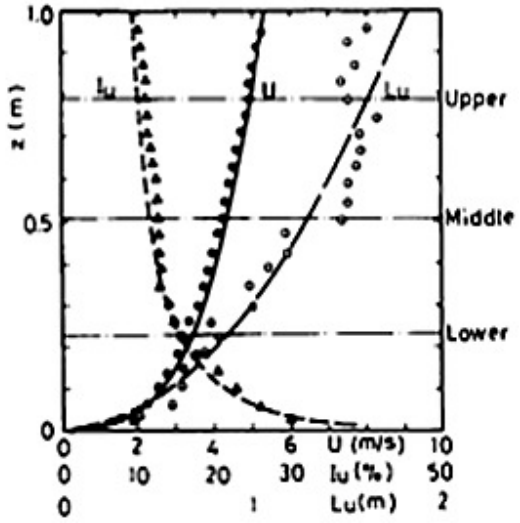


**Figure 41 - Results from the 66-fan set-up, with lines of turbulence intensity ($I_U$), length scale ($L_U$) and flow speed (U) - Nishi et al (1995)**

Air injection has also was also tested by Sluman et al (1980) but was not of a homogenous shear nature and therefore discounted.

Sarkar et al (2002) at Iowa State University presented a design, running at a freestream flow up to 20ms$^{-1}$, creating gusts that were up to 5.4ms$^{-1}$ greater than freestream mean flow speed. The device used a system to block the flow from the fans to create large, longitudinal gusts (sending the flow through a bypass duct). The nominal velocity variation was 1.5% over the tunnel centreline with an intensity of 0.15%. Gusts were measured to reach 97% of maximum velocity within 2.2s, rising from 20.0 to 25.4ms$^{-1}$ with an acceleration of 2.45ms$^{-2}$. Unfortunately, no turbulence intensity or length scales were measured as the gust sections were not intended to control these. A major concern is whether such a system would be able to cycle sufficiently quickly for the longitudinal waves to be maintained, as a variation over 2.2s would create a period of 4.4s, being far too slow for automotive test work. This is because the longitudinal waves need to be in the order of length of the tunnel, which is generally around 5.0m, and if operating at 30ms$^{-1}$ this would require a ramp-up and down time under half a second. However, the idea has potential if it can be operated at a higher frequency.

Docton et al (1996) undertook a review of crosswinds generated in the on-road environment and simulated crosswinds in Durham University's wind tunnel by installing additional fans to blow a lateral wind flow over a test vehicle. The ground velocity was set at 15ms$^{-1}$ and by matching the axial velocity component of the crosswind to the main jet, a gust perpendicular to the vehicle was created. By translating an aperture in a belt across the crosswind fan exit, also moving at the wind shutter or axial wind speed, the gust propagated along the length of the test model (Figure 42).

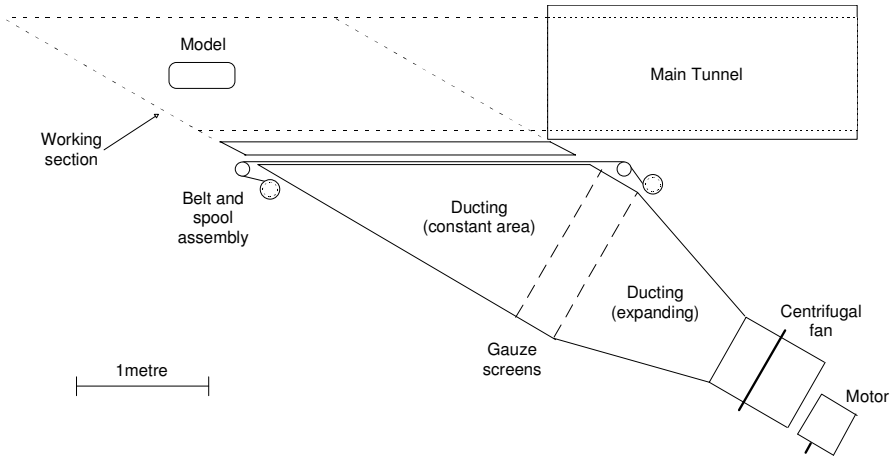


Figure 42 - Schematic plan view of simulation apparatus - Docton et al (1996)

The velocity at various heights in the test section created by the side crosswind inlet is shown in Figure 43, with two clear lateral velocity peaks evident, each with a peak velocity of 8ms$^{-1}$, and an average

velocity in the region of 4ms$^{-1}$, thus generating a gust in the region of 20 - 30$^{o}$ of yawed flow (where $^{x}/_{h}$ represents a model vehicle's width extremities).

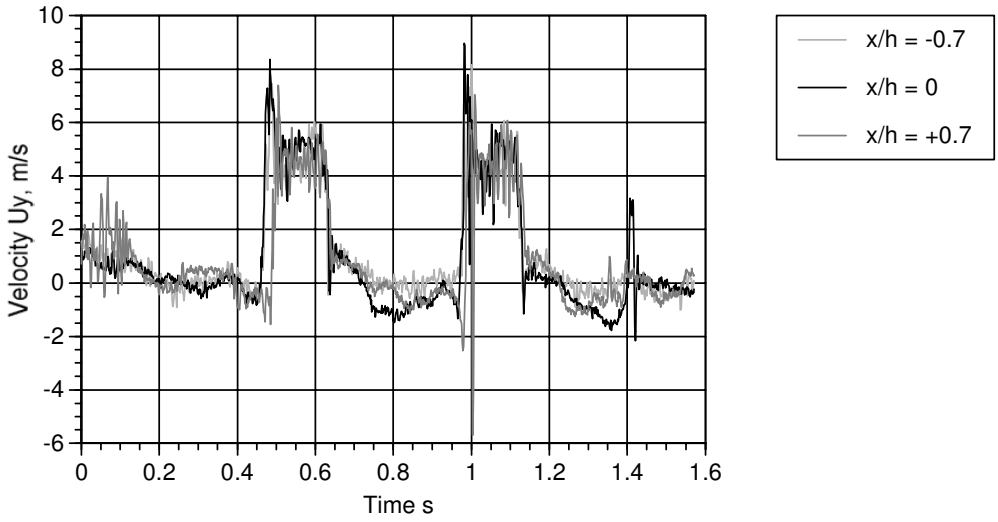


Figure 43 - Cross-stream velocity at differing heights in the working section- Docton et al (1996)

Ryan et al (2000) investigated the simulation of transient crosswind gusts and their aerodynamic influence on passenger cars. Tests used a highly modified version of Docton's original design to generate finite length, crosswind gusts with a relative yaw angle of 20 - 30$^{o}$ that can be developed at the rate of 1000 per hour. By phase averaging over a large number of cycles the effects of aerodynamic and electronic noise were significantly reduced. Two aerodynamic models were tested in this facility, each being subjected to transient crosswind gust in the order of 10 model lengths, with main tunnel running at 27ms$^{-1}$. The facility installed by Ryan, as shown in Figure 44, offered the ability to propagate a perpendicular crosswind over the test vehicle giving an effective yaw of 22$^{o}$.

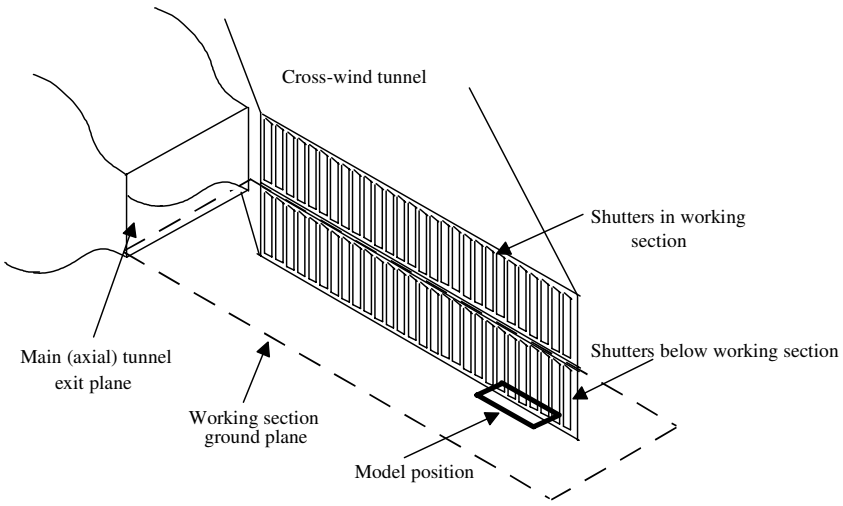


Figure 44 - Installation of an enhanced crosswind facility at Durham University - Ryan et al (2000)

The plot of the gust profile generated is shown in Figure 45 with a clear peak yaw angle of 34° and then a sustained yaw angle of 22° for around 0.5s in duration being created. Shutter control allowed the length of the gust to be changed from zero to infinity. There is a sharp initial increase in lateral velocity and then a more trailed off ending to the gust, decaying in lateral velocity over around 0.2s.

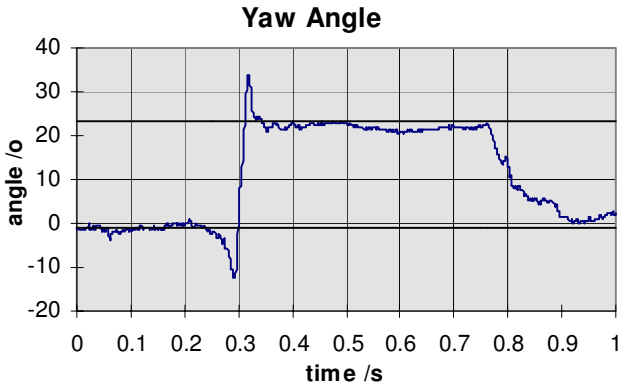


Figure 45 - Gust profile of the crosswind facility developed - Ryan et al (2000)

## 2.4 Vehicle's Response to the Effects of Turbulence

The importance of turbulence to the performance of vehicles is reviewed in this section, with a focus on drag or sideforce variations caused by the introduction of inlet turbulence. This section is broken down into three categories: larger, similar to or smaller than the vehicle size (around 4 - 5m in length).

At this time it is also worth presenting definitions of aerodynamic admittance ($\chi^2$) quantifying a vehicle's response to the externally imposed unsteadiness due to unsteady surface pressures

variations caused by the on-road wind conditions and the transfer function (H(f)) of the yaw to vehicle response:

$$\chi^2(f) = \frac{S_c(f)}{\left(\frac{dC}{d\beta}\right)^2 S_\beta(f)} \text{ and } H(f) = \frac{C(f)}{\beta(f)} \quad [13]$$

where C represents an output variable (e.g.: yaw coefficient), β represents an input variable (i.e. yaw angle) and $S_C(f)$ and $S_\beta(f)$ represent the spectra of C and β respectively at frequency f (Sims-Williams (2010) and Bearman et al (1994)).

Results in this thesis are, following convention such as Passmore et al (2001) and Schröck et al (2011), presented in terms of χ, that is the square-root of Equation 13, though are labelled as Admittance (χ) for the respective axis titles.

### 2.4.1 Length Scales Larger than Vehicle Size

Carlino et al (2007) at Pininfarina developed measurements techniques for evaluating aerodynamic response in conjunction with the operation of the TGS system installed at Pininfarina. A medium sized saloon car experienced a range of frequencies for simple oscillating TGS motion with the resultant sideforce and yawing moment coefficient given in Figure 46 and Figure 47, showing a clear periodic variation with the TGS operation (though amplitudes were not presented).

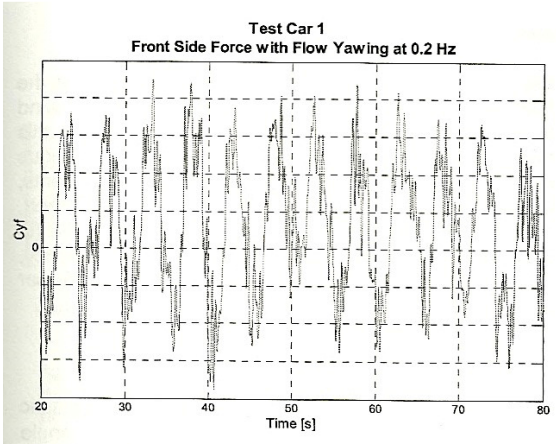


Figure 46 - Time history of the oscillating part of the front sideforce coefficient $C_{YF}$, in the case of flow yawed at 0.2Hz - Carlino et al (2007)

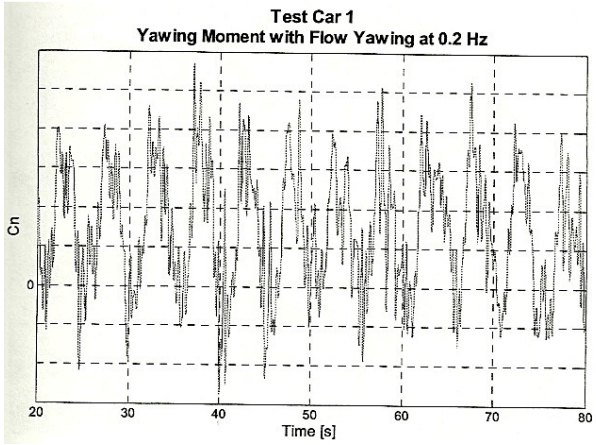


Figure 47 - Time history of the oscillating part of the yaw moment coefficient $C_N$, in the case of flow yawed at 0.2Hz - Carlino et al (2007)

Figure 48 details the variation in sideforce and yawing with frequency, defined as force coefficient (C) over yaw, β, showing a gradual decline from 1.2 to around 0.7 of magnitude in each as TGS frequency increases from stationary to almost 1Hz.

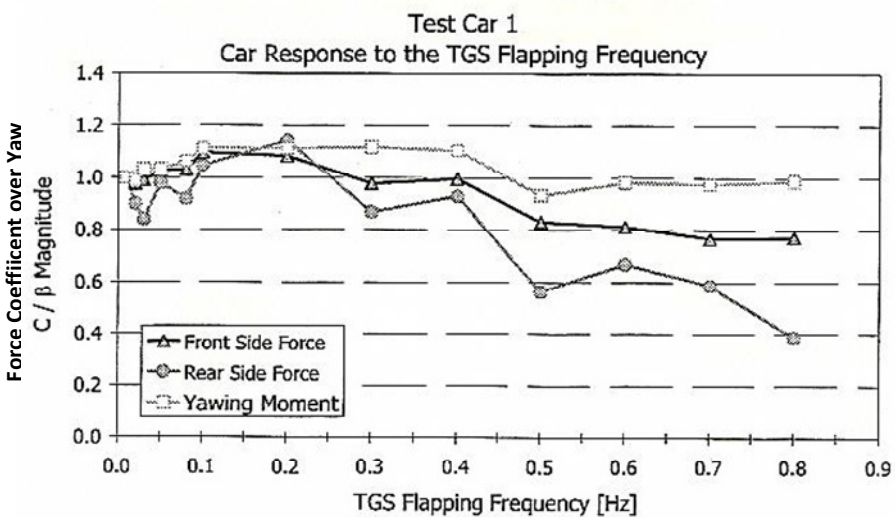


Figure 48 - Test Car 1; sideforce and yawing moment response to flow yawing at various frequencies - Carlino et al (2007)

The C/β ratio is normalised with respect to the same force or moment ratio as at the quasi-static frequency of 0.01Hz

The results show a comparison between 3 Box and Station wagon configurations of a SAE model (shown in Figure 49), which showed a notable reduction in coefficient gradient as TGS frequency increases towards 1Hz.

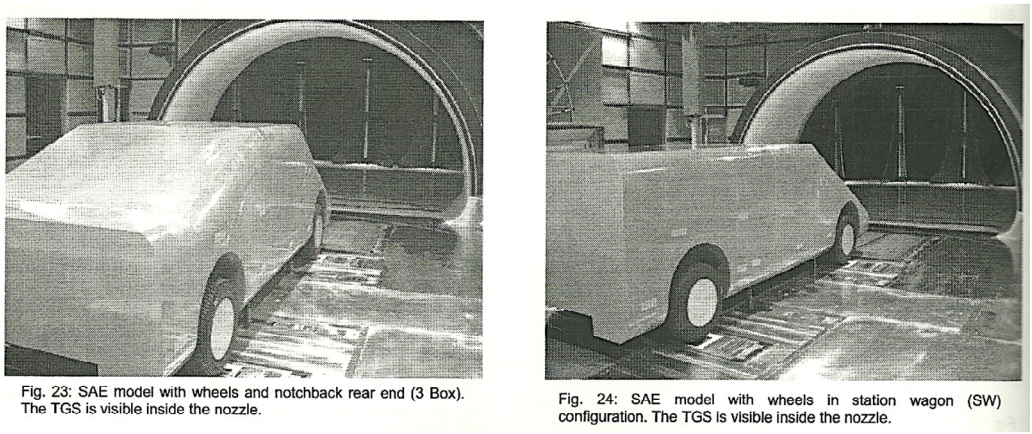

Fig. 23: SAE model with wheels and notchback rear end (3 Box). The TGS is visible inside the nozzle.

Fig. 24: SAE model with wheels in station wagon (SW) configuration. The TGS is visible inside the nozzle.

Figure 49 - Left; SAE model with wheels and notchback rear end (3 Box). Right; SAE model with wheels in Station Wagon (SW) configuration - Carlino et al (2007)

In both images the TGS is shown inside the nozzle

Finally, the gradient of aerodynamic coefficient (C) over yaw angle ( $\beta$), that is $\left(\partial C / \partial \beta\right)$, showing the vehicle's sensitivity in yaw and sideforce to TGS excitation, is presented in Figure 50 to Figure 53.

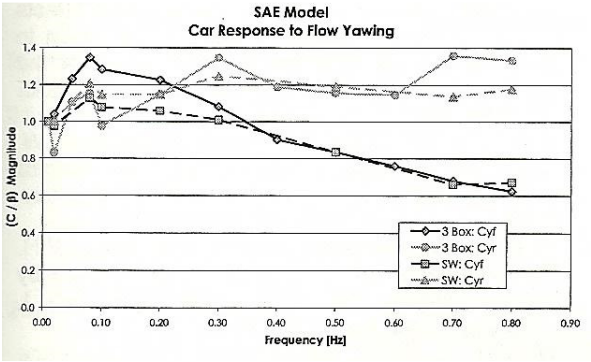


Figure 50 - SAE model in 3 Box and Station Wagon (SW) configurations showing $C_{YF}$ and $C_{YR}$ (left) and $C_N$ (right) over flow yaw angle - Carlino et al (2007)

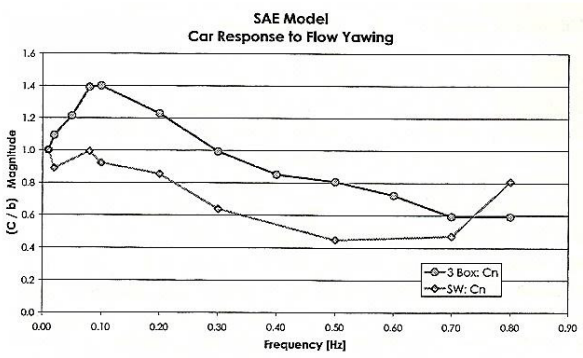


Figure 51 - SAE model in 3 Box and Station Wagon (SW) configurations showing $C_{YF}$ and $C_{YR}$ (left) and $C_N$ (right) over flow yaw angle - Carlino et al (2007)

Where the C/β ratio is further normalised by the ratio as was measured at the quasi-static frequency of 0.01Hz

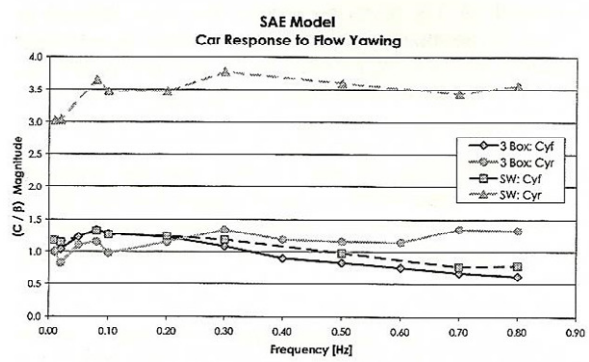


Figure 52 - SAE model's (with wheels) response to crosswind in the case of 3 Box and SW rear ends - Carlino et al (2007)

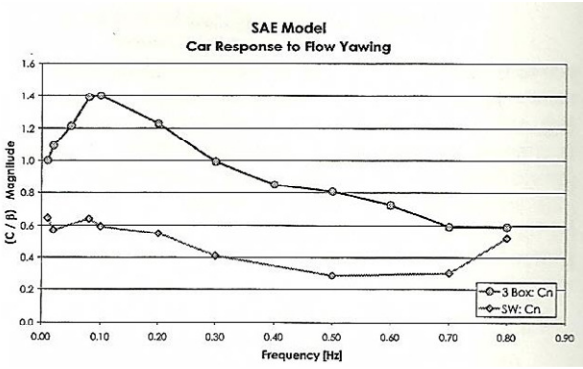


Figure 53 - SAE model's (with wheels) response to crosswind in the case of 3 Box and SW rear ends - Carlino et al (2007)

Where the C/β ratio is further normalised by the ratio as was measured at the quasi-static frequency of 0.01Hz

Holdsworth (2005) using his TGS developed at Durham University, observed that increasing the operating frequency from 0.16Hz to 0.20Hz showed, on the topside of the vehicle, vehicle boundary layer $C_P$ variances of up to 20% between steady and turbulent tests. This suggests that the effect of inlet turbulence can be very substantial from a drag and lift perspective.

Howell et al (2002) undertook vehicle coast-down and tunnel drag tests to assess the difference between tunnel drag and real-world values, using a Land Rover Freelander, with the aim to gain improvements in fuel efficiency from aerodynamic adjustments. Tunnel testing was conducted at the MIRA test facility, running at 100kph. The typical vehicle drag coefficient was measured to be between 0.41 and 0.49, with 5° yaw reducing drag by around 0.05. Drag coefficients in the tunnel were always above the coast-down, around 0.10 - 0.20 $C_D$ difference (for a nominal coefficient of around 0.45), suggesting that unsteadiness leads to a significant measurement difference.

Lawson et al (2007) compared on-road to wind tunnel analysis of pressure measurements with a focus on the A-pillar area (a region known for separation, and hence high drag and wind noise). Comparisons were made between on-road and wind tunnel measurements (Figure 54) showing that the variation in sideglass pressure coefficient with yaw angle (β) is over-predicted in the wind tunnel (i.e. steady environment). Note that due to the lack of significant figures in the paper's presented scale, differences in pressure can be inferred from the contours' shading.

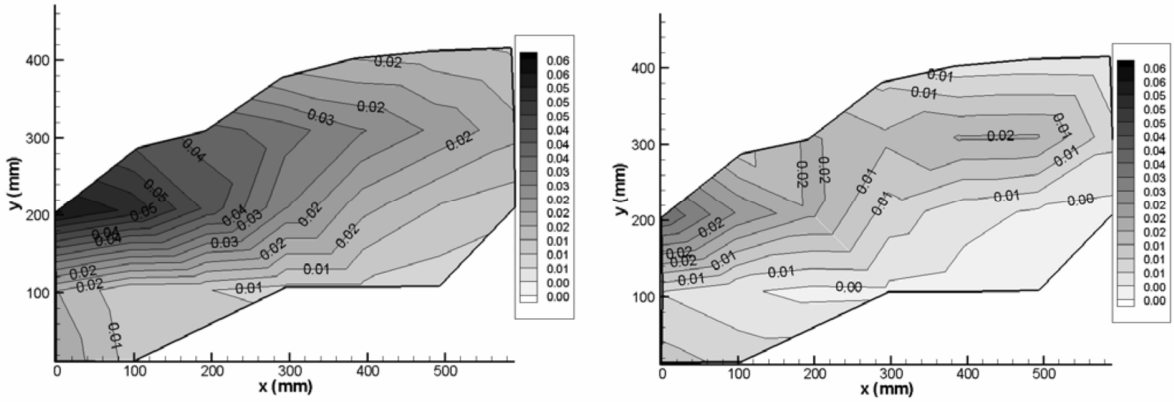


**Figure 54 - $dC_P/d\beta$ ($deg^{-1}$) based on Wind Tunnel Pressures at −10° and +10° yaw (left) and $dC_P/d\beta$ ($deg^{-1}$) based on on-road measurements (right) for a Rover 200 model - Lawson et al (2008)**

Lawson et al (2008) presented a further review of surface static car pressures on the road and under tunnel test conditions. Road tests were carried out under light winds (<2.5$ms^{-1}$) at a vehicle speed of 26.8 $ms^{-1}$, measured using a 3-hole probe on the vehicle's roof. All pressure probes were referenced to a fixed pressure reference chamber. Side glass measurements showed the lowest pressure closest to the A-pillar, with a fluctuation of up to 15% in pressure between the dynamic pressure and total relative velocities. This suggests that the air flow cannot be treated as quasi-steady since the instantaneous pressure at a given yaw angle is different to the pressure which would be obtained at the same yaw angle for constant conditions. Therefore, though the instantaneous yaw angle appears to be the most important factor influencing the pressure coefficient on the model surface, the level of surface pressure unsteadiness is larger than would be expected due to yaw angle fluctuations alone. The spectral relationship between surface pressure and yaw angle indicates that the impact of yaw angle fluctuations is reduced by a factor of 2 for reduced frequencies above unity. Therefore the use of steady yaw angle tests to model turbulent flow seemed to be unsuitable, and the higher frequencies of flow operating above the quasi-steady limit were of significance.

Watkins et al (1998) undertook a test with a vehicle that had a rear spoiler which, with remote angle control, varied the rear flow from being attached to detached. Disc surface static pressure tappings

were used and the cabin pressure was set as the reference pressure. It was found that at the roof leading edge the pressure coefficient retained a constant value irrespective of the yaw angle. Road to tunnel comparisons were made where the pressure measurements were found to be mainly identical. The bonnet flow experienced a higher acceleration than compared to static results (resulting in a slightly lower pressure coefficient throughout). This could be due to the higher turbulence in the atmospheric environment, causing a reduction in the separation bubble at the bonnet's sharp leading edge, hence increasing local velocity, though this explanation does not explain why the increased velocity was sustained over the entire bonnet.

The more likely route of an explanation is that the imperfect ground simulation in the tunnel resulted in a higher physical location of the stagnation point, hence a lower acceleration up to the bonnet hood, which would explain the maintained increased acceleration over the length of the bonnet. It was noted that a repeat of the on-road measurements, made with and without the spoiler, showed very high correlation in front of the spoiler, hence the difference between tunnel and road measurements would be likely to again come from an inappropriate tunnel ground simulation. The road data showed a more complex flow structure around the A-pillar than the tunnel data, which is consistent with Lawson's results, suggesting further analysis of these effects is important. Backlight data showed little difference between road and tunnel results. This does show, however, that the variation in turbulence (i.e. tunnel to road test differences) would affect the pressure over a car body, and hence its lift and drag values, and accurate simulation would quantify these discrepancies.

Baker et al (2000) used hot-wire rakes to record the turbulence properties of lorry wakes and to assess how the wake region propagates with distance and differing vehicle geometry. The effects of crosswinds changed the flow field around the vehicle significantly, with very high flow velocity peaks seen around the vehicle's nose.

Hopkins (2007) showed that the turbulence intensity depends upon the unsteadiness from the naturally occurring wind, that is the wind created from driving at speed and the turbulence caused by roadside objects and other vehicles. The creation of on-road turbulence could also explain the difference between wind tunnel and on-road car analysis. Hopkins investigated the effect of other vehicles on the road showing that the turbulence intensity increases as the proximity decreases between vehicles, highlighting that vehicles do create high intensity turbulence.

Schröck et al (2009), using the FKFS Turbulence Generation System (presented earlier in Figure 36), exposed the SAE vehicle model in both notchback (shown earlier in Figure 49) and hatchback configuration to a steady yaw angle sweep by turntable rotation (as opposed to TGS imposed yaw).

The results, Figure 55, showed a typical variation in sideforce coefficient with yaw angle, but notably that the hatchback was more sensitive to yaw than the notchback model.

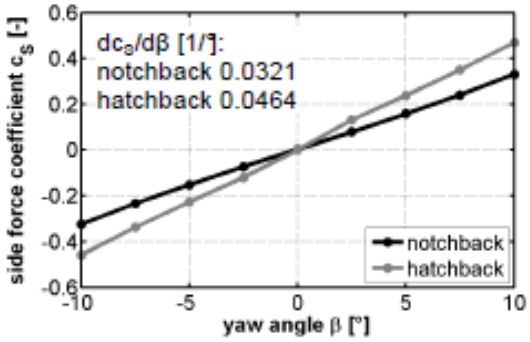


Figure 55 - Sideforce and yaw moment coefficient of a steady-state yaw sweep - Schröck et al (2009)

Further analysis of the vehicle response to varying inlet yaw angle showed that the admittance approaches a constant value for low frequencies (i.e. near to unity) and reduces to zero as frequency increases. As such, at low frequencies the flow structures are sufficiently large to be treated as steady-state, but since the admittance functions do not reach unity, the response over the entire frequency range is not equivalent to the steady yaw angle approach.

Further investigations using the FKFS TGS system, the design of which was detailed earlier and in Schröck et al (2009), are presented in Schröck et al (2011). Using the SAE notchback model (presented in earlier in Figure 49) aerodynamic admittance (as defined in Equation 13) was evaluated for the model subjected to a varying inlet yaw trace (similar to that shown in Figure 37), with the principal behaviour of an aerodynamic admittance function being at or near to unity at lower frequencies and reduce to zero as frequency increases, with a peak above unity as the inlet frequency is at the vehicle or measurement system (i.e. force balance) resonant frequency. The aerodynamic admittance of sideforce is shown in Figure 56 and of yaw moment is shown in Figure 57. The frequency axis is defined by Strouhal number,

$$Sr(f) = \frac{f.l}{u_\infty} \qquad [14]$$

where f is the measured frequency, l the wheelbase of the model (1m in this case) and $u_\infty$ the freestream velocity of 160km.h$^{-1}$, giving a maximum Strouhal number of 0.15 correspondingly to 2.7Hz. The SAE model shows initial unity admittance at very low frequency (as if a steady-state yaw sweep was conducted), peaking at mid-frequencies showing a vehicle response with greater yaw dependency, and then as expected a significant reduction in vehicle response as frequencies increase further.

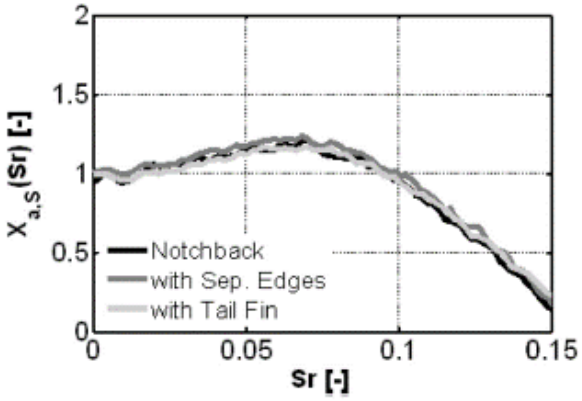


Figure 56 - Aerodynamic admittance of sideforce - Schröck et al (2011)

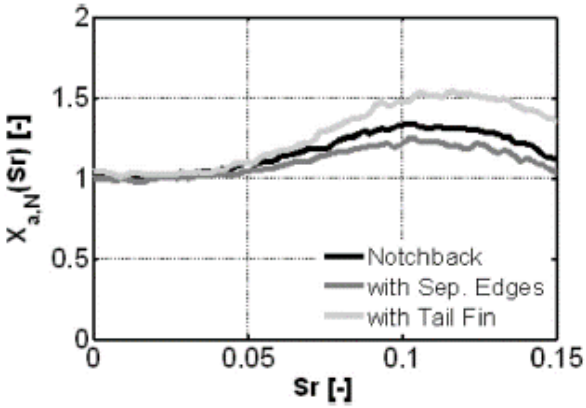


Figure 57 - Aerodynamic admittance of yaw moment - Schröck et al (2011)

Passmore et al (2001) undertook an investigation translating a generated gust over a model-scale vehicle to assess the gusts' effect on vehicle stability. Passmore noted that drag reduction techniques such as the rounding of vehicle front-end profiles and the region around the rear pillar can cause greater yaw sensitivity and that curved geometries, combined with air flow unsteadiness, can cause variable flow separation leading to unsteady aerodynamic loads. Such varying aerodynamic loads cause large differences in front and rear side forces and yaw moments especially in crosswind conditions. The Davis fastback model, Figure 58, was exposed to a range of gusts, the set-up of the gust generator being as detailed in the review of Passmore et al (2001) earlier in this chapter. A steady-state yaw sweep was completed to trend side pressure coefficient with yaw angle. A plot of the difference in static pressure coefficient between the both sides of the model during being exposed to a transient sine wave yaw sweep is shown in Figure 59, showing a very strong correlation of model side pressure with yaw angle.

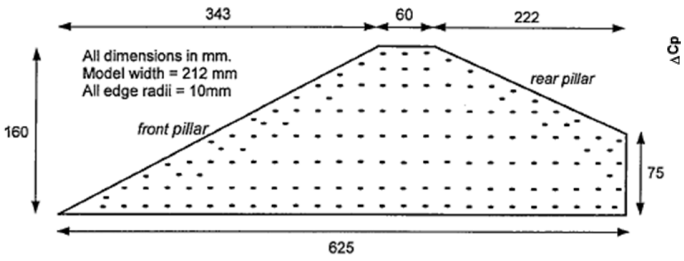


Figure 58 - Davis model dimensions and pressure tapping locations - Passmore et al (2001)

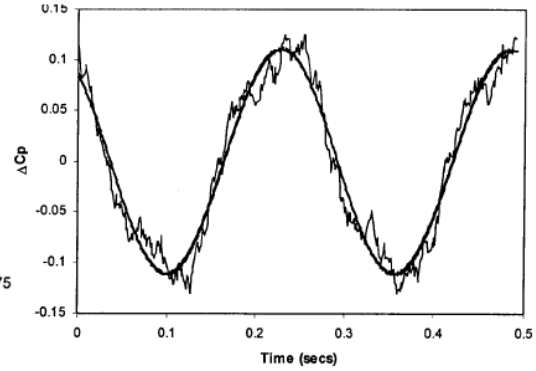


Figure 59 - Single tapping transient $\Delta C_P$ variation and sine fit - Passmore et al (2001)

Passmore then undertook a quasi-steady prediction process by combining the sinusoidal aerofoil angle input with the measured steady-state yaw against pressure coefficient trend. The aerodynamic magnification factor $(\chi_a)$ was determined by taking the ratio of the amplitudes of the transient to the quasi-steady sine wave outputs (which is correspondingly the square root of aerodynamic admittance). As such, the magnification factor is essentially a comparison of the pressure coefficients between the transient and the steady-state yaw sweep. The resultant trend, Figure 60, shows greater than unity admittances over the frequency range and especially at low frequencies indicating yaw sensitivity (i.e. transient flow effects). Lower than unity admittances at the intermediate reduced frequencies demonstrate that the quasi-steady prediction overestimated the transient sideforce. Admittances did not reduce at higher frequencies, but it should be noted that the peak aerofoil yaw angle was reduced with frequency to less than ±2° at the highest frequency, correspondingly increasing the signal-to-noise ratio.

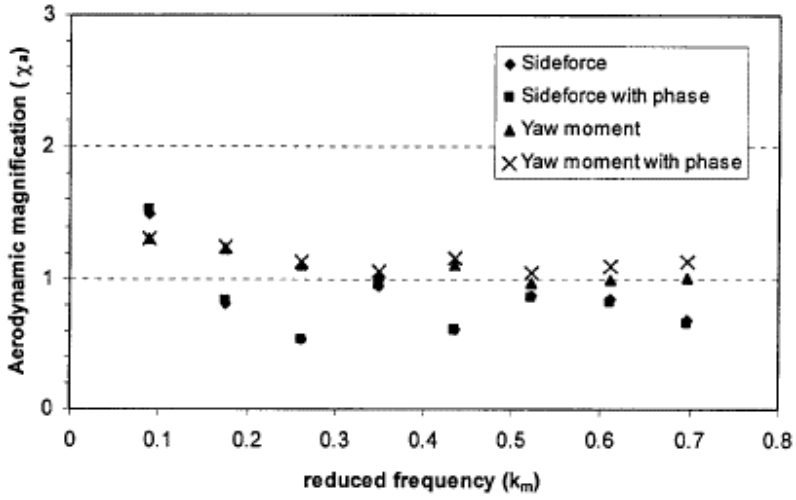


Figure 60 - Sideforce and yaw moment aerodynamic magnification against reduced frequency - Passmore et al (2001)

### 2.4.2 Length Scales of Order of Vehicle Size

This section reviews the differences between on-road and tunnel tests. Previous work undertaken by Lawson et al (2007) and by Holdsworth (2005) showed that the introduction of turbulence did not varying the pressure distributions significantly over a vehicle, but that the simulation of upstream vehicle wakes was significant. Buckley et al (1976) highlighted the effect of upstream vehicles, as did Watkins (1990) and Cooper et al (1981). Work by Cooper and Campbell (1981) was undertaken to theoretically adjust laminar test work to that of unsteady tests, and this was achieved with some success, though mainly for lower-frequency, high energy gusts (i.e. crosswinds).

Teunissen (1980) found that yaw angles between 0.5$^{o}$ to 2.0$^{o}$ are important for crosswind sensitivity from a driver's perspective, with 4$^{o}$ of yaw at 200kph combined with 30kph gust velocities and intensities up to 12$^{o}$ being realistic for describing overtaking scenarios. Numerical analysis was undertaken with an idealised square, 3D vehicle model with a crosswind flow inlet (sinusoidal inlet wave at 1Hz). The results showed that the sideforce on the vehicle moved rearwards during a gust (i.e. increasing yaw moment), causing a shear and torque on the vehicle, which would significantly influence vehicle stability.

Garry (1982) reviewed the effects of backlight design and found that changes in flow at high intensities (>10%) were significant for lift and drag variation, though the increased TLS associated with these high intensity flows was probably as significant. Newnham et al (2006) found that with a two-box car shape, turbulence greatly affected the trans-critical Reynolds number and Watkins et al (2001) found that increasing turbulence was similar to increasing Reynolds's number, such as the trans-critical flow around spheres. Dryden et al (1936) and Bearman et al (1983) suggested that forces which act over the rear of a car are sensitive to unsteadiness variations, whereas Mala et al (1999) showed that length scale is likely to be the dominant factor when turbulence intensity is high and constant (i.e. >20%). These sources all suggest that the variation on vehicle drag and stability is greatly affected by turbulence, but the attributed significance of intensity against length scale requires clarification.

Cogotti (2004) showed drag and lift coefficient and pressure fluctuations all increase with turbulence. Rear lift coefficient varied greatly with turbulence due to varying reattachment as well as front lift coefficient fluctuations and also (to a lesser extent) drag. Increased vehicle buffeting was also noted, thereby affecting vehicle stability and ride comfort. Front bonnet panel lift increased and disc brake cooling, recirculation of exhaust gases, backlight soiling and sunroof booming all showed variances

with turbulence. Aero-acoustics also showed notable variances, with loudness and roughness increasing with turbulence.

Cogotti (2004) tested a Peugeot 406C behind a mid-sized, hatchback car in the wind tunnel. The leading car trailing flow was characterised by two downwash vortices, with peak intensity at 13% at 0.5m in front of the following car's bumper. Overall drag coefficient dropped -0.029, with front lift decreasing by -0.084 and rear lift up by +0.017. The TGS caused the Peugeot's drag coefficient to drop -0.005 from a 'no upstream car' datum. Cogotti suggested that the differences measured in vorticity magnitude could be attributed to the cars being too close together in the first test, as opposed to errors in the TGS test. These results suggest that the effect of turbulence on vehicle lift can be notable, which affects vehicle stability. Table 2 summarises the effect of displacing downwash and upwash wake to drag and front lift variation (the vorticity was controlled in order to simulate tunnel TGS phase, amplitude and frequency).

**Table 2 - Test results - Cogotti (2005)**

| | **Displacing downwash wake** | **Displacing upwash wake** |
|---|---|---|
| **Drag variation** | Decrease | Increase |
| **Front lift variation** | Increase | Decrease |

Table 3 shows that the effect of the TGS turbulence on lift, drag and moment forces was significant and that the effect of the turbulence on vehicle performance is notable and should be considered in the automotive aerodynamic design.

**Table 3 - Coefficient variation for differing tests - Cogotti (2005)**

| | **$\Delta C_D$** | **$\Delta C_{LF}$** | **$\Delta C_M$** |
|---|---|---|---|
| City car - upstream downwash wake | -0.021 | 0.037 | 0.021 |
| City car - upstream upwash wake | 0.013 | -0.077 | -0.031 |
| Soft top city car - upstream downwash wake | -0.023 | 0.060 | 0.042 |
| Soft top city car - upstream upwash wake | 0.021 | -0.079 | -0.043 |

Docton et al (1996), using the crosswind facility shown earlier in Figure 42, tested a 'Docton' model which was a rounded-corner rectangular cuboid with endplates as is shown in Figure 61 and has numerous static pressure tappings along the side perimeter, thus allowing the integration of pressures in order to resolve the force profile for the model.

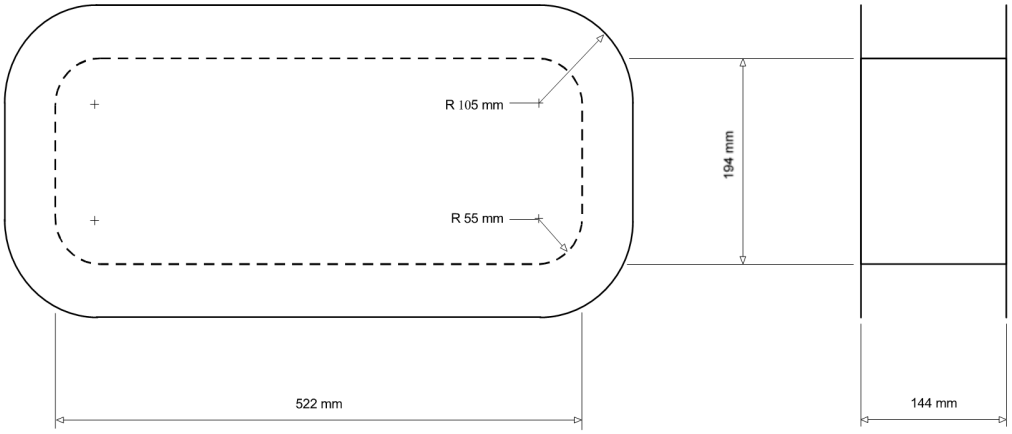


Figure 61 - Docton model geometry - Docton et al (1996)

Figure 62 presents the surface pressure results for the model exposed to the same gust profile shown earlier in Figure 43 at differing leeward tapping locations (0 being at the leading edge and 10 being $^1/_3$ down the respective model side). It can be seen that the side force increases over the first third of the vehicle, and further plots (not shown) of more downstream tappings show the same trend in smaller magnitudes as downstream distance increases. The windward surface pressure plot showed a similar trend but with inverted pressure traces at similar magnitudes.

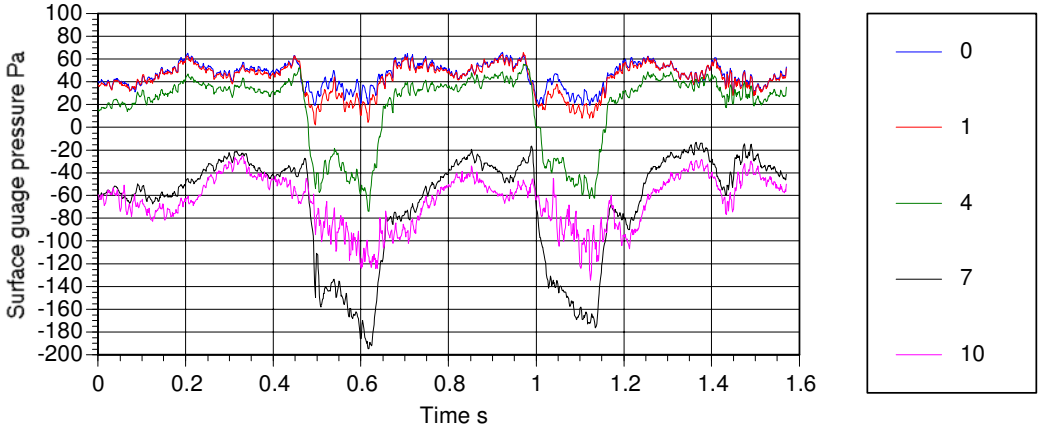


Figure 62 - Transient model surface pressure at various tapping locations (Leeward side) - Docton et al (1996)

In Figure 63, showing sideforce, the gust can clearly be seen to impose a sideforce of approximately 4N on the model, with the majority of force occurring on the windward side, but that additionally a change of pressure on the leeward side adds to the net force.

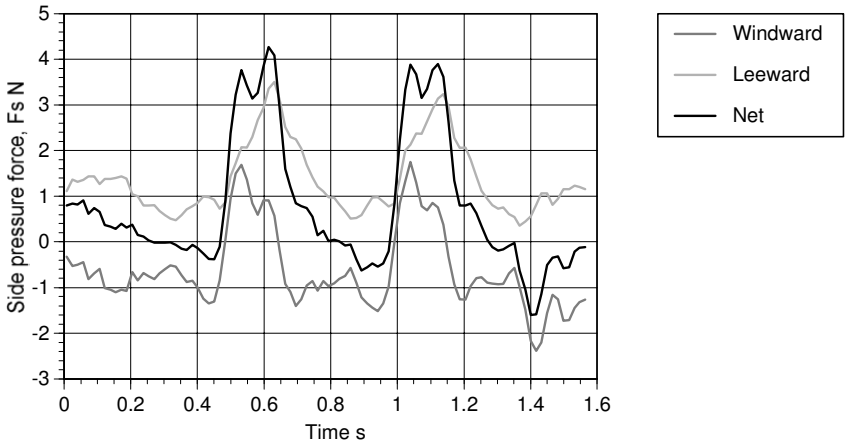


Figure 63 - Transient side pressure force on the model - Docton et al (1996)

Plots of yawing moment (not shown) demonstrated peaks of 0.4Nm, with both the windward and leeward side contributing almost equal quantities to the net moment. In comparison of the yawing moments before and after the gust, the actual gust only increases the yawing moment on each of the windward and leeward sides by an approximate delta of 0.15Nm, but that the two sides summed, causing a large net yawing moment. Therefore the variation in side pressure (i.e. over a sideglass) will cause a far greater net yawing moment on the vehicle.

Drag force on the model was shown to vary before and after the gust, moving through a reduction in drag by 70% from the steady flow condition, peaking at 140% of the steady flow condition drag, which would cause a notable drag buffet.

Reviewing the model vehicle's response to Ryan's (Ryan et al (2000)) crosswind gust facility (shown earlier in in Figure 45), Figure 64 shows the resultant sideforce coefficient trace for the 'Durham' model as the gust propagated. There is a rapid pressure development on the windward and leeward sides and the model's response closely reflects the onset yaw variation, though a decrease in sideforce coefficient at 0.38s is, for a short period of time, in the opposing direction to the onset yaw direction. That flow development occurs up to t = 0.6s, with the region of separated flow taking up to 7 model lengths to become established. Therefore the increase in sideforce is due to delayed leeward A-pillar and under-floor flow vortex development. It should be noted that a difference in the 'infinitely' long gust of the crosswind facility did not agree with the steady yawed flow case, with a 6% difference in crosswind dynamic pressure noted.

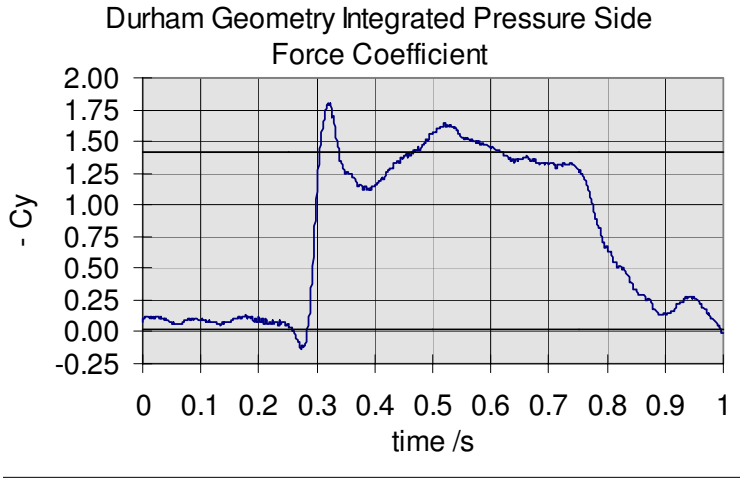


Steady values: axial flow = -0.02, yawed flow = -1.41.

Figure 64 - Model geometry used with integrated pressure sideforce coefficients - Ryan et al (2000)

Yawing moment coefficient for the 'Durham' model showed an over-, and then under-shoot similar to the sideforce coefficient, with the over-shoot caused by the delayed leeward A-pillar and under-floor vortex development. Pressures on the model's upper surface also showed rapid development, but the lift coefficient does not reach a maximum until t = 0.55s after which time the gust arrived at the model, suggesting that pressure development must continue.

An increase in upper surface lift between t = 0.36s and t = 0.45s was also seen, partially due to the increase in wind tunnel dynamic pressure, but also due to delayed flow development in regions of separated flow where the closed separation bubble in the windshield to roof junction, and the vortex at the windward side of the side-roof to C-pillar are not seen (which would have an associated pressure coefficient decrease).

At t = 0.30s the effects of the crosswind gust anomalies, (i.e. high total pressure and yaw angle overshoot) results in spurious surface static pressure data, with the roof experiencing a brief reduction in pressure coefficient and correspondingly the model showing an increase in upper surface lift coefficient. The continual variance of the lift coefficient, as opposed to the sideforce and yawing moment that settle during the gust, is due to small pressure changes on the windshield surface but not due to the unsteady region of separated flow.

The model showed significant transient force and moment overshoots, which were found to be a consequence of delayed pressure development in regions of separated flow and with full speed flow

development requiring up to seven model lengths of crosswind gust. Docton and Ryan showed that forces under these transient flow conditions are very different from steady-state.

Pearce et al (1998) measured the effects of unsteady crosswind forces and moments on ground vehicles using $^{1}/_{50}^{th}$ scale rail vehicle model (which was at full-scale 17m long, 3.2m wide and 5.5m high) in a 4m high by 2m wide wind tunnel of 20m test section, with sideforces and moments increasing greatly with yaw angle and the variation levelling when yaw angles exceeded 40°. A similar effect was seen for both steady or gust like crosswinds. Sideforce was shown to be the most dominant force and effect.

However, the lift force was seen to greatly increase when yaw was larger than 45°, with differing sources of instability being created at high yaw angles, potentially from body induced turbulence. Admittances, starting at unity at low frequencies, were seen tail-off at high frequencies with a peak in lift force coefficient between 10 - 20Hz, relating to a Strouhal number 0.1 - 0.2, probably caused by wake vortex shedding. Aerodynamic weighting functions were presented which predicted that the sideforce coefficient will approach its equilibrium value with no overshoot, but that an overshoot of around 20% for the lift force coefficient.

### 2.4.3 Length Scales Smaller than Vehicle Size

Shorter length scales affect a vehicle's performance differently to longer scales. These effects, due to higher frequency inlet turbulence, were categorised by Bearman et al (1994) as three main mechanisms in turbulence on bluff bodies: i) accelerated transition to turbulent flow within shear layers, ii) enhanced mixing and entrainment and iii) distortion of freestream turbulence by the mean flow-field, each affected by intensity and length scales. All of these flow effects, due to the higher frequencies, ultimately affect the pressure measurements over a car, which mean that the peak loads on a vehicle can be greater, yet still inconclusive if the average load values change.

As an overview, several sources were reviewed which investigated testing vehicles in yawed flow with a turbulent inlet generated by a grid. Macklin et al (1997) concluded that simple yawed testing in this manner underestimated the true transient loads that the vehicle experienced. It was found that the addition of turbulence had offered a smaller variation range than the load variation under the 'steady' inlet condition and that below 15° yaw the static tests (i.e. no grids) gave a conservative view of the loads, whereas above 15° yaw the dynamic results were generally larger than the static tests. This suggests that testing with and without turbulence can have a prominent effect on the measured drag force.

Watkins et al (1990) and Nguyen et al (1997) reviewed tunnel to on-road turbulence and conducted tests with static grid generated unsteadiness. It was noted that cars are more aerodynamically unstable due to the centre of pressure of the sideforce tending to move forward as cars become more streamlined. Previous work on fluctuating sideforce was undertaken by Davenport (1961), Vickery (1966), Melbourne (1993), Bearman et al (1994), Saunders (1974), Basu (1986) and Hunt et al (1992). With respect to cars, Saunders et al (1987) measured force and moment spectra for cars and trucks, and Gilhaus et al (1986), Coleman et al (1993), Coleman et al (1994) and Bearman et al (1994) all conducted other turbulence studies. All of these sources made observations of the variation in drag and sideforce measurements with the introduction of high frequency turbulence, namely the increased peak loads and varying flow Reynolds' number in the critical flow region.

A series of experiments by Newnham et al (2008) were undertaken to see how flow characteristics would alter with varying corner radii with turbulence. Turbulence ranges of up to 3.4% intensity at $15ms^{-1}$ were created with mesh grids. Key results showed that the separation bubble instability increased with turbulence intensity. In laminar conditions the separation bubbles were found to be relatively stable, however at an intensity of 1.4% the bubble was far less stable and increasing to a peak intensity of 5.13% caused large 'flapping' of the free shear layer and its intermittent collapse. Velocity ranges in the separated region showed peaks 30% greater than at low turbulence, with the time-averaged separation bubble getting shorter. Increasing turbulence did reduce the Reynolds's number at which transition to fully attached flow occurred, but also the changes in the flow field at constant Reynolds's number with varying turbulence intensity were seen to be driven by the increased turbulence in the free shear layer and not only by any earlier transition, differing to results presented earlier by Schröck et al (2011).

Gilhome et al (2002) undertook further tunnel to road comparison tests, again showing disparity between laminar and turbulent measurements, with a focus on the pressure distribution over a car's door. The consideration of turbulence was described as falling into two main schools of thought - the first that turbulence perturbations largely cancel out and the second that the induced additional effects are not captured by steady-state, low turbulence testing techniques. Bearman & Malarkey (1994) stated, 'Aerodynamic forces caused by gusts may be predicted safely by assuming the air flow to behave in a quasi-static way.' As such his experiment set out to see if steady-state wind tunnel testing was a valid assessment of on-road front door aerodynamic flows. The results showed that the tunnel did not estimate the on-road environment door loads accurately, as the door aerodynamic

loads in on-road low turbulence were less than the peak door loads that were experienced in the wind tunnel. Door pressure measurements in low turbulence wind tunnels were lower than those for on-road conditions.

At yaw, the wind tunnel average force produced conservative estimates, whereas the wind tunnel significantly underestimated the peak force when compared with the on-road turbulent testing conditions. The conclusion reached was that turbulence increases door pressure loads (and an increase in turbulence is generally proportionate to any length scale increases). Further, rotating wheels (and hence their resultant turbulence) moved the coefficient of pressure rearward over the door and reduced aerodynamic forces over the door. Consequentially the low turbulence tunnel results are lower than on-road results, unlike work by Bearman et al (1994), Macklin et al (1997) and Nguyen et al (1997) who used static meshes with turbulence up to 4% intensity and 0.8m TLS to assess the effect of shear and crosswind turbulence for road vehicles. These tests were useful in testing freestream turbulence effects, and it was found that the variation in turbulence level made little difference to the effect on the vehicle.

Tests conducted by Bearman et al (1994) and Nguyen et al (1997) using sideway crosswind flows, with induced unsteadiness from mesh grids in the crosswind inlet, showed that, at tests running with the car at $0^o$ and $30^o$ yaw (at 4.2% turbulence intensity), the mean sideforce increased with yaw angle and side area. The experiments showed that there was a slight increase in mean drag, sideforce and yaw moment coefficient with increasing turbulence. It was found that the increase in fluctuating sideforce was directly proportional to the increase in turbulence intensity. The paper also noted that the fluctuating sideforce for a streamlined car could be up to 50% lower than that of a sharp-edged car (and the streamlined car drag force is around 50% less than that of the sharp-edged car).

Studies completed by Bearman et al (1994) looking at the effects of steady crosswinds and gusts on the SAE simplified geometry vehicle model found variances in drag, sideforce and yawing moment with lateral flow increases. Crosswinds were induced using a pair of oscillating aerofoils and turbulence inducing grids, though the quality of the on-road simulation was stated to not be precise. The aerodynamic forces behaved in a quasi-steady manner (albeit overestimating the measured unsteady forces and moments), with a nearly linear relationship between vehicle forces and yaw up to $20^o$. Bearman et al (1994) and Nguyen et al (1997) show that on the whole, the effect of high frequency turbulence is to vary drag, side and moment force measurements on a vehicle and therefore are important to the design of vehicles and their aerodynamic optimisation.

Howell (1995) presented the results of the large Rover crosswind test facility at MIRA for tests on a mid-sized SUV vehicle, which showed that the prediction methods available did not evaluate the crosswind sensitivity correctly. A two degree-of-freedom model gave a crude assessment of a vehicle's crosswind response, but the model was still using a large scale facility, and refinements were still required for suspensions with strong roll-steer characteristics. Ultimately the complex facility did not offer a precise crosswind measurement technique.

## 2.5 Background Research Overview

The literature review focussed on four major topics, turbulence measurement approaches, real world data of on-road turbulence, dynamic and passive TGS systems and previous studies assessing the effect of aerodynamic unsteadiness on a vehicle's performance. This review also leads into a TGS specification in the following chapter, which includes a further review of the more promising TGS systems presented. A summary of some of the typical energy spectrum of past and currently available turbulence generation systems is presented in Figure 65. An overview of the variety of unsteady air flows measured in the on-road environment showed a wide range, from 1 - 50m TLS at intensities from 0 - 15% or greater. Clearly therefore a TGS needs to be able to create a wide range of length scales, with care to ensure that the decay rate of turbulence intensity and the growth of turbulence length scale, as the flow propagates downstream through a test section, is small over a model's plan view. This factor reiterates that all measurements must be recorded at model front, middle and rear extents, to map the decay and to ensure that a TGS creates comparable on-road turbulence.

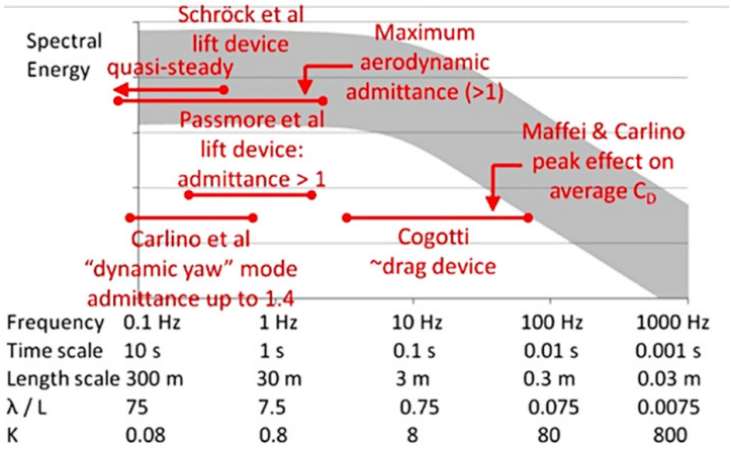


Figure 65 - Spectral range of turbulence and corresponding generation systems - Sims-Williams (2010)

The adjustment from real world to model scale must be allowed for. The Durham 2m wind tunnel operates at a 25 - 35% model size, requiring measured TLS's must be adjusted suitably. Wordley et al

(2009) offered the greatest review of flow conditions for a variety of environments, suggesting that to recreate this wide range of flow conditions TLS of 2 - 14m (full scale) should be created longitudinally with intensities from 2 - 14% and with intensity decaying with increased TLS, as per his spectra plots. Further tri-axis intensity ratios ranging from isotropic (u, v, w) = 1 : 1 : 1) to a ratio of (u, v, w) = 1.0 : 0.8 : 0.6 should be aimed for. The issues associated with creating isotropic length scales for unsteady flows do not seem to be completely justified due to the wide range of results found and therefore simply the length scales suggested by Wordley et al (2009) should be matched.

A wide variety of dynamic systems were found to have been tested, though some were potentially overly complex or expensive. The Pininfarina vane system, Cogotti (2004), and oscillating horizontal bars both generated length scales that would be desirable (<14.0m x 30.0% = <4.2m TLS). Varying tunnel blockage and bypass flows could generate the larger length scales required longitudinally.

Static systems were also reviewed and the length scales generated were all relatively short. This is not to say that passive systems are of no value in automotive aerodynamic test work, but that their generated length scales were generally below 0.5m (<2.0m x 30.0% → <0.6m) so they cannot offer the principle length scale range desired. Tests by Iyengar et al (2001) found that a tunnel freestream unsteady flow of around 2% intensity was reduced to under 0.5% using grids, and further if the tunnels' freestream flow is of very low background turbulence (<0.5%) that grids might be of use to adjust the turbulence level at the upper end of the frequency spectrum. However, until such tunnel analysis and preliminary testing have been completed, static systems will be left dormant as they are unable to generate the length scales desired.

Assessing the importance of unsteady air flow in testing, it is fair to conclude that the results are varied. Certainly some tests suggest the principle coefficients values (i.e. $C_D$, $C_Y$) varied nominally, but other work by Newnham et al (2006), made clear that the points of separation and reattachment over vehicles and alike are highly affected by unsteady incoming flow. Further, there is a large discrepancy between real-world drag tests (i.e. coast-down technique by Bischof (2008)) and tunnel test data, and unsteady incoming flow must constitute a major factor of this difference. Cogotti (2003) showed that the response of a vehicle to being in the wake of a lead vehicle was significant to efficiency, performance and aero-acoustics, and improvements in unsteady flow testing would definitely offer value to the research and development of vehicle aerodynamics. It is therefore concluded that current sources suggest that resolving unsteady air flow generation will be of real benefit.

This chapter therefore summarises the turbulence frequencies and intensities that have been experienced in the on-road environment. In chapter 3 a 2D CFD simulation is undertaken to determine, from a general perspective using a simplified geometry, the frequency range at which a vehicle response occurs to unsteady turbulence. The chapter evaluates at what frequency quasi-steady approaches are non-longer valid in order to develop an understanding of how vehicle stability and drag varies at differing aerodynamic excitation frequencies. In chapter 4 an on-road study is undertaken to firstly confirm the turbulence frequencies and intensities that exist on the road from a vehicle's perspective. Then secondly, through the simultaneous measurement of a roof probe and sideglass pressures, an admittance-based technique is developed to determine at what frequencies a vehicle response is seen to occur from unsteady turbulence as opposed to effects that can be assessed through quasi-steady approaches.

From the results of chapter 2, 3 and 4 the frequencies at which significant turbulence frequency exists in the on-road environment and the frequencies at which a vehicle response is seen are known, leading to a specification for a TGS (i.e. required frequency and intensity for simulation). Chapter 5 then presents a CFD study to develop a TGS design, with the output being an aerodynamic specification. In Chapter 6 and 7 this aerodynamic specification is then developed with the aim being a mechanical specification of the TGS covering the control system, linkage and rates of operation. In Chapter 8 the objective is to take the new TGS and understand its operation with the output being a set of control parameters that will ensure accurate turbulence generation in both harmonic and non-harmonic test cycles. Finally in Chapter 9 a model of the vehicle tested on-road (in chapter 4) is tested using the TGS, with the objective being to assess the simulation approach of using models to understand the unsteady aerodynamic effects on full-scale vehicles. The outcome of the thesis is therefore a test approach using an admittance based technique to compare unsteady turbulence effects from quasi-steady effects, a TGS that can replicate the on-road environment and a method for taking on-road measurements and simulating them in the wind tunnel environment.

# 3. CFD Study of Effects of Inlet Turbulence on an Idealised 2D Model

A 2D geometry model of car's plan shape was modelled and simulated with a varying inlet (i.e. dynamic) yaw angle flow. The objective was to see how a simplified model would respond to varying sinusoidal inlet frequencies, amplitudes and flow conditions as well as the effect of simple geometry variations to the model's response. The caveat of using a simplified vehicle geometry is that the conclusions are focused on determining the orders of magnitude of frequency that are relevant and therefore from the results only a macroscopic view can be taken of vehicle or geometry specific effects, with this being a fundamental study of the frequencies involved. However, the results show how the effect of varying inlet lateral frequency can affect geometries in the order of the scale of a road vehicle. This approach can be used to investigate the admittance between inlet flows and vehicle response forces, developing understanding of the quasi-steady frequency threshold and the effects of viscosity on the threshold, as well as allowing numerous geometries to be tested in a relatively rapid succession.

## 3.1 CFD Case Configuration Background

CFD software, both Ansys Fluent 12.1 (a RANS based solver) and Exa Powerflow 4.3c (a lattice Boltzmann based solver) are used extensively in this thesis for developing and understanding transient flow properties. The two arenas of use are in the development of a TGS design and furthering the understanding of the effects of transient air flow in 2D and 3D simulations of vehicle models. As both of the solvers have a range of settings related to their intrinsic calculation methods, an overview of the parameters used and theory supporting the judgements made are discussed in this section.

Fluent (used mainly for steady-state studies) and Powerflow (which simulates time-variant flows, used for steady and transient simulations) both have differing characteristics and turbulence models. It is appropriate to consider the merits and limitations of their respective inherit designs and define the major elements of a test case that are used throughout.

A lattice Boltzmann solver is based on a discrete equation derived from the kinetic theory Boltzmann equation, with the basic quantity in the method being a single-point distribution function. The discretisation in a lattice Boltzmann solver is chosen in such a way that the resulting relevant flow dynamics do not suffer from discrete lattice effects and fluid dynamic quantities (such as the fluid velocity, density, and pressure) can be obtained through post-processing. Additionally turbulence modelling can be solved via a relaxation process and boundary condition modelling. A lattice

Boltzmann solver often has the advantages of being stable for highly nonlinear flows. It can be readily parallelised, offers a more fundamental treatment of the boundary layer and does not need to explicitly solve pressure dynamics. However, the lattice Boltzmann solver is optimised for low Mach number applications and by being fully explicit is more suitable for large-scale turbulent flow simulations.

CFD simulations can approach turbulence through either simulating the turbulence or modelling it. Simulation of turbulence requires 3D transient solvers with low numerical dissipation to converge. They also require a mesh resolution in the order of the Reynolds Number to the power of 3. Therefore at automotive Reynolds number orders, some turbulence modelling is required to account for the macroscopic effects of the turbulent flow structures that are not resolved directly by the simulation. Reynolds Averaged Navier-Stokes (RANS) based methods attempt to model all scales of turbulence. However, theoretical models for anisotropic turbulence do not exist and thus RANS methods attempt to adapt turbulence models developed from the theory of the turbulence length scales. RANS based methods also require a fine mesh resolution and higher order schemes for simulating accurate near-wall properties.

Fluent uses a Reynolds-averaging (or ensemble-averaging) method to avoid direct simulation of the small-scale turbulent fluctuations when employing the Navier-Stokes equations. RANS models decompose the flow into its time-averaged (i.e. average velocity) and fluctuating quantities (i.e. change of velocity with time). Fluent offers numerous models of turbulence, of which the two that are deemed most appropriate for automotive simulations are the Spalart-Allmaras (an one-equation model) and K-ω (a two equation model) due to their balance of computational efficiency and accuracy. The Spalart-Allmaras model (Spalart et al (1992)) is a relatively simple model that solves a modelled transport equation for the kinematic eddy (turbulent) viscosity, designed initially for aerospace applications involving wall-bounded flows, and has been shown to give good results for boundary layers subjected to adverse pressure gradients.

The Spalart-Allmaras model is effectively a low-Reynolds-number model, requiring the viscosity-affected region of the boundary layer to be properly resolved. In Fluent the Spalart-Allmaras model has been implemented to use wall functions when the mesh resolution is not sufficiently fine, which is suitable where accurate turbulent flow computations are not critical. It is therefore better for unstructured meshes, but can struggle with homogeneous, isotropic turbulence and is less able to rapidly accommodate large changes in length scale. The standard K-ω model is an empirical model

based on model transport equations for the turbulence kinetic energy and the specific dissipation rate. As it is composed of two-equations, and more developed, it is suggested to be more accurate for more turbulent applications with greater pressure gradients.

In conclusion, Powerflow is a turbulence modelling application that, in using particle collisions to model air flow, is naturally an unsteady solver and inherently more stable. Fluent can offer very accurate flow simulation, but is a time-averaged solver and was found to be more time-consuming in case set-up and operation than Powerflow for unsteady cases. In this thesis, Fluent is initially used for modelling 2D TGS designs, but Powerflow was found to be able to similarly model 2D flows whilst having the ability to simulate unsteady and dynamic mesh 3D models more readily. Therefore, for the modelling of transient effects on vehicle models, Powerflow is used exclusively. In terms of the specific case set-ups for each solver, whether modelling unsteady or time-variant flows in 2D or 3D, the details are supplied in the appropriate chapter as they directly connect with the presentation of the respective results.

## 3.2 Study Approach

The simulation was conducted using Exa Powerflow, a lattice-Boltzmann based solver CFD package. One objective of the study was to simulate the experiment undertaken by Ryan (2000), where a sharp-edged gust case propagated over an idealised model (developed by Docton (1996), Figure 66 and Figure 67). The Docton model is used throughout this study at the same size and scale as in his work. Figure 66 and Figure 67 illustrate the computational flow domain and the 11 nested regions of mesh refinement. The cell resolution adjacent to the model in the simulations was 2.0mm (a relatively fine mesh), using the same mesh considerations and scaling as is detailed in Gaylard et al (2010). Periodic walls were used in ±Y, with the inlet set as a 'velocity inlet' and the outlet set as a 'characteristic static pressure outlet'.

The test domain had 10 vehicle lengths upstream and 15 downstream of the model (i.e. 26 vehicle domain length) and 10 either side (so 21 vehicle domain widths), based upon Sims-Williams (2001). Powerflow is a time-resolved (unsteady) solver and the time step size used was $1.05 \times 10^{-5}$s.

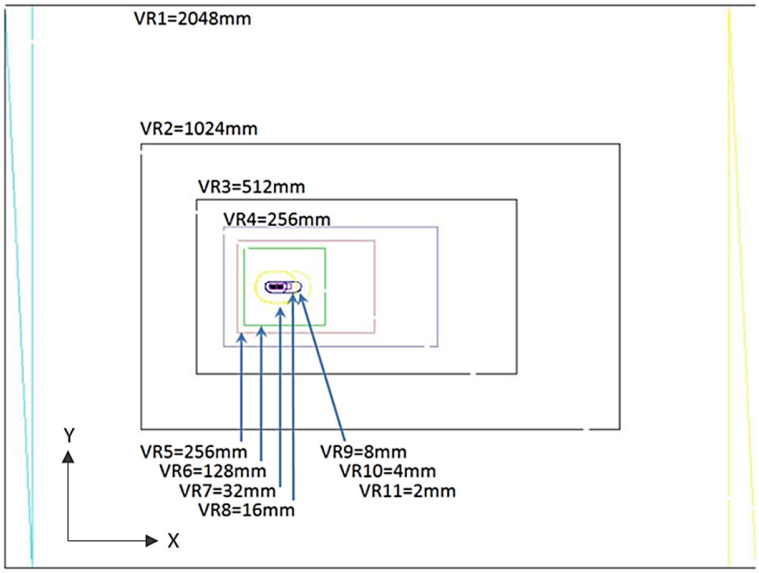


Figure 66 - Powerflow case domain; note the range of variable resolution regions

Further mesh refinement around the model can be seen in Figure 67. The size of the Docton model is shown in the literature review where his research, Docton et al (1996), is presented.

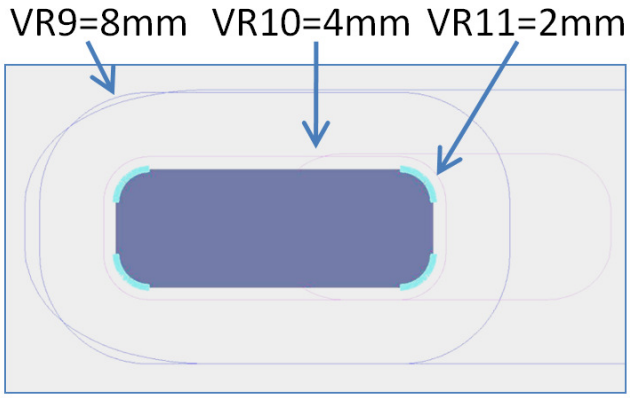


Figure 67 - Powerflow domain with multiple VR regions and the Docton model

## 3.3 Steady Yaw Analysis

As an initial approach, a case optimisation study was completed to fulfil the following criteria:

- Axial velocity of 30ms$^{-1}$, 8-seconds case length and the number of 'flush-throughs' and cycles maintained
- Mesh variation test confirmed voxel and Variable Region set-up
- Fixed time-step size and long processing times to allow appropriate flow propagation in the low frequency cases

- High logging frequency maintained and time step kept to less than 1 x $10^{-5}$ s
- Case time-steps advanced until forces were found be consistent for at least 0.5s in the steady cases (from which the forces were time-averaged over the 0.5s) and for at least an integer set of periods to translate the entire domain in the unsteady inlet cases with consistent force oscillations (from which the last set of periods are presented or averaged as appropriate). A fixed convergence metric was not set.

A set of simulations was conducted with the Docton model set at a range of steady yaw angles from 0° to 10° in 2° increments. For all simulations presented here the axial component of inlet velocity was constant (30ms$^{-1}$) and an additional crosswind component ($U_Y$) was introduced to create yaw. This means that the total resultant velocity is larger for higher yaw angles. This is a better replication of the on-road experience than the common wind tunnel practise of running at constant velocity and yawing the vehicle. Non-dimensional coefficients are based on the axial (i.e.: nominal driving velocity) rather than the total resultant velocity. Figure 68 illustrates the variation of drag coefficient with yaw angle, showing an increase in drag coefficient until 2° of yaw (due to increased frontal area), and then a decrease as downstream flow separation increases. This profile is due to a combination of an increase in flow separation on the leeward side of the vehicle at early increases in yaw and an increase velocity magnitude with yaw angle (as axial velocity was kept constant) causing the drag coefficient to drop with yaw angle.

Additionally, in difference to turntable induced yaw without a tangential correction, the drag is kept aligned with the vehicle.

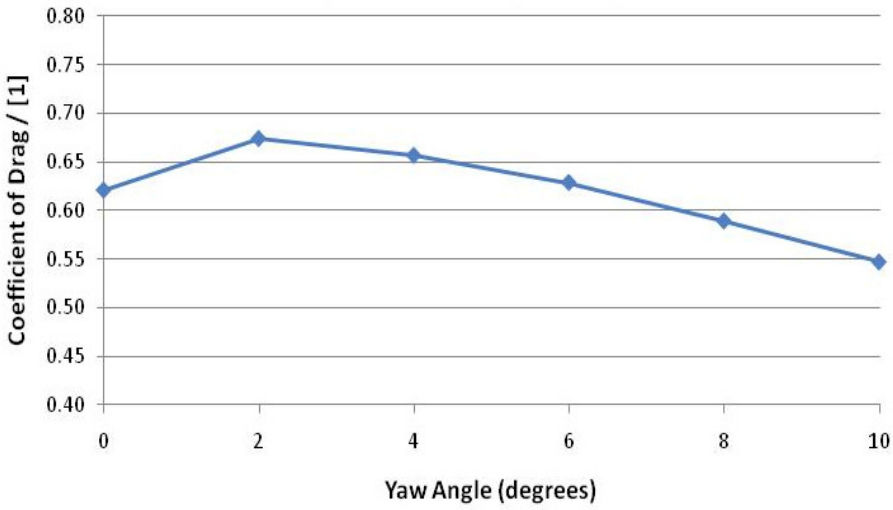


Figure 68 - Drag coefficient against yaw angle for the steady-state cases

Figure 69 illustrates the corresponding variation of sideforce coefficient, showing a linear variation of sideforce with yaw angle which is compared with, and increases at a lower rate than, the idealised lift slope ($2\pi\alpha(^{l}/_{w})$) predicted by potential flow theory. The ideal slope demonstrates the effect of yaw on a symmetric aerofoil, showing that the variation in sideforce is more complex than simple flow theory would predict due to flow separation on the leeward side of the model at low yaw angles.

The strong linearity of the experimental result is representative of the idealised model design and 2D flow structure showing a straightforward increase in sideforce with yaw, whereas in 3D complex flow structures would be generated with increases in yaw angle causing a non-linear sideforce variation.

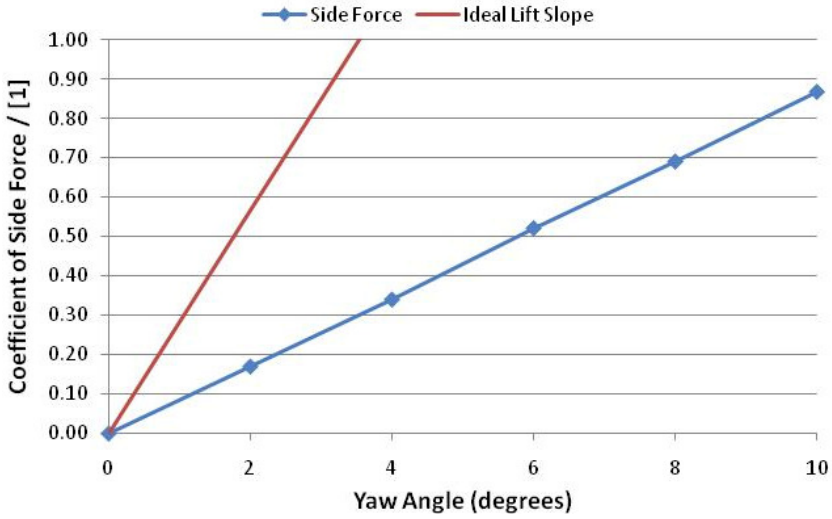


Figure 69 - Coefficient of sideforce with yaw angle for the steady-state cases

## 3.4 Harmonic Inlet Tests

A series of harmonic test cases were modelled using the Docton model. Inlet turbulence was set at 1% intensity at 1m turbulence length scale, with the axial velocity fixed at $30ms^{-1}$ and lateral velocity varied as the inlet yaw velocity. The default yaw angle peak was $\pm6^{o}$, varying as a sinusoidal wave.

Tests were conducted at frequencies of 0.03, 0.15, 0.33, 1.75, 3.5, 7.0 and 10.0Hz, which were selected to ensure the capture of the critical reduced frequency threshold. All results are presented in terms of reduced frequency based upon vehicle length.

In order to determine a reference, steady-state equivalent drag coefficient (i.e. zero frequency point) the values from the 'steady-state' simulations were summed together in proportion to the area under the sine curve that they occupy for a $6^{o}$ sine wave (i.e. basic numerical integration). This gave a steady-state value of $C_D$ = 0.62 (the inlet yaw trace is plotted on the secondary axis in grey at

0.01 reduced frequency on graphs shown later in this chapter for simplicity of comparison). Similarly, the drag coefficient standard deviation was 0.12 and the standard deviation of sideforce coefficient was 1.46 (under quasi-steady conditions).

The major constraints determining the simulation parameters for each configuration were: a fixed mesh resolution for all cases, which fixes the physical time elapsed per time step, the number of 'flush-throughs' (labelled FTS, that is the number of times that flow at the freestream velocity would replace all the fluid within the computational domain), the number of periods that will be simulated and the physical processing time for each case. This resulted in cases with between 1 and 8 million time-steps. In order to maintain a consistent number of measurements per period for the wide range of inlet frequencies, parameters were established as in Table 4. For low frequency yaw fluctuations the physical time simulated is dictated by a requirement to simulate multiple yaw fluctuation periods, while for high frequency yaw fluctuations the physical time simulated is dictated by a requirement for multiple flush-throughs.

**Table 4 - Test set-up matrix**

| Freq. (Hz) | Periods | FTS | Physical Time (s) | Reduced Freq. | Logs / Period |
|---|---|---|---|---|---|
| 0.03 | 2.5 | 50.2 | 82.7 | 0.03 | 634 |
| 0.33 | 11.5 | 21.1 | 34.7 | 0.29 | 443 |
| 1.75 | 60.7 | 21.1 | 34.7 | 1.53 | 136 |
| 3.50 | 44.2 | 7.7 | 12.6 | 3.06 | 136 |
| 7.00 | 44.2 | 3.8 | 6.3 | 6.12 | 136 |
| 10.0 | 63.1 | 3.8 | 6.3 | 8.75 | 127 |

The harmonic flow can be visualised as shown in Figure 70 and Figure 71, where the plots of approximately 1Hz and 5Hz inlet wave have been plotted in scale with the model to show the proportion of the wavelength to vehicle length (the figure is illustrative, the actual frequencies and wavelengths differed). The key point is that wave lengths used ranged from shorter than vehicle length to lengths much larger than vehicle length and hence scales comparable to vehicle length are in the middle.

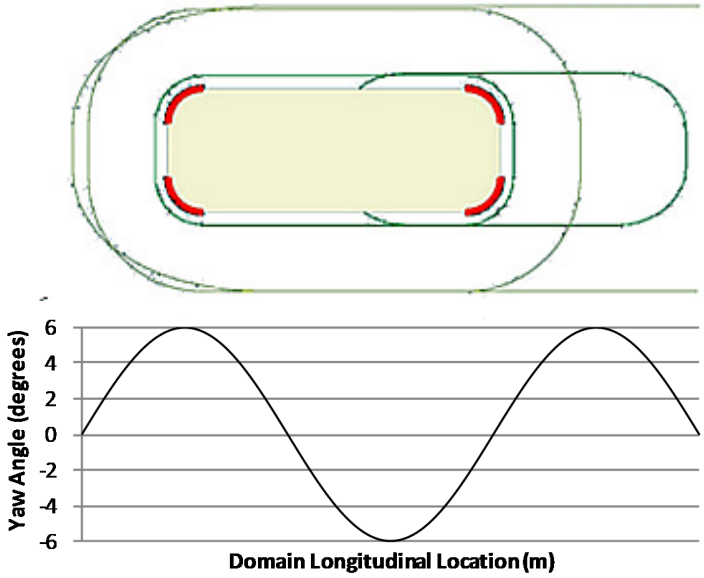


Figure 70 - Yaw scale at, illustratively, ωR = 3.00 (10Hz)

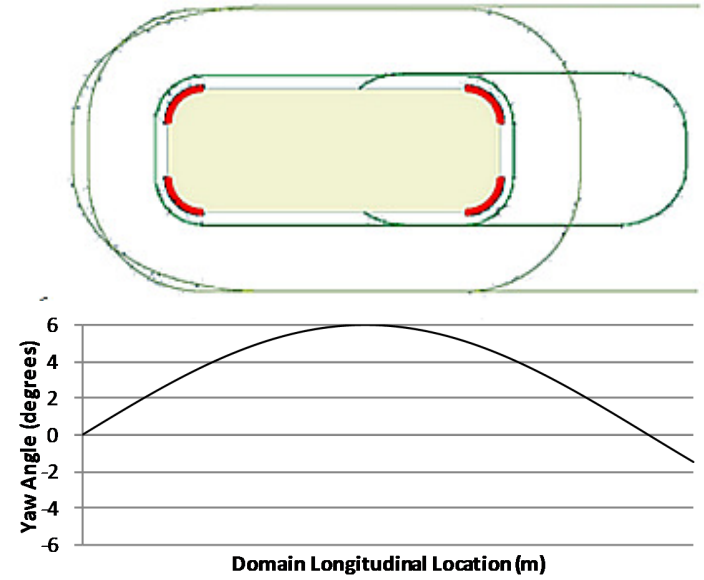


Figure 71 - Yaw scale at, illustratively, ωR = 0.30 (1Hz)

Investigations completed include varying Reynolds number, exploring non-linearity in the vehicle's response to yaw fluctuations of different magnitudes and cases comprising of multiple, superimposed frequencies. Further geometry cases were evaluated for varying corner radii and vehicle width. The geometries tested covered relatively significant aspect ratio variations of the Docton model. The widths ranged from 132.3 to 284.0mm following studies by Sims-Williams (2001). The complete range of studies conducted was as follows:

- Yaw angles of 0, 2, 4, 6, 8 and 10° for a steady 30ms$^{-1}$ inlet, using the Docton model.

- Frequency analysis at 0.03, 0.15, 0.33, 1.75, 3.5, 7.0 and 10.0Hz for ±6° yaw.
- A viscosity analysis running the test case at 0.03, 1.75, 3.50 and 10.0Hz for ambient Viscosity x4 and ambient Viscosity/10000.
- 30mm, 55mm and 80mm corner radii at 0.03, 1.75, 3.50 and 10.0Hz.
- 132.3, 194.0 and 284.0mm widths (i.e. aspect ratio variance) at 0.03, 1.75, 3.50 and 10.0Hz.
- 3, 6, 12 and 20° peak yaw angle tests at 0.03, 1.75, 3.50 and 10.0Hz.
- Superimposed frequencies of 3.50 + 0.33Hz and 3.50 + 10.0Hz.

### 3.4.1 Frequency Range

A range of frequencies were tested from $\omega_R$ = 0.03 to $\omega_R$ = 8.80 (i.e. 0.03Hz to 10.0Hz) for 6° peak yaw. All the cases display a pressure fluctuation at approximately 3.5Hz ($\omega_R \approx 3$ based on model length, Strouhal Number 0.27 based on model width). The physical time bases for the different cases varied by more than two orders of magnitude and so in some cases the vortex shedding was at a relatively much higher frequency than in others, where it was at a lower frequency than the yaw fluctuations. In Figure 72 the traces have been reset such that the yaw angle plotted corresponds with the angle at the front of the vehicle and as such any phase shift shown between the frequency traces is a true phase difference experienced by the model. For the $\omega_R$ = 0.03 and 0.33 cases, the fluctuations due to vortex shedding have been filtered from the output traces for clarity. Note that the drag varies at twice the driving frequency of the yaw sine wave since both positive and negative yaw each have the same effect on drag.

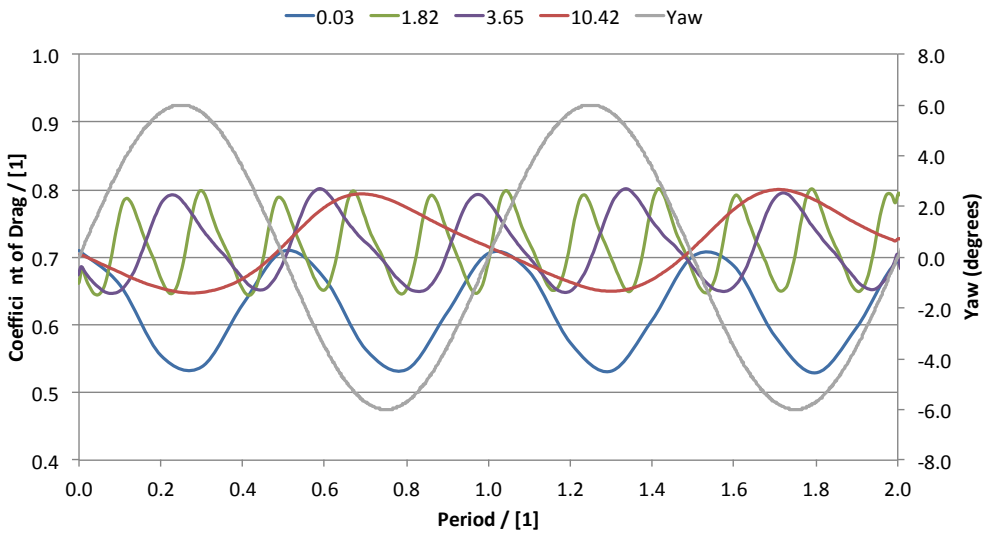


Figure 72 - Filtered results of drag coefficient with period number

Figure 73 presents the corresponding variation in sideforce coefficient, which naturally averages to zero over an integral number of cycles. It is apparent that the sideforce varies greatly over the gust cycle. Note that, as expected, the sideforce oscillates at the same frequency as the driving frequency.

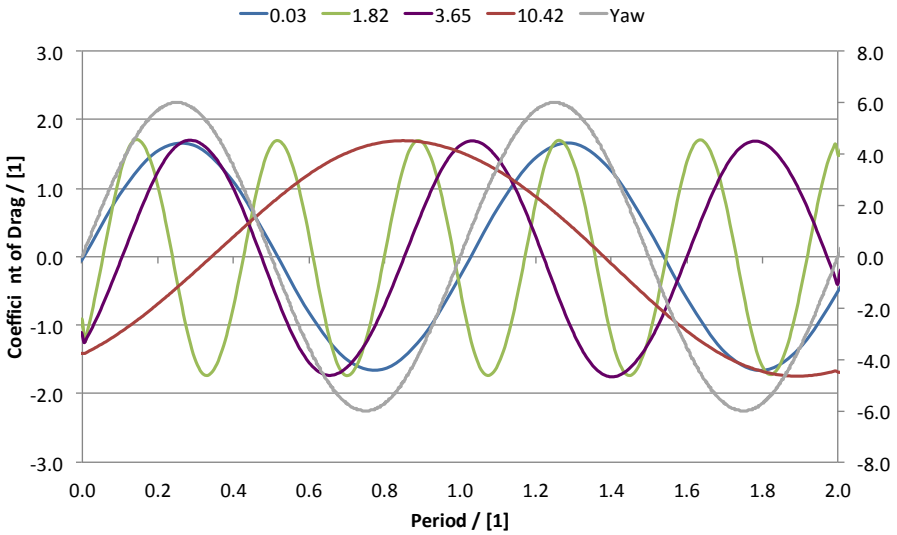


Figure 73 - Filtered coefficient of sideforce with period

Figure 74 illustrates the change of average drag coefficient variation with reduced frequency across the set of simulations (using the $\omega_R = 0.03$ case as a baseline). Averages and standard deviations were always calculated over an integer number of periods. The point plotted at a reduced frequency of 0.01 is the true quasi-steady case derived from simulations at steady yaw angles. It is evident that a prominent drag increase ($\Delta C_D = 0.10$) occurs between reduced frequencies of 0.3 and 1.5. Fundamental work in aerodynamics (as discussed by Corin et al (2008) and others) has indicated that reduced frequencies below $\omega_R = 0.1$ would be expected to be quasi-steady, but for the unsteady effect to become significant for reduced frequencies somewhere between 0.1 and 1.0 and the result of Figure 74 fits appropriately with this theory. The drag coefficient effect between $\omega_R = 0.3$ and 1.5 observed here would correlate to a full-scale frequency of 0.33 - 1.75Hz, equivalent to length scales of 17 - 90m or 4 to 20 vehicle lengths. This result is in keeping with the observations that the flow around a model subjected to a step change in yaw angle requires about 7 vehicle lengths to reach a steady-state.

This figure also shows that for reduced frequencies above 1.5, further changes in drag coefficient are small, indicating that for this geometry at least, shorter length scales do not create significantly different effects.

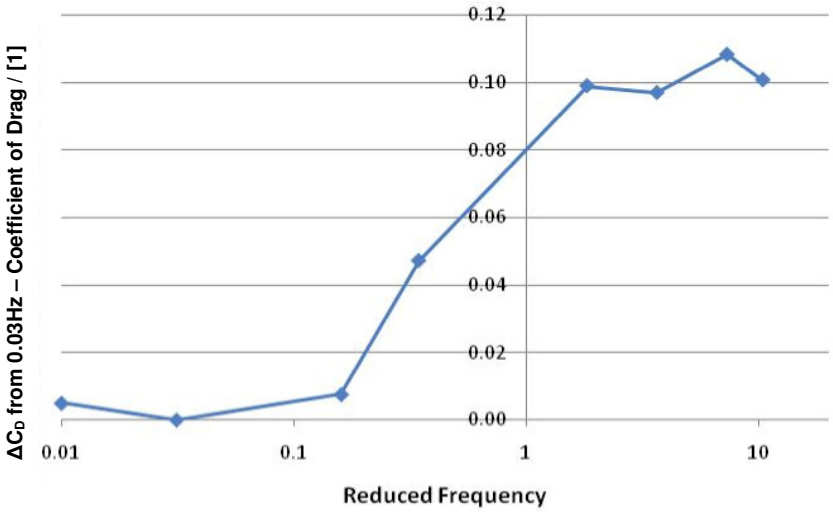


Figure 74 - Variation of normalised average drag coefficient with reduced frequency

Figure 75 illustrates the magnitude of the time variation of sideforce as well as drag and demonstrates an approximately similar critical frequency range. As expected, the magnitude of the force fluctuation decreases with increasing frequency. In Figure 75, if the standard deviations were divided between one another and combined, the result would be comparable to aerodynamic admittance.

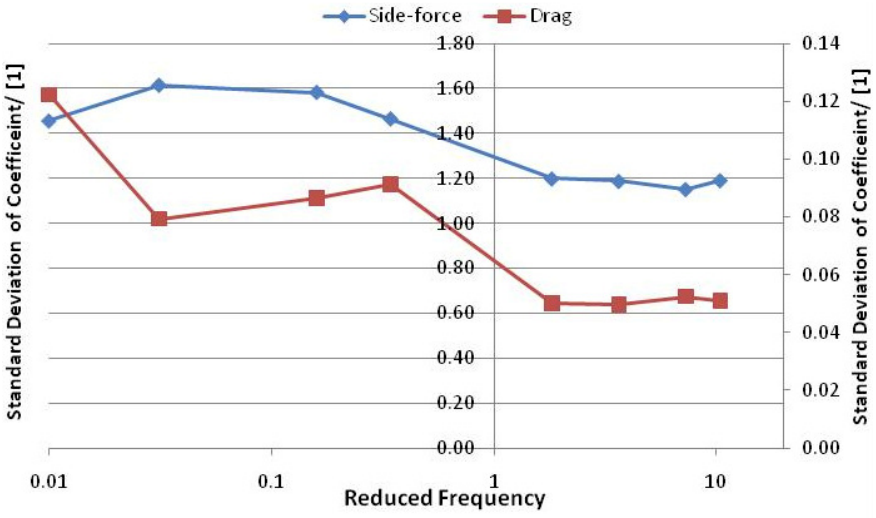


Figure 75 - Drag and sideforce coefficient deviation with reduced frequency

### 3.4.2 Reynolds's Number Variation

Reynolds number effects were investigated by changing the fluid viscosity. Increasing the viscosity by a factor of 4 created a flow with a low Reynolds number, corresponding to a small-scale model test, whilst reducing the viscosity by four orders of magnitude (changing the Reynolds number to the order of $x10^{10}$), resulted in a flow condition that is much more inviscid in nature. Though the flow is still not inviscid, the significant change in viscosity makes it possible to identify whether the non-quasi-steady effects observed earlier are more likely to be viscous or inviscid effects. Figure 76 shows the change of the averaged drag coefficient with reduced frequency at the three different Reynolds numbers.

While Reynolds number measures the viscous effects that cause a significant variation on the total drag, the model sensitivity to yaw fluctuations at different frequencies is broadly consistent in magnitude, and in terms of critical reduced frequency, over a Reynolds number variation of several orders of magnitude, centred on the frequency region of interest for road vehicles. It can be concluded that the non-quasi-steady effects (that is the effect of varying inlet frequency, as found earlier) occurs regardless of Reynolds number. Of course reducing the viscosity by several orders of magnitude does not create entirely inviscid flow and the CFD turbulence model is not designed to operate at such low viscosity orders, but nevertheless the result of a consistent slope between the three cases shows that the change in drag and sideforce is not caused just because of viscous effects (i.e. separation bubbles) and that time-averaged changes are more significant in effect than dynamic flow changes.

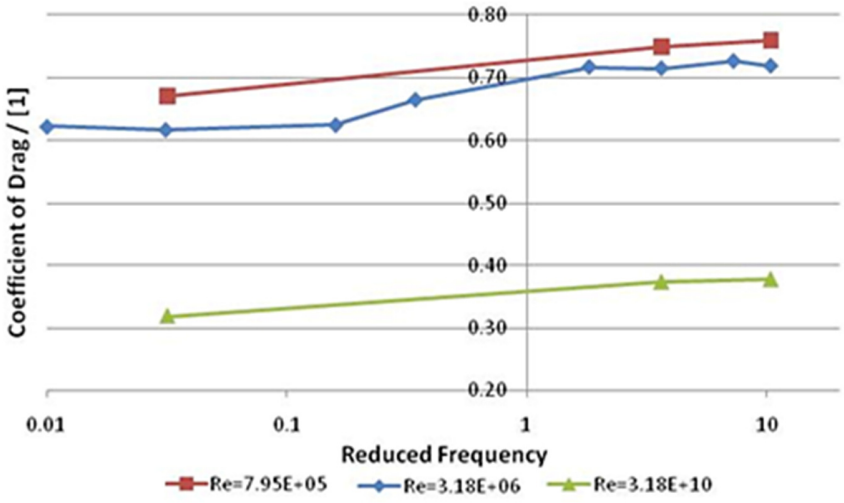


Figure 76 - Normalised drag coefficient (relative to lowest frequency in respective subset) with reduced frequency

Figure 77 shows the reduction in sideforce deviation with frequency and again this effect is not irrelevant with the altered viscosity.

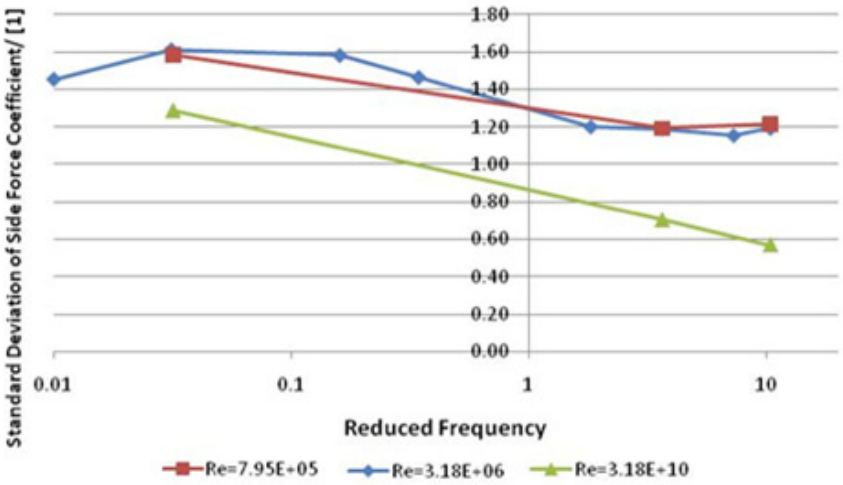


Figure 77 - Sideforce coefficient deviation with reduced frequency

### 3.4.3 Yaw Amplitude Variation

Figure 78 shows the change in drag coefficient with reduced frequency for a range of yaw amplitudes. The result confirms that the variation in peak angle does not significantly affect the critical reduced frequency limit. Surprisingly, increasing yaw magnitude does not to produce a corresponding change in average drag. This is in part because at all yaw angles the axial velocity component is the same. It is evident in Figure 79 that the sideforce deviation at low frequencies is much more prominent than at higher frequencies, and further that above the critical reduced frequency limit the sideforce deviation becomes consistent over the peak-yaw angle range. It should again be noted that the resultant velocity is large at high peak yaw angles, hence the increased sideforce coefficients. This is not simply because the yaw angle has been increased, but due to the increased total resultant velocity.

Nevertheless, Figure 79 illustrates that there is an increase in transient force with an increase in frequency, but that the correlation of the effect is not linear with the forcing function. The concept of an aerodynamic admittance or transfer function sitting between the forcing function and the vehicle response would essentially assume a linear response to the forcing function and therefore the response would not be correctly modelled.

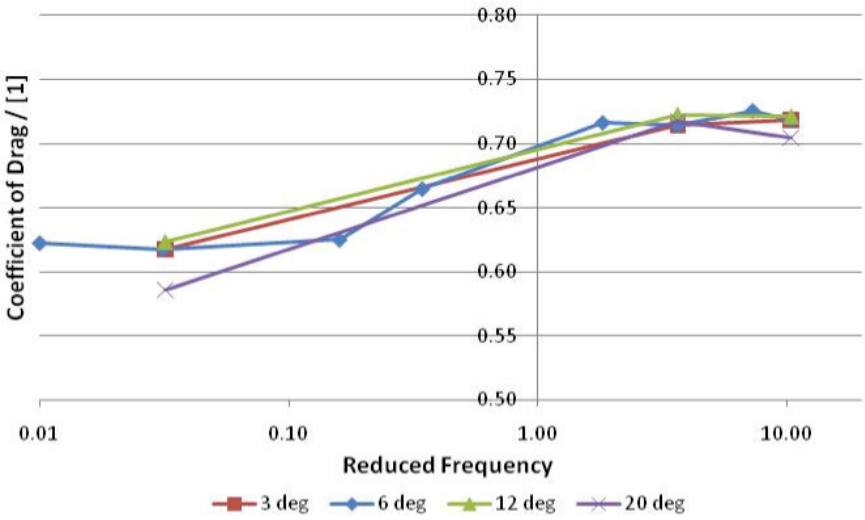


Figure 78 - Drag coefficient against reduced frequency for a variation in peak yaw angle

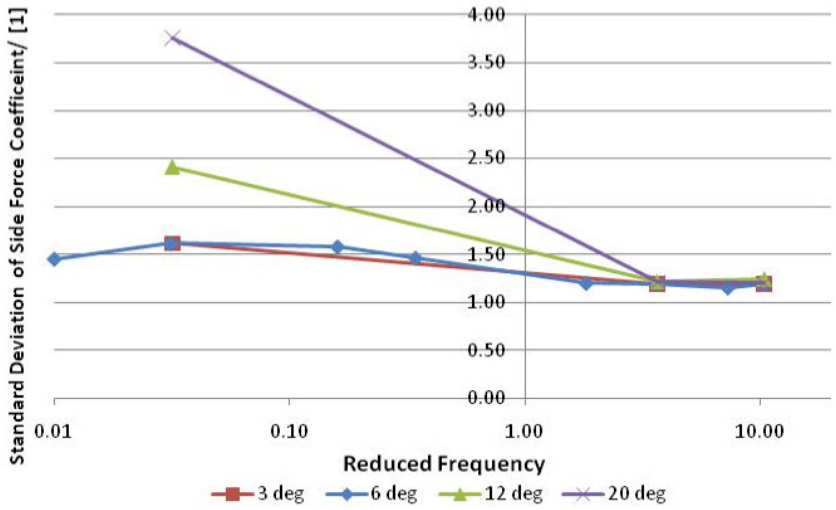


Figure 79 - Sideforce coefficient deviation with reduced frequency and varying amplitude

### 3.4.4 Superposition of Multiple Frequencies

A linear aerodynamic admittance means that the incremental impact of a forcing function at a particular frequency would be the same as the impact of that forcing function in isolation. Superimposing two independent yaw fluctuations at different frequencies tested this hypothesis. The superimposed cases were a 3.5Hz ($\omega_R = 3.0$) case, seen as a frequency very close to the quasi-steady limit, which was added to a 0.03Hz ($\omega_R = 0.03$) in the first case and a 10Hz ($\omega_R = 9$) frequency in the second case. In comparing the effect of adding a lower frequency to the 3.5Hz ($\omega_R = 3$) case and similarly a higher frequency to the 3.5Hz case, it is possible to test linearity and whether multiple frequencies impact the critical frequency limit.

It is shown in Figure 80 that the resultant drag coefficient of a case is based upon the frequency which creates the greatest drag coefficient. For example, the drag coefficient at 3.5Hz ($\omega_R = 3.0$) case is around 0.72, whereas the drag coefficient at 0.03Hz yaw frequency ($\omega_R = 0.03$) is around 0.62. However, superimposing the two in equal ratios (both at full energy, that being 6° for both sine waves) has resulted in the actual drag coefficient being that of the 3.5Hz case, not the lower drag coefficient from the 0.03Hz case nor the sum of the two separate drag coefficients. This effect is repeated with a 10Hz superposition inlet. This leads to the same conclusion as the yaw magnitude test, that the model aerodynamic response is non-linear. It is also suggested that the resultant drag coefficient experience by an idealised geometry will be that of the greater drag from any significant frequency component, which will namely be the frequencies above the quasi-steady limit, as these frequencies have been shown to generate the highest drag coefficients.

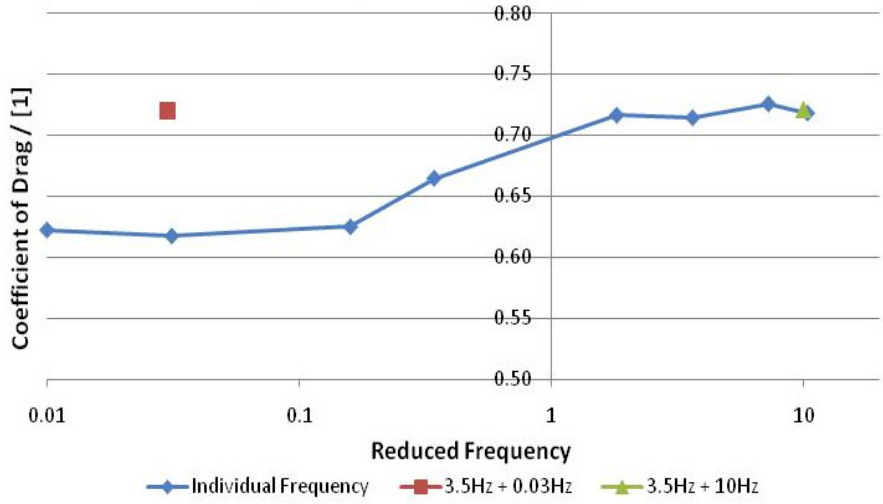


Figure 80 - Drag coefficient with reduced frequency for varying super-position

Figure 81 again correlates with earlier graphs showing a 25% reduction in drag coefficient variation for increased inlet frequency. Additionally, it is of interest that as the drag force corresponds to the highest drag coefficient from the superimposed inlet frequency with the highest individual drag coefficient, the sideforce deviation result relates to the lowest individual component. As such though the drag will be greater, the required test frequency range is smaller, which reduces the peak intensity requirement for a simulation (i.e. therefore to test at frequencies which create the greatest vehicle response).

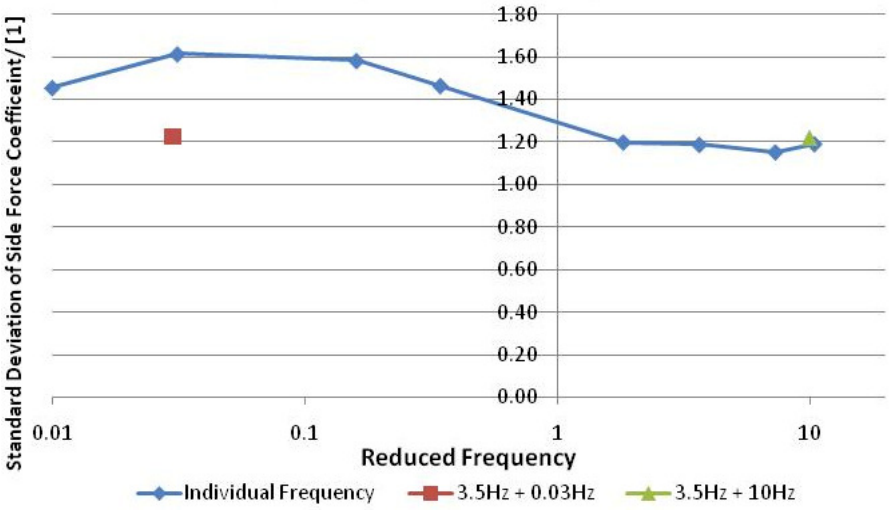


Figure 81 - Deviation of sideforce coefficient with reduced frequency for two super-positions

Figure 82 and Figure 83 further illustrate this point. It can be seen that the effect of having two frequencies is non-summative, and that the result is more comparable to running either at double the peak yaw angle or the drag of the highest individual frequency drag measurement.

In these figures the X-axis notation (i.e. 6@3.65) denotes the peak yaw angle (i.e. 6°) at (@) a given reduced frequency (i.e. 3.65) and where two are shown, these are added together. This is also shown in the sideforce coefficient plot, where the superposition result is similar to running the case at double the peak yaw angle. This gives the resultant sideforce from the individual frequency that has the lowest sideforce deviation in its own right.

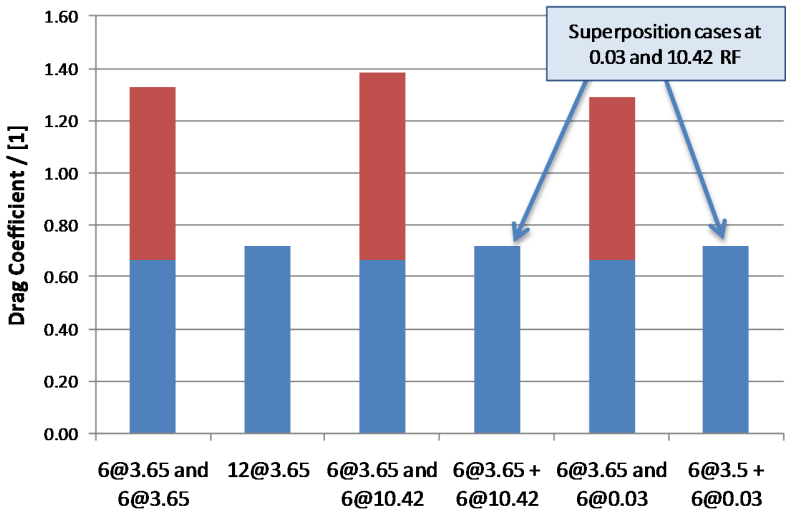


Figure 82 - Comparison of drag coefficients for similar inlet set-ups

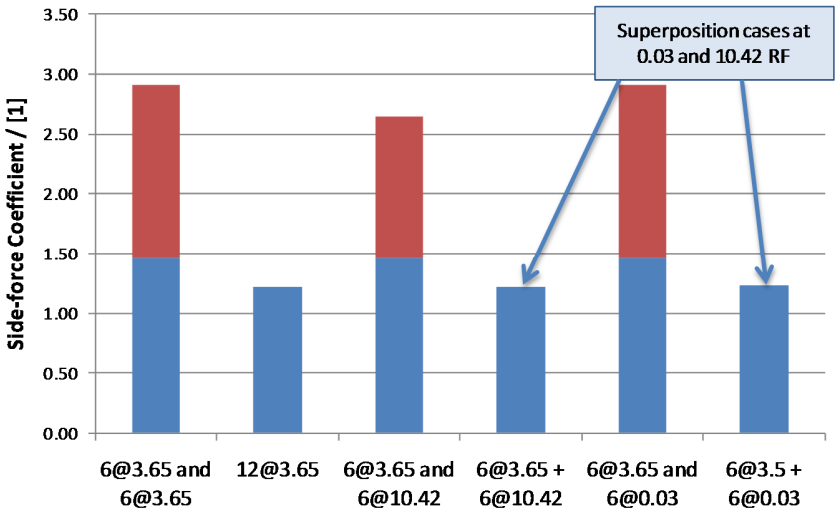


Figure 83 - Comparison of sideforce coefficients for similar inlet set-ups

With multiple frequency inlets, the drag force strongly tends to the individual frequency with the highest individual drag coefficient, as is shown in Figure 84.

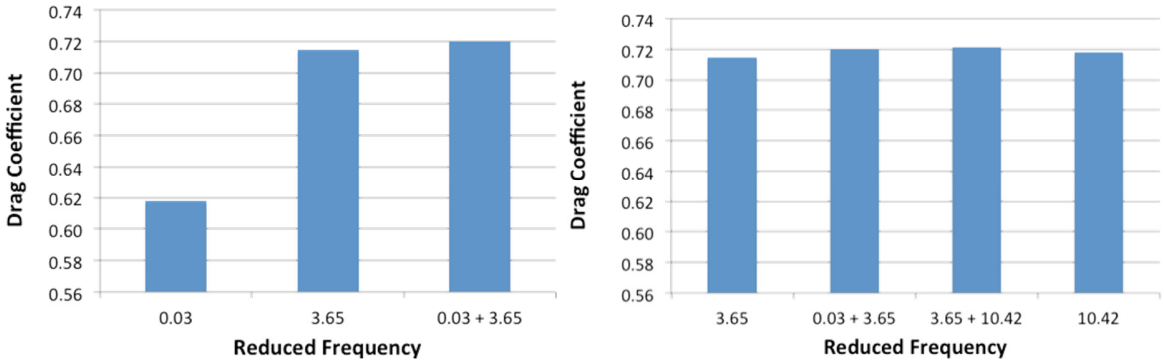


Figure 84 - Resultant drag coefficient will tend to highest drag of individual component frequency if multiple frequencies are super-imposed

### 3.4.5 Effects of Model Width and Corner Radii

The normalised plots of drag coefficient in Figure 85 and Figure 86 show that the critical reduced frequency limit is maintained, but that the effect of the frequency increase on drag coefficient is affected by the model's geometry. Note that the 'Wid' and 'Rad' values denote the respective width and corner radius of the model in millimetres based upon the Docton model presented earlier. Figure 85 shows that as a model's width is reduced (i.e. the model is less bluff) then the effect of an increase in frequency becomes more prominent. It is also evident that after the critical reduced frequency is exceeded, the drag coefficient plateaus. Figure 86 demonstrates that the reduction in corner radius (i.e. sharper corners) causes the effect of a frequency increase to become more significant.

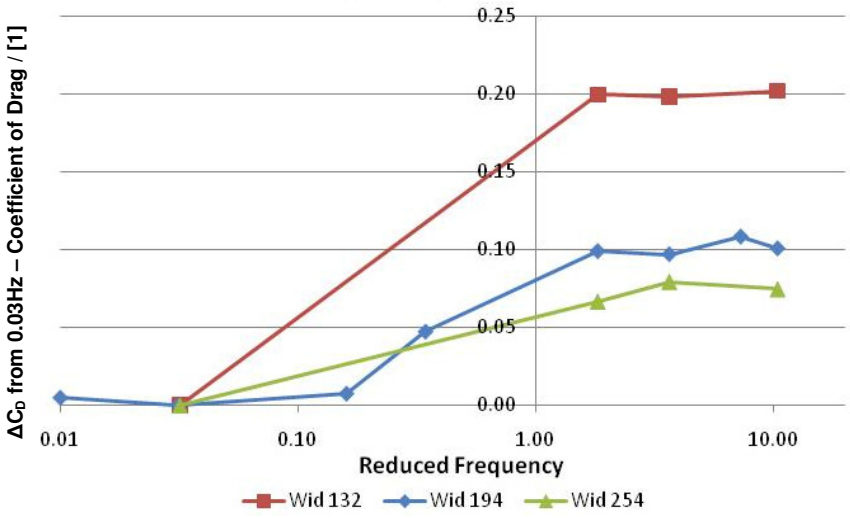


Figure 85 - Drag coefficient with reduced frequency for varying widths

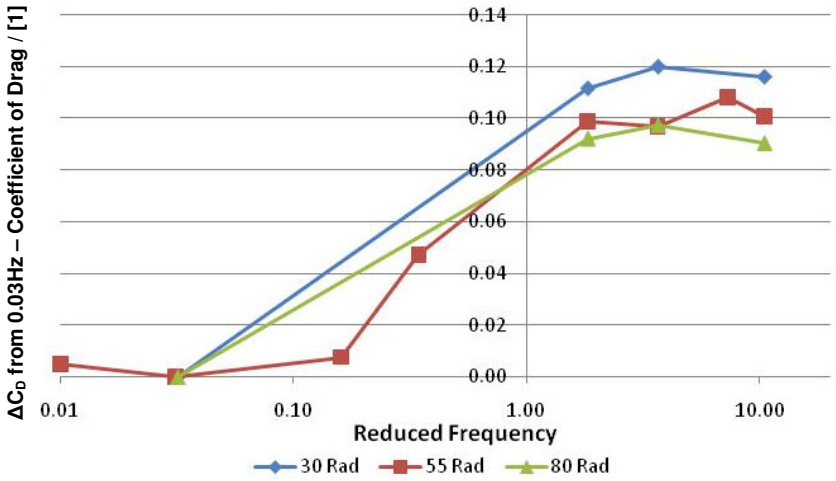


Figure 86 - Normalised drag coefficient with reduced frequency for varying corner radii

Figure 87 and Figure 88 detail the reduction in sideforce deviation with increase an in frequency, as seen in earlier results. In conclusion, models that are long in aspect ratio and with sharp corners experience a greater drag increase in line with frequency than wider models that have more rounded corners.

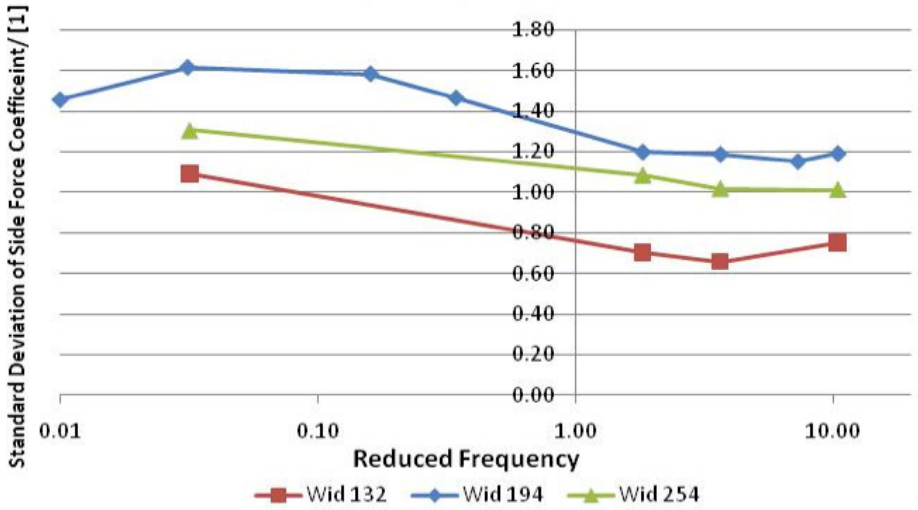


Figure 87 - Deviation of sideforce coefficient with reduced frequency for varying widths

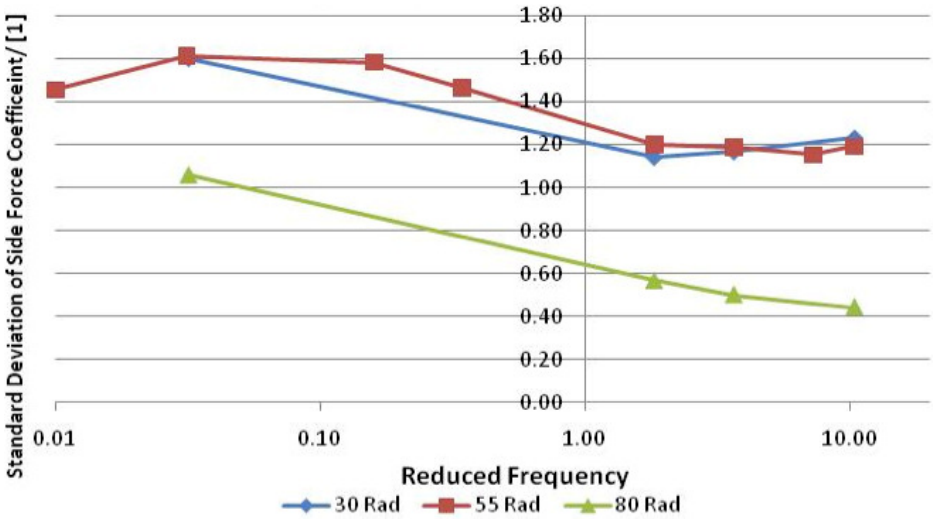


Figure 88 - Deviation of sideforce coefficient with reduced frequency for varying corner radii

### 3.4.6 Superposition of Constant Yaw Offset

The results presents in this chapter so far have all been with a sine inlet function with a zero yaw angle mean flow. In practise, the average yaw angle seen on the road is typically a few degrees and turbulence fluctuations will be superimposed upon that mean value. All of the CFD tests described here were also fully evaluated with a mean yaw angle of 3° and a superimposed sine fluctuation. In these cases, the amplitude of the sine wave was 3° rather than 6° (i.e. halved) otherwise the combined sum would be double previous cases making a comparison less straightforward.

An example of the results for this scenario is given in Figure 89. The study confirmed that the critical reduced frequency threshold was similar, albeit slightly more abrupt, than for the zero mean yaw cases, returning a result just above $\omega_R = 0.03$. This alternative condition also produced similar conclusions with respect to the impact of varying viscosity and model geometry.

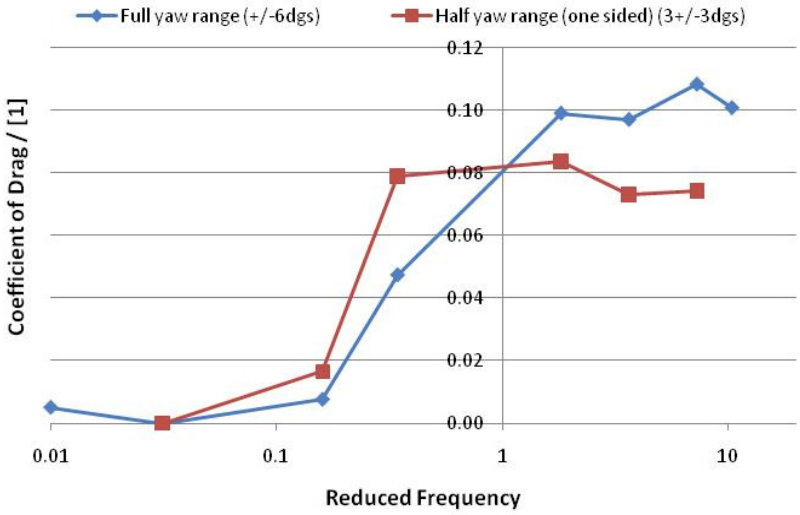


Figure 89 - Effect on drag coefficient with and without yaw offset

## 3.5 Conclusions

A study was completed to understand the fundamental effect of varying incoming flow yaw to the response of a vehicle. Though a simplified model was used, the approach allowed the investigation of the admittance between inlet flows and vehicle response forces, and helped to develop an understanding of the quasi-steady frequency threshold and the effects of viscosity on the threshold, as well as allowing numerous geometries to be tested. It was found that for most measures, and especially for time-averaged drag, the flow could be treated as quasi-steady for reduced frequencies below 0.3, in line with expectations. The most significant changes were observed in a critical reduced frequency range between $\omega_R = 0.3$ and $\omega_R = 1.5$. This range corresponds to scales of 4 - 20 vehicle lengths, or 17 - 90m or periods of 0.6 to 3.0s, or frequencies of 0.33Hz to 1.75Hz (for a full scale vehicle at $30ms^{-1}$). Frequencies larger than this range will still have significant effects, but in this case the effects showed little frequency sensitivity once above the critical range. This result is summarised in Figure 90, where the variation of drag force coefficient with inlet yaw frequency trace is shown (as presented earlier in Figure 74, therefore the Y-axis scale is removed to de-clutter the plot) overlaying a range of turbulence generation systems resultant frequencies, highlighting the frequency range where non-quasi-steady effects demonstrate a significant vehicle response.

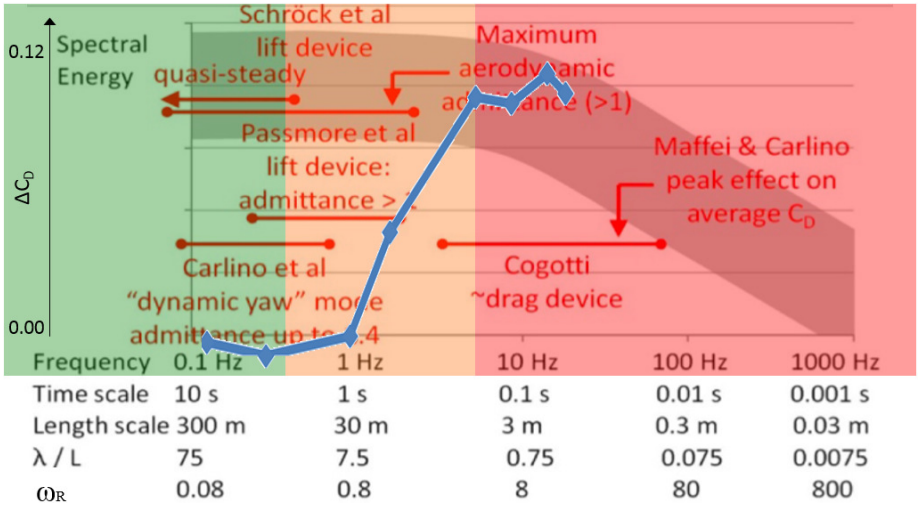


Figure 90 - Summary of critical frequency region

Of course a real vehicle will have small physical geometry and features (e.g. wing mirrors) creating more yaw sensitive flow regions, which will respond to higher frequencies than the general vehicle. The critical reduced frequency range for these features will therefore correspond to smaller physical scales, and so will bring importance to these scales smaller (but not larger) than the 4 - 20 vehicle length scale. The effect of the yaw variation (at constant axial velocity) was to increase the time-averaged drag coefficient and the deviation of drag coefficient and sideforce coefficient. These effects increased with frequency, through once at the critical frequency threshold, they then plateaued, with then higher frequencies producing the same effect as frequencies just above the critical frequency threshold.

The dynamic effects were largely independent of Reynolds number, including for near-inviscid conditions. This indicates that the sources of non-quasi-steady response are not viscous in origin. Increasing yaw amplitude or combining multiple frequency components did not have a summative impact on the time-averaged or time varying drag and sideforce. Care therefore needs to be taken in trying to describe vehicle response to transient conditions using linear concepts such as transfer or admittance functions. When superimposing different frequencies the resulting average drag was close to that of the individual frequency component with the highest individual drag coefficient. The sideforce deviation was also consistent with the individual frequency that had the lowest pressure deviation in the frequency range. It was found that narrow bodies with sharper corners caused a greater time-averaged drag coefficient change with frequency as compared with rounder or wider bodies.

## 4. Mid-Sized European Hatchback On-road Study

In order to develop the analysis of the effects of on-road turbulence, a study was completed using the Durham University's mid-sized European hatchback vehicle (Rover 200, R3) to record the on-road aerodynamic environment and to model the flow characteristics over the sideglass, which is a highly yaw-sensitive region. The results from this data collection not only improved the understanding of flow in the sideglass region, but the results also allowed the characterisation of on-road turbulence. From the study, at the end of this chapter, an example flow trace is presented that was replicated in a wind tunnel using a 40% model of the vehicle, which additionally offered results on the effect on vehicle drag and lateral stability from on-road turbulence.

The same vehicle was tested in the MIRA full-sized wind tunnel at three yaw angles by Lawson et al (2007), and the data is repeated here as a quasi-steady comparison with the on-road data collection. It should be noted that the yaw increments used by Lawson were too coarse to resolve fine detail.

### 4.1 MIRA Wind Tunnel Results

Contour plots of pressure coefficient against yaw angle are given in Figure 91 (−10°), Figure 92 (0°) and Figure 93 (+10° of flow yaw), with tapping ID numbers shown, from Lawson et al (2007) and Lawson et al (2008). Note the general increase in pressure coefficient at positive yaw.

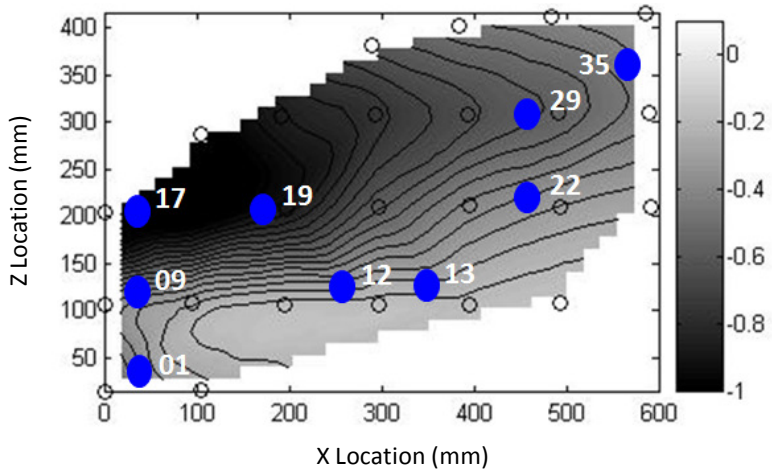


Figure 91 - Contour plot of static pressure coefficient, Lawson MIRA data, -10° yaw - Lawson et al (2007)

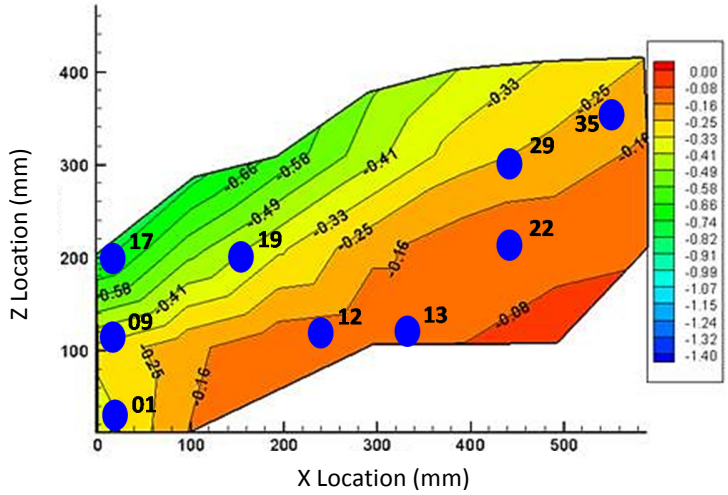


Figure 92 - Contour plot of sideglass static pressure coefficient Lawson MIRA data, 0° yaw - Lawson et al (2008)

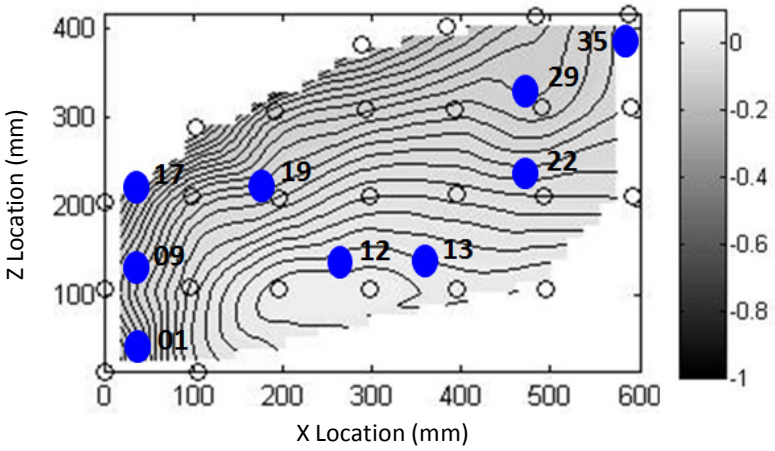


Figure 93 - Contour plot of static pressure coefficient, Lawson MIRA data, +10° yaw - Lawson et al (2007)

## 4.2 On-road Data Collection Method

### 4.2.1 Vehicle Sideglass and Roof Probe Set-up

Following Lawson's data collection at MIRA, it was desirable to undertake a more complete data collection of sideglass tappings recorded simultaneously with a 5-hole roof probe. The 5-hole probe was mounted as per Oettle et al (2010) with 9-window tappings recorded simultaneously. The 5-hole probe was calibrated in Durham University's laboratory and the calibration results are included in the Appendix. Due to a limit of the number of recording channels available, the tappings were distributed over the sideglass with greater resolution around the mirror wake region. The general window air flow characteristic was broken down into three main areas, areas largely affected by the mirror wake, the A-pillar and then those which are sufficiently far from either of the geometry features to be a combination region (i.e. a hybrid), as presented in Table 5, with the colour-coding detailed in Figure 94.

Table 5 - Tapping ID and dominant geometry feature of each region's flow environment

| Tapping ID | Dominant Region Environment |
|---|---|
| 01 | Mirror Wake |
| 09 | Mirror Wake |
| 17 | A-Pillar |
| 19 | A-Pillar |
| 35 | A-Pillar |
| 12 | Hybrid |
| 13 | Hybrid |
| 22 | Hybrid |
| 29 | Hybrid |

Tapping locations were as shown in Figure 94, with a typical tapping shown in Figure 95.

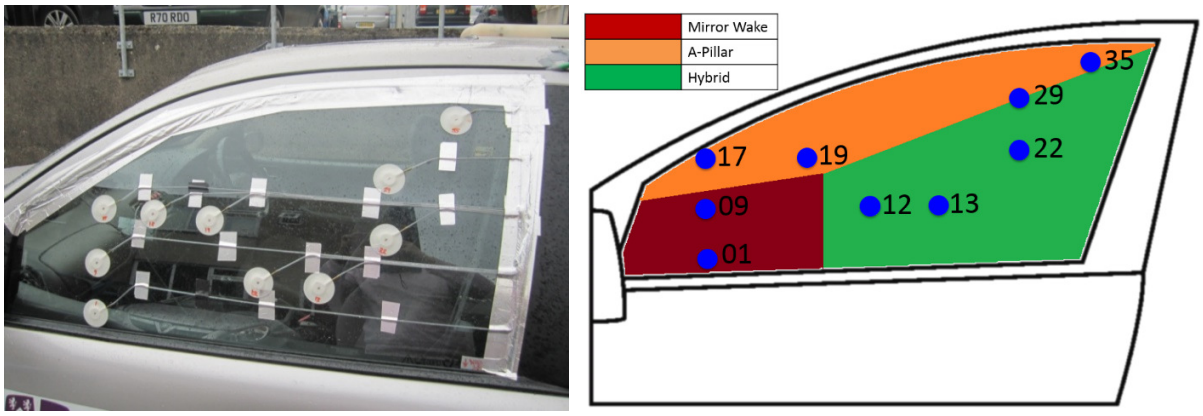


Figure 94 - Sideglass tapping locations for Rover 200 on-road data measurement

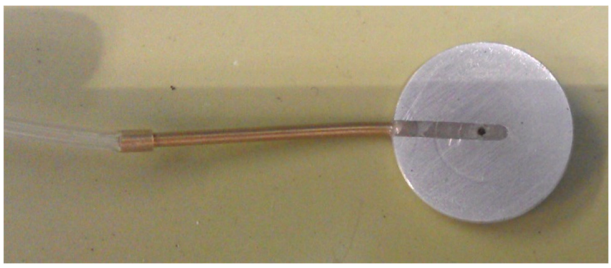

Figure 95 - 'Lollipop' surface-mounted, static pressure tapping used for Rover 200 MIRA and on-road pressure data measurement

Coefficients of pressure were taken from the raw probe measurements using the laboratory probe calibration and were non-dimensionalised by probe velocity:

$$C_{P_{(tapping)}} = \frac{\left(P_{TAPPING} - \left(P_{T-PROBE} - P_{DYN-PROBE}\right)\right)}{P_{DYN-PROBE}} \quad [15]$$

All pneumatic connections were made using 1mm internal diameter, PVC tubing. Care was taken to use identical tube lengths for all surface pressures. The sideglass tappings and roof probe in both the MIRA and on-road tests were corrected using a transfer function correction technique. For the on-road pressure measurements, a tubing transfer function correction was applied for magnitude and phase, as described by Sims-Williams et al (1998).

The tubing system transfer function was determined by simultaneously recording the changing pressure in a small, sealed chamber using two independent pressure transducers. One transducer measured the pressure directly from the sealed chamber (denoted the reference transducer) whilst the other transducer was located at the end of the combined pressure tapping and tubing that was to be calibrated. The sealed chamber was also connected to a further chamber that is formed between a loudspeaker cone and a rigid plastic plate, with the loudspeaker and plate interface being airtight. A swept sine wave was fed to the loudspeaker at 0 - 220Hz over 0.5s, which in turn causes pressure fluctuations in the small chamber. The physical mounting of the tapping in the test chamber is shown in in Figure 96 and Figure 97. The transfer function is then calculated as:

$$\text{Transfer Function} = \text{TF(f)} = \frac{B(f)}{A(f)} = \frac{B(f)A^{*}(f)}{|A(f)|^{2}} \qquad [16]$$

where A(f) is the Fourier transform of the pressure recorded by the reference transducer at frequency f and B(f) is the Fourier transform of the transducer connected to the tapping and tubing arrangement under test.

Figure 96 and Figure 97 illustrate the tubing transfer function calibration set-up of a disc probe and, although only a simplified tubing arrangement is shown in the figures, this process needs to include the entire tubing system (i.e. from probe or tapping to transducer bank).

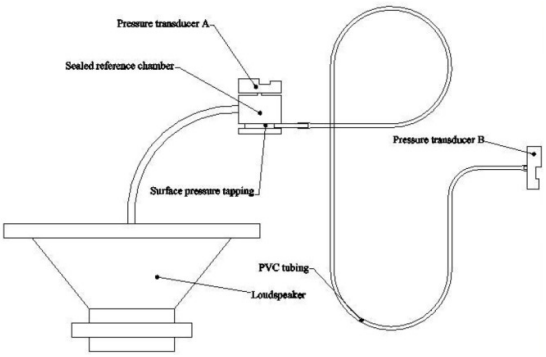


Figure 96 - Transfer function (TF) correction apparatus

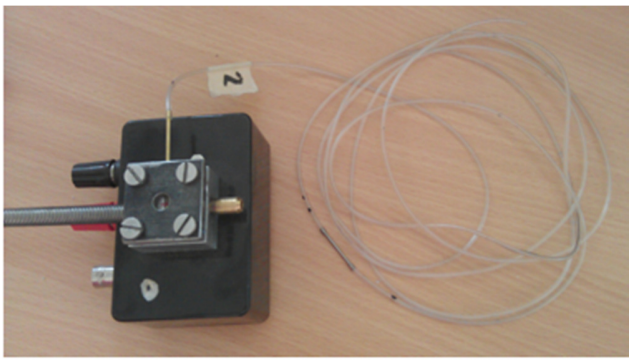

Figure 97 - Lollipop tapping in TF correction test chamber

A transfer function correction (as per Sims-Williams (1998)) was applied to sideglass, pressure taps and 5-hole probe measurements in order to accurately determine the time varying flow onto the car and the vehicle's aerodynamic response. For the on-road data collection, the transfer function is as given in Figure 98 (roof probe) and Figure 99 (sideglass tapping), with the correction being applied to both the 5-hole probe and the sideglass tappings up to a frequency limit of 220Hz, which were themselves recorded at 800Hz through a 250Hz, -12dB, second-order filter.

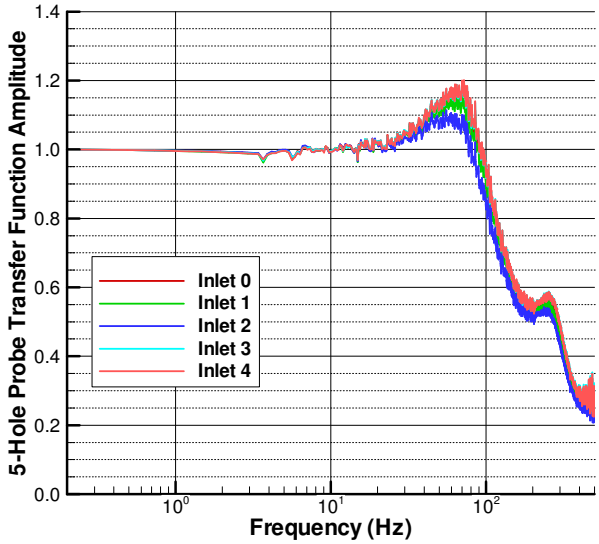


Figure 98 - Probe Transfer Function

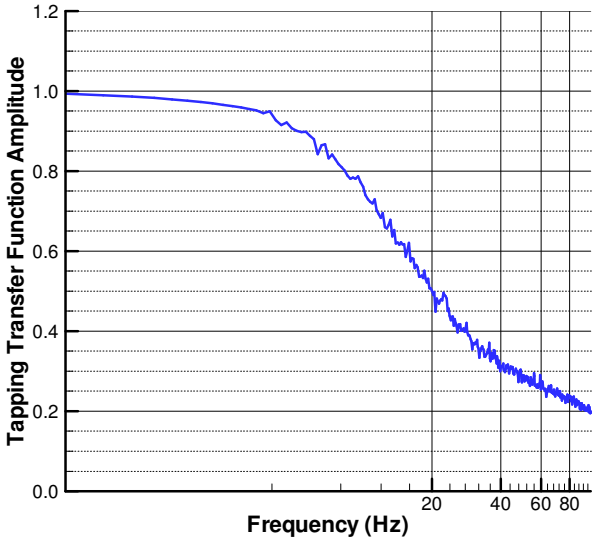


Figure 99 - Tapping Transfer Function

Roof probe alignment was as Oettle et al (2011), located as far forward as possible (with the constraint of the sun-roof surround) to be similar to Lawson et al (2007), shown in Figure 100.

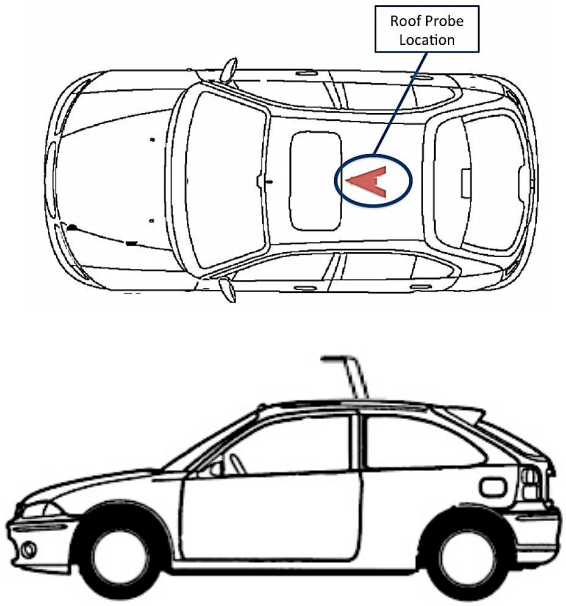


Figure 100 - Roof probe to B-pillar alignment for on-road data measurement, positioned as per Oettle (2011) and similar in design to that of Lawson et al (2007)

In Figure 101 the data and power schematic for the on-road data collection is shown.

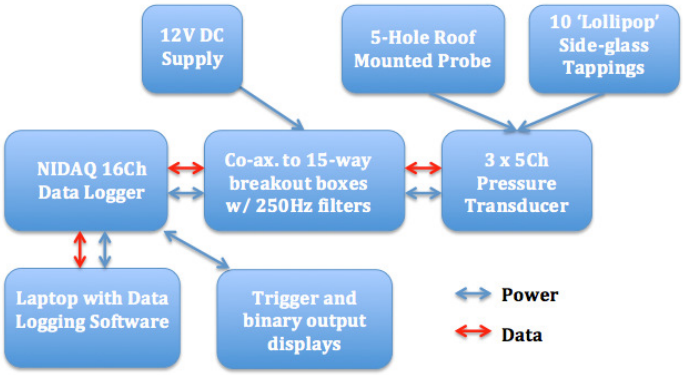


Figure 101 - Data and power connection map for on-road data acquisition

### 4.2.2 CFD Validation of Roof Probe Mounting Location

A 3D CFD study was performed to compare probe mounting locations, with the experiment details given in Oettle et al (2012) and the results given in Figure 102 and Figure 103 showing a comparison between the probe lateral velocities over time. It can be seen that both a roof probe (shown in Figure 102) and a probe ahead of the vehicle show elevated velocities (shown in Figure 103), but the

advantage of the roof probe is that the measured yaw is closely time-aligned with surface pressure recordings on the sideglass. The roof probe exaggerates the longitudinal ($U_X$) and lateral velocities ($U_Y$), but as these are both increased the effect on resultant measured yaw angle is nominal. However, the probe in front of the vehicle exaggerates the lateral ($U_Y$) velocity but attenuates the longitudinal velocity ($U_X$), which will sum and compound to significantly affect the resultant measured yaw angle from the true incoming air flow yaw angle. It is worth reiterating at this stage that where axis components are referred to as longitudinal, lateral or vertical, that is the velocity, pressure or force in the component direction relative to the body's resultant vector (e.g. vehicle direction in reference to the vehicle or flow direction in reference to onset turbulence).

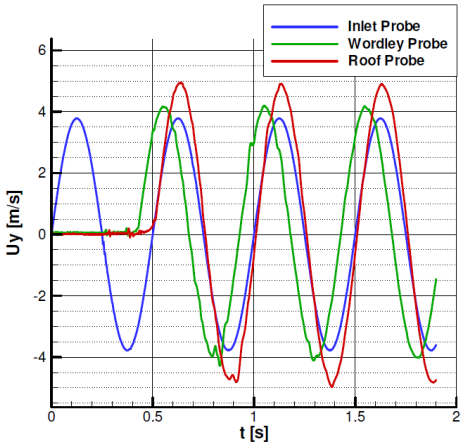


Figure 102 - Probe lateral velocity against time from CFD data

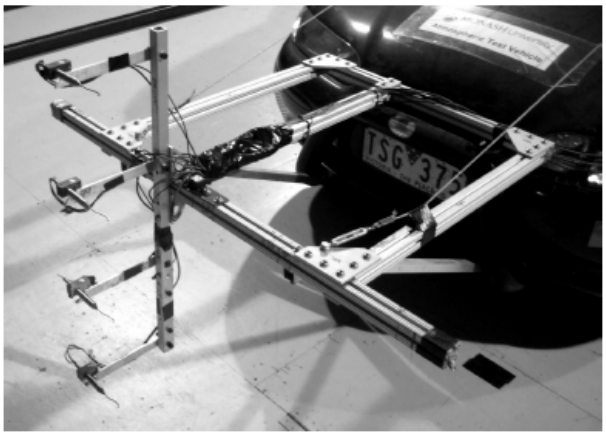

Figure 103 - Ahead of vehicle wind-velocity probe - Wordley et al (2009)

### 4.2.3 Data Analysis Approach

Raw data and the subsequent numerical processing were performed using an analytical software suite developed at Durham University, called 'Durham Software for Wind Tunnels' (Sims-Williams (2012)). Figure 104 details the process that is followed to convert raw transducer voltages into the metrics plotted in the results section, with each block representing an individual program and the corresponding chapter numbers shown.

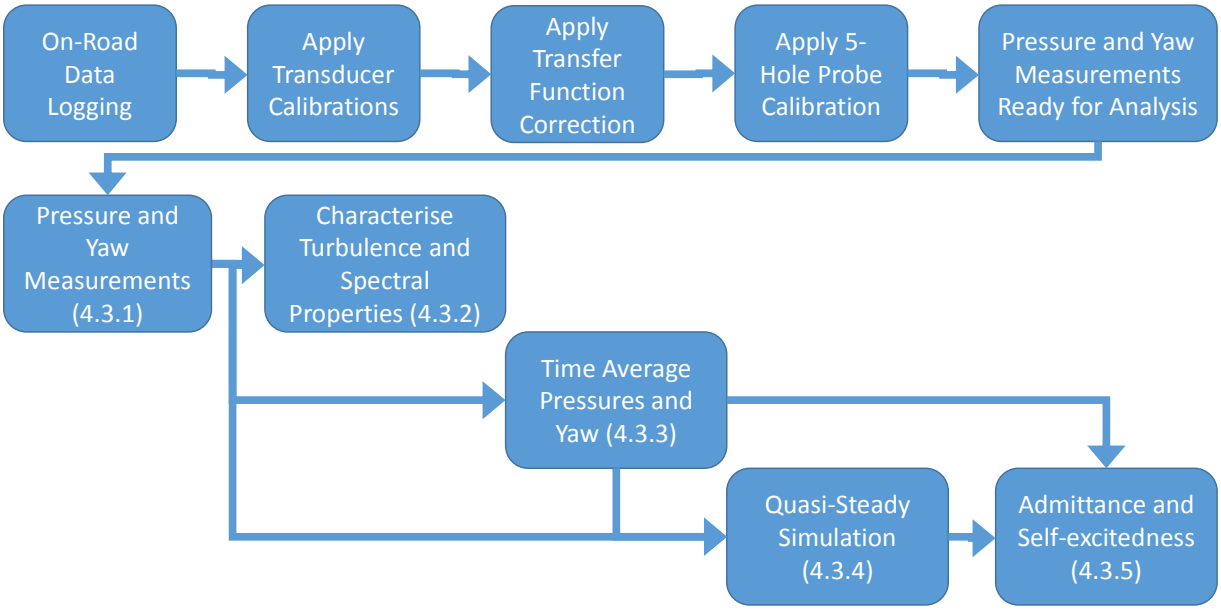


Figure 104 - Numerical processes that raw data is evaluated through before results are generated

The wind tunnel provides a steady method of assessing the sideglass pressure profile response at a variety of discrete yaw angles. If the vehicle travelling in the unsteady on-road environment behaves in a manner as simulated in the wind tunnel, the response can be said to be quasi-steady. Any deviations between pressures simulated in the wind tunnel and on-road are deviations in the quasi-steady response of the vehicle. To assess the quasi-steady nature of the vehicle's response, a simulation technique was developed to compare the response of the vehicle with how it would be expected to behave in the wind tunnel.

Firstly a method used during the analysis is to 'bin-average' data in order to create an approximated quasi-steady-state data set using the entire data sample. This term is used to describe splitting the range of yaw data (i.e. +10° to -10°) into uniformly distributed increments of 2° each in width. Measurements recorded (i.e. vehicle velocity, sideglass pressures, velocity variation, etc.) are then compiled ('binned') into each of this incremented widths (i.e. measures with the instantaneous yaw being, say, ≥8° to <10°), and then the results averaged. This is just a straightforward process to average the continuously time-variant on-road measurements and is shown in result graphs as the 'Bins' result. This gives an output file (i.e. correlating the averaged sideglass pressure with the roof probe recorded yaw angle) which details for each yaw bin what the average measured sideglass pressure coefficient was. The same process can be used from wind tunnel data generated by a yaw sweep to give a yaw angle against sideglass pressure coefficient correlation.

Hence, using this averaged pressure against yaw correlation output file, a time history of instantaneous yaw angle can be linearly interpolated to predict (i.e. 'look-up') the sideglass pressure coefficient. Using the data collected on the road, combined with the steady wind tunnel response, for each instantaneous measured yaw angle on-road, the $C_P$ value as predicted from the wind tunnel and on-road was generated. These predicted fluctuations in surface pressures were then assessed against those actually measured on-road. This process is referred to as the quasi-steady simulation method in this thesis (and as the 'simulated' result on graphs).

Once the data was processed, the results were then analysed via a variety of methods, as listed in Figure 105 with the corresponding chapter sections shown.

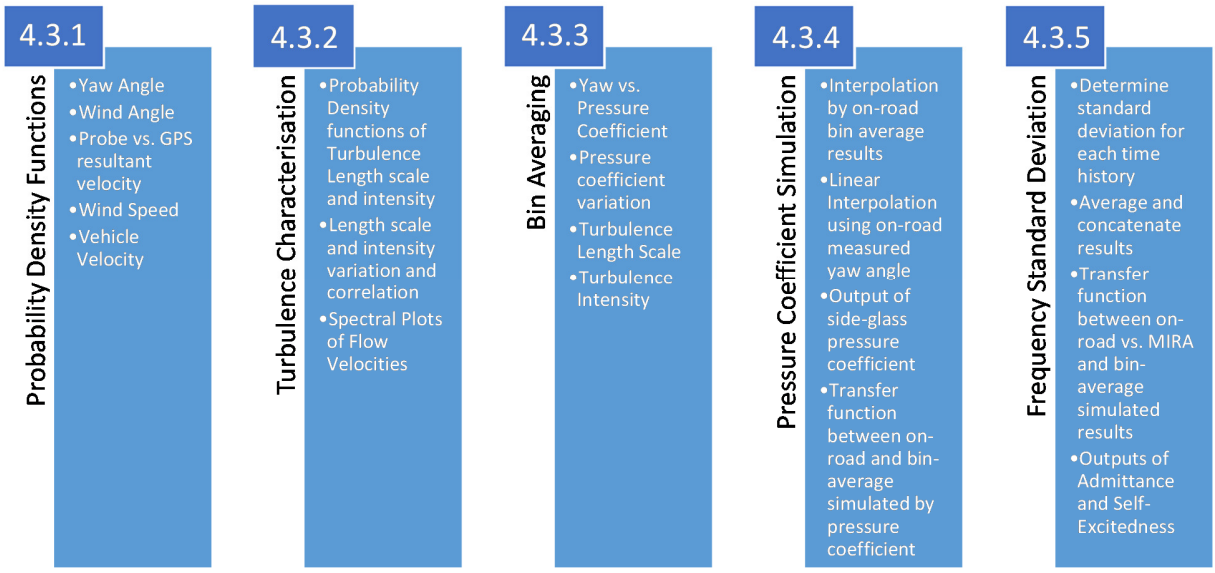


Figure 105 - Analysis map of processed data, combining MIRA results and on-road flow data measurements

## 4.3 On-road Data Collection Results

The Rover 200 was driven from Durham to Scotch Corner on the A1(M), a dual and triple lane highway, at 70mph for all measurements. Measurements were taken over 4 different return trips, each spaced several days apart, capturing a range of wind weather from a still day to a day of high winds. The 32-second recordings were taken at arbitrary occasions during the drive, with varying traffic intensity. A series of plots were made which are shown in this section detailing the results covering the range of flow angles and turbulence encountered for all 275, 32-second measurement cases recorded at 500Hz (i.e. 16,384 samples per 32-seconds), totalling 147 minutes of flow data. An example yaw

trace against time is shown in Figure 106, showing a variation in yaw angle during the time period, within a range of +8° to -10°, varying constantly over the sample.

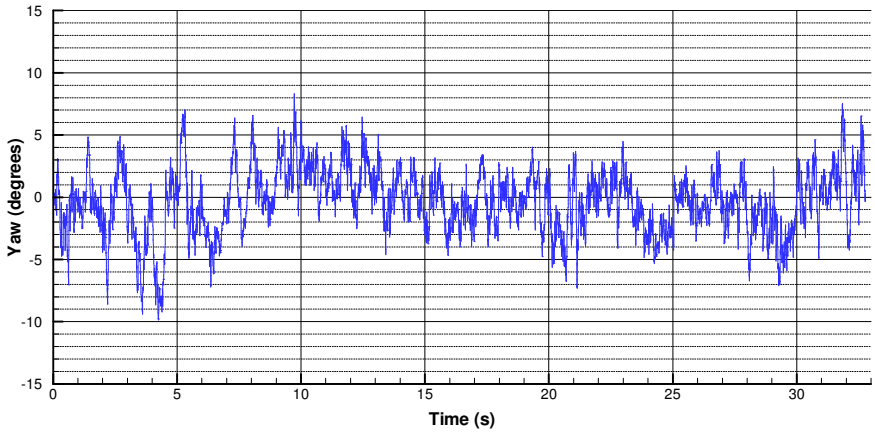


Figure 106 - Example on-road yaw against time trace recorded on a Rover 200 using the 5-hole roof probe

Figure 107 shows the probability density function (PDF) of yaw angles experienced, showing a nominal offset of around +0.5°, but that almost the entire flow yaw is within ±5° and more than two thirds is within ±3°.

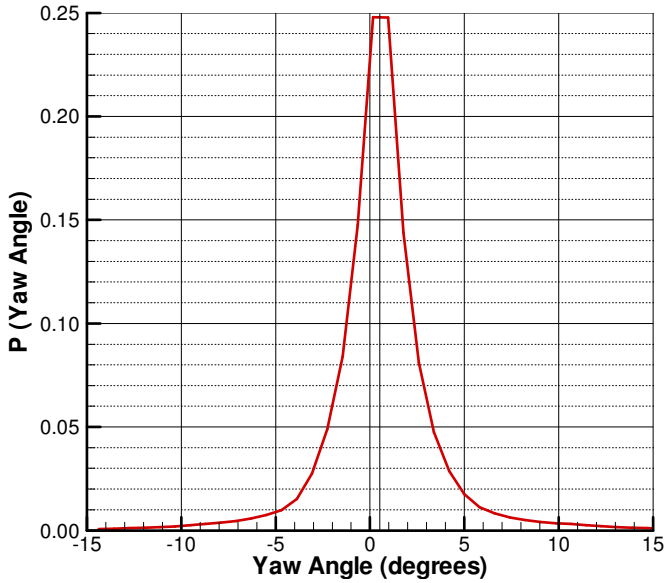


Figure 107 - PDF of flow yaw angle

### 4.3.1 Vehicle Velocity Distributions

In order to quantify the expected roof probe longitudinal velocity speed-up (i.e. as seen in the 3D CFD earlier, roof probe velocities are exaggerated due to flow speeding-up as it passes over the roof of a

vehicle), probability density plots of roof probe velocity against GPS velocity and yaw angle against roof probe velocity were made, as in Figure 108 to Figure 111. This speed up could be due to either GPS latency error due to fluctuating vehicle velocity, which would see a Probe/GPS velocity magnitudes centred around 1.0, or could be due to the acceleration of flow over the vehicle's roof. Firstly Figure 108 shows that the vehicle velocity was at an average of 30.7ms$^{-1}$ (69mph) and has a standard deviation of ±0.6ms$^{-1}$ (1.5mph).

The distribution is very close to symmetrical, showing that the velocity was closely maintained with deviations in acceleration or retardation being equal in number and of duration. Figure 109 then shows the probability density function of probe over GPS velocity. It can be seen that the nominal value is 1.06, showing a typical speed up of around 6%. The distribution is also mainly symmetrical, though plateaus at factors of 1.2 – 1.4, potentially due to certain aerodynamic effects at particular yaw angles, but was not of sufficient significance for further analysis. Note that probability distributions, as mentioned in the literature review, can exceed unity, as long as the area under the curve sums to unity.

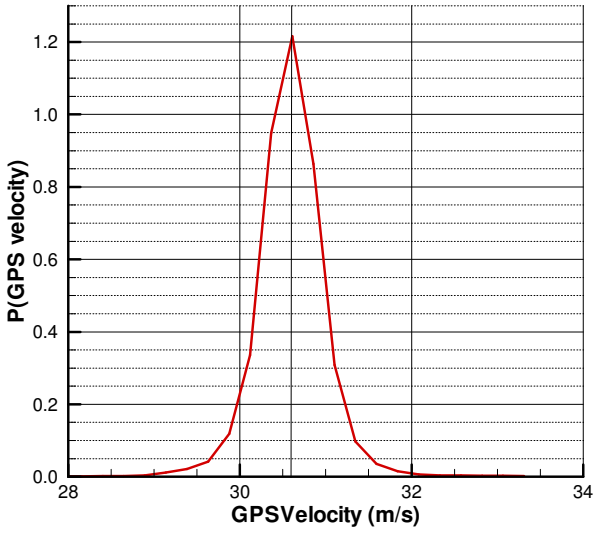


Figure 108 - PDF of GPS Velocity

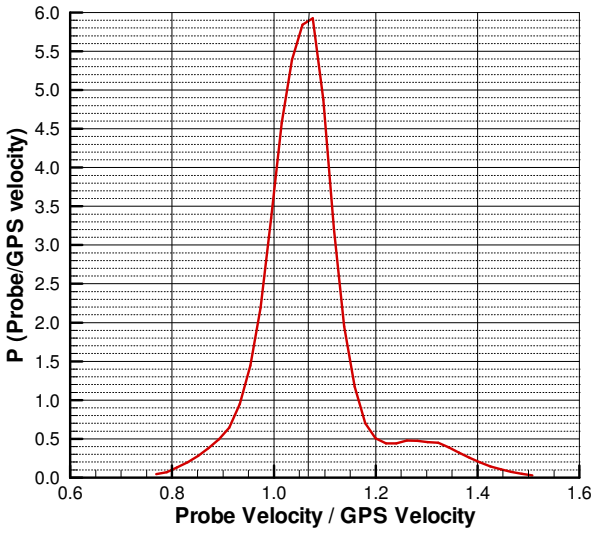


Figure 109 - PDF of probe bulk velocity / GPS velocity

Further analysis of the variation of roof probe divided by GPS velocity magnitudes, with standard deviation error bars superimposed, is presented in Figure 110 and shows that the probe velocity speed up was greater at negative yaw than positive yaw and again with the 6% speed up at 0$^{o}$ yaw being shown. The wide standard deviation bars show that the wind velocity can vary over a significant range at each yaw angle, but that the standard deviation is consistent over the entire yaw range. Figure 111 demonstrates that though the velocity can vary significantly, the number of data samples is sufficient

to determine accurate and repeatable measurements with narrow 95% confidence intervals. Note also that the confidence interval widens at the yaw range extremes as the number of samples within each yaw angle bin decreases at the yaw extremes.

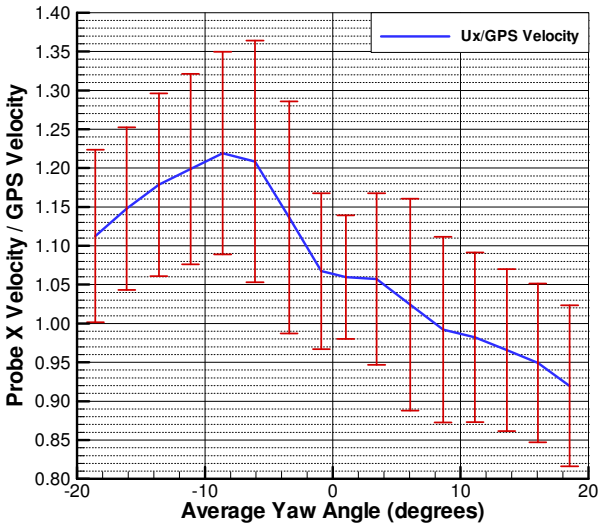


Figure 110 - Probe / GPS velocity standard deviation error bars

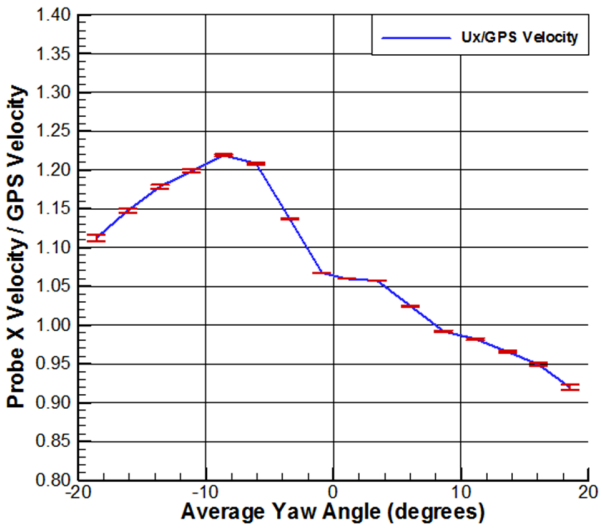


Figure 111 - Probe / GPS velocity 95% confidence limits

The asymmetric yaw effects are could be due to differing flow conditions caused by a systematic connection between yaw angle and headwind and tailwind, as shown in Figure 112. Additionally, the effect could be due to a Reynolds number sensitivity, and a test undertaken where the roof probe velocity speed-up against reported yaw, for varying vehicle speeds, would indicate which effect is dominant. In order to ensure that the data set is not skewed by having a constant, strong wind direction on one day, a large data set was recorded, taken over several days.

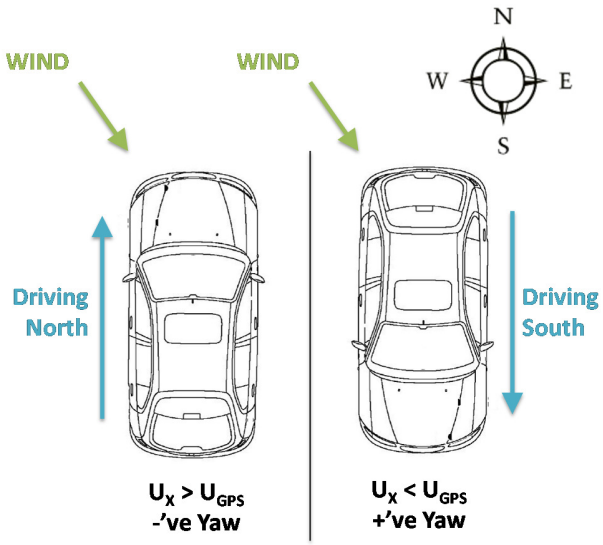

Figure 112 - Effect of headwind on flow asymmetry

### 4.3.2 Turbulence Analysis

The range of turbulence length scales and intensities in the air flow were evaluated, as shown in Figure 113, demonstrating a probability density function plot of turbulence length scale (TLS) generated through the auto-correlation method. Length scales are seen to exist in the range of 2 - 11m. Figure 114 shows turbulence intensity (TI), with a peak at 2.5%, and with the majority of intensities in the range of 2 - 10%, which lie in the same turbulence intensity region as presented in Wordley et al (2009). The distributions of these two graphs are again typical of those seen in earlier references. It should be noted that the window size of the auto-correlation (i.e. a 4-second sample) at 70mph ($31.3ms^{-1}$) limits the potential length scale to approximately 4x vehicle speed (i.e. around 125m).

However, these lengths were considered to be quasi-steady and that a 4-second window was well above the time required to capture all transient flow events (see Chapter 2).

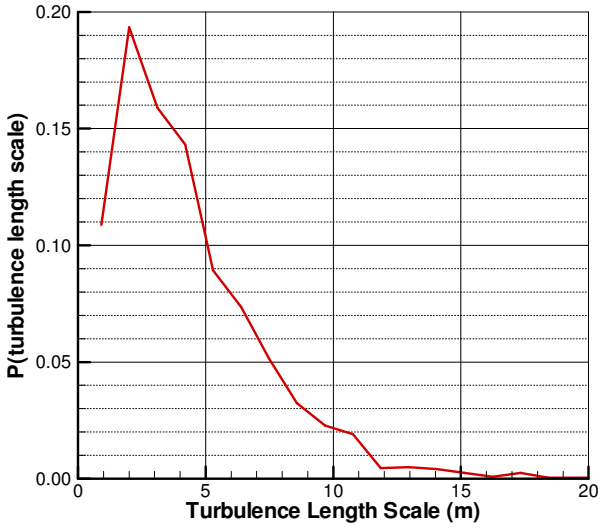


Figure 113 - PDF of turbulence length scale

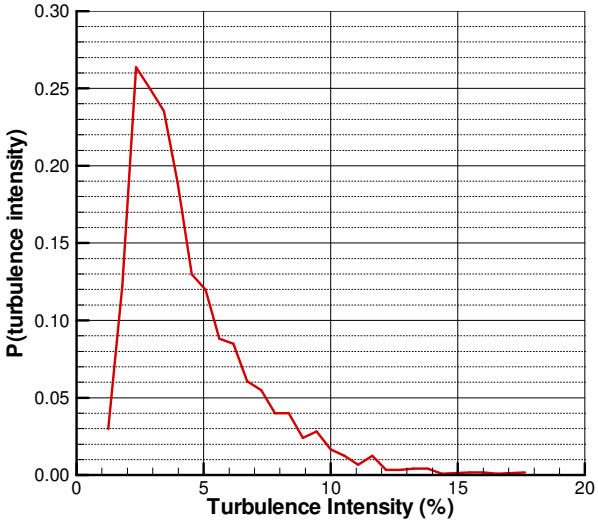


Figure 114 - PDF of turbulence intensity

Figure 115 to Figure 118 show turbulence intensity against length scale plots for flow velocity magnitude and then component velocities, plotted with each point representing 4-seconds of all of the flow measurements recorded. Figure 115 shows a clustering of length scales and intensities less than 8m and 7%, all in the lower left quadrant as plotted. Figure 116 demonstrates that longitudinal intensities shorten as turbulence intensity drops below 5%, with the majority of length scales being less than 15m, caused by the vehicle's velocity being in the longitudinal direction.

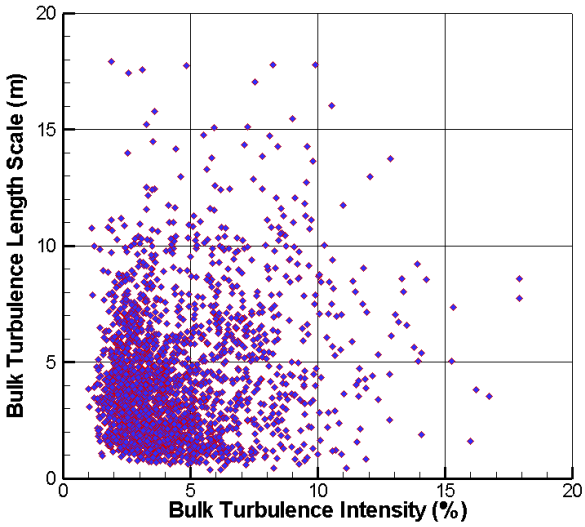


Figure 115 - Bulk TI vs. TLS plot

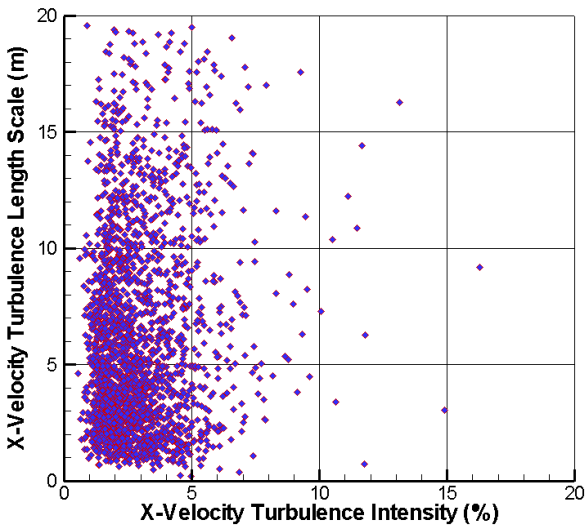


Figure 116 - X-axis TI vs. TLS plot

Figure 117 presents the lateral turbulence measurements with intensities similar to that of longitudinal turbulence, beneath 5% intensity, but with shorter length scales, typically less than 8m as seen in the bulk turbulence plot of Figure 115. Figure 118 shows vertical turbulence components, which sources presented earlier, typically suggest have intensities and length scales around a third of bulk measurements. This reduction in intensity and length scale with vertical turbulence was seen in the on-road measurements, with intensities under 4% and length scales less than 4m. The reduction in turbulence length scales and intensity is due to the ground limiting the length scales achievable and suppressing the flow deviations required for higher intensities.

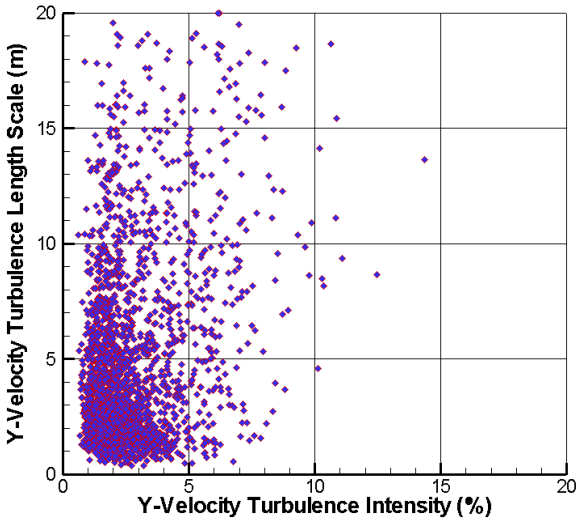


Figure 117 - Y-axis TI vs. TLS plot

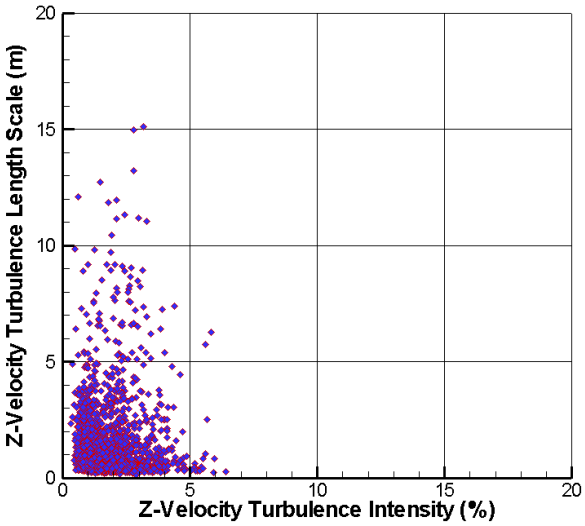


Figure 118 - Z-axis TI vs. TLS plot

More detailed analysis of the turbulence is given in Figure 119 and Figure 120 with both standard deviation and 95% confidence intervals shown. Figure 119 shows an increase in turbulence intensity with yaw angle, almost triple that at zero yaw or 4%, up to 11% at ±20°, but with consistent standard deviation throughout and symmetric results. The increase in turbulence will be due to the extended flow over the vehicle as is typical with flow that has a Reynolds' number dependency.

Figure 120 demonstrates that the 95% confidence interval is very tight, offering high confidence on the repeatability of the data sampled.

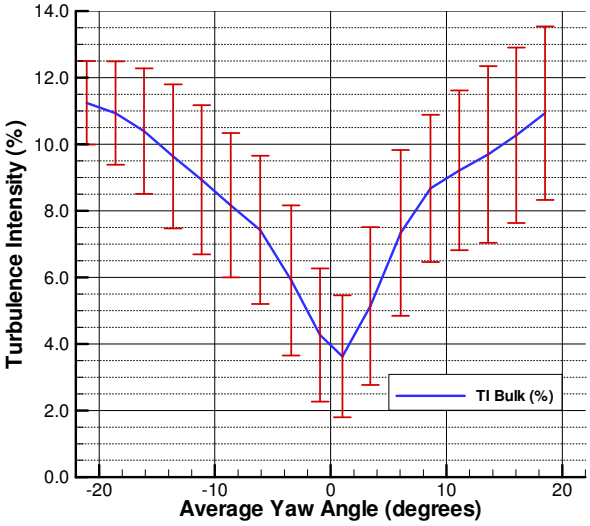


Figure 119 - TI vs. Yaw with standard deviation error bars

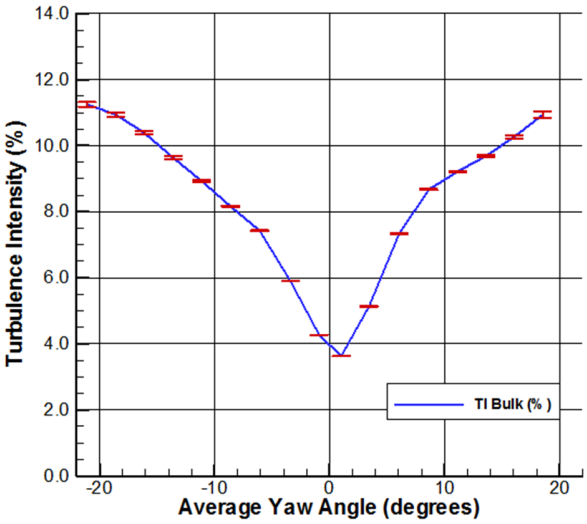


Figure 120 - TI vs. Yaw with 95% confidence error bars

Figure 121 and Figure 122 show spectral energy plots (frequency multiplied by auto-spectral density) of bulk and lateral flow velocities. It can be seen in both cases that the majority of energy is experienced below 10Hz, with the bulk velocity decaying slightly sooner than the lateral velocities.

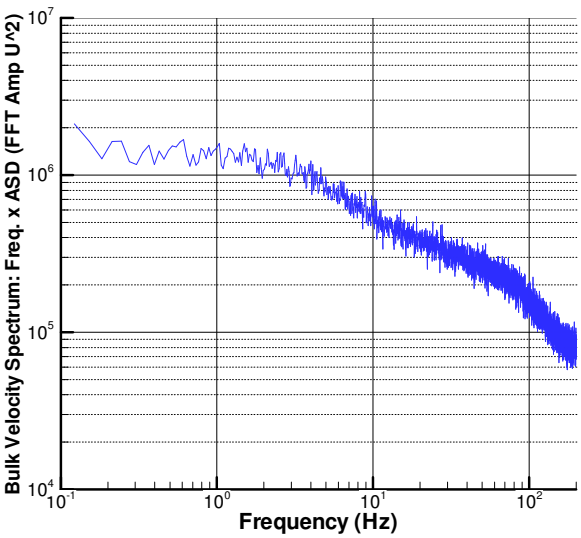


Figure 121 - Spectral energy plot of bulk velocity

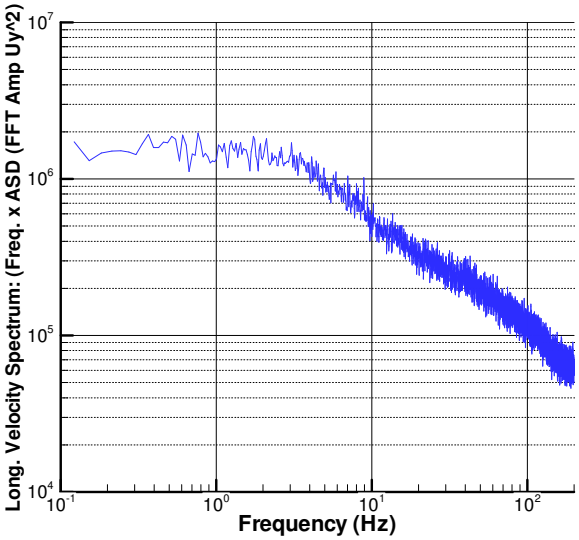


Figure 122 - Spectral energy plot of lateral velocity

### 4.3.3 Time-averaged Pressure Coefficients on the Sideglass

This section presents sideglass pressure coefficients at the range of yaw angles experienced, with the results time-averaged from the entire data set. The presented plots demonstrate the flow interactions around the A-pillar, mirror wake and vehicle side over the range of yaw angles. Note that in each graph an insert of tapping location on the sideglass window is given.

Figure 123 shows the results of the bin averaging process of all sideglass pressure coefficient measurements against yaw angle, with bins of ±1° in size. At positive yaw angles all pressure tappings show a linear increase of pressure coefficient with yaw angle. In negative yaw, where separation occurs around the vehicle's side and downstream of the A-pillar and mirror location, the pressure coefficients vary depending on tapping location. Particular tappings of note are 17, 19 and 29 due to the large pressure coefficient drop at extreme yaw angles. These tappings are all located in the A-pillar wake region and as flow separation occurs over the sideglass region at higher negative yaw, the level of turbulence and hence pressure loss due to viscous effects is increased.

It is noteworthy how tapping 01 and 09 are both physically located beneath tapping 17, yet they avoid the more dramatic reduction in pressure loss as they are located in the mirror wake region, where the flow is more turbulent as it streams over the mirror. However, due to the flow perturbation that occurred, tapping 01 and 09 exhibit lower pressure coefficients than other sideglass tappings due to the energy loss experienced. It is also of interest to note tapping 35, in the upper right corner of the

window in the A-pillar region, also shows pressure coefficient losses greater than other sideglass tappings.

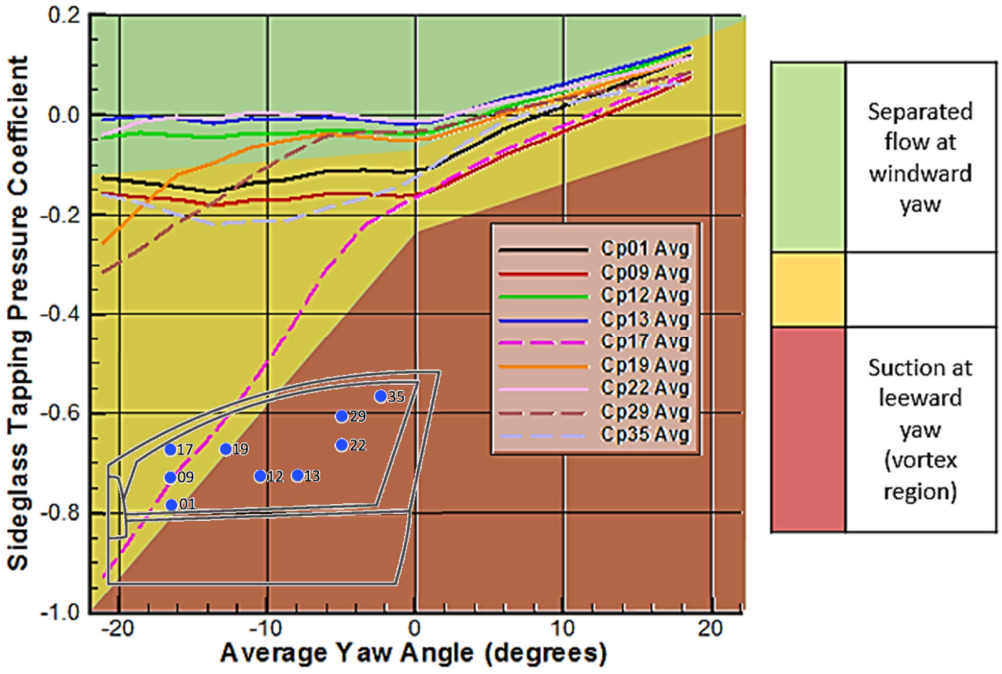


Figure 123 - Sideglass pressure tappings of bin-averaged data shown against yaw angle

The results are presented in sets covering the dominant region flow characteristic. Tapping 01 and 09 will be shown covering the mirror wake region and tapping 17 and 19 presented covering the A-pillar region. Figure 124 is shown again as a reminder of the flow regions, with the presented tappings circled.

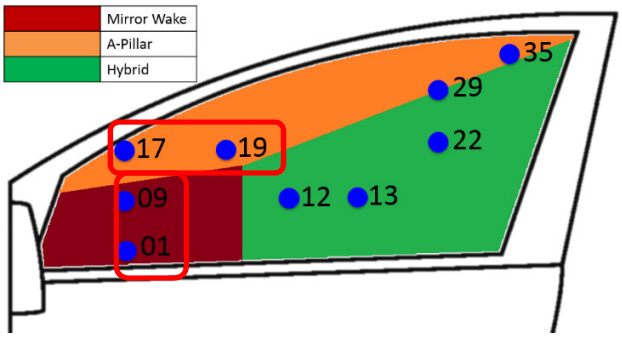


Figure 124 - Flow region type with the presented tappings circled

In order to consider more detailed effects, pressure coefficients for each subsequent tapping pair are plotted in Figure 125 to Figure 128, with both standard deviation and 95% confidence intervals superimposed. In the legend of the graphs, the 'Bins' refers to the data points being 'bin-averaged' as

described in Chapter 4.2.3. Each graph also has the MIRA wind tunnel results plotted for −10°, 0° and +10° (Lawson et al (2007)).

The flow in the mirror wake region is shown in Figure 125 and Figure 126, showing tappings 01 and 09. The increasing standard deviation of the results with yaw angle in both directions from 0° yaw is due to increase flow unsteadiness caused by the tappings being in the freestream just under the mirror wake region. The 95% confidence intervals in Figure 126 further confirm the repeatability of the data.

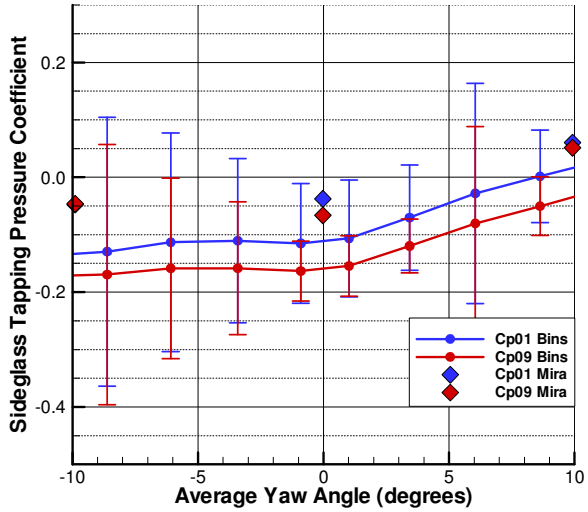


Figure 125 - Tapping 01 & 09 with standard deviation error bars

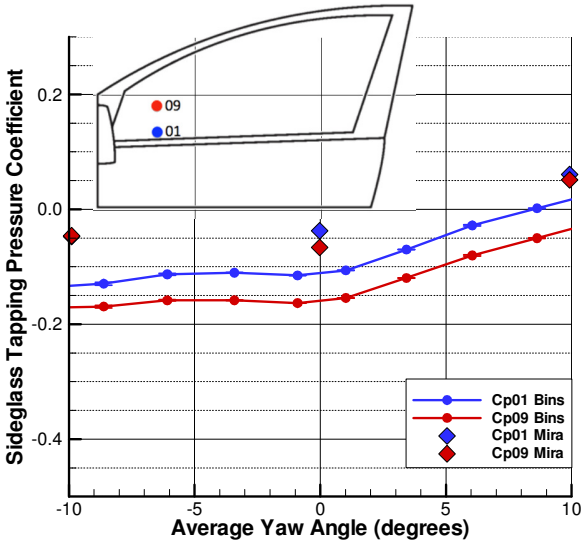


Figure 126 - Tapping 01 & 09 with 95 % confidence interval error bars

Figure 127 and Figure 128 present the A-pillar region results from tappings 17 and 19. Being in the A-pillar region, these results both show significant reductions in pressure coefficient at negative yaw angles and greater pressure consistency at positive yaw angles. The curves also show the typical pressure difference against the MIRA results, though similar gradients are noted with tapping 17, but differ with tapping 19, potentially due to minor tapping location accuracy or minor wake region location differences between on-road and tunnel tests.

The difference between the road and tunnel results highlights the need for measurements to cover a small yaw angle step variation over the full yaw range to accurately determine the pressure actual variation (i.e. high yaw angle measurement resolution), as the lack of MIRA tunnel data prohibits drawing more detailed conclusions when compared against the bin-averaged data. Again the 95% confidence intervals of Figure 128 offer confidence to the accuracy of the data.

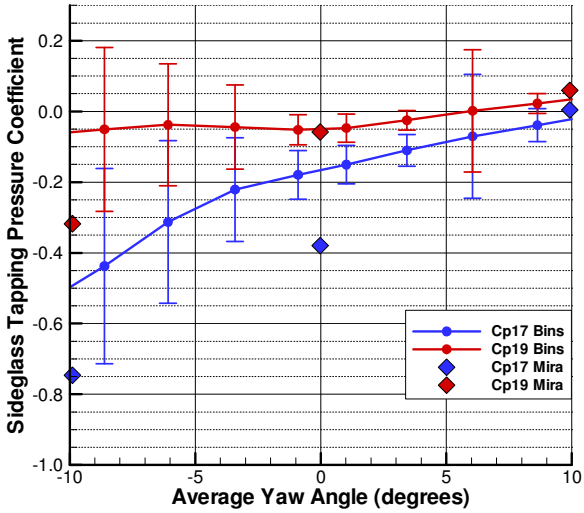


Figure 127 - Tapping 17 & 19 with standard deviation error bars

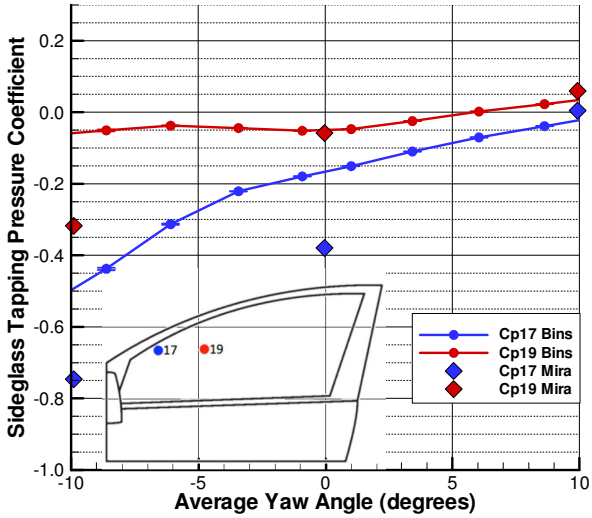


Figure 128 - Tapping 17 & 19 with 95 % confidence interval error bars

### 4.3.4 On-road to Bin-Average Transfer Functions

Figure 129 is presented to show a typical recording of sideglass pressure coefficient against time and the quasi-steady simulated result. As a reminder, the simulated result was found by looking up the averaged sideglass pressure coefficient from a data set using the instantaneous yaw angle in a time trace. This data set was generated by averaging all of the sideglass pressure coefficient results that fell within 2° wide bins of yaw angle (creating 29-bins covering the range of yaw angles encountered of -30° to +30°).

The graph also presents a representative gust event shown at 7-seconds in Figure 129 and the simulation trace is created by reprocessing the recorded data using a linear interpolation algorithm with the flow yaw angle as the master variable. The graphs show accurate simulation using this quasi-steady result method, especially for the re-creation of the gust shown in Figure 129 at 7-seconds. The simulated result also shows a reduction in noise as would be expected by such a technique.

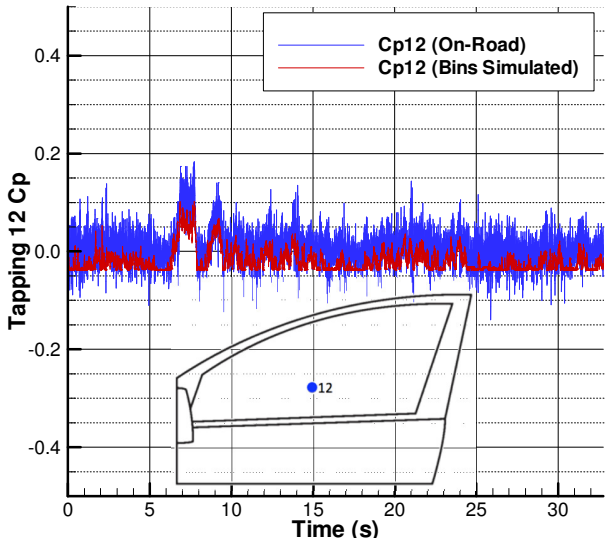


Figure 129 - Tapping 12 pressure coefficient, data set 31

To further evaluate the frequency-based effects of the flow at their respective tappings, transfer functions were generated of the measured pressures between on-road and simulated on-road data (i.e. bin-averaged pressure coefficient measurements looked up by instantaneous yaw angle), an example of which is given in Figure 130. At low frequencies some unsteadiness is shown as there is not a unity amplitude (i.e. an amplitude of 1 is defined as a perfect correlation of pressure variation with flow yaw) but since the transfer function starts close to unity the method generally works well (i.e. a change in the yaw angle is seen by the quasi-steady simulation).

As the frequency increases to around 10Hz the transfer function plot shows a rapid increase in amplitude signifying that an increase in pressure unsteadiness (i.e. unsteady pressure fluctuations in this scenario) has become significant (i.e. greater than 2 in transfer function amplitude) in comparison to the quasi-steady simulation. These increases are expected to be due to minor vehicle geometry features that are relatively of less significance to total vehicle drag or lateral stability. Figure 130 shows that at frequencies above 1Hz these factors become noticeable and above 10Hz are significant, and therefore at such high frequencies the simulation method cannot accurately determine the sideglass pressure coefficient from the flow yaw angle, and hence the results have been truncated. Only one trace is presented as all tappings demonstrated a similar characteristic.

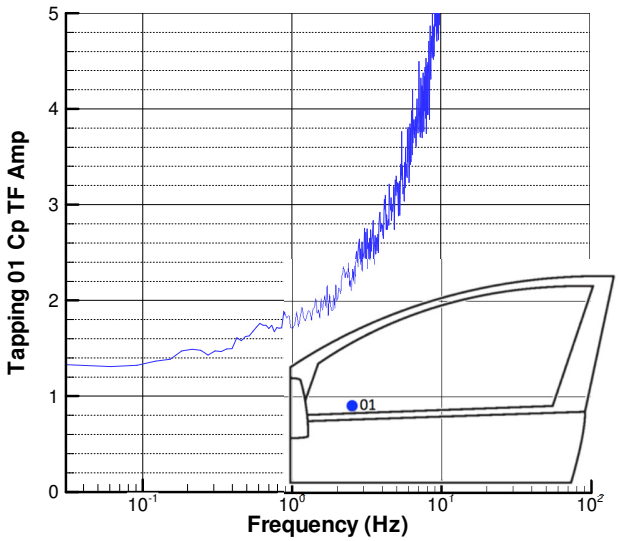


Figure 130 - Transfer function of pressure coefficient for tapping 01

### 4.3.5 Evaluation of Pressure Coefficient Yaw Sensitivity and Self-excitedness

In order to further understand the turbulence and pressure fluctuations over the sideglass area, a frequency band pressure coefficient standard deviation analysis was undertaken. This method filtered each 4-second data measurement into 6 respective frequency bands, and then evaluated the standard deviation of each 4-seconds data sample between the on-road and simulated test result in order to see at what frequency range the simulation becomes less valid due to the self-excitedness of the air flow turbulence becoming dominant. Frequency bands were divided up as in Table 6, with the widths of each frequency band set to distribute the entire frequency range (0.2 - 178Hz) into equal log based bands, expect for the final band which was truncated to ensure that the frequency response was within the ideal response region of the lollipop tappings and tubing frequency bandwidth (i.e. <100Hz).

Table 6 - Pressure coefficient standard deviation frequency bands

| Start Frequency (Hz) | End Frequency (Hz) | log(Start Frequency Hz)$_{10}$ | log(End Frequency Hz)$_{10}$ | log(start Hz)$_{10}$ – log(end Hz)$_{10}$ |
|---|---|---|---|---|
| 0.2 | 0.6 | -0.70 | -0.22 | 0.48 |
| 0.6 | 1.8 | -0.22 | 0.26 | 0.48 |
| 1.8 | 5.6 | 0.26 | 0.75 | 0.49 |
| 5.6 | 17.8 | 0.75 | 1.25 | 0.50 |
| 17.8 | 56.0 | 1.25 | 1.75 | 0.50 |
| 56.0 | 100.0 | 1.75 | 2.00 | 0.25 |

Scatter plots were generated of measured against simulated sideglass pressure coefficient standard deviation, for each frequency band, with an example shown in Figure 131 as an illustration and the approach to interpreting these explained first with the actual experimental result discussed later.

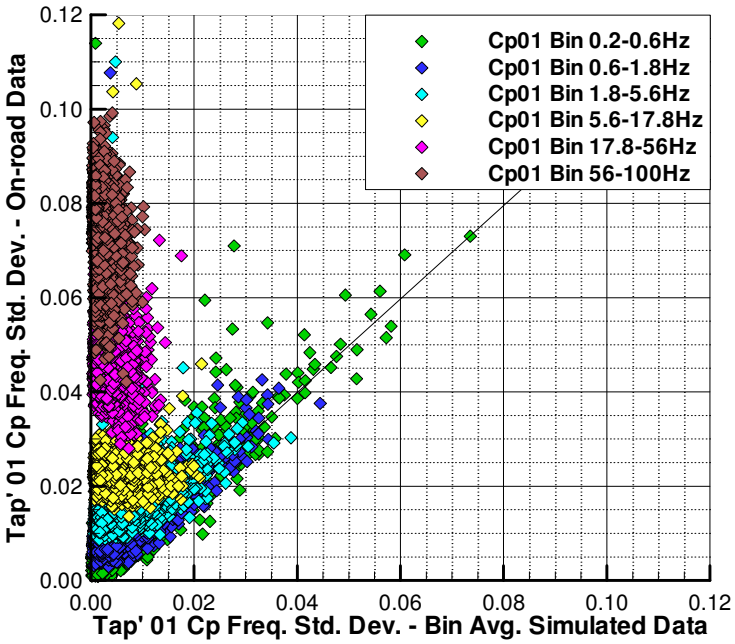


Figure 131 - Example of sideglass pressure coefficient standard deviation plot

The key element to note for the frequency band standard deviation graphs is where a frequency band has points clustered on the 45° axis (i.e. the drawn line). This line depicts where the pressure fluctuations encountered in these window regions are equally present in both the on-road pressure measurements and the quasi-steady simulation pressure results. As such, data points near to the 45° line represent effects that can be deemed to being 'quasi-steady'. They are therefore representative of effects based upon probe flow yaw angle. When the results lie above the 45° line, they are representative of effects less dependent on yaw angle and more dependent on local flow effects such as the aerodynamic effects of minor vehicle geometry (i.e. causing self-excited turbulence).

Each point of the plot corresponds to 4-seconds of data (with 4-seconds determined from the reduced frequency analysis presented in the literature review). 4-seconds is sufficiently long a duration to capture low frequency variations (i.e. the effects of a change in yaw is measured on the sideglass) and to apply some noise reduction, but not so long in duration that yaw and pressure variations are averaged out. It should be noted that in the FFT algorithm of this process a rectangular window was

used as it was found that this minimised the zero-frequency (DC component) blend and associated frequency issues that can come with a Hanning window.

Through the regression of a linear curve to the cluster of points within one frequency band, the gradient and intercept of that regression can be obtained. In this scenario, the gradient represents the pressure fluctuation aerodynamic admittance between the on-road and bin-average measurements, with the intercept defining the magnitude of background self-excitedness (which is unsteadiness not correlated with yaw). When the results of the frequency band are highly yaw dependent, a gradient around 1.0 would be expected (the 45$^{o}$ line on the cluster plots), and deviations from a gradient of 1.0 would represent effects that are less dependent upon yaw. This can then be further analysed by considering the intercept of the regression, detailing the self-excitedness of the pressure deviation, which are deviations that are independent of yaw and more down to local flow viscous effects.

Finally, in the generation of these plots, admittance data points that had a regression coefficient ($R^2$) that was extremely low were filtered out. This is because, by examination of a cluster of points, for example the 17.8 - 56.0Hz band in Figure 134, a regressed line could have a similar probability of really taking any direction as the cluster is highly spurious and therefore the determined regressed gradient is less representative of the actual true admittance. The intercept could also therefore be highly affected by a wildly deviant gradient, but as the occurrence of the cluster is intrinsically close to the Y-axis the intercept still offers insight into the self-excitedness component (even if minor corruption can occur). A more detailed explanation of how the admittance and self-excitedness values are evaluated is given in the next section.

Comparisons of the on-road measured and the quasi-steady simulation results have been shown in earlier sections of this chapter. However, these measurements are unable to display the frequency components of the turbulence, just the overall average by yaw angle. The highly transient nature of turbulence dictates that the correlation between the actual on-road measurements and the quasi-steady simulation technique will be most valid at lower frequencies. This is where the change in yaw angle is below a certain frequency, (say, arbitrarily, <5Hz) and the on-road flow is represented by quasi-steady flow characteristics. At higher frequencies (say, arbitrarily, >5Hz) the variations in sideglass pressure become less representative of the incoming flow yaw angle, as they are dominated by small geometry flow effects (i.e. vortex shedding off the A-pillar).

This therefore gives the ‘admittance’, which is the correlation between on-road and simulated pressures and should be directly proportional at lower frequencies, and the self-excitedness, which is

the level of turbulence generated by flow trailing from small vehicle geometries, which should be nominal at lower frequencies. Note that based upon the interpretation of admittance given in the literature review and as typically presented (i.e. Passmore et al (2001) and Schröck et al (2011)), the admittance plots are technically the square root of admittance (i.e. χ), also termed aerodynamic magnification, and are therefore not plots of $\chi^2$, and are labelled as Admittance (χ). When the numerous 4-seconds data points are plotted on a scatter graph, therefore, the clusters of points are generated from different frequency bands and a linear line can be regressed over these, which will have a gradient (i.e. admittance) and intercept (i.e. self-excitedness). An example of the output for tapping 01 is shown below (the actual assessment of the result will be made later), in Figure 132. Note that in all of the admittance and self-excitedness graphs presented in this section, the input measurement is sideglass pressure coefficient. A legend is shown adjacent to Figure 132, detailing how the systematic connection between yaw angle variation and sideglass pressure variation (i.e. sideglass pressure yaw sensitivity) can be interpreted from the scatter plots.

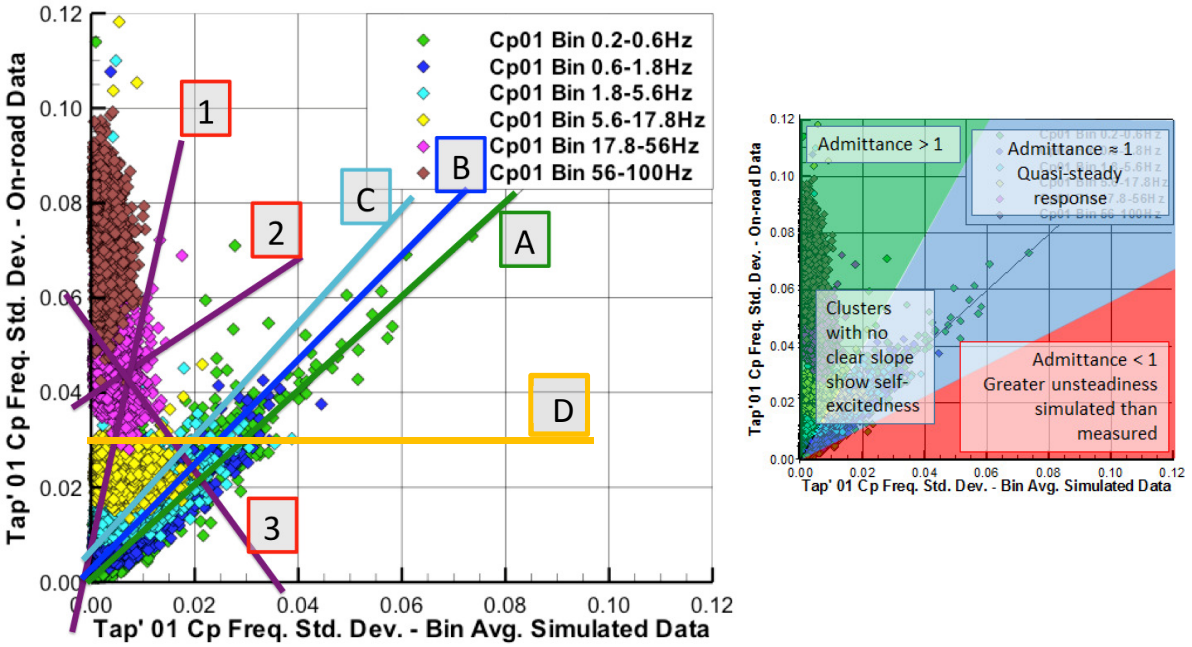


Figure 132 - Interpretations of evaluating the gradient and intercept for clustered data points

Take, for example, the green line, denoted 'A', which represents the gradient of the green cluster of data points, whose results are from the 0.2 - 0.6Hz band. It is quite clear from the shape of the clusters in this band that the gradient is close to unity (i.e. at 45°), with a near to zero intercept. Additionally, reviewing the blue line 'B' (0.6 - 1.8Hz) and cyan line 'C' (1.8 - 5.6Hz), the gradient is increasing above unity, with a non-zero intercept being introduced. Regression of these frequency data clusters is

therefore rather robust. However, as the frequency bands increase, for example the purple frequency band of 17.8 - 56.0Hz, the clusters become more circular and therefore the result of the regression process becomes less trivial, and as such visually a trend line denoted by either the '1', '2' or '3' purple lines in Figure 132 could be potentially valid. In this situation, therefore, the regression method for analysing the data clusters is of most validity at lower frequency bands, but at higher frequencies the gradient of the regressed linear trend line (and therefore by association the Y-axis intercept value) will be highly dependent on the narrow deviations in distribution of only a few data points. If a pressure tapping had no variation with probe measured yaw angle, presented as line 'D', the data set would be represented by a horizontal line at a Y-axis height representative of the level of pressure unsteadiness that the tapping experienced (e.g. a completely pressure invariant tapping with no yaw sensitivity would cause a horizontal line at Y-axis = 0).

The consequence of this is that evaluations of the admittance and self-excitedness made by the regression method will have accurate values at lower frequency, but at higher frequencies the reported admittance can tend to positive or negative infinity readily and equally the self-excitedness can easily become relatively large in value. These effects are real (i.e. large pressure fluctuations do occur), but that if the pressure fluctuations are not yaw dependent, then the reported admittance and self-excitedness is unreliable. The physical interpretation is, therefore, that at the higher frequency bands values in admittance of self-excitedness that vary wildly from the lower frequency band results represent air flows that are highly dominated by pressure fluctuations independent of the incoming flow yaw angle and are artefacts of flow from localised vehicle geometries (i.e. door seal radii). Therefore where admittances or self-excitedness are reported less than zero this is an artefact of the process, as an admittance or self-excitedness of less than zero has no physical representation.

The results are presented in sets covering the dominant region flow characteristic. Tapping 01 will be the primary tapping for the mirror wake region results presentation, shown with tapping 09, tapping 17 will be shown with tapping 19, 29 and 35 covering the A-pillar region and then tapping 12 will be shown with tapping 13 and 22 covering the 'hybrid' region. Figure 133 is shown as a reminder of the flow regions, with the primary region tappings circled.

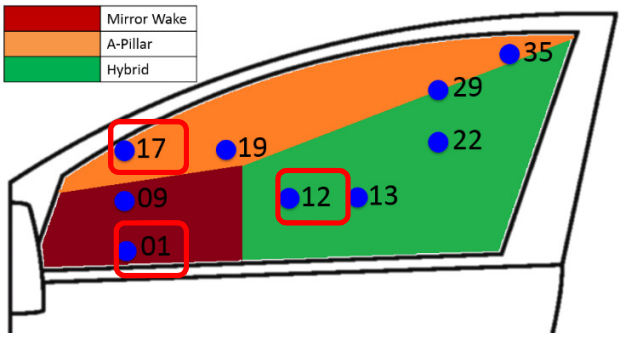


Figure 133 - Flow region type with the region's primary tapping for the presentation of results circled

Taking Figure 134, tapping 01 in the mirror wake region, it can be seen that frequencies less than 5.6Hz are closely clustered to the 45° line, showing that the pressure fluctuations are represented similarly in both the on-road pressure measurements and the quasi-steady simulation measurements. However, as frequencies increase to over 5.6Hz, and especially in the final two frequency bands of 17.8 - 56.0Hz and 56Hz - 100Hz, the cluster of points shows little similarity to the quasi-steady simulated results, and hence are effectively artefacts of the high frequency, local turbulence as opposed to being related to prominent yaw angle changes. One of the major reasons why the higher frequency bands show poorer quasi-steady simulation is due to the intrinsic short nature of the turbulence length scales in these frequency bands. At 30Hz, which is at $32ms^{-1}$, the turbulence length scales are under a metre in length and hence though the roof probe may record them, they are varying too rapidly to reach and affect the sideglass pressure tappings.

The slope and intercept from Figure 134, can be plotted as functions of frequency, giving the admittance plot (regression gradient) as in Figure 135 and the self-excitedness plot (regression intercept) as in Figure 136.

Figure 135 demonstrates that the admittance reduces with frequency showing a drop in yaw dependence above 1Hz with a notable increase in self-excitedness above 10Hz. In both of these graphs, the dependence of yaw with admittance and the increase self-excitedness measurements become significant above 10Hz, clearly a limit where quasi-steady effects no longer hold.

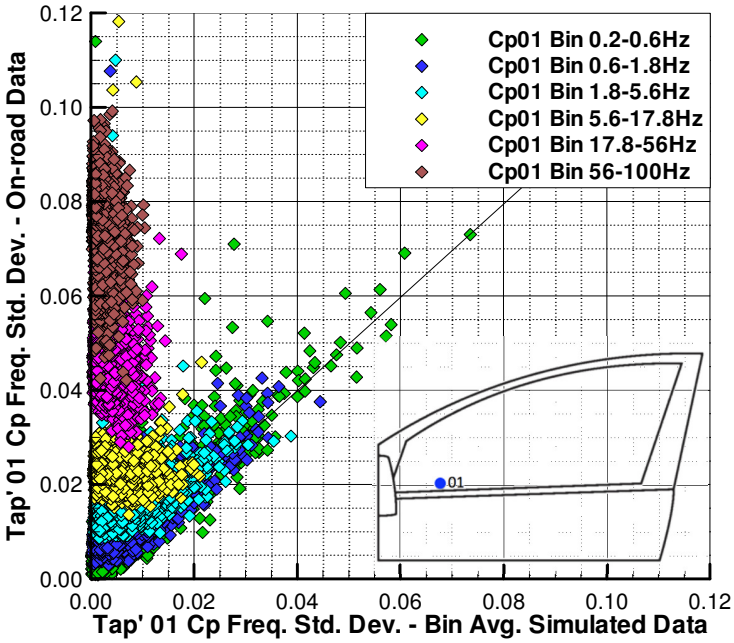


Figure 134 - Tapping 01 frequency band standard deviations for all measurements

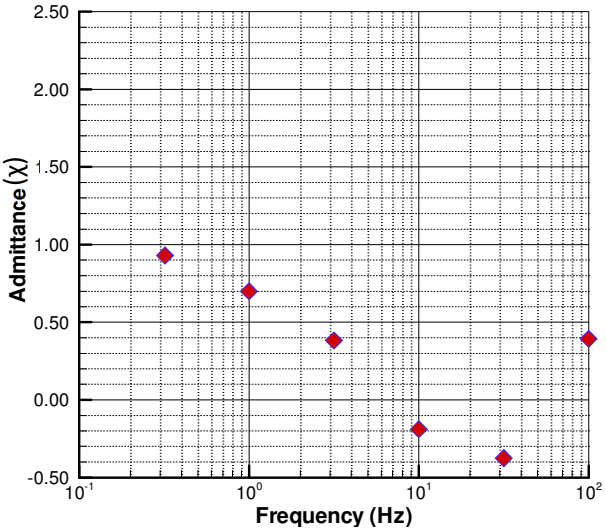


Figure 135 - Pressure coefficient frequency standard deviation frequency admittance plot of tapping 01

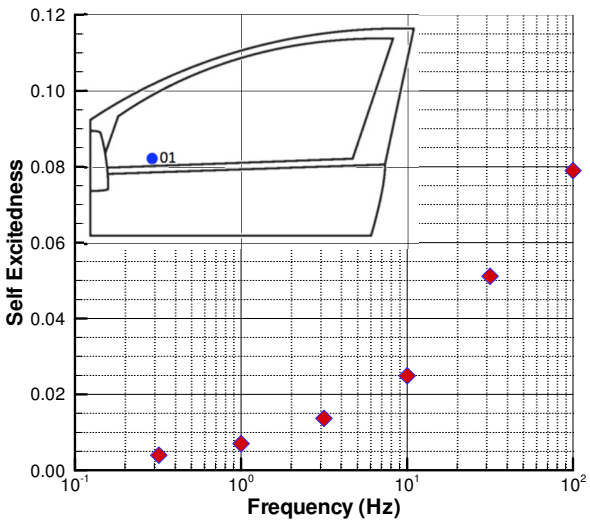


Figure 136- Pressure coefficient frequency standard deviation frequency self-excitedness plot of tapping 01

For tapping 09 admittance and self-excitedness results are shown in Figure 137 and Figure 138. Again the admittance is seen to drop at around 1Hz and self-excitedness to increase above 5Hz and by 10Hz self-excitedness becomes significant. It is of value to note that the quasi-steady simulation technique is able to capture the pressure fluctuations in a highly turbulent region. As such, in a highly turbulent region, the standard deviation of frequencies are less yaw dependent due to the reduced yaw sensitive nature of the mirror wake region (yaw sensitivity determine by an admittance greater than unity).

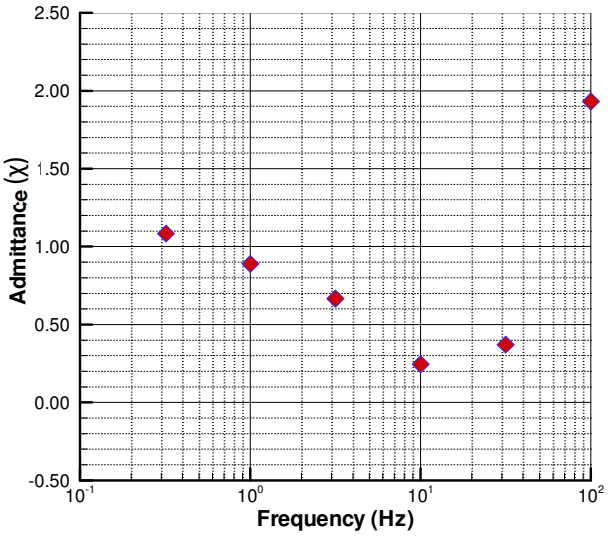


Figure 137 - Pressure coefficient frequency standard deviation frequency admittance plot of tapping 09

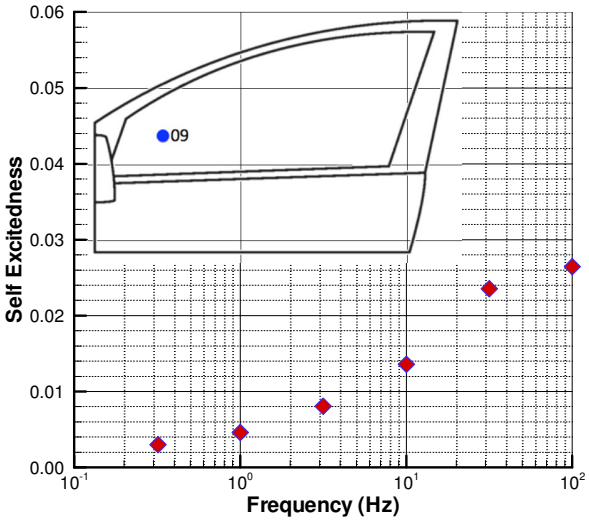


Figure 138 - Pressure coefficient frequency standard deviation frequency self-excitedness plot of tapping 09

At tapping 17, represented by Figure 139, demonstrates A-pillar flow behaviour, and the data point clustering alters greatly than earlier. This is a more steady air flow region with yaw effects well represented by the quasi-steady simulated result. Flow in this region has just accelerated around the A-pillar and has suffered little local disturbance as it enters the sideglass region (it should also be noted, referring back to the set-up image in Figure 94, that the window seal was taped over by aluminium tape, making the typical window seal to A-pillar step less of an issue). Deviation from the 45° line still occurs at 5.6Hz, and is notable by 17.8Hz as previously seen in tapping 01.

Further, the range of standard deviation has increased again as the nature of the region is more sensitive to the incoming flow yaw (clear gradients in each frequency cluster of regressed slopes greater than unity). There is also an increase in frequency band cluster height, as seen in previous pressure coefficient deviation plots, since the pressure fluctuation standard deviation increases with yaw angle as at greater yaw angles the flow contains a higher degree of instability (as shown in Figure 125).

The effect of being more yaw dependent is shown in Figure 140, admittance, and Figure 141, self-excitedness. The admittance plot shows that there is again a good on-road to quasi-steady simulation correlation up to about 5Hz, but then rapidly deviates above 10Hz. This is also shown in the self-excitedness plot of Figure 141, where above 10Hz self-excitedness increases. However, it is of interest that as this region is more stable than others seen so far, the level of self-excitedness is very low up to 5Hz, particularly as there are few flow obstructions in this region.

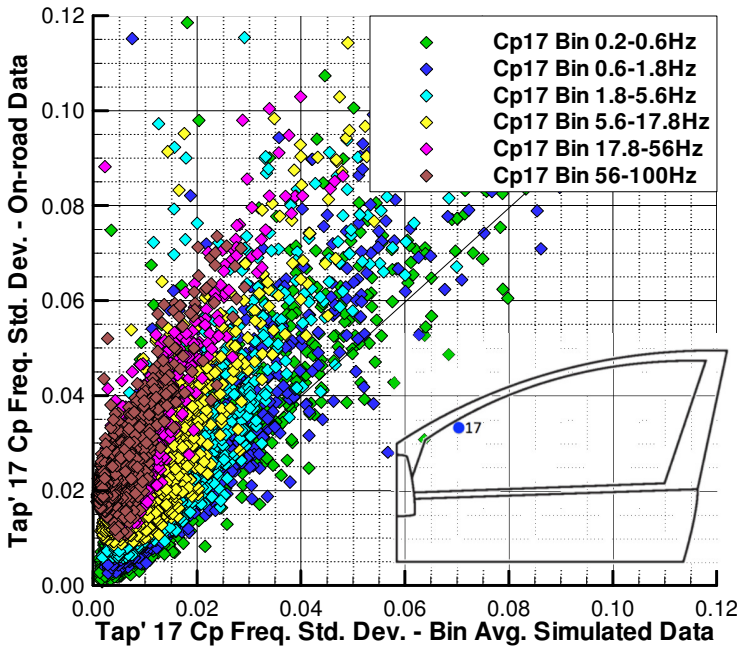


Figure 139 - Tapping 17 frequency band standard deviations for all measurements

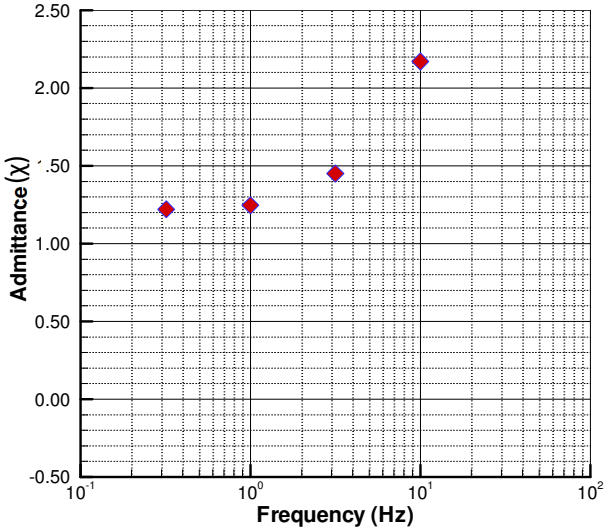


Figure 140 - Pressure coefficient frequency standard deviation frequency admittance plot of tapping 17

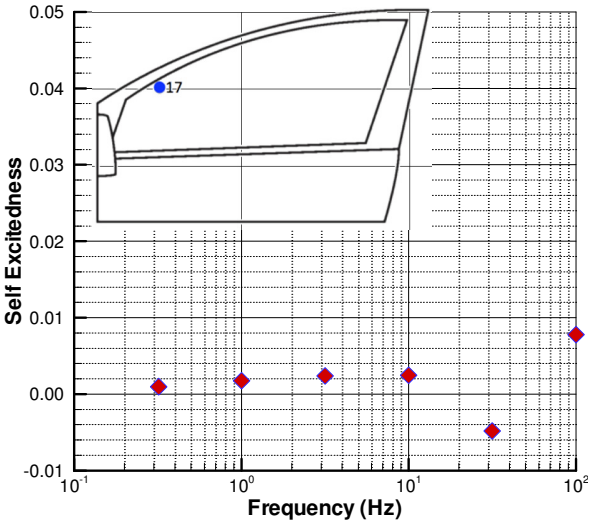


Figure 141 - Pressure coefficient frequency standard deviation frequency self-excitedness plot of tapping 17

Tapping 19 is also in the A-pillar region, where the wake has widened and again effects are seen that are similar to those of tapping 17. The quasi-steady simulation is representative of the on-road pressure measurements and the clustering is tight due to the local flow being less significant on the pressure standard deviation of the incoming yaw flow, and more due to the variant pressure deviations of this turbulent region. Again, the quasi-steady simulation breaks down around 5.6Hz and is clearly differing by 17.8Hz, in Figure 142, the admittance plot, and Figure 143, the self-excitedness plot,

further highlight these effects. Admittance is consistent up to 5Hz and then dramatically increases and self-excitedness is low up to 5Hz as local geometry are less significant and the general flow field more affects the flow.

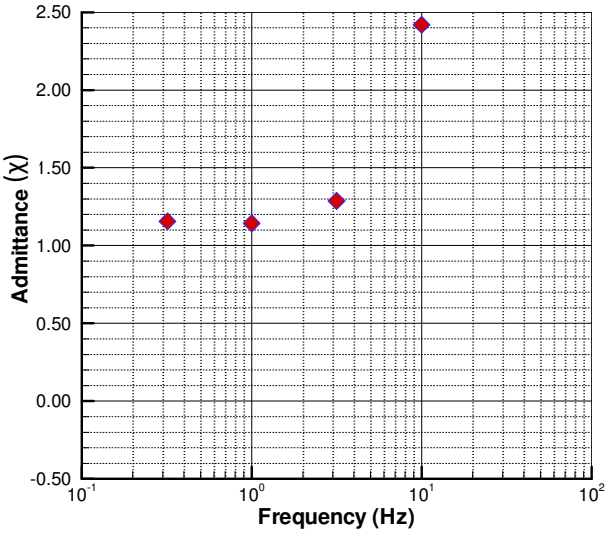


Figure 142 - Pressure coefficient frequency standard deviation frequency admittance plot of tapping 19

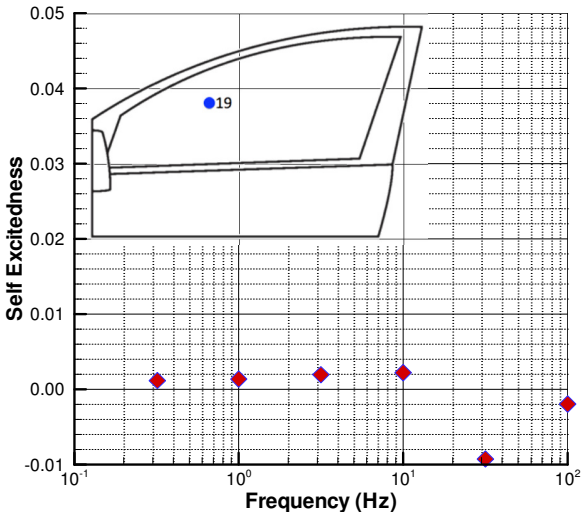


Figure 143 - Pressure coefficient frequency standard deviation frequency self-excitedness plot of tapping 19

Tapping 29, located as the most downstream of all the tappings seen so far, is still showing evidence of the A-pillar. Figure 144 shows the admittance and Figure 145 shows the self-excitedness of tapping 29. Being a more stable flow region, the effect of the standard deviation of upstream pressure fluctuations becomes prominent, and this can be seen in the admittance being poor from 1Hz and becoming extremely poor above 5Hz with self-excitedness, shown in Figure 145, growing above 10Hz.

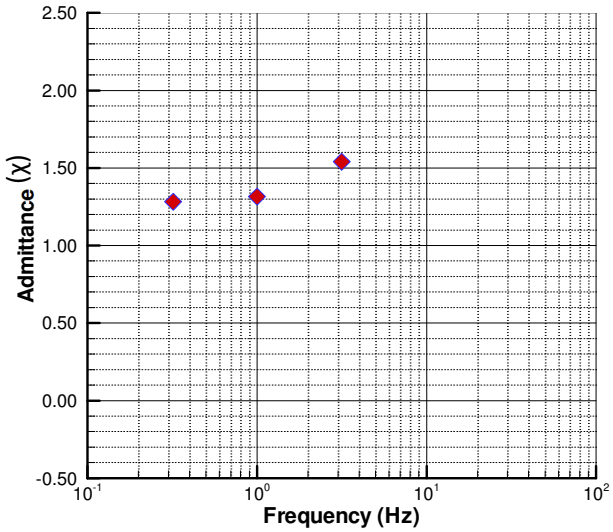


Figure 144 - Pressure coefficient frequency standard deviation frequency admittance plot of tapping 29

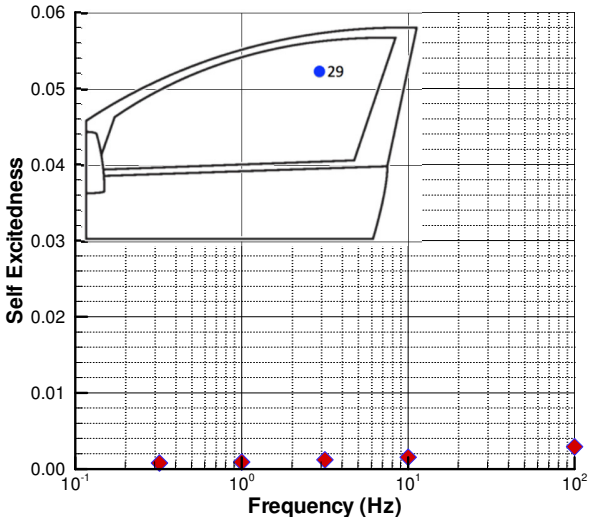


Figure 145 - Pressure coefficient frequency standard deviation frequency self-excitedness plot of tapping 29

Tapping 35 is located in a region far downstream on the window and in an area of good flow stability, though interaction from the A-pillar is still seen. Figure 146 and Figure 147 show the admittance and self-excitedness of tapping 35's pressure fluctuations. As the flow in the region is intrinsically more stable (the A-pillar influence is reduced as the A-pillar is almost horizontal at this location) the admittance function is robust to a higher frequency, up to 5Hz, and only deviates above 10Hz. However, as the region is intrinsically of low turbulence, yet the yaw based pressure fluctuations are more prominent, this is evidence of an increase in self-excitedness especially when compared to more unstable tappings such as tapping 29.

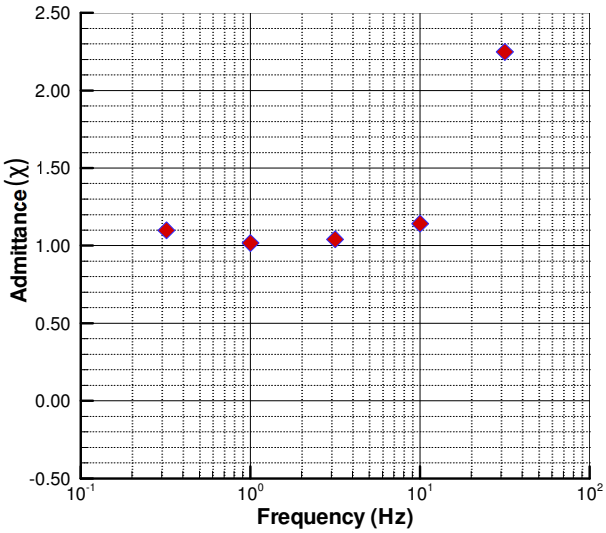


Figure 146- Pressure coefficient frequency standard deviation frequency admittance plot of tapping 35

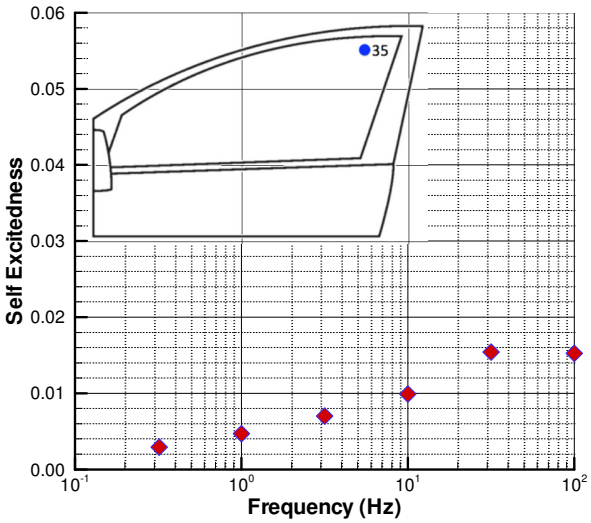


Figure 147 - Pressure coefficient frequency standard deviation frequency self-excitedness plot of tapping 35

Tapping 12, given in Figure 148, is in the hybrid region, showing a different response to the A-pillar and mirror wake regions. Pressure coefficient standard deviations are predominately yaw dependent, but yet again, above 17.8Hz the results gradually move away from the 45° line showing decreasing yaw dependence as frequency increases.

Further detail of the admittance and self-excitedness of these results are shown in Figure 149, admittance, and Figure 150, self-excitedness. As this area is in the hybrid region, it is less turbulent and therefore more yaw sensitive, with admittances valid up to 10Hz, which then greatly deviate. The self-excitedness plot also shows a similar response, that up to 1Hz, even 5Hz, self-excitedness is not too significant, but then becomes rapidly notable. The delay of the admittance decrease and self-excitedness increase is due to the smoother local geometry that causes the turbulent viscous effects. This smoother region combines with flow that is already relatively turbulent in nature due to being downstream of the mirror wake region, demonstrating a moderate pressure coefficient frequency standard deviation and hence the reduced admittances.

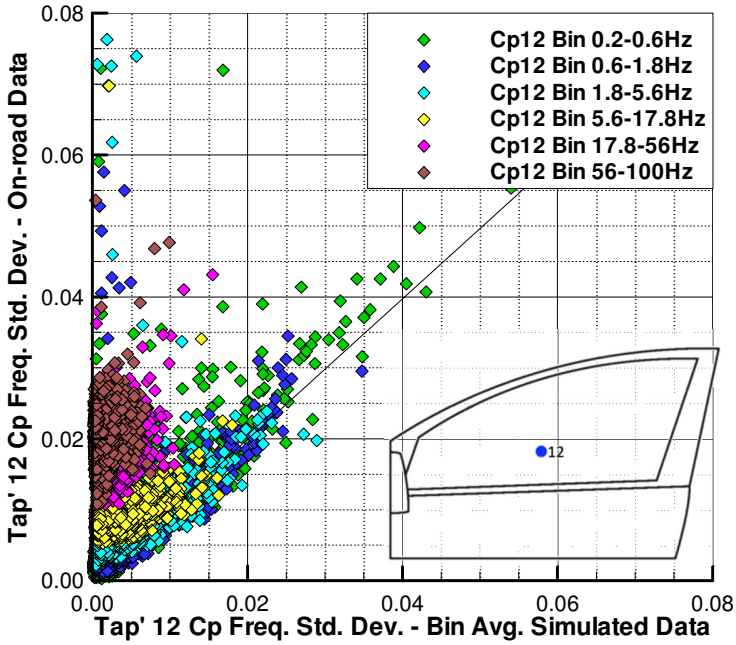


Figure 148 - Tapping 12 frequency band standard deviations for all measurements

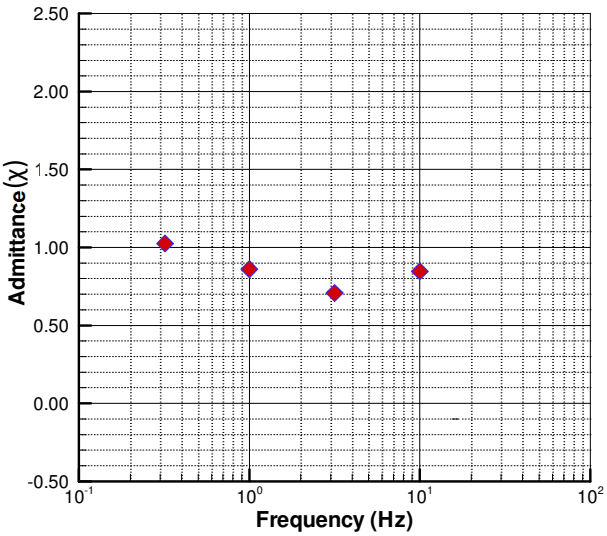


Figure 149 - Pressure coefficient frequency standard deviation frequency admittance plot of tapping 12

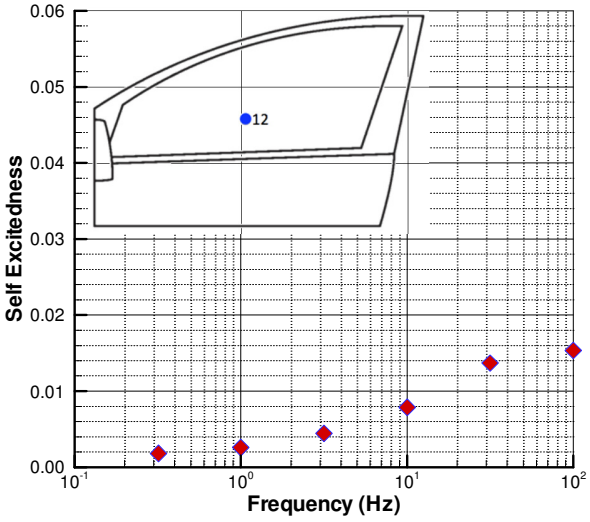


Figure 150 - Pressure coefficient frequency standard deviation frequency self-excitedness plot of tapping 12

Tapping 13, in the hybrid region and slightly further downstream than tapping 12, additionally shows similar effects of strong yaw dependence up to higher frequencies due to being in a yaw sensitive region, with correspondingly less frequency standard deviation. Figure 151, admittance and Figure 152, self-excitedness, again, for this hybrid region, show that the yaw dependent effects are valid far down the sideglass, with the admittance values being reasonable even up to 5Hz, and only greatly deviating

by 10Hz. This is confirmed by Figure 152, where self-excitedness is not too prominent up to 5Hz, but becomes so above 5Hz, and especially so above 10Hz.

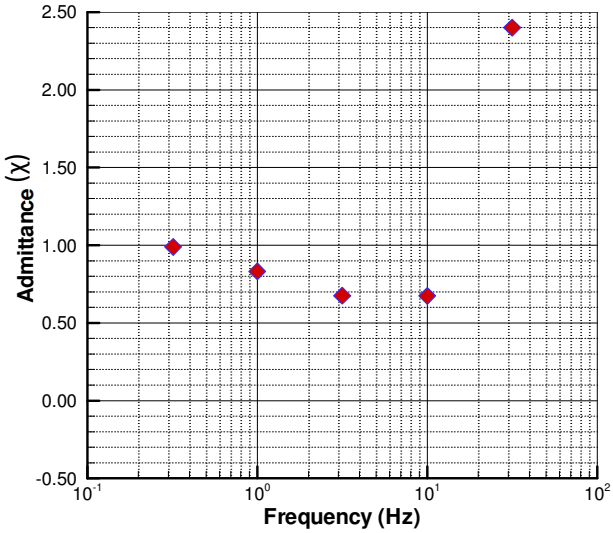


Figure 151 - Pressure coefficient frequency standard deviation frequency admittance plot of tapping 13

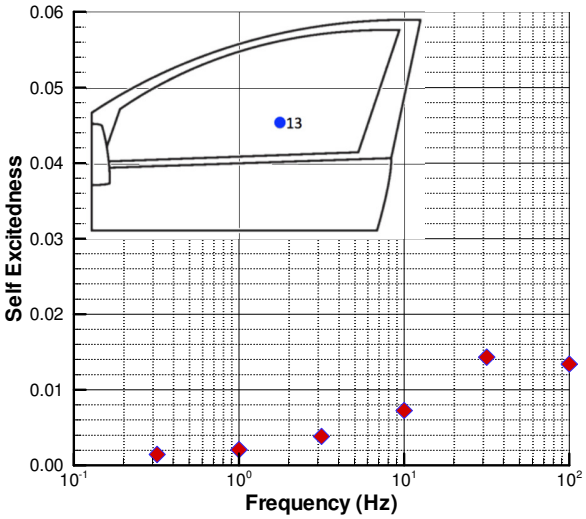


Figure 152 - Pressure coefficient frequency standard deviation frequency self-excitedness plot of tapping 13

Tapping 22 is also in the hybrid region with the admittance plot, Figure 153, and the self-excitedness plot, Figure 154, showing a robust quasi-steady simulation up to 1Hz, then a drop in the region up to 10Hz, and is spurious above 10Hz. Self-excitedness is also seen to increase at 5Hz, but is otherwise relatively low. Again, the admittance and self-excitedness deviations are less due to the region being slightly turbulent but more due to the high yaw sensitivity. Therefore the quasi-steady simulation is more robust as the standard deviation of pressure fluctuations in this region is less diverse.

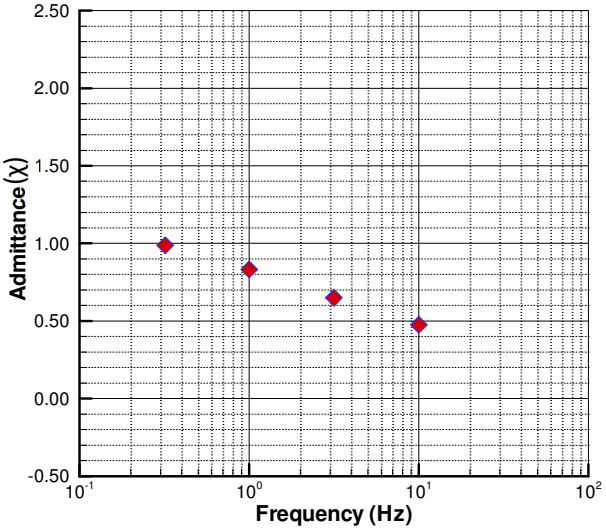


Figure 153 - Pressure coefficient frequency standard deviation frequency admittance plot of tapping 22

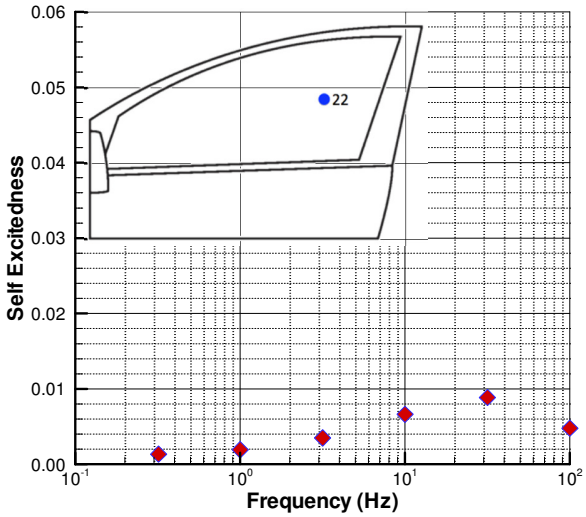


Figure 154 - Pressure coefficient frequency standard deviation frequency self-excitedness plot of tapping 22

In order to aid reviewing the wide selection of results shown, Table 7 was generated as a partially subjective review of the main result parameters:

Table 7 - Pressure fluctuation standard deviation results review for all tappings

| Region Type | Tapping | Intrinsic Turbulence Level | Admittance at ≈5Hz | Quasi-steady Simulation around 5Hz (i.e. Yaw based dependence) | Self-Excited ness Level 5Hz | Data Points Cluster Height above 5Hz |
|---|---|---|---|---|---|---|
| Mirror wake | **01** | High | Low | Poor | High | Tall |
| Mirror Wake | **09** | Medium - Low | Low | Medium | High | Medium |
| A-pillar | **17** | High | High | Good | Low | Tall |
| A-pillar | **19** | Medium | High | Good | Low | Small |
| A-pillar | **29** | Medium | High | Poor | Low | Medium |
| A-pillar | **35** | High | High | Medium | High | Medium |
| Hybrid | **12** | Low | Central | Good | High | Small |
| Hybrid | **13** | Low | Low | Good | High | Small |
| Hybrid | **22** | Low | Low | Good | Medium | Small |

**Notes:**

- Intrinsic turbulence level is an assessment of the typical level of turbulence at the tapping (i.e. mirror wake = high, in smooth air flow = low)
- Admittance above 5Hz is an assessment of whether the admittance is greater than ±0.5 from 1.0
- Quasi-steady simulation above 5Hz is measure of the clustering of points near to, or far from, the 45° axis
- Self-excitedness level is an assessment of whether the self-excitedness is ±0.5 from 0.0
- Data cluster size is a review of the height of the high frequency clusters

## 4.4 Comparison of Frequency Band Deviation Range with Average Yaw

In order to further explain the height of the cluster of data points within a frequency band (i.e. consider Figure 134, the higher frequency bands show a large range in deviation and no correlation with the quasi-steady simulation) a comparison between the frequency band standard deviation and the average yaw for each frequency band is made in Figure 155 to Figure 160, for tapping 01 (in the mirror wake region). This is in order to answer whether the pressure coefficient standard deviation is consistent over the entire yaw range, or is the increase in flow instability at greater yaw angles causing more of the sideglass tapping pressure variation at the higher frequencies.

This effect would be noticeable as a gradient of the cluster of data points over the yaw angle range. At low frequency bands, as in Figure 155 to Figure 157, it can be seen that there is no clear gradient in the data sample and these frequency bands all show good correlation between the road-data and quasi-steady simulation results. However, as the bands increase in frequency (notably Figure 158 to Figure 160) a slightly negative gradient can be seen as the frequency increases. This shows that some of the standard deviation range in a frequency band is due to the incoming flow unsteadiness caused by the vehicle's shape not just local geometry. Tapping 01 was used as a base line as it showed the greatest standard deviation range, especially at high frequency bands, of all of the tappings.

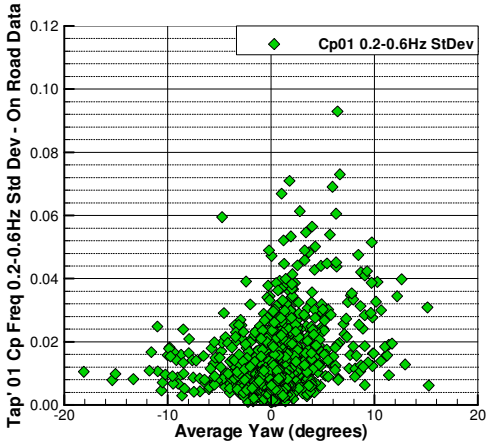


Figure 155 - Plot of tapping 01, frequency band 0.2-0.6Hz, $C_P$ Standard Deviation against average flow yaw angle

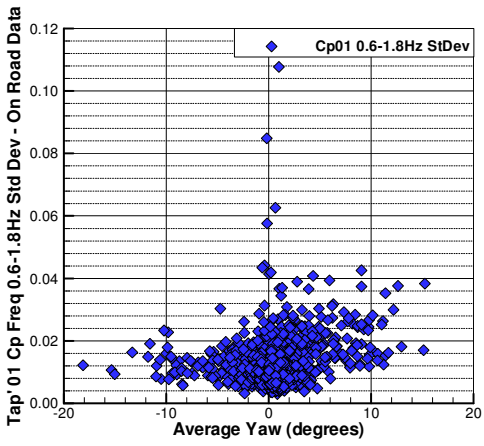


Figure 156 - Plot of tapping 01, frequency band 0.6–1.8Hz, $C_P$ standard deviation against average flow yaw angle

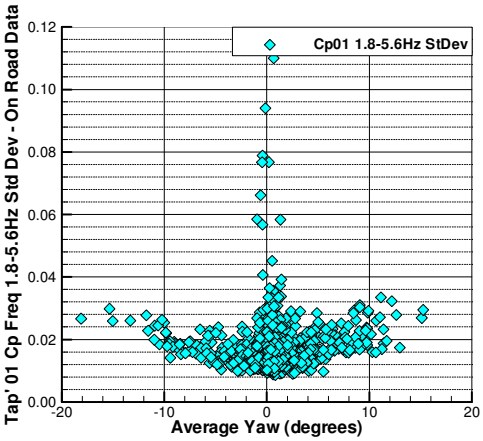


Figure 157 - Plot of tapping 01, frequency band 1.8-5.6Hz, $C_P$ standard deviation against average flow yaw angle

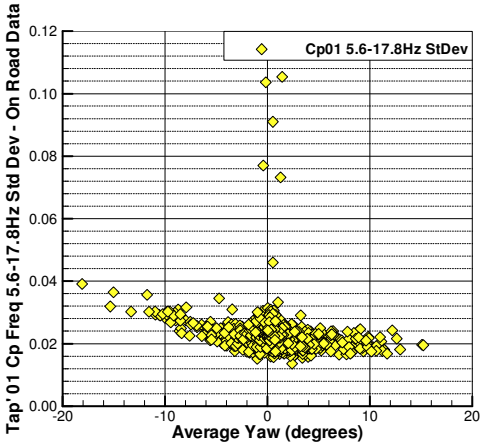


Figure 158 - Plot of tapping 01, frequency band 5.6–17.8Hz, $C_P$ standard deviation against average flow yaw angle

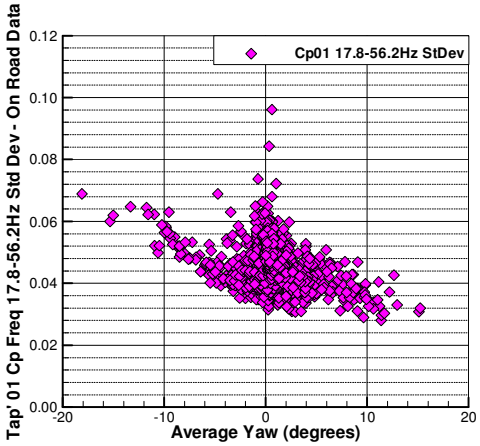


Figure 159 - Plot of tapping 01, frequency band 17.8-56.2Hz, $C_P$ standard deviation against average flow yaw angle

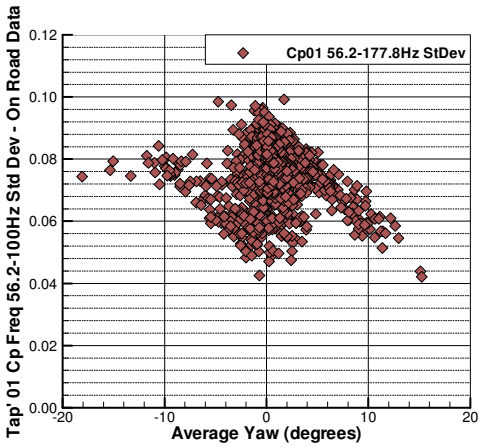


Figure 160 - Plot of tapping 01, frequency band 56.2–177.8Hz, $C_P$ standard deviation against average flow yaw angle

## 4.5 Example On-road Case for Onward Investigations

For onward CFD and wind tunnel investigations requiring an unsteady inlet profile, it is favourable to have a representative case of on-road flow data that depicts the typical flow of the population data. Ideally this case would also contain gusts that oscillate either side of zero degrees, whilst staying within $\pm 10^{o}$ (a yaw range seen to encompass the characteristics of the majority of the on-road environment), yet with the odd prominent peak yaw angle. Based upon these criteria, 6 measurement cases were short listed, with a typical challenge being that often a case would not be representative of the population data as it would have excessive large angle variations (i.e. symptomatic of a windier day). A good case would be depicted by a wider PDF of yaw angle and higher turbulence intensity than typical, whilst not being so unique to be atypical of the population data. Figure 161 represents a case that met

these considerations, number 21 of the 275 recorded, of a windy day, yet meeting the desired characteristics. As CFD cases have to be of much shorter duration than can be simulated by a TGS, a 4-second window of a gust was also extracted from the trace (4-seconds used as determined by reduced frequency in the literature review), and this period is bounded by a red box in Figure 161, whereas a TGS would simulate the entire 32-second case.

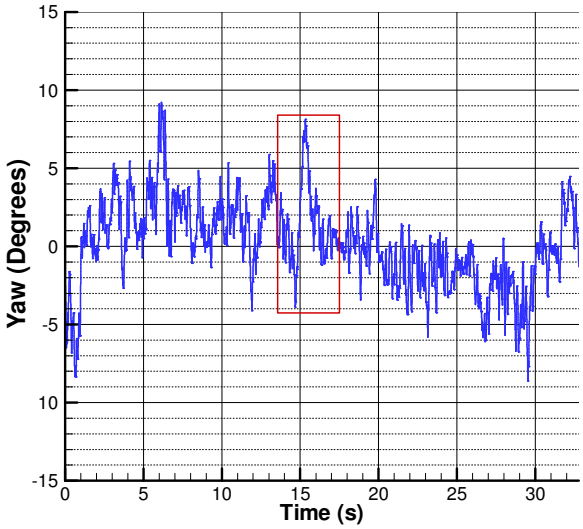


Figure 161 - Yaw plot trace of Case 21, with the 13.5–17.5s window CFD gust highlighted

In order to analytically verify the suitability of this case alongside those also short-listed, the measurement case was assessed on its probability density function of yaw (i.e. P(Yaw)) against that of the population result, and the values of its turbulence intensity against turbulence length scale data points. Figure 162 shows the PDF of case 21 against that of the population data and out of all the cases assessed it showed some important characteristics. Namely, these were its symmetry and its relatively steep gradient of P(Yaw) decay with yaw angle, as occurs in the population data set.

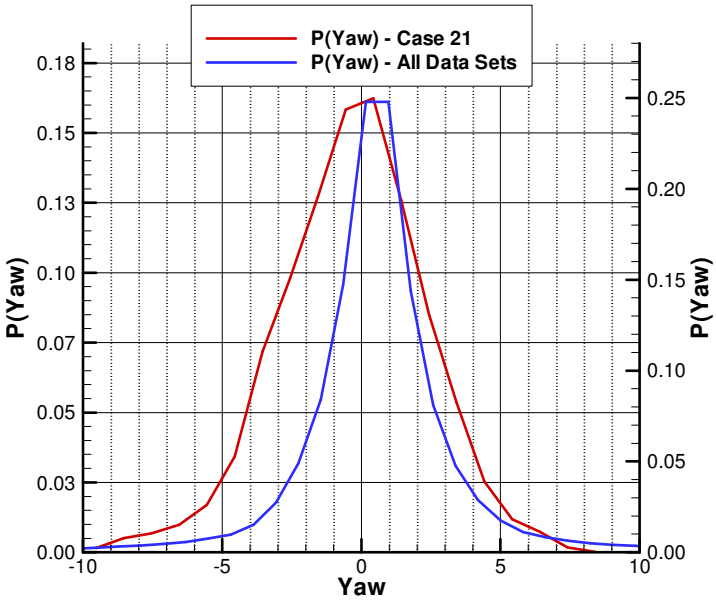


Figure 162 - PDF of population data yaw angle with selected case 21 yaw plot

The cases were then evaluated for their results from a turbulence intensity against turbulence length scale assessment, in 4-second rolling windows, as in Figure 163. It was important that as many as possible of the data points from the 4-second rolling windows of turbulence stayed under an 8%/8m cut-off in order to still be representative of the population data (i.e. to be a gust, but not to be an extreme event). It can be seen in Figure 163 that case 21 had all but one of its data points in this bound and the results sat comfortably alongside the population data.

Additionally the two data points bounded in green boxes depict the turbulence measured for the 4-second CFD gust segment, and again it can be seen that the sample is a fair representation of the population data.

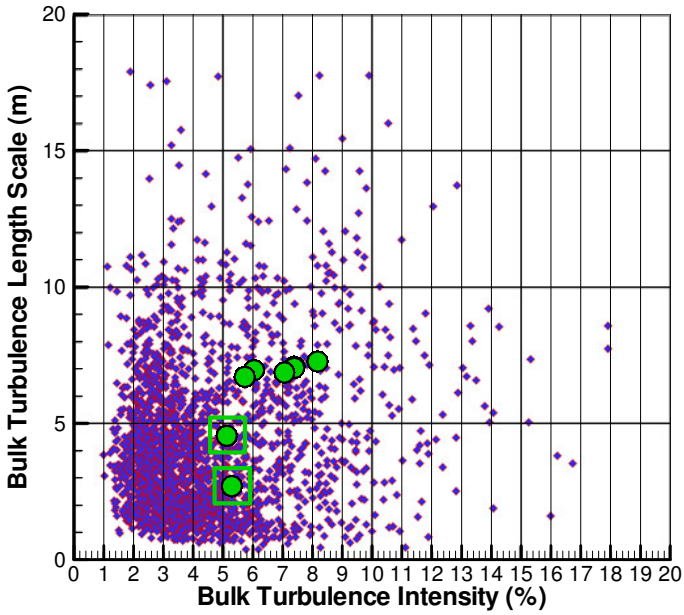


Figure 163 - Case 21 with TI and TLS points plotted

Points in green are from the 4-s gust case, where the two TI vs. TLS highlighted points with the green box are from the 4-second gust segment of the 32-second sample

## 4.6 Conclusions

In this chapter a large on-road study of transient flow conditions has been completed using a roof-mounted 5-hole probe and 9 sideglass static pressure tappings. Rover 200 sideglass pressure measurements recorded at MIRA were presented, though the results only offered a small snapshot of yaw against pressure variation due to the limited range of yaw angles under which the test was completed. A 3D CFD test was completed that showed longitudinal and lateral flow velocities recorded by a roof probe are increased relative to the freestream velocities, but that these exaggerations of flow velocity did not corrupt yaw measurements.

275, 32-second on-road measurement runs were recorded and the data was broken into 4-second sections. Yaw angles of the air flow were found to be within ±10°, with the vast majority within ±4°. The correlation between roof probe velocity magnitude and the GPS data was found to be robust, with a typical speed-up on the roof probe of 6%. Turbulence length scales and intensities were found to lie mostly below 8.0m and 8.0% respectively and above 0.50m and 0.50% respectively. Turbulence length scales were found to peak (by the auto-correlation method) at around 2.0m and intensities at 2.5%. A strong negative correlation between length scale and intensity was shown for all 3-axes of flow velocity, with a gradient of approximately −1.5m/% for bulk velocities, increasing in negativity as the axial components were assessed in the order of X, then Y and then Z axes. Confidence intervals of 95%

were narrow and the variation in standard deviation of the data was found to be smaller in order of magnitude than the variation in the data sets, showing good validity of data capture.

A quasi-steady simulation process was completed using the roof probe instantaneous flow yaw angle as the dependent variable to bin-average sideglass tapping pressures, creating a yaw against sideglass pressure profile map, completed for all 9 tappings. The results showed that using yaw at below 5Hz as an input into the quasi-steady simulation process is valid and pressure variations at the sideglass tappings can be resolved from the roof probe. However yaw as an input becomes less reliable by 5Hz and above 5Hz the admittance greatly deviates and self-excitedness significantly increases showing little yaw dependency. This suggests that at these frequencies the probe cannot offer an accurate simulation of the sideglass tapping pressure.

Tappings in the mirror wake region (tappings 01 and 09) were less yaw dependent than other sideglass regions (with admittances less than unity) due to its intrinsic high flow unsteadiness and correspondingly the region showed significant levels of self-excited turbulence. In this region the admittance decays less rapidly than in a more yaw sensitive region as the intrinsic turbulence of such a region (i.e. mirror wake) seems to suppress large pressure fluctuations, even though such a region will experience a pressure coefficient step change relative to other sideglass regions. The results also show that the self-excited component only becomes notable above a certain frequency threshold (typically >10Hz) as the local geometry that causes the high frequency viscous effects, and hence the high standard deviation of turbulence, will have less effect when the flow has already transited to a highly turbulent state.

Tappings in the A-pillar wake region (17, 19, 29 and 35) showed yaw dependency with admittances greater than unity at frequencies under 5Hz. Pressures in the A-pillar region were less valid at lower frequency bands due to the aerodynamically unstable nature of this region, and correspondingly the pressure tappings in more aerodynamically stable regions (i.e. tapping 35, just fore of the B-pillar) showing better correlation up to higher frequency bands. The hybrid region (12, 13 and 22) showed yaw dependency and low levels of unsteadiness. In any of the three region types, the simulation process showed that above around 10Hz the self-excitedness of the turbulence becomes significant.

Ultimately, the admittance is generally below unity in mirror wake, and then around unity for the remainder of the sideglass except near to the A-pillar, where the admittance is generally greater than unity. Self-excitedness is, as expected, highly dependent on geometry and is therefore more commonly observed in the mirror-wake region. It is also worth noting that the A-pillar region has a high

quasi-steady sensitivity to yaw, but that in the transient, unsteady results the response to yaw is even more significant (hence an admittance greater than unity). This therefore shows that high yaw sensitivity does not necessarily correlate with an admittance greater than unity. These results are summarised in Figure 164.

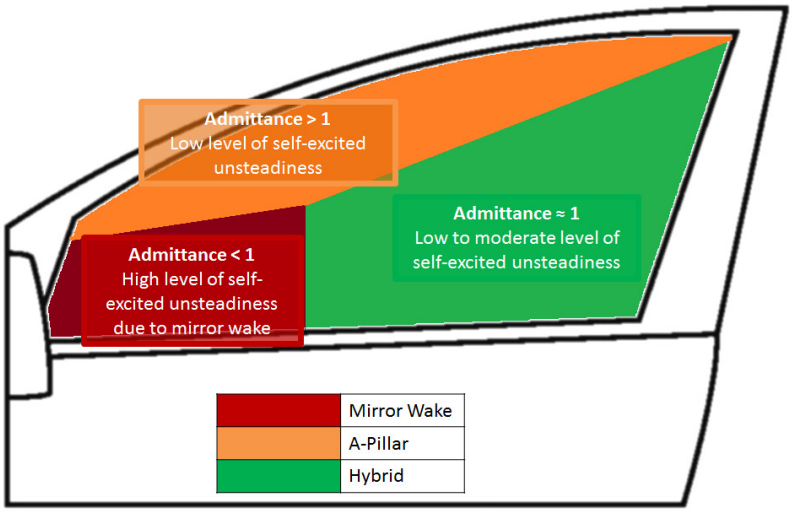


Figure 164 - Summary of the dominant aerodynamic characteristic for each of the three defined sideglass regions

More detailed analysis of pressure fluctuations against averaged yaw angle showed that the standard deviation clusters widen in regions with lower intrinsic turbulence, as those regions are more yaw sensitive. Additionally the pressure coefficient standard deviation was shown to increase with yaw angle, evidenced by the frequency band cluster widening at higher frequency bands, due to the more highly yawed incoming flow having a greater instability and hence exhibiting intrinsically more pressure fluctuation.

Finally, one particular case of 32-seconds was evaluated, from which a 4-second gust was also extracted, which had properties representative of the entire data population for onward CFD and wind tunnel investigations requiring a transient inlet trace.

# 5. TGS Design Development through 2D and 3D CFD Studies

This chapter details studies completed using both 2D and 3D CFD simulations to develop a design for an active Turbulence Generation System to be retro-fitted to Durham University's 2m wind tunnel based upon an initial specification compiled from both the literature review and on-road results. The objective of the TGS system is to replicate an unsteady aerodynamic environment (i.e. on-road flow conditions) and to provide a tool to investigate a vehicle's response to unsteady flows (i.e. harmonic test frequencies). Definitions of the tunnel layout and terminology are shown graphically for the 2D model in Figure 166 and for the 3D model in Figure 180.

## 5.1 TGS Specification from On-road Measurements

The specification for the TGS is defined from two objectives. The first is the appropriate recreation of length scales and intensities with inputs from the air flow characteristics measured on-road (i.e. Wordley et al (2009)) and the necessary bounds of an active TGS. The second is the quality of air flow, namely that the flow across the cross-sectional width of the tunnel is consistent and sufficiently wide to flow around all of a model, even under extreme yaw conditions. An initial review of results presented in the literature review suggests that a TGS should generate:

- A power spectrum as per the length scale and intensity spectrum plots of Wordley et al (2009).
- Turbulence frequencies in the region of 0.1 - +10Hz.
- Turbulence length scales corresponding to, at a full-scale in (u, v, w), approximately 2.0, 1.8, 1.8m.
- Peak yaw angle amplitudes in the ±6 - 10$^{o}$ range.
- Air flow reaching intensities in (u, v, w) of approximately 2 - 14, 2 - 8, 2 - 8%.
- Flow conditions variable such to meet the range for the 'Road-side obstacles' to 'Smooth Terrain' on-road environments proposed by Wordley et al (2009).
- Flow that does not decay significantly down the test section length

### 5.1.1 TGS Frequency Bounds

This section considers the frequency range in which an active TGS should operate, bounded by the quasi-steady limit at a lowest frequency to an upper frequency limit which is combination of the frequency at which the spectral energy in the on-road environment and a vehicle sensitivity reduces and where passive turbulence generation devices (i.e. static grids) become effective.

An appropriate metric for assessing the effect of turbulence frequency (i.e. TLS) on a vehicle can be gained by considering the reduced frequency (i.e. Corin et al (2008)). The reduced frequency, as shown in the literature review, is defined in this analysis by a threshold proposed by Corin of 0.1 as a quasi-steady limit, (i.e. in this case, a number which represents the threshold above which the effect of inlet turbulence can be considered to become significant). The function is made non-dimensional based upon flow velocity and vehicle size. A reduced frequency approach can therefore yield an appropriate TGS driving frequency when a velocity and size is specified. The time period threshold at which on-road vehicles experience quasi-steady turbulence can be evaluated by:

$$\omega_R = \frac{2\pi\sqrt{A}}{TU} \Rightarrow T = \frac{2\pi\sqrt{A}}{\omega_R U} \Rightarrow T \approx 4.0s \quad [16]$$

where $\omega_R < 0.1$ (from Corin et al (2008)), U is vehicle driving test speed ($25ms^{-1}$) and a typical mid-sized vehicle frontal area A of $2.5m^2$.

This gives a lower frequency limit of 0.3Hz where, at frequencies below this, a quasi-steady approach could be adopted. This corresponds to a length scale of around 100m full-scale, or 30m in tunnel scale (30%). Clearly this is a large length scale to simulate, but is possible with oscillating aerofoils. The opposing upper frequency bound is composed of the frequency where the on-road spectral energy is seen to decrease (shown to be around 10Hz full-scale from Wordley et al (2009) - Figure 10), where a vehicle's response is seen to reduce (≈10Hz full-scale) and the length scale that can be generated using passive methods. The maximum length scale that can be created by passive methods (i.e. Static grids, Newnham et al (2006)) is limited by the distance between the grid bars, which is constrained by the test section width and height. Durham University's 2m wind tunnel jet is 1.8m x 1.1m, which implies by this rule of a maximum feasible length scale being 1.1m. However, as usually more than 2 bars would be required, a figure nearer half of this is realistic, giving a length scale in the tunnel of 0.55m, or 1.80m at full-scale. An alternative perspective is the shedding frequency of a cylinder from the Strouhal number (using 0.2 for a cylinder). A 0.5m cylinder in the tunnel air flow of $25ms^{-1}$ could generate frequencies of down to 10Hz:

$$f = \frac{S_{TR} v}{d} = \frac{0.2 \text{x} 25.0 ms^{-1}}{0.5m} = 10Hz \quad [17]$$

At a tunnel speed of $25ms^{-1}$, this means that passive grids can generate length scales at most of 2.5m. However it should also be mentioned that grids are drag devices and generate high frequency,

turbulent wakes. As such a lower bound of 0.5m tunnel scale is appropriate, but the 2.5 - 0.5m could be achieved using a grid design if required. However a 0.5m TLS corresponds to a frequency where significantly less spectral energy exists on the road. Therefore, from an aerodynamic and mechanical perspective, frequency bounds of an active TGS device between 0.5 - 20Hz (30 - 2.0m TLS) are valid. It is of value to note that this region also includes typical suspension Eigen frequencies (≈1Hz) and the noise modulation frequency to which human hearing is at is greatest sensitivity (≈4Hz) (Sims-Williams and Mankowski et al (2013)).

### 5.1.2 Generation Approach

The objectives of the TGS are secondly defined by the flow conditions experienced by road cars. Sims-Williams (2010) reviewed the use of a variety of turbulence generation systems operating up to 100Hz, based on analysis based upon a similar spectral energy curve of that of Wordley (2009). The plot, Figure 165, is given as an overview of the typical turbulence generation frequencies against types of generation systems. The coloured regions show approximate areas that are notable for quasi-steady effects (green), transitioning from quasi-steady to unsteady (i.e. significant potential vehicle response) (amber) and low on-road spectral energy (red).

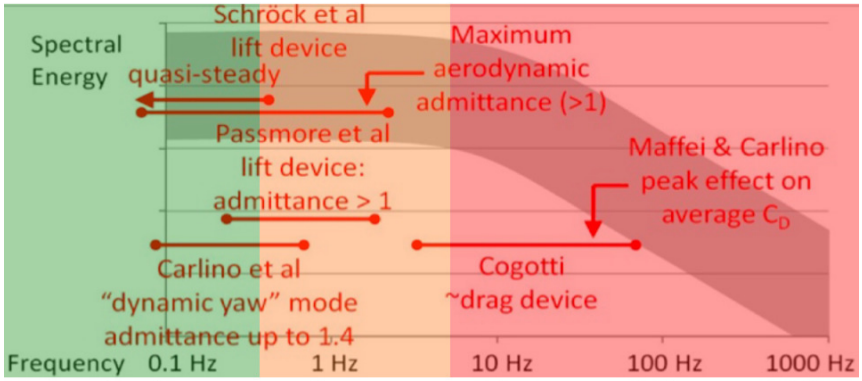


Figure 165 - Active TGS bounds for full-scale tests - modified from Sims-Williams (2010)

At FKFS, Schröck et al (2009) were able to generate turbulence of up to ±6° of yaw using a set of oscillating aerofoils operating at 10Hz. At 25ms$^{-1}$ (Durham University 2m Wind Tunnel's typical operating speed) this would relate to around 10% intensity ([25.0] /[25.0tan(6)]) at a length scale of 2.5m, which would correspond to a full-sized scale of around 8.0m. Therefore an objective would be to use oscillating aerofoils to generate turbulence at a tunnel length scale of 10.0 - 2.4m.

However, this does leave a gap between 2.4 - 1.0m full-scale which Wordley et al (2009) highlights is a key range for turbulence generation and requires intensities of around 12% (figure 2). This gap could be filled using a design similar to that at Oldenburg University (Knebel et al (2010)), which has generated length scales of around 1.20m in a 0.90m$^2$ tunnel. If the system could be suitably scaled to Durham's 2m wind tunnel, this could suitably generate the 2.4 - 0.5m length scales. Additionally, as mentioned earlier, the shedding frequency of 0.5m cylinder in 25.0ms$^{-1}$ of air flow could achieve a 10Hz (i.e. 2.40m) wave. However, the onward focus will be in the 10 - 2.4m TLS range.

Flow measurements by Wordley suggest a range of 4.2m at 2% to 0.5m at 13% intensity (i.e. Figure 9), with the spectral energy level being consistent down to from 4.2m to 2.4m tunnel scale. These targets are achievable in the 4.2m to 2.4m TLS range using aerofoils, which are also suitable for the consistent spectral energy amplitude targeted with intensities requiring >±9$^o$ of aerofoil yaw amplitude.

### 5.1.3 Quality of Air flow

1. Ideally the test model will not experience trailing vortices from a lift or drag device. This will improve the consistency of the air flow over the model and reduce the likelihood of inconsistent 'patches' of high flow turbulence on any regions of the model.
2. The wake from lift devices are less of an issue than wake from a drag device. However if lift devices are to be used, they will ideally be positioned at the width of the test section and not have aerofoils in the middle section of the nozzle.
3. The aim is that the flow velocity and yaw angle will be consistent over the model's extents (defined as ±500mm in Y and ±700mm in X from turntable centre).
4. The useable width of the test section can be reduced due to the jet narrowing in cross-section when under yaw. Aligned with the earlier objective of not having inconsistent flow over the model, the useable test section width should be greater than the model's width to ensure that the model does not experience the jet's shear layer which would have large effects on measured pressure, lift and drag over the model.

### 5.1.4 Mechanical Operation

1. If aerofoils are used, they should be able to operate to at least 10Hz, with the aerofoil amplitude and frequency being electronically controllable (i.e. variable during a test cycle).
2. If a jet width variation method is used, it should be controllable to allow variable frequency and phasing, with a movement time suitable for the tested frequencies.

3. If a collector width variation is used, it should be suitably phased to the front aerofoils to compensate for the particle travel time down the length of the tunnel.

## 5.2 TGS Design Modelling Methodology

In order to design and develop a potential TGS design, CFD analysis was undertaken to determine the potential length scales and frequencies achievable by various TGS configurations. CFD simulation gave the opportunity to assess potential designs without the constraint of resolving mechanical issues. CFD simulations are able to model device movements and determine the expected flow at frequencies and amplitudes well above what is mechanically achievable. The CFD tests progressed through 2D static and dynamic mesh tests to 3D RANS and Lattice Boltzmann based tests. The basic configuration for the RANS (i.e. Fluent) 2D and 3D cases was a:

- 2D horizontal section through of Durham University's 2m wind tunnel. This gave a test section length (nozzle to collector) of 5.1m, with an inlet width of 1.75m and a collector width of 1.90m.
- For static test cases, a triangle mesh geometry with mesh size at 0.01m around aerofoils, with a maximum cell size of 0.02m throughout the entire mesh.
- For time-variant test cases, a dynamic re-meshing undertaken at every time-step. Constraints of mesh geometry using 0.003 - 0.050m cells with a maximum skewness of 0.65 were followed.
- Aerofoil oscillation defined using a Fluent UDF (macro code function) with a sinusoidal input.
- Minimum time step resolution of 100 time-steps for 1 particle track through the test section (0.001s time step for a 5.1m/25.0ms$^{-1}$ = 0.2s per track - also referred to as flush-throughs).
- Minimum of 30 time-steps per aerofoil oscillation period with 80 iterations per time-step.
- Minimum unsteady run time of 0.5s offering approximately 2.5 tunnel particle tracks (flush-throughs) and a minimum of 10 aerofoil oscillations per simulation run.
- Tunnel main inlet set as a velocity inlet of 25ms$^{-1}$.
- Side inlet velocities set to 25ms$^{-1}$.
- K-Omega turbulence model.
- 1$^{st}$ order implicit unsteady flow solver with fixed time-step size.
- Results given measured $U_X$ and $U_Y$ at the turntable centre (TTC) (1.8m downstream of nozzle inlet).

## 5.3 CFD 2D Test Cases Overview

The primary output metrics were yaw angle amplitude, longitudinal velocity consistency and lateral velocity symmetry, measured over lines of constant X and Y axis through the test section, centred on the turntable centre (TTC), with further analysis from these giving turbulence length scales and intensity. Assessments of the velocity drop over the test section due to the TGS operation (i.e. due to varying inlet and outlet size, etc.) and regions of recirculated flow caused by the TGS operation were also made. The evaluated length scale was determined from the time period between subsequent yaw angle peaks and was correlated with aerofoil oscillation frequency. The results of average longitudinal velocity at TTC and longitudinal velocity range were noted as these are important for the flow quality and uniformity. Finally, aerofoil frequencies were derived from a range with the lower limit being at the quasi-steady threshold of 0.3Hz and the upper limit being where the on-road spectral energy is seen to notably decrease, which is around 30Hz at tunnel scale (i.e. the frequency at which an active system becomes unnecessary). Therefore the dynamic CFD cases were run using aerofoil frequencies of 0.1, 1, 5, 10, 20 and 30Hz.

## 5.4 Initial TGS 2D Model Design

The first design utilised a pair of front aerofoils placed at the side of the nozzle, with their location chosen to prevent their wakes from passing over the test model. Yaw angles were measured at TTC where the angles are at a minimum as greatest yaw is experienced in the flow directly trailing that of the oscillating aerofoils (i.e. laterally furthest from the aerofoils).

The 2D tunnel model design is as in Figure 166.

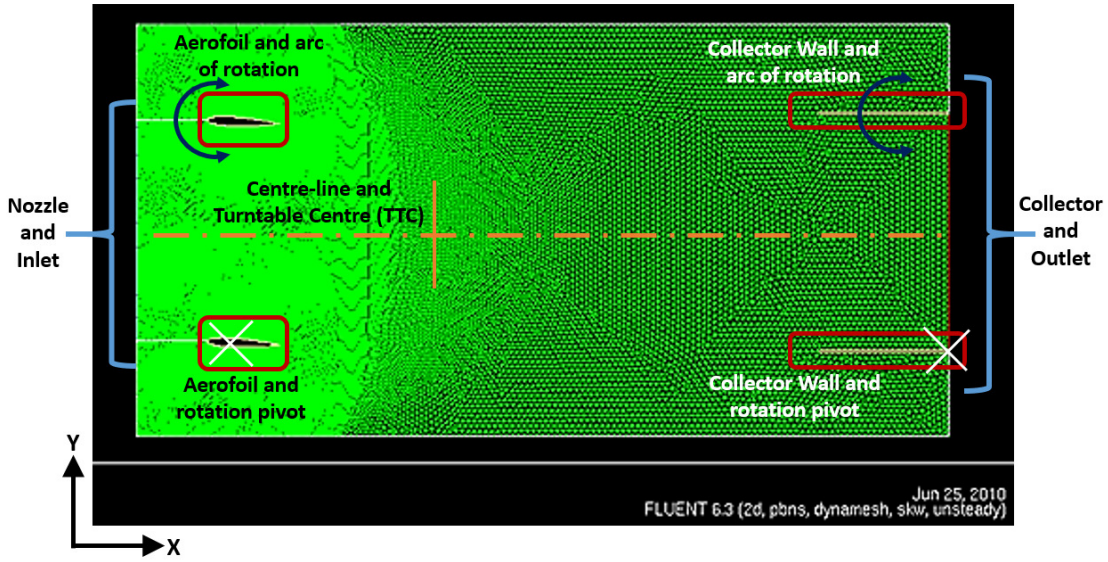


Figure 166 - Initial model of the TGS with moving inlet side aerofoils and collector walls

## 5.5 TGS 2D Results with Oscillating Front Aerofoils only

Tests were run with both the inlet aerofoils oscillating only to ±9°, the collector oscillating only and then the two working in conjunction with one another. Additionally static tests were conducted with fixed aerofoil angles. In initial scoping test cases, it was found that movement of the collector created large regions of recirculated air flow, with rapid yaw angle decay as the flow propagated downstream, though notable yawed flow was created. Due to the large regions of recirculated flow, a moving collector design was not investigated any further.

Tests with the front aerofoils, oscillating on their own and in phase, were completed. An assessment of the TGS performance was based upon the generated flow yaw angle around the aerofoils and whether the yaw sustained as it propagated downstream. Over the full range of frequencies tested a good flow yaw angle consistency was found, but peak yaw angles were low (<±4°).

It was found from the scoping tests that having 2-aerofoils on the nozzle edge is sufficient to cause the desired flow yaw. It was also found that oscillating the collector caused large regions of slow speed recirculation and required a large mass to be moved. It was therefore decided to drop the moving collector walls but keep the nozzle side aerofoils. Further, the mechanical complexity increases with the number of aerofoils used and a 2-aerofoil arrangement removes the need for aerofoils across the test section width, which eliminating the resultant wake over the model (except at extreme yaw

angles), making a 2-aerofoil set-up desirable. However, the results suggested a method to increase the peak yaw angle by allowing more air flow to enter and leave the tests domain at widths beyond the typical nozzle and collector widths.

## 5.6 TGS Design in 2D using Front Aerofoils only with Multiple Inlets and Outlets

In order to sustain the yaw angle and increase peak flow yaw angle as it flows downstream, the idea of additional inlets either side of the nozzle and outlets either side of the collector was proposed, which would also ensure that the nozzle's jet width could be maintained under yawed flow conditions. For example, incidence on the inlet aerofoils would enable inlets to open in the Y+ side of the inlet, and the collector exhaust outlets could be opened in the Y- side of the exhaust, (with the appropriate consideration to phasing and particle track time) which would encourage the flow yaw to be more uniform and sustained.

In static tests conducted in the scoping tests, it was found that yawed flow was forced to quickly return to an axial direction in order to flow into the collector, causing a rapid decay in yaw angle with downstream location. In order to create more sustained yaw, additional inlets and collector outlets were added to either side of the respective ends, as shown in Figure 167, which open in conjunction with the aerofoil oscillation to improve flow yaw consistency. As a development of the model's accuracy a large volume of air was placed upstream of the inlets to include the time required to accelerate the air flow when an inlet was opened. In comparison to earlier tests without the additional inlets and outlet, where the flow was found to have to turn dramatically to reach the collector, it was found that the flow did not have to turn at the downstream location to reach an outlet.

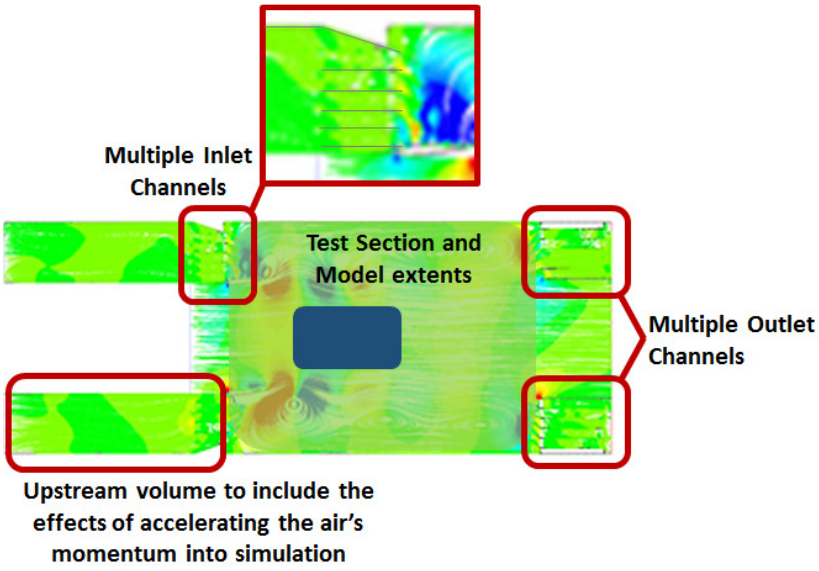


Figure 167 - 2nd model design with additional side inlet and outflow vents and front only oscillating aerofoils

The model has 5-inlets either side of the nozzle defined as a velocity inlet (of 25ms$^{-1}$) to match the nozzle's velocity. The other boundary conditions were maintained as in the first model configuration. To create the shutter action in CFD the 5-inlets are modelled as radiators using a 'UDF' (a small macro program) with their porosity switching at different aerofoil angles, depending on their lateral location. As such, as an initial design, at the instant when the aerofoil angle is at an angle of incidence that a particle track under yaw propagates to a lateral location at the collector which is beyond the width of the collector, the corresponding inlet and outlet shutter open.

This design would require very fast moving shutters on the vents, but is otherwise practical. Initial tests showed that the air flow had good uniformity (within ±1° of yaw) across the test section. The nozzle jet's width was maintained down the test section and the flow velocity at the turntable centre is at the freestream velocity, unlike the front aerofoil only test results where a velocity reduction was seen.

A series of frequencies were tested at 0.1, 1, 5, 10, 20 and 30Hz for the new multiple inlets and outlets model all with an aerofoil angle driving to ±9°. Measurements taken and presented are lines of ±Y at ±0.5m from TTC (located at X = 1.8m, Y = 0.0m) and lines of ±X at ±0.7m from TTC as well as X and Y axis lines centred on the TTC. The region bounded by these lines represents a region slightly greater than the plan-view size of a model that would be tested in Durham University's 2m wind tunnel. Figure 168 to Figure 171 show the yaw experienced at turntable centre, Y+ and Y- for the range of tested frequencies, showing a consistent peak yaw angle of ±6° achieved across the test section width for all frequencies tested. Yaw angles of 6° correspond to 10% turbulence intensity.

The only notable discrepancy is that at higher frequencies (i.e. 30Hz) the oscillations are sufficiently rapid that a consistent wave is unable to be maintained, however reasonable intensities are still created at what is a very high frequency of mechanical operation.

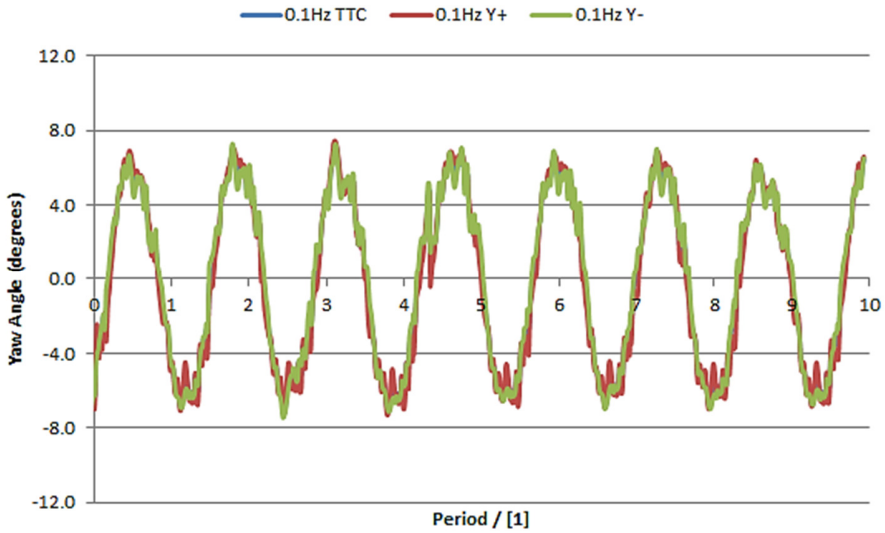


Figure 168 - 0.1Hz TTC, +Y and -Y plots, 0.1Hz at ±9° aerofoil angle yaw

Figure 169, Figure 170 and Figure 171 are the traces of the final few periods plotted for all cases, again with +Y and -Y corresponding plots. It is of interest to note the in-phase and amplitude correlation between the +Y and -Y limits, showing consistent flow yaw over the turntable area. At higher frequencies (20Hz and 30Hz), Figure 171, it is clear that the uniformity has decreased. This is most likely due to intermediate frequency (i.e. 1 - 10Hz) turbulence components occurring naturally in the tunnel superimposing with the high frequency air flow.

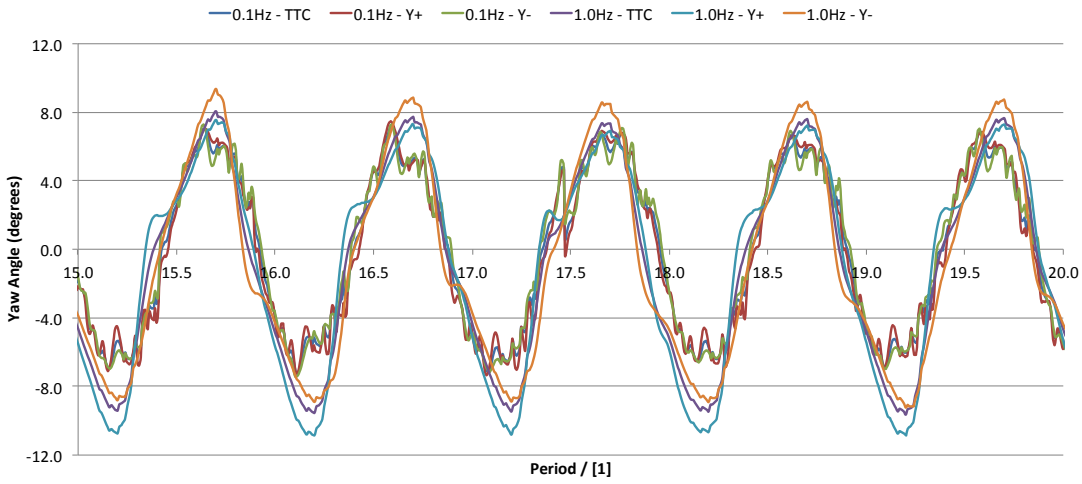


Figure 169 - Plots of all frequencies at TTC, +Y and -Y locations - 0.1 and 1.0Hz driving frequency at ±9°

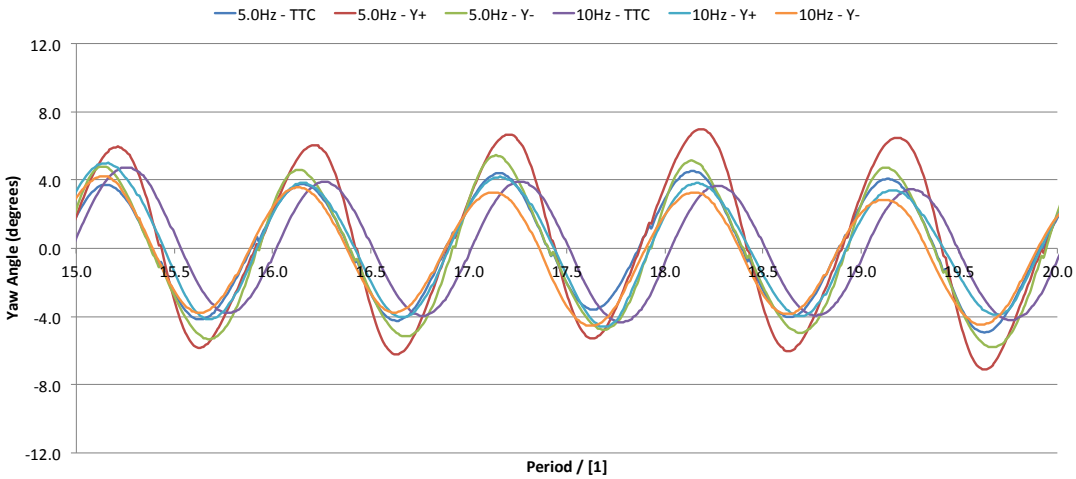


Figure 170 - Plots of all frequencies at TTC, +Y and -Y locations - 5.0 and 10.0Hz driving frequency at ±9°

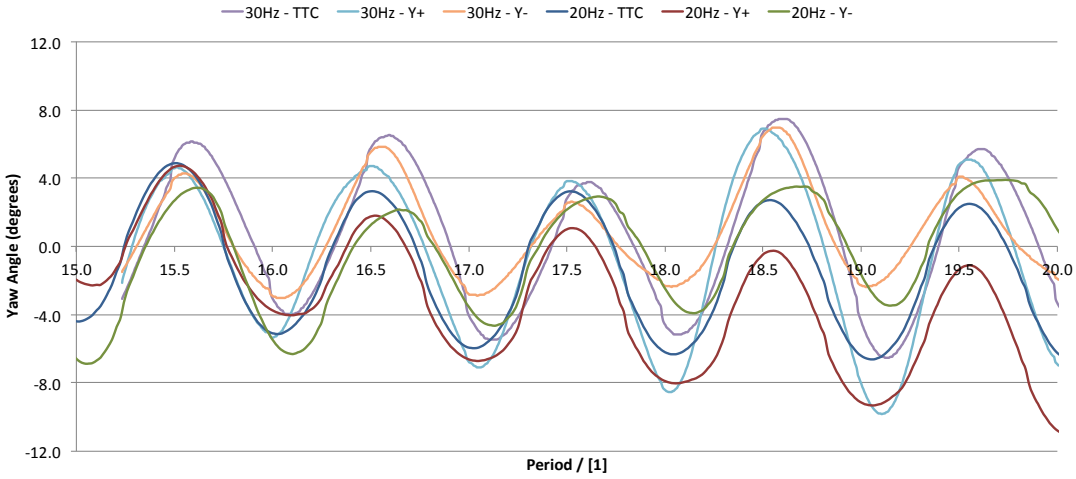


Figure 171 - Plots of all frequencies at TTC, +Y and -Y locations - 20.0 and 30.0Hz driving frequency at ±9°

Further analysis of the results from the flow simulations showed the induced flow yaw angles propagating downstream, demonstrating good yaw angle consistency, the jet's width being maintained and the flow not having to turn dramatically at the downstream end in order to flow into an outlet. Static and total pressures for the range of frequencies were assessed and good flow consistency over the test section and the yaw angles was achieved over a wide test-section width. Yaw decay rates were found to be low over the longitudinal axis and the no significant vortex shedding or other undesirable wake affects downstream of the aerofoils was found. Additionally, no large regions of flow recirculation were found suggesting general tunnel operating stability and a lack of large viscous-effects (i.e. pressure loss) in the system due to the TGS's operation.

The results show that the multiple inlet and outlet configuration offers a greater test section width and velocity uniformity as well as larger peak yaw angles and more consistent yaw as the flow propagates downstream than seen in the aerofoil only configuration, with yaw angles of ±6° were achieved. Figure 172 is a plot of the yaw amplitude range (maximum peak to minimum peak) and deviation of yaw for the spectrum of tests.

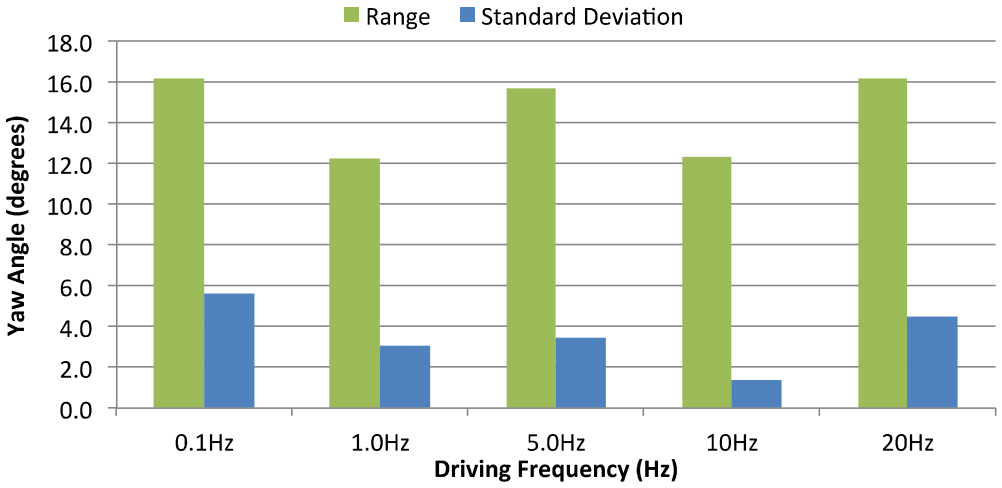


Figure 172 - TTC yaw angle variation over the tested frequency range

Figure 173 shows the range and average longitudinal velocity at the TTC for all of the frequencies tested. This result demonstrates that the reduction in flow velocity due to the TGS is not excessive, and that on average in the TGS operation, the reduction in tunnel velocity will be only 0.5ms$^{-1}$ caused by the varying inlet and outlet widths.

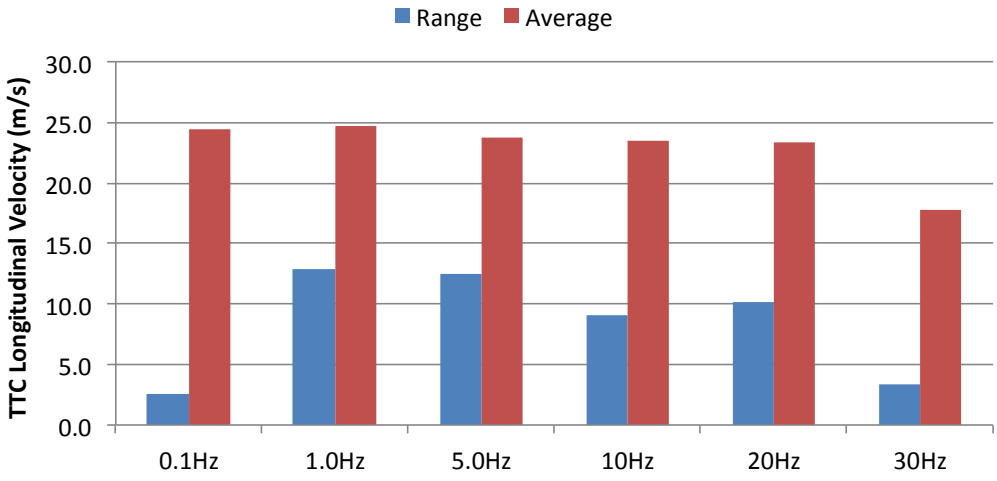


Figure 173 - All frequencies tested, TTC velocity range and average

Figure 174 shows the calculated turbulence intensities suggesting that, at the quasi-steady threshold frequency (5Hz at tunnel scale), the TGS generates high turbulence intensities and that the intensities generated are all sufficient to meet the TGS specification (i.e. 10%).

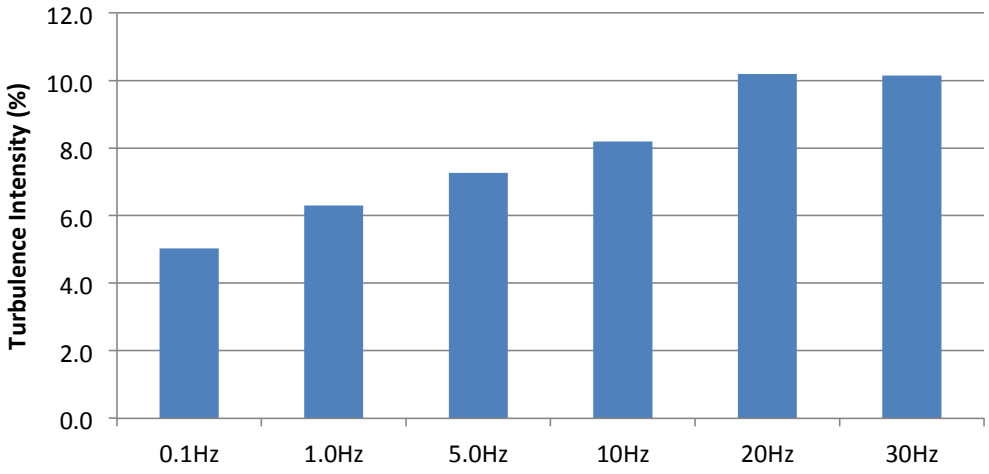


Figure 174 - All frequencies, auto-correlation turbulence intensities

## 5.7 Static 3D Model

The 2D CFD simulations that have been presented were completed to develop the initial design of a wind tunnel TGS system. It was found that aerofoils placed either side of the inlet nozzle, with additional inlets and outlets, when all operated in a co-ordinated fashion, would achieve the required TGS yaw range and flow uniformity.

In order to more fully understand the flows generated from the proposed multiple inlet\outlet and twin aerofoil TGS design, a 3D TGS design study using CFD simulations was then completed, being a steady flow simulation case with static aerofoils. Due to the high computational demands for 3D simulations, initial steady-state simulations were completed with the aerofoils at a peak yaw angle of ±9.0$^{o}$ inlet aerofoil incidence, with only the appropriate inlets and outlets open.

The tunnel set-up was as earlier experiments, with an axial velocity of 25ms$^{-1}$ of 0.02m TLS, 1% intensity turbulence at inlet. The measured aerofoil force data, with moments about the aerofoil's quarter-cord, were assessed and the generated aerodynamic forces were nominal and did not present a mechanical design challenge. Tests were also conducted at aerofoil yaw angles of 4.5$^{o}$. As a reminder, measurements were taken at lines of ±Y at ±0.5m from TTC (located at X = 1.8m, Y = 0.0m) and lines of ±X at ±0.7m from the TTC as well as X and Y axis lines centred on the TTC.

Figure 175 shows the normalised velocity magnitude by X-location, between the tunnel nozzle centre (distance 0.0m) to tunnel collector centre (distance 4.5m), which could vary due to the changing width of the jet. The turntable centre is located at 1.8m in X-location where the flow velocity is within 2% of the inlet velocity and good uniformity across the jet's width even with 9° of flow yaw.

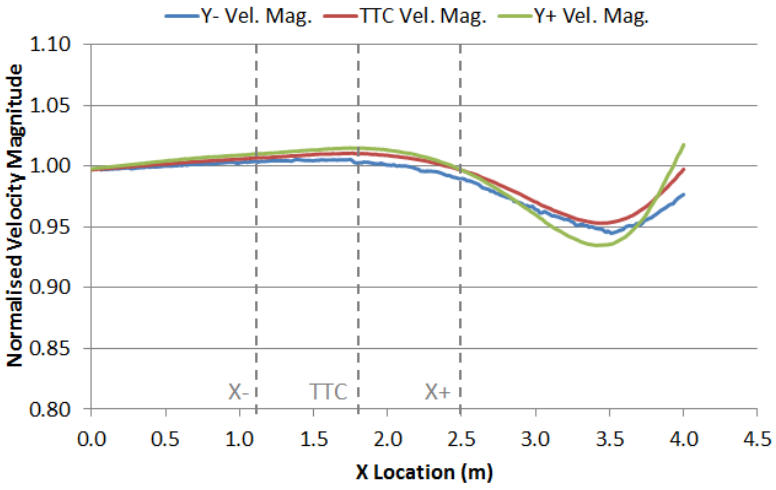


Figure 175 - Velocity magnitude against X-location for 9.0° case (normalised by freestream velocity)

Figure 176, normalised velocity magnitude by Y-location, shows good flow consistency across the jet's width with a useable (i.e. test vehicle) width of ±0.6m in the Y-axis (shown by the orange dashed lines). Due to the flow yaw a region of low speed flow is seen at the Y- extent of the jet (i.e. the beyond the shear layer), which is as expected.

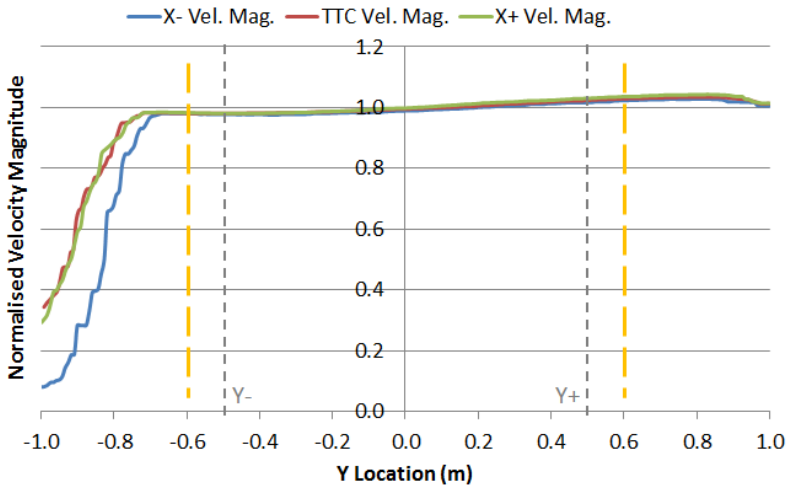


Figure 176 - Velocity magnitude against Y-Location for 9.0° case (normalised by freestream velocity)

Figure 177 shows a relatively consistent yaw angle of 7 - 9° down the length of the tunnel. Especially of interest is how the flow yaw closely matches the aerofoil incidence, which is expected in a static test case whereas the time-variant test cases showed achieved peak dynamic yaw angles of only ±6°. The variation around 2.0m is where the jet expands out between the nozzle and collector, before turning into the collector, and though noted is not a significant issue in the TGS operation mode.

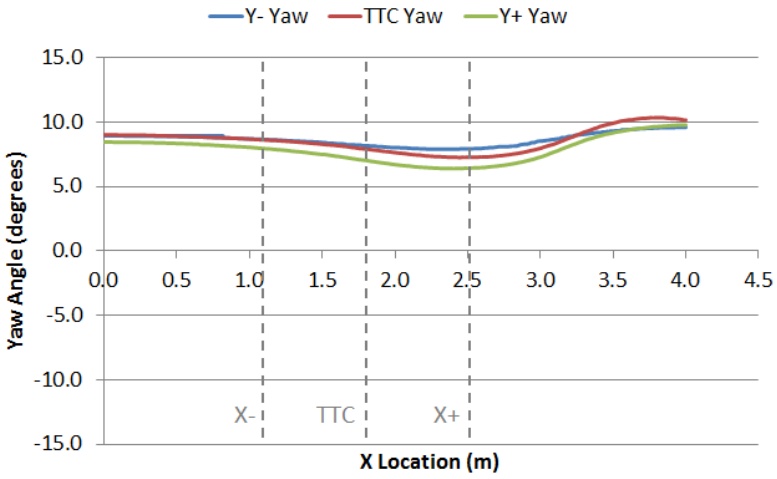


Figure 177 - Yaw angle against X-Location for 9.0° case

In Figure 178, yaw angle against Y-location, a consistent flow yaw across test section width is shown and the flow yaw is at values close to the aerofoil incidence. However, as seen in Figure 176, the region of a shear layer is noticeable at the Y- location. This graph also supports a useable test width of ±0.6m (shown by the orange dashed lines), though flow yaw would vary by ±1° across this width.

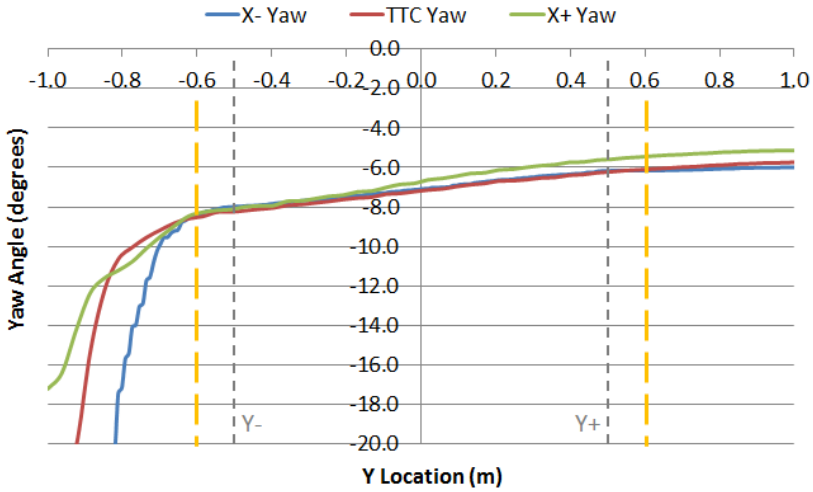


Figure 178 - Yaw angle against Y-Location for 9.0° case

Figure 179 shows a pathline plot, with the major features shown being the consistency of yawed flow over the test section, the yawed shear layer and the flow consistency in the region that the test model would be located.

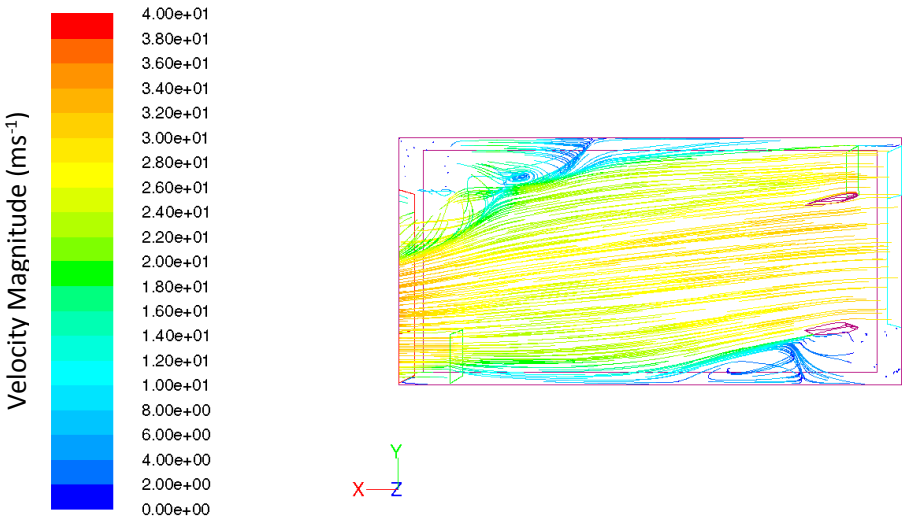


Figure 179 - Pathline plot, aerofoil at 9.0°, coloured by velocity magnitude ($ms^{-1}$) - plan view

## 5.8 TGS 3D Dynamic, Time-variant Model

In order to complete a true unsteady simulation, the TGS model was re-created in Exa Powerflow (4.3a) using a rotating mesh geometry for the aerofoils. The model was identical to the construction used in the 3D Fluent case, except, as the rotating mesh geometry had to be defined by a volume of revolution, the aerofoils were moved downstream approximately 0.2m, leaving a 0.1m gap between the trailing edge of the nozzle and the leading edge of the aerofoil. The aerofoils were, however, still pivoted about ¼ chord. All other parameters were identical, with a resolution of 220 voxels over the characteristic length of 5.1m (the nozzle to collector distance), giving a moderate mesh resolution of 20mm per cell. Simulations were run at 10 and 30Hz aerofoil oscillation rate, with approximately 300,000 time steps covering 8-seconds of flow. To reduce processing run-times by initialising cases with a developed flow structure, cases were seeded with a static case (i.e. no aerofoil oscillation) that had run for 10-seconds of flow simulation. Data was recorded in a region around both the aerofoils to offer a force-time trace as well as recording flow parameters within the area that would encompass a model. Velocities were extracted from this region along the same axes as in the Fluent 3D case, and resolved to determine yaw angles in time.

Figure 180 shows an image of the case geometry.

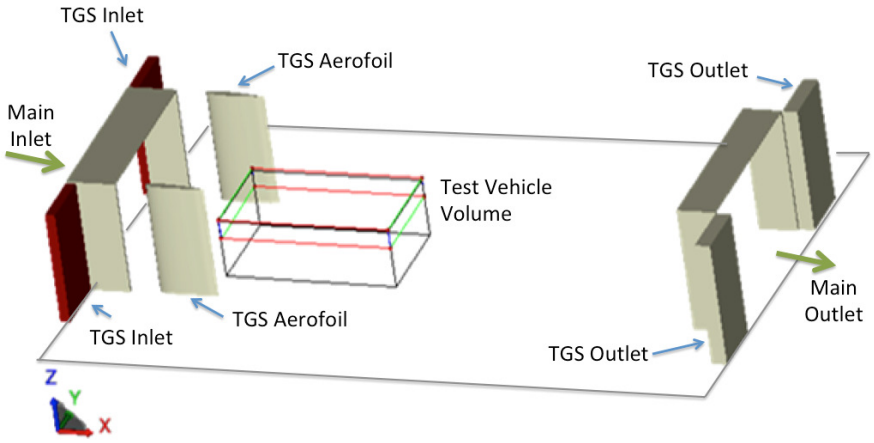


Figure 180 - 3D tunnel model for Powerflow simulation

### 5.8.1 Phasing Front Aerofoils with Additional Inlets and Outlets

In order to ensure that the additional outlets actuate in a coordinated fashion with the additional inlets to maximise flow uniformity and yaw generation, the phasing of the front aerofoils with the additional inlet and outlets requires careful consideration, particularly to factor for the particle track propagation time. When the front aerofoils and inlet and collector outlets oscillate, they need to do so out of phase to account for the time of flight through the wind tunnel. The condition of in-phase is defined as when the front aerofoil and rear collector width extents are angled to create the most direct particle track (i.e. the trailing edge of the front aerofoil and the leading edge of the collector extents are co-linear in the particle's track). Therefore the completely out-of-phase condition is when the front aerofoils are $180^{o}$ ($\pi$) phased (Figure 181), such that the front aerofoil's trailing edge is at, for example, the most negative yaw when the collector is at its greatest, for example, positive yaw (i.e. causing greatest flow yaw). The arrangement is identical if additional inlets and exhausts are considered, with the symmetrical shutter opening and closing at the same time for the in-phase condition and vice-versa.

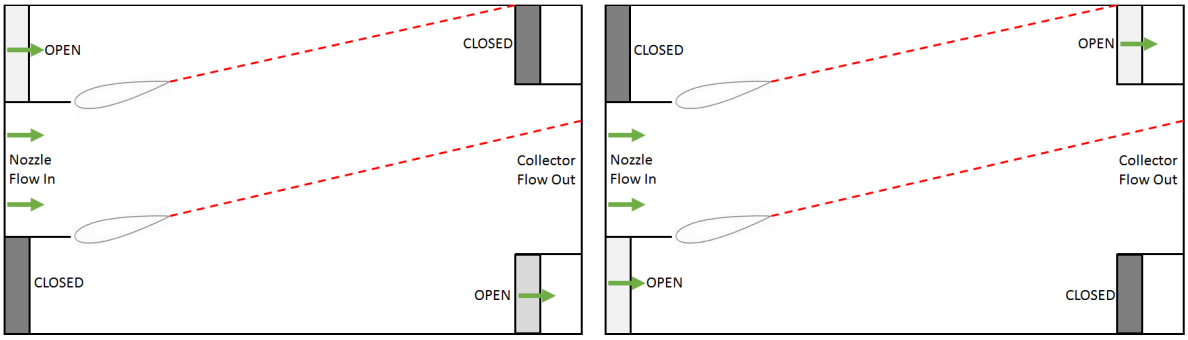


Figure 181 - Aerofoil to inlet and outlet phasing. 180° out of phase condition (left) and perfectly in phase condition (right)

However, this definition is simple if there is no time delay between a particle entering and leaving the test section. The test section was 5.1m long and the velocity inlet was set at 25ms$^{-1}$, which causes a flow time for a particle to be 0.218s. Therefore the sinusoidal phasing between the front and rear oscillations, at each frequency, were evaluated as:

$$\text{Phase Difference} = 2\pi(\text{Particle Flight Time (s)})(f) \quad [18]$$

where f is the aerofoil oscillation frequency. The necessary timing adjustments are made in the subsequent tests.

### 5.8.2 TGS 3D Model with Aerofoil Oscillations at 10Hz

Figure 182 shows the variation in flow velocity down the test section length. The flow velocity is acceptably consistent with velocities within ±1.5% across the height range of 1.0 - 0.5m. A slight velocity speed-up is seen at recording locations further above the tunnel floor, which was set as a fixed ground. All results are for an instantaneous snapshot as opposed to being averaged over a period. Measurements were taken at lines of ±Y at ±0.4m from TTC (located at X = 1.8m, Y = 0.0m) and lines of ±X at ±0.6m from TTC as well as X and Y axis lines centred on the TTC. Note that the three lines on the graphs now presented represent heights as opposed to in the 2D results where they represented width-wise locations. Where expressed, low, mid and high measurement locations were at 0.1, 0.3 and 0.5m in the Z-axis respectively.

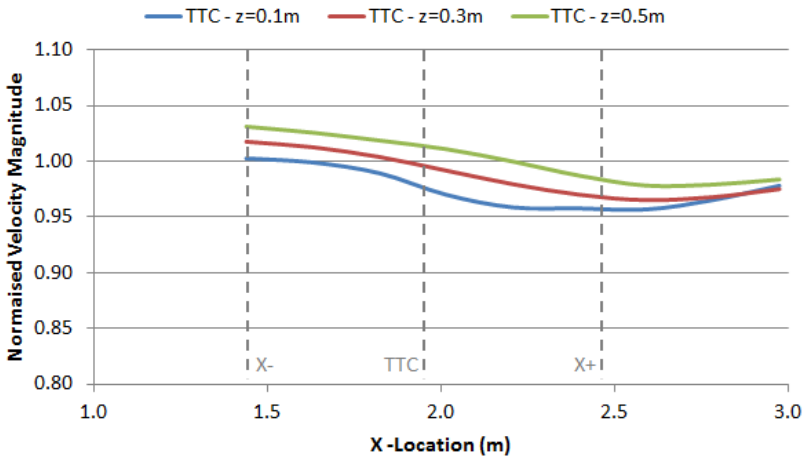


Figure 182 - Normalised instantaneous velocity magnitude against X-location for 10Hz case at a discrete timestep for Y=0m

Figure 183 shows the velocity variation with tunnel width (Y-axis) taken at turntable centre (TTC). The velocity does show a variation but is relatively consistent, and certainly the difference in velocity magnitude between the height levels is comparable to the variation over the tunnel width. The difference is due to the diagonal yaw of the shear layer in the tunnel, and this effect, if found to be important, could be mitigated by running the rolling-road. The asymmetric nature of the plot is because this is an instantaneous result from a dynamic system. Therefore, though there is zero yaw on the aerofoils, there is hysteresis in terms of yawed flow. If the result was taken at 180° of aerofoil phase, the mirror image about the graph's Y-axis would be seen.

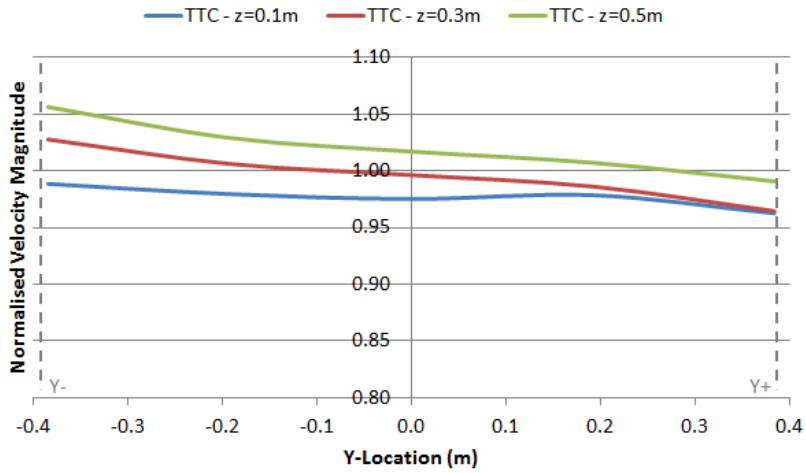


Figure 183 - Normalised instantaneous velocity magnitude against Y-location for 10Hz case at a discrete timestep for X=1.8m (TTC)

Figure 184 shows a large yaw angle variation with tunnel longitudinal location and of note are the lower yaw angles generated than in the steady-state case. The plot shows that at the moment captured the TTC experienced zero yaw as the sides of the jet were correspondingly experiencing greater magnitudes of yaw. This can therefore be visualised as the yaw propagating down the test section, nozzle to collector, as the aerofoils oscillate, and hence the peak values in Figure 185 will be the actual yaw and corresponding turbulence intensity generated.

The variation in yaw at the three heights is acceptable, particularly as a model would exist in the sub-0.3m height range where yaw variation is approximately ±0.5°.

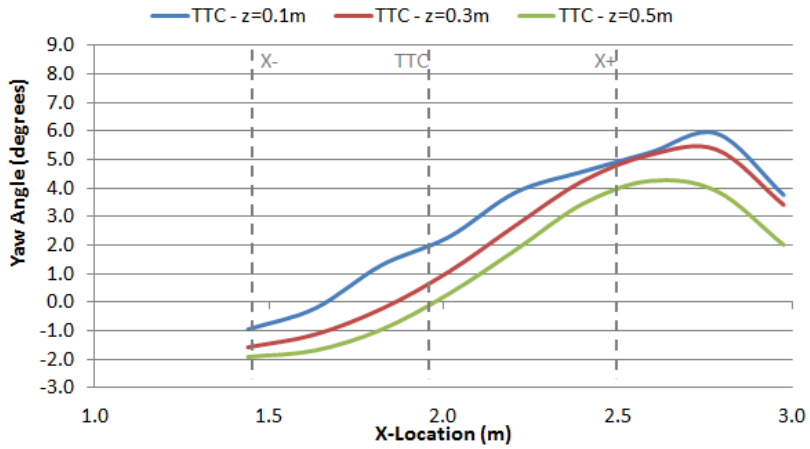


Figure 184 - Yaw angle against X-location for 10Hz case - snapshot at peak aerofoil displacement at Y=0m

An important result from the lateral yaw trace is what peak yaw angle was achieved and its uniformity over the jet's width. In order to determine the true peak angle, the X-location offering the greatest peak angle results from Figure 184 was used and re-plotted against Y-location at the three measured heights. The peak yaw angles were achieved at X = 2.8m, with the corresponding results shown in Figure 185, where 6° of yaw was achieved at TTC. Yaw uniformity is moderate with height, within ±1° between Z = 0.1 – 0.5m, and within ±0.5° over a typical over a typical model's height range of Z = 0.1 - 0.3m. The variation in yaw over the width is worth noting and is due to the aerofoils being at the nozzle sides, therefore the flow is least yawed furthest from the aerofoils (i.e. at the centre of the jet).

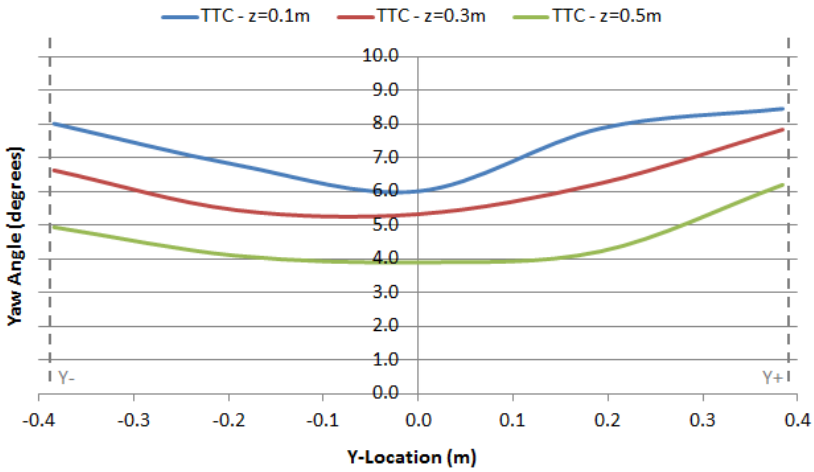


Figure 185 - Z-axis constant yaw against Y-location (at X=2.78m) for 10Hz case

Pitch variations were assessed, though not shown. Pitch angles were all acceptable but did suggest that the inclusion of a horizontal aerofoil at the top of the nozzle for pitch corrections, as well as adding an extra axis of turbulence generation, would be of value.

Table 8 reports the force loads experience on the aerofoils during the test cycle. The forces are all of an acceptable magnitude, (100 – 200N) and should not propose significance mechanical issues during operation.

Table 8 - Aerofoil force results for the 10Hz case

| | Average Aerofoil Force | | |
|---|---|---|---|
| | **X (N)** | **Y (N)** | **Z (N)** |
| **Average:** | 91.7 | 60.6 | -0.8 |
| **Std. Dev.:** | 24.1 | 55.0 | 1.7 |
| **Max:** | 191.2 | 224.6 | 3.4 |
| **Min:** | 6.1 | -113.8 | -6.5 |

Tests with the aerofoils oscillating at 30Hz were also undertaken, but it was found that at this higher frequency the aerofoils were moving at such a rate that the air flow was unable to be fully turned during each cycle, and therefore the quality and uniformity of yawed air flow was notably less than at 10Hz. Also, from the on-road conditions reviewed and the specification of the TGS detailed at the beginning of this chapter, oscillation rates greater than 10Hz are not necessary to model on-road effects (i.e. lower spectral energy in the on-road environment at such a frequency). Consequently the results have been omitted.

## 5.9 TGS 2D and 3D Model CFD Simulation Conclusions

Initial scoping CFD simulations of a static 2D model found that using a moving collector to encourage yawed flow caused large regions of recirculation. The tests did show that flow yaw angle was periodic with aerofoil oscillation rate and that other frequencies of yaw angle variation did not become dominant in the test section. The scoping tests did show, however, that two aerofoils placed at the nozzle sides could generate yaw up to ±4$^{o}$ with acceptable lateral uniformity, but an unacceptable yaw decay rate with longitudinal location. From this a 2D CFD static model was tested with additional inlets and outlets placed adjacent to the nozzle and collector, respectively. The results from these tests showed an increased peak yaw angle of ±6 - 8$^{o}$ with notably better yaw angle uniformity both longitudinally and laterally.

Tests were conducted with the multiple inlet and outlet model at frequencies ranging from 0.1 - 30Hz, with acceptable yaw angles generated over the entire frequency range. No regions of flow recirculation were found and hence the design was further analysed using a 3D simulation model. Static 3D simulations in Fluent of the TGS multiple inlet and outlet design showed achievable yaw angles up to ±6 - 8$^{o}$ and acceptable flow uniformity both longitudinally and laterally throughout the tunnel's test section. Yaw variation of less than a ±1$^{o}$ was found over a test model's plan-view area and velocity magnitude decay was nominal across a model's width. The 3D TGS model was then designed in Powerflow and a transient simulation was completed, running at 10Hz and ±9$^{o}$ of aerofoil angle. Flow yaw angles of up to ±6$^{o}$ were generated, again with acceptable flow uniformity throughout the test section.

The tests showed that the yaw angle will propagate downstream for a large distance if additional inlets and outlets exist, but that without these the yaw angle of the flow will simply follow a bowed path through the test section. Higher frequency tests (>10Hz) showed poor flow uniformity with the aerofoil oscillation rate being beyond the limit of the momentum required to deviate the air flows' path. At higher oscillation rates a decrease in peak yaw angle was shown (but up to 10Hz is still suitable for the length scale and intensity targets suggested). This outcome suggests that the TGS design should focus on higher peak aerofoil angles (i.e. 15$^{o}$) at 10Hz as opposed to higher aerofoil oscillation rates. The simulations demonstrated that static simulations will show approximately a 1.0 : 0.9 ratio between aerofoil angle and flow peak yaw angle, whereas the dynamic simulations typically showed a ratio near 1.0 : 0.7. This ratio suggests that an aerofoil amplitude of 15$^{o}$ would yield a flow yaw angle in the

region of 7 - 9$^{o}$ at the model's location (i.e. approximately 60 - 70% of aerofoil angle), for frequencies up to 10Hz, though the peak yaw angle will vary with aerofoil oscillation rate.

In review, therefore, the CFD results offer confidence in the proposed TGS design and though the final flow yaw angles are not as high as desired, the angles would be suitable for the design of a TGS able to recreate real-world on-road flow conditions in a test environment.

# 6. TGS Mechanical Design

## 6.1 Overview

This chapter specifies the operation of the TGS system and the development of its mechanical specification. The installation of the TGS system was a large project undertaken over a year of time including several months for its installation and commissioning. The aerodynamic development and mechanical design of the TGS was undertaken as part of this thesis, with an external contractor, Labman, constructing and installing the system at Durham University. The specification for the design given to the external contractor is presented Appendix 2. The system can provide consistent test cycle conditions in air flow speeds of up to $35ms^{-1}$ and with the ability to run (with regular and thorough maintenance) for extended durations (i.e. hours). The system's aerodynamic capabilities are investigated during the Commissioning study, Chapter 8.

The turbulence generation process is performed though the interaction of three 0.6m chord length, NACA0012 aerofoils of 1.1m in length, two imposing yaw and one imposing pitch. Each unit was bespoke to actuate force in the form of programmable oscillatory motion. Sets of shutter valves operate in conjunction with the aerofoils to control the inlet (five shutters) and outlet area (four shutters) of the wind tunnel working section. These shutters operate to achieve rapid increase and decrease in flow area of the inlet and outlet, each independently controlled for either side of the wind tunnel. Two additional sets of shutter valves create a controlled change of area in the rear collector.

The system was installed as a permanent feature in the 2m wind tunnel at Durham University, of which the base design is shown in Figure 186. The 2m wind tunnel at Durham University is a $^3/_4$ open jet tunnel with a total length of approximately 20m, with further details of the original tunnel design given in Sims-Williams (2002). The inlet nozzle has a contraction ratio of approximately 4:1, excluding the bellmouth. The 5.5m long test section jet has a cross sectional area of $2m^2$ (aspect ratio 1.5 : 1.0) and the tunnel operates at speeds up to $30ms^{-1}$. At the end of the test section the collector directs the flow into the two main diffusers, which feed into a fan chamber consisting of two fans totalling 130kW in power. These exhaust vertically via two exhaust diffusers.

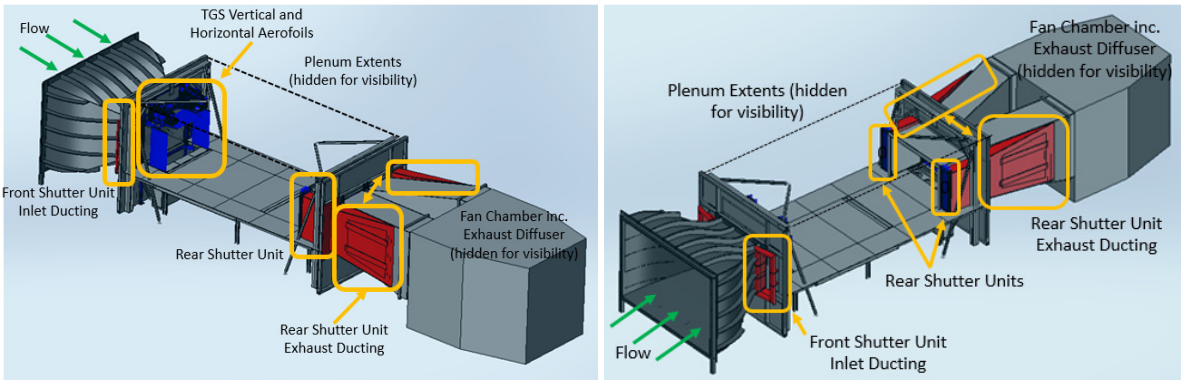


**Figure 186 - Perspective view of TGS ducting in red with the TGS device in blue (plenum chamber omitted for clarity)**

Laterally and horizontally mounted aerofoils of the TGS provide oscillatory forces, which act to modify the air flow through the wind tunnel, creating variable angles of yaw and downwash throughout the length of the tunnel. The controlled interaction of the TGS components across a range of programmable frequencies, phases and amplitudes creates variations in the dynamic flow yaw angle. Flow control relies on the conversion of rotary motion to oscillatory motion via two servo motors per aerofoil. The whole TGS is powered by a single 15kW supply.

Additionally a series of shutter units (Figure 187) mounted at either side of both inlet and outlet regulate air flow into and through the wind tunnel. Testing was successfully carried out to validate the applicability of rotary solenoid actuation on the shutter valves running up to 10Hz. In the design, careful attention was paid to the response times achievable for the high torque, high inertia characteristics of the shutter application. The additional inlet shutters are incorporated into the design such that the overall jet width, when viewed in plan, is maintained even when the air flow is yawed (otherwise the effective jet width would decrease with flow yaw angle).

The main collector mounted shutters (called the longitudinal shutters) cause the flow through them to accelerate and retard as they open and close due the consequential change in the collector flow area. As the lateral aerofoils yaw the inlet flow, the two shutter units of five (inlet) and two units of four (outlet) shutter valves open and close in a programmable, cascading motion, matching the frequency and phasing of the aerofoils, maintaining the ratio of inlet to outlet area.

Interlocks and over-load monitoring ensure safe operation the system and maintenance was designed to be minimal, with only pre-operation checks required. All drive components (i.e. each solenoid and motor) can be controlled independently and each has a dedicated channel from the system's

programmable logic control system (PLC). The system is controlled via a desktop PC using bespoke software coded in Visual Basic.

The tunnel-floor standing TGS is fully integrated into the current wind tunnel at Durham University and is mounted on a separate frame to minimise vibration transmission from the system to the wind tunnel structure to protect the integrated and sensitive measuring equipment.

## 6.2 TGS Hardware Overview

The TGS consists of the following, fully integrated key components:

- Two laterally mounted NACA0012 profile, 0.6m chord, 1.14m height, aerofoils capable of variable amplitude oscillation from 0 to ±15$^{o}$ at a frequency variable up to 10Hz.
- A single horizontally mounted NACA0012 aerofoil capable of variable amplitude oscillation from 0 to +30$^{o}$ (i.e. to generate downwash only) at a frequency variable up to 10Hz, having a height of 1.14m and a chord of 0.60m.
- Two sets of inlet shutters comprising five shutter valves, each capable of achieving a 0 - 90 (manually variable) - 0 degree rotational actions at frequencies up to 10Hz. Shutters are 0.06m wide, 1.14m tall.
- Two sets of exhaust shutters comprising four shutter valves, each capable of achieving a 0 - 90 (manually variable using an adjustable stop limit) - 0 degree rotational actions at frequencies up to 10Hz (i.e. complete cycle within 0.1s). Shutters are 1.20m tall, width 0.06m.
- Two sets of collector shutters comprising two shutter valves, each capable of achieving a 0 - 90 (integrated) - 0 degree rotation at frequencies up to 8Hz. Actuation of these shutter valves causes a reduction in collector area of up to 40%. Shutters are 0.12m in width and 1.20m in height.

The aerofoils were manufactured from a moulded carbon-fibre shell to the NACA0012 profile with internal carbon-fibre tooling section providing additional strength and rigidity. Carbon-fibre end plates provide a suitable mounting structure for the required shafts and drive train interface components and an internal and external ‘top hat’ layering of the carbon-fibre over the end plates ensured high inertial loading resistance. The aerofoils’ mass and moment of inertia were minimised to ensure that the maximum oscillation frequency was achieved. An over-view of the TGS hardware is shown in Figure 187.

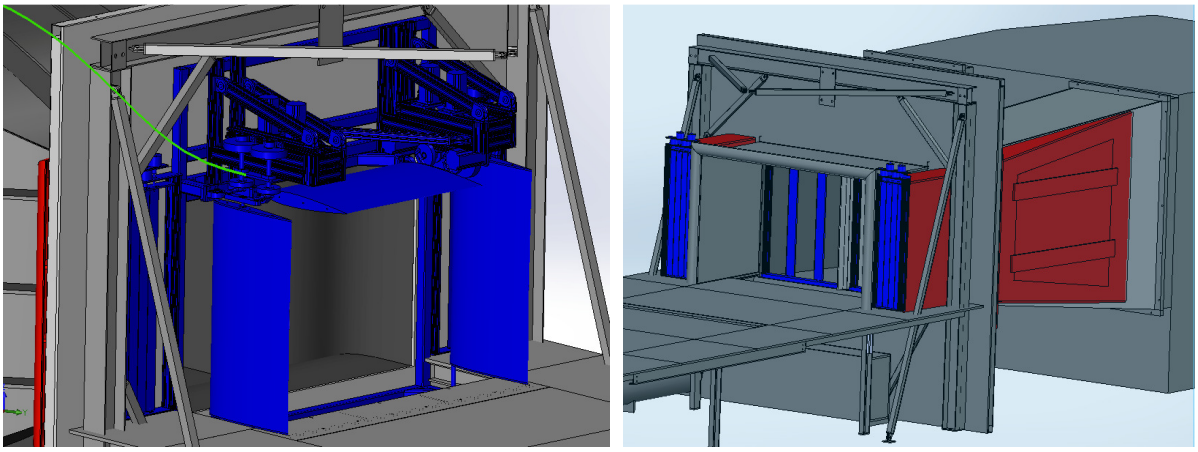

Figure 187 - TGS aerofoil and front shutters (left) and rear shutters and longitudinal shutters (right) with respective ducting shown in red (plenum not shown for clarity)

## 6.3 Oscillation Control

The motor linkage (Figure 188) achieved some key operating requirements:

- The variation of the frequency of each motor, when in constant phase, controls the aerofoil oscillation frequency.
- The variation in phasing of each motor controls aerofoil peak angle.
- The motors can operate in a continuous rotational motion, reducing peak torque and power.
- The configuration allows arbitrary motion through programming one or both servo motors.
- The linkage configuration allows sinusoidal aerofoil motion with real-time frequency amplitude and phase adjustments at large amplitudes and frequencies (i.e. not restricted by motor inertia when motors operate in a continuous, one-direction, motion).

Two, 2kW motors move each aerofoil, each motor powering a separate shaft, turning a set of circular discs with eccentrically mounted connecting rods. These are connected by rods to a rectangular bar near the middle right of the aerofoil, which is pivoted at its centre, and therefore only has this one-degree freedom of movement. The mechanism is shown in Figure 188 and Figure 189, where the two motor cranks rotate simultaneously.

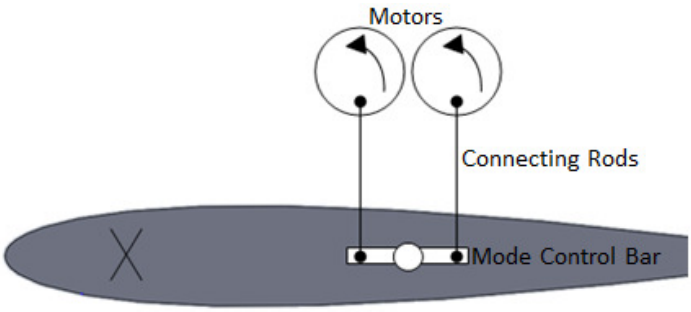


Figure 188 - Simplistic plan view of an aerofoil with its dual motor linkage to control peak angle and oscillation rate via motor frequency and phasing

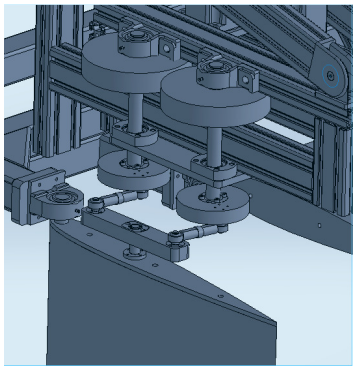

Figure 189 - Dual-motor linkage system as installed

Through this mechanism, essentially 4 operating modes exist:

1. Both motors operate at the same, constant speed but at different phase separations allowing variable amplitude sinusoidal motion. This mode achieves the largest aerofoil accelerations (amplitude and angular velocities) as motor rotational inertia does not have to be overcome.
2. The two motors operating at different speeds, allowing two harmonic frequencies to be superimposed.
3. One motor operating at constant speed allowing large amplitude, high frequency oscillation while the second motor can simultaneously provide a superimposed programmed motion (i.e. second crank not operating in full revolutions).
4. Both motors operating in an arbitrary motion (i.e. cranking backwards and forwards), driving any arbitrary motion of the aerofoil, subject to the acceleration limits that can be achieved by the motors.

All control is through an Ethernet interface to the PLC control unit that operates on a 4ms clock (i.e. each command is updated every 4ms). The TGS software is used to control, synchronise and vary the phase and speed of the six motors, providing motion of the aerofoils. Within the control framework, the motors can be programmed to create a range of constant and arbitrary motion profiles and the software provides synchronised actuation commands to the PLC to activate the shutter valves correspondingly with the motion of aerofoils. This also ensures that the shutters can operate in a cascading and velocity-phased motion, aiding flow uniformity and maintaining yaw between the nozzle and the collector.

## 6.4 Inlet and Exhaust Shutters

The shutter units, shown in Figure 187 and Figure 191, are individually actuated by a high torque rotary solenoid controlled by individual input and output ports of the control system. Shutters are housed as a unit within a rigid frame, which is damped from the external structure through vibration mounts, fixed to a secondary, rigid frame. The carbon-fibre shutter flaps provide lightweight, rigid bodies with low inertia. Actuation of the shutter valves is provided through rotary solenoids with each shutter valve actuated by its own solenoid.

## 6.5 Shutter Frequency Response

The closest reproducible response square wave output by the shutter units, under the solenoid actuation at the highest frequency of 10Hz, provides a response demonstrated (as a guide) by the computer generated trace shown in Figure 190. This response was achieved continuously in testing and provides a minimum shutter-open time of 20ms when operating at 10Hz. At this maximum operating frequency the mechanical response is, effectively, a saw-tooth wave. Ideally, a square-tooth wave would have been achieved and the extent of the effect of instead having a saw-tooth wave at the highest operating frequencies is assessed in the commissioning study. Of course, at lower frequencies (and notably at frequencies below 5Hz) the wave profile is, from an aerodynamic perspective, square.

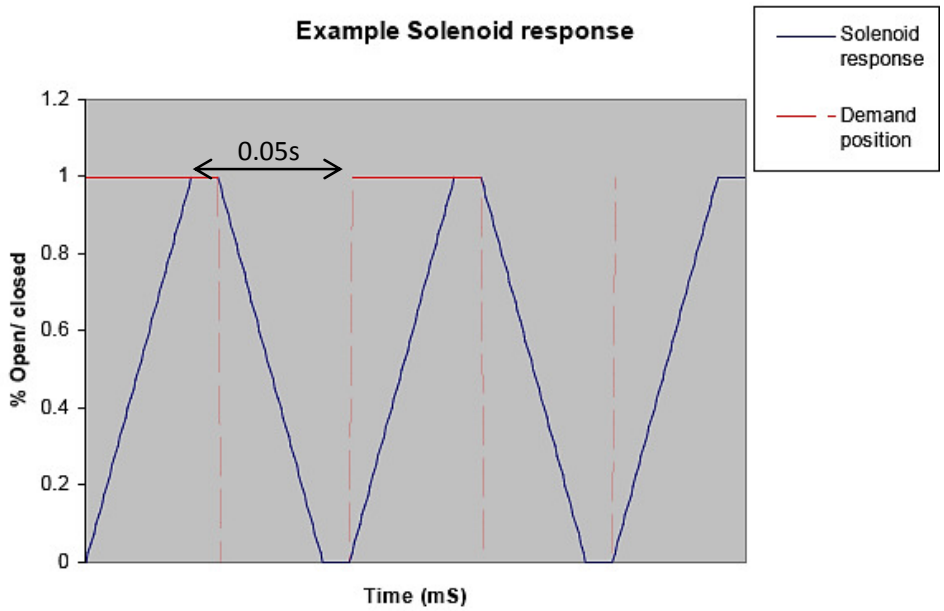


Figure 190 - Shutter solenoid example response. Note that the inflexion points are slightly rounded in actual operation due to the acceleration period of the shutter

## 6.6 Rear Collector Shutters

The rear collector shutters (which create longitudinal velocity pulsations) are manufactured to the same design as the inlet and exhaust shutters and mounted as two units, with two shutters per unit (i.e. 4 shutters in total). The shutters provide an almost saw-tooth response waveform (ramp open, ramp closed) as in Figure 190. When the collector shutters operate, a reduction in collector flow area occurs. The change in flow area happens more quickly than the fans can compensate, therefore an increase (and then decrease on opening of the shutters) of velocity in the wind tunnel occurs.

## 6.7 Software operation

The TGS control software uses a method of multi-axis control by emulating synchronised speed of each motor and shutter axis from a virtual master axis, allowing for a straightforward system control process. The operator sets the desired frequency of the master axis and then, through a user defined virtual speed ratio and phase, the control of the subsequent motors is determined. This virtual speed ratio mechanism allows the running of a multiple axes to create a range of chosen speeds, within the performance limitations of the TGS.

To synchronise the shutter control commands into the process, the software views the shutters as an additional set of axes to control, thus speed their operating rotational rates from the master axis. The control framework ties the inputs of the exhaust shutters to the corresponding inlet shutters, ensuring that the inlet and exhaust shutters on each side of the wind tunnel actuate in unison, with a phasing factor for the tunnel flow longitudinal velocity (i.e. time taken for air to travel the test section length). The rate of the shutter cascade can be geared to test cycle requirements whilst maintaining frequency synchronisation with the aerofoils.

## 6.8 Arbitrary Air flow Control

A key specification desire was to ensure that the TGS could create fully arbitrary motion, within the limits of the motors' power output. The TGS provides motion to produce test conditions in which the air flow is representative of dynamically variable length scale and intensity conditions. The arbitrary turbulence in the air flow can be created by the TGS through constant, dynamic variation of aerofoil oscillation amplitudes. Such motion is achieved, in one method, by the TGS through varying the speed ratio and phase between each of the two motors. This represents a programmed range of non-stop, dynamically varying amplitudes during the aerofoil oscillation operation. A second method of arbitrary

motion can be achieved simply by driving the motor cranks to differing angles at varying time intervals. A time against position input file defines the overall TGS motion.

## 6.9 TGS Ducting

Additional ducting was installed at the inlet and exhaust ends of the wind tunnel. Images of the installed TGS system are shown in Figure 191 and Figure 192, where the inlet ducts are presented sealed for non-TGS operation, which minimises any flow leakage.

The inlet ducting was kept as short as possible to minimise the inertia of the air in the duct, with as large a bellmouth as was feasible to pre-accelerate the air flow as much as possible. The rear auxiliary exhaust ducting is a section from the rear shutters to the tunnel diffuser walls (the rear shutter unit is located in line, in the X-axis, with the collector inlet). The flow is therefore maintained in the X-axis (i.e. no turn) until it meets the main diffuser, where it joins the flow of the main collector mass flow. The angle between the auxiliary ducting flow to diffuser flow is below $10^{o}$ to minimise viscous losses (i.e. flow turning angle when the flows meet). An actuated door is installed, which can be remotely controlled, to move between a TGS and non-TGS mode by sealing the main diffuser from the auxiliary diffuser where the two meet. From the tunnel rear wall to the main diffuser the contraction ratio of the auxiliary ducting is matched to that of the main diffuser contraction ratio, encouraging similar flow velocities (though this does, naturally, depend on the number of shutters open per side). No splitters were placed between shutters as with only a nominal gap between each shutter, flow leakage is nominal.

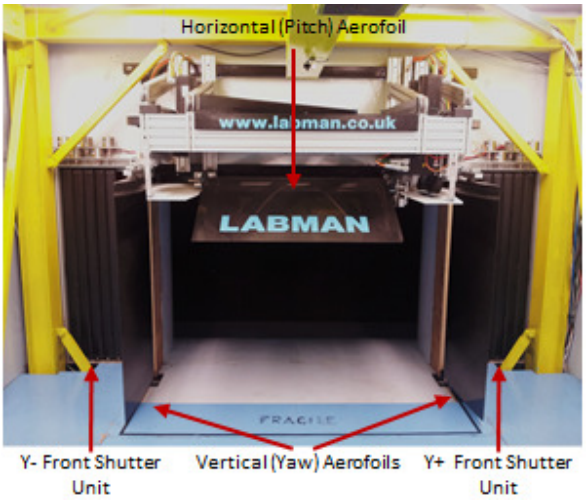


Figure 191 - TGS system installed into Durham University's 2m Wind Tunnel

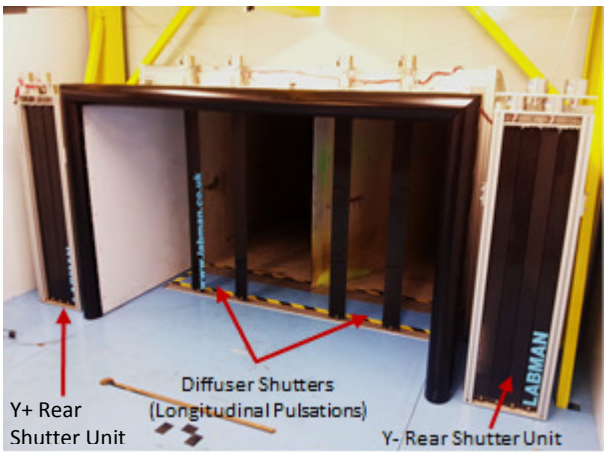


Figure 192 - Auxiliary inlet and exhaust ducting for the TGS shutters

As shown in Figure 193, the inlet ducts are sealed during non-TGS operation to minimise any flow leakage.


Figure 193 - Additional inlet and exhaust ducting to feed the TGS front and rear shutter units

## 6.10 Conclusions

This chapter details the mechanical considerations made for the TGS mechanical design and installation. The TGS system is capable of operating up to 10Hz with a ±15° with twin lateral yaw aerofoils and one horizontal aerofoil creating pitch. The system uses additional mounting frames and ducting to be fully integrated with the current wind tunnel installations, and allows a timely changeover between TGS and non-TGS test operations. A twin motor configuration allows real-time motor peak angle and phasing adjustments and solenoid operated shutter units at the test section inlet and outlet operate in a coordinated unison with the aerofoils.

# 7. TGS Arbitrary Mode Operation and Control

## 7.1 Overview

The TGS system is controlled through a PC Ethernet connection to a PLC that controls the servo motors and the shutter solenoid actuations. The control system use a virtual master axis that is defined by a rotational frequency and speed. From this master axis a speed ratio and phasing is defined to control each and every motor. As a pair of motors drives each aerofoil and the desired input is aerodynamic yaw data, and the desired output metric is simulated yaw angle in the wind tunnel, there was a segment of the control process that needed to be evaluated in order to optimise the use of the aerofoils. The considerations presented relate to arbitrary control of the TGS system (i.e. rapidly varying peak angles) as opposed to harmonic motion that only requires the motors' rotational speed and phase to be set once per test cycle. This chapter covers two main processes, the first to determine the best approach for controlling aerofoil angles and the second is the best approach for processing on-road data into TGS instructions. The key methods that are assessed are:

- Methods for controlling the TGS aerofoils in an arbitrary mode
- Methods for converting on-road yaw data into TGS aerofoil angle data

And for these methods, the key parameters that need to be established are:

- Motor rotational frequency, controlling time between yaw peak angles
- Motor-to-motor phasing on each aerofoil, controlling amplitude of yaw

In order to constrain the task, a few desirables were determined:

- The input to the control software would be at the start and end yaw angles, the start and end times of the motion and the initial position of the motors.
- All other factors, such as the physical limits of the system etc., would be constrained within the software.
- The software would need to determine the optimum phasing and speed of the motors to achieve the desired motion and that it would derive the motion and also determine shutter actuation from this.
- Ideally the motors would rotate continuously, without reversing, to minimise inertial loads.
- The software should be able to take high frequency on-road aerodynamic data and scale and resample this data such to be suitable for the software to generate TGS instructions.

- Output the final motion map to a comma-separated file suitable for reading by the OEM control software.

It should be noted that a simple program that can generate basic harmonic motion was supplied by the OEM, and was suitable for initial testing, but needs additional input to be able to generate representative on-road and multiple environment equivalent outputs (i.e. arbitrary motion). As mentioned in the previous chapter, arbitrary motion can be generated through frequency and phase adjustments, but also achievable by simply driving the motor cranks rapidly to differing angles. The considerations presented in this chapter relate to the challenges with both methods.

## 7.2 Direct Arbitrary Control Method

As a first stage of this process, a direct control model was created using only motor angle and frequency to reach target yaw angles. This is where the motors are set in phase and are simply rotated between $0^o$ and $180^o$ through the $+90^o$ side, but never above $180^o$ or below $0^o$. In this manner an aerofoil yaw angle (which is translated into a motor crank pivot average position) can be readily achieved by simply advancing or reversing the two motors to a certain angle position, with the time-period between each yaw angle determining the angular rate of rotation of the motors. The simplicity, though, is compromised because the motors therefore have to reverse and advance, which requires them to overcome the full inertial loads of the aerofoil mass and linkage system, limiting the peak oscillating rate and the high acceleration rates cause large structural loads. Additionally this method always requires 8 commands (2 phase and 2 speed commands for 2 motors), which could be reduced by pre-processing.

## 7.3 Phase and Frequency Control Method

### 7.3.1 Frequency and Phase Adjustment Constraints

The use of dual motors to control each aerofoil offers a unique set of challenges, namely that the motion is a sinusoidal combination of two motors. When considering moving from one angle to angle, the motors initially could be at any angle in their $360^o$ of rotation. Therefore both the phasing and speed of both motors must be considered to move an aerofoil between yaw angles within a fixed time period. As an introduction, an example is shown in Figure 194, demonstrating the effect on aerofoil angle if the two motors operating on one of the aerofoils in the TGS run at differing speeds and phase.

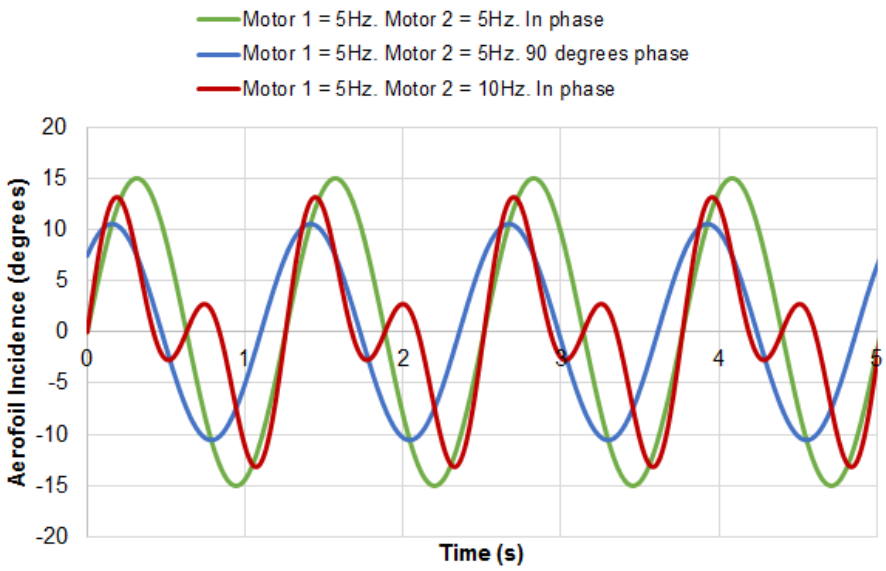


Figure 194 - Aerofoil motion for differing motor speeds and phasing

The first factor is that the PLC has an actuation time to implement a new control variable update (e.g. change gear ratio from 1 to 2, or change phasing from 0° to 90°), such that within one second of time around only 20 commands can be sent. Therefore, for example, if 2 aerofoils are being driven, and an actual change in yaw angle requires each motor to change both its speed and phase, then to change the yaw angle of 2 aerofoils could require 8 commands, hence only 2 - 3 updates may be possible within a second. It is therefore imperative to minimise the number of commands required by the PLC by determining the minimum number of operation commands required to fulfil an aerofoil motion change.

The key parameter to determine an aerofoil's start and end location is the average displacement of the pivot on the two motor cranks, as this determines the lateral displacement of the pivot on the aerofoil. If the motors are perfectly in phase then the maximum aerofoil displacement can be achieved and at 180° of motor crank phase, zero aerofoil displacement can be achieved. Hence, the achievable peak angle within a rotation of both motor cranks becomes a function of the initial motor-to-motor phasing. If the desired aerofoil yaw angle is achievable at the initial phase (e.g. if phased 90°, peak yaw angles up to approximately 10° can be achieved) then the motors can simply continue to 'roll-on' (i.e. just keep rotating) at their current phase to the next desired yaw angle. However, if the desired yaw angle is not achievable at the motors' current phase (i.e. at higher aerofoil yaw angles) then the phase between the motors needs to be changed. Once the phase is changed, the two motors can continue rotating to the desired angle. Finally, in order to control the time period over which a yaw angle

change is complete, a speed adjustment to the two motors may also be required. This process is detailed in Figure 195.

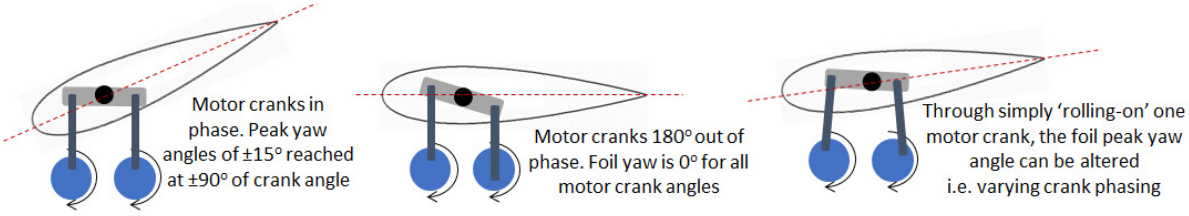


Figure 195 - Method of 'rolling-on' motor cranks and adjusting crank-to-crank phasing to control aerofoil peak angle

Such an approach, however, can cause the aerofoils to exceed the target peak angle in their motion between peak angles (i.e. kicking-out), as shown in Figure 196 (where the motor crank pivots are at their maximum and minimum displacement at +90° and -90° respectively). For example, if both motors are in phase and their current crank angle is 60°, the aerofoil will be at an angle of +8°.

If the next desired aerofoil angle is +6°, with motor rotation continuing in the same direction (to minimise inertial loading), the motor crank angle will increase from +60°, up to +90°, causing an aerofoil angle of +15° and then onto approximately +150°, which would achieve a resultant aerofoil angle of approximately +6°.

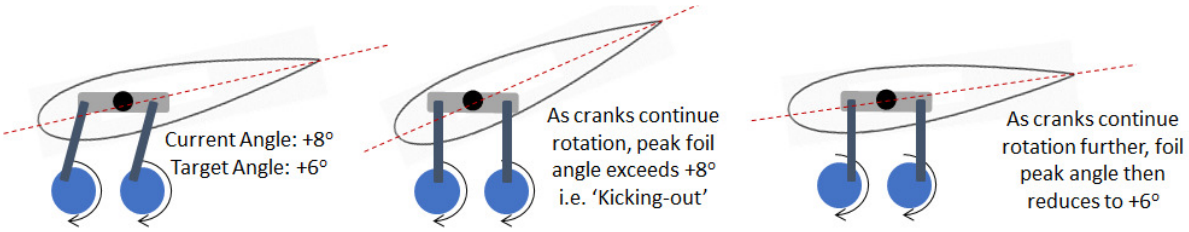


Figure 196 - Motor crank motion that causes a aerofoil to 'kick-out'

As such the actual aerodynamic yaw generated would not track between angles of, for example, +8°, +6°, but actually +8°, +15°, +6°. This 'kick-out' of the aerofoil is undesirable and can only be avoided by phasing the motors as opposed to just continuing their rotation. Therefore, if such an occurrence exists, it is better to achieve the target yaw by phasing the motors. Further, if the motor is to be both phased and rolled-on, the ideal option is to phase the two motors first, then roll them on to the desired angle.

It was therefore necessary to model how the phasing and frequency of the motors should be adjusted to move between peak yaw angles in order to select an optimum method. Once selected, the actuation of the shutters can be determined from the aerofoil's angle of incidence. In controlling the shutters,

the only parameter is at what aerofoil angle they should open and close. Incidentally, this consideration process is also valid for the horizontal aerofoil.

### 7.3.2 Aerofoil Motion Modelling

The process to model the optimum approach to adjust each motor is detailed in this section, using a known initial time and yaw angle and a target time and yaw angle, with a general overview of the process shown in Figure 197.

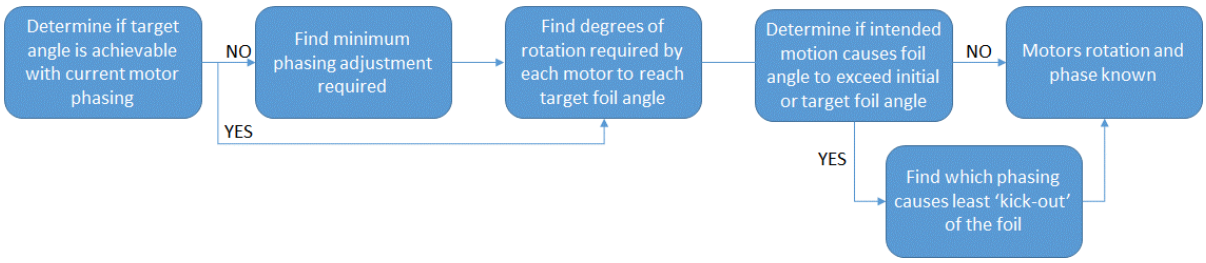


Figure 197 - Process map for TGS control using motor frequency and phase adjustments

Firstly, the start and end yaw angles are set and the motors cranks pivots' initial position are known (and may not be equal, i.e. not in phase). The peak angles achievable without further phasing the motors is then assessed by modelling rotating both of the motors through 360°. If the target peak angle is possible, then the result is output as a number of degrees to rotate both motors. However, if this peak angle cannot be achieved, the approach then considers phasing firstly motor 1, then independently motor 2, to see how far either motor needs to be phased before the peak angle is achievable through motor rotation. The outputs are the minimum phasing angle adjustment required and the angle through which each motor needs to rotate.

The second option, using phasing of both motors to move between yaw angles is assessed. The simplest way of finding the optimum phase options is to initially fix motor 1's crank phase, and rotate motor 2 crank though 360° and find if the required yaw angle is achievable from this motion alone. If not, then advance motor 1 by one degree and repeat by phasing motor 2 through 360° again. This thus assesses at most the 360 x 360 potential permutations of motor 1 to motor 2 phasing to find the minimum phasing rotation required of the two motors. The process then repeats the process using motor 2 as the principle motor. The output from this process is therefore 2 pairs of motor 1 and motor 2 phase angles. The algorithm picks the pair with the lowest standard deviation (as this is the pair that requires the least total movement split between the two motors) and outputs this result.

The time required between peak yaw angles is then used to determine the required rotational rate (i.e. frequency) each motor should complete the phasing and rotation adjustment stages. This

approach assumes a high rate of acceleration for each motor (i.e. nominal time to reach new rotational frequency). The approaches of changing aerofoil angle by rotation alone, rotation plus phasing or phasing alone are then compared and the option that requires the fewest commands (ideally with the aerofoil never exceeding the initial or target yaw angle) is selected.

## 7.4 Shutter Actuation Control

With the aerofoil motion determined, the shutter opening and closing against time profile is then evaluated. This is an assessment of the correspondingly aerofoil angle at which the shutters open and close. The process complexity depends on whether the aerofoils are moving from a positive yaw to a negative yaw or vice-versa, as the shutter behaviour varies between left and right shutter units. The rear units are simply follow the inlet shutter units, just with a time delay for the air flow to propagate through the test section. Therefore, at an instantaneous moment in time, 8 conditions exist depending on the direction of the aerofoil motion (i.e. decreasing in yaw or increasing in yaw) and whether the aerofoil angle is above or below the angle at which a shutter opens or close, as detailed in Table 9.

**Table 9 - Shutter actuation logic map. The start and end parameters being time, the closing and opening against yaw parameters being aerofoil angle.**

| Foil Yaw Angle Direction | Shutter to close based on foil yaw angle | Shutter to open based on foil yaw angle | Front Left Shutter | Front Right Shutter | Rear Left Shutter | Rear Right Shutter |
|---|---|---|---|---|---|---|
| Decreasing | No | Yes | Closed | Open | Open | Closed |
| Decreasing | No | No | Open | Open | Open | Open |
| Decreasing | Yes | Yes | Closed | Closed | Closed | Closed |
| Decreasing | Yes | No | Open | Closed | Closed | Open |
| Increasing | No | Yes | Closed | Open | Closed | Open |
| Increasing | No | No | Closed | Closed | Closed | Closed |
| Increasing | Yes | Yes | Open | Open | Open | Open |
| Increasing | Yes | No | Open | Closed | Open | Closed |

Through evaluating at which aerofoil angle a shutter should open and close, a time against trigger profile can be generated. After this analysis, the results are saved into a comma-separated file for upload to the PLC. The parameters set the speed and phasing of each motor at a time in milliseconds, the peak acceleration rates of the motors and the angle at which the shutters open and close based upon the virtual master axis.

## 7.5 Processing On-road Yaw Data for TGS use

In order to process on-road yaw and pitch data into aerofoil yaw angles, the on-road data needs to be simplified such that it is suitable for analysis. A flow diagram of this process is shown in Figure 198.

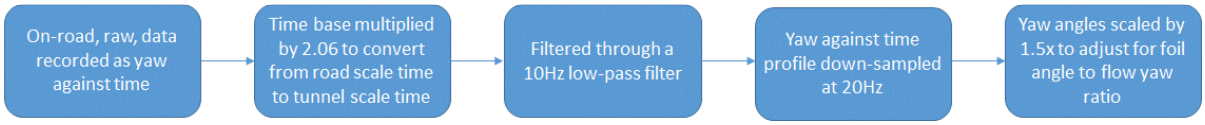


**Figure 198 - Process for converting on-road yaw measurements to a TGS yaw against time profile**

Firstly the on-road data file was converted from 'road time' to 'tunnel time', that is both factoring that the tunnel runs in TGS mode at 25.0ms$^{-1}$ as opposed to the recorded road speed of 30.9ms$^{-1}$ (69mph from the on-road study), which results in turbulence wavelengths lengthening by a factor of $^{30.9}/_{25.0}$ = 1.23, but also that the wind tunnel model is 40% scale, which shortens the equivalent wavelength by a factor of $^{1.0}/_{0.4}$ = 2.50. Thus the resultant scale factor is $^{2.50}/_{1.23}$ = 2.06. As such the 32-second on-road data sample is rescaled to approximately 16-seconds.

The second stage of the process is applying a low-pass filter to the road data, as the road data contains a wide range of turbulence frequencies, but the TGS can only generate frequencies up to 10Hz. To correct for this, a 10Hz low-pass filter is applied (i.e. a square edged filter, with some blending at the cut-off frequency to avoid inducing a high frequency from a sharp cut-off). This process assumes that sine waves are being generated, yet the TGS could generate a saw-tooth wave at 10Hz which would have energy at frequencies greater than 10Hz. However, the aim of the process is to minimise the high frequency yaw changes that the TGS cannot replicate, and contain less energy on-road but would confuse the process of generating a TGS yaw against time trace.

The data is then down-sampled from its recorded rate of approximately 1,000Hz (at 'tunnel time' scale) to 20Hz. Note that this sampling rate is double the TGS maximum oscillation rate (i.e. Nyquist sampling) to avoid further sampling issues. A linear interpolation method is used to evaluate yaw (and pitch) values where the precise tunnel-time falls between the on-road recorded time intervals. This gives a flow yaw against time profile, which has to be scaled upwards by around 1.5 to factor in the admittance between aerofoil angle and subsequent flow yaw angle. Finally the aerofoil angles then need to be converted into motor crank angles, through straightforward trigonometry, for the input data file of the TGS control software. To determine the aerofoil displacement from the motor crank angle, the following equation can be used:

$$\text{Foil Angle} = \tan^{-1}\left(\frac{\overline{l_1 + l_2}}{L}\right) \text{where } l_1 = r_1 \sin(\theta_1) \text{ and } l_2 = r_2 \sin(\theta_2) \qquad [19]$$

where $l_1$ and $l_2$ are the displacements of the motor crank pivots, $r_1$ and $r_2$ are motor 1 and 2 crank pivot radius (≈ 55mm) and $\theta_1$ and $\theta_2$ are the motor 1 and 2 crank rotation angles, respectively, and L is the aerofoil pivot to motor connecting bar pivot distance (≈ 205mm).

This process of re-sampling gives a true image of the yaw against time trace that the TGS could potentially replicate (ignoring mechanical constraints). A comparison between the raw on-road data and the 10Hz low-pass results can be seen in Figure 199.

Additionally a comparison between the 10Hz low-pass results and the 20Hz down-sampled results is given in Figure 200. An analytical assessment is made in the next section assessing the effect on signal attenuation between each stage of the process.

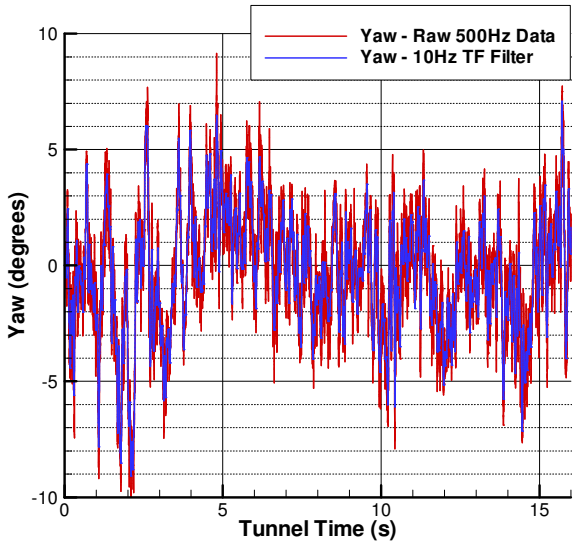


Figure 199 - Raw on-road data against 10Hz low-pass filtered data

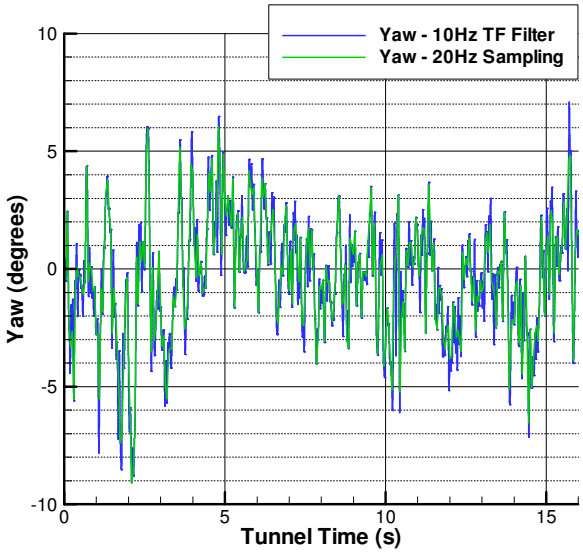


Figure 200 - Data comparison of before and after 20Hz sampling

Finally a comparison between the on-road raw data and the 20Hz-sampled data can be seen in Figure 201, showing a good visual correlation between the two traces. Again, an analytical comparison is made later in this chapter.

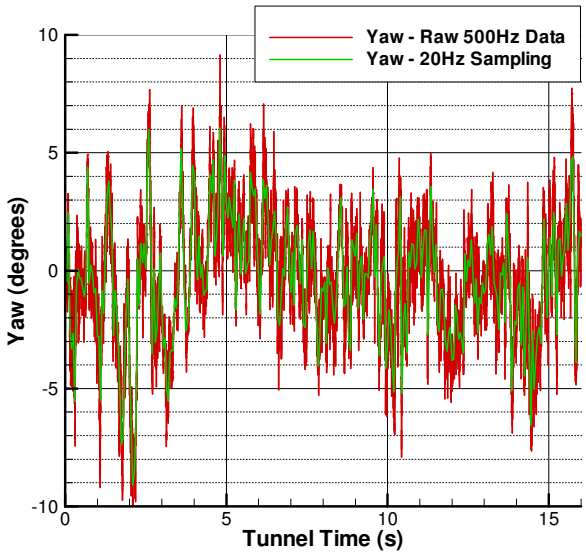


Figure 201 - On-road data against 20Hz-sampled data (after 10Hz low-pass filtering)

## 7.6 Analysis of Post-Processed On-road Data for TGS Use

After the signal processing of the on-road yaw and pitch data, the conversion from a yaw against time trace needs to focus on generating a signal that, as accurately as possible, replicates the original on-road trace. With this focus, two approaches were then assessed by which the data could be converted into a TGS time against yaw profile. The first is to simply convert the yaw data into time against aerofoil angles. However this approach does not consider the harmonic nature of the aerofoil operation, nor the consideration that the TGS operates at frequencies (i.e. up to 10Hz) potentially greater than the time period over which the dual motors can be updated for phase and frequency (due to communication time overheads). Therefore a second approach is to use a Fourier transform method to determine the peak FFT frequency and phase of the input yaw signal, and drive the TGS motors to these settings, using a rolling window.

### 7.6.1 Method 1: Yaw against Time

This method simply filters the post-processed time against yaw trace for the peak inflexion points, and uses the resultant point-to-point profile as the TGS time against yaw profile. Shown in Figure 202 is the post-processed on-road 20Hz sampled yaw trace with the red dots showing the essential inflexion points that the aerofoil will reach during its motion. A plot of this inflexion-based method profile against the yaw data down-sampled to 20Hz is shown in Figure 203, showing a good visual correlation.

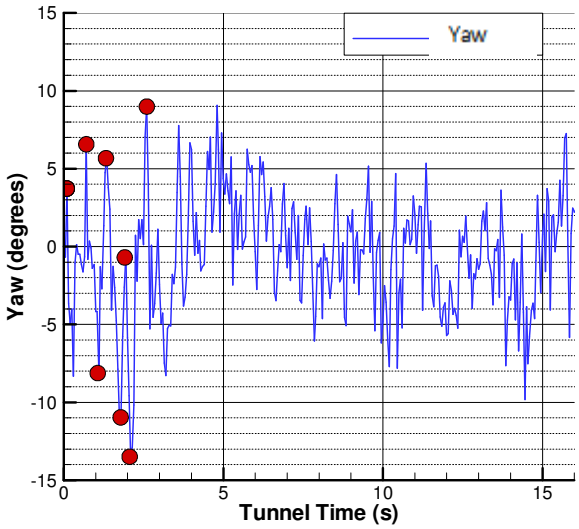


Figure 202 - Inflexion based analysis of yaw trace using 20Hz-sampled data

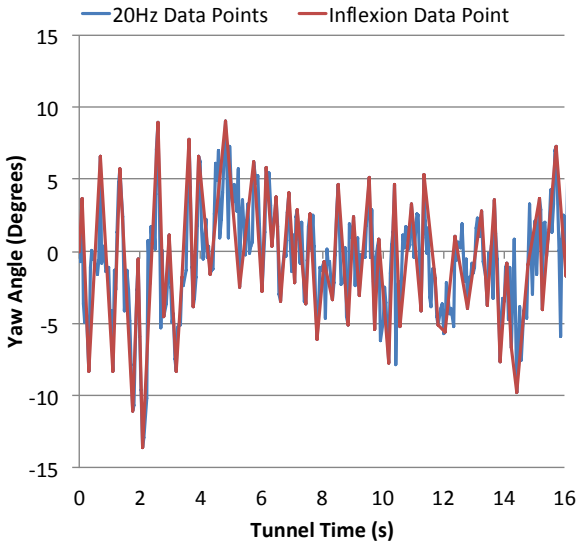


Figure 203 - Inflexion and 20Hz based yaw angle traces

### 7.6.2 Method 2: Frequency and Phase against Time

This method uses a Fourier transform analysis of the post-processed yaw against time profile to find the peak frequency and phase for incremental sections of the yaw against time profile. This approach aims to utilise the sinusoidal nature of the two rotating motors, and by simply determining the necessary frequency and phase at which to rotate the motors, the aerofoils can be programmed to create the desired inlet yaw waveforms. Three input files went through the FFT analysis, firstly the original on-road measurement, denoted as the 'raw' data, the post-processed 20Hz sampled data file and the inflexions data file from method 1 (just presented). These three input files were then analysed for their dominant phase and frequency. In order for the high frequency turbulence of the on-road flow conditions to be resolved, it was necessary to run a rolling window analysing the spectral properties, and a range was determined to be a window with a size less than 4-seconds at full vehicle scale, (equating to ≈2-seconds at tunnel time scale) but with an update rate greater than 0.25s, as this is the time required for a full set of instructions to be actuated by the TGS control system.

Hence the initial analysis used a 2-second (4,096 data samples) rolling rectangular window outputting data samples at 0.5-second intervals from the FFT evaluation. Once the spectral analysis was completed, the spectral peak amplitude was found and this would determine the dominant frequency and phase to run the TGS aerofoils at, updated every 0.25 seconds. Additionally a search frequency for the FFT algorithm was set, which constrains the lowest frequency that the FFT algorithm can resolve

(which is within the quasi-steady zone of a vehicle's aerodynamic response). As the fastest the TGS can operate is 10Hz, this gave a potential search frequency range of 0.25 – 10.0Hz (though the bin nature of the FFT program meant that frequencies slightly either side of this may be returned).

With these considerations determined, each of the 3 input files (i.e. raw data, 20Hz sampled data and inflexion data) were all scaled via linear interpolation to 16,384 data points over the tunnel time period of 16-seconds. The 3 input cases were then analysed through the FFT algorithm using a minimum search frequencies of 0.1, 0.5, 1.0, 3.0 and 5.0Hz (as it was believed that the minimum search frequency could have a notable effect on the output frequency at each interval).

Once the frequency, phase and amplitude were determined for the whole time trace, it was necessary to compare the result of simulating the TGS yaw against time profile using this sinusoidal approach. The simulation method of using the FFT peak results was simply a sinusoidal reproduction of the result using the corresponding amplitude, phase and frequency as:

$$\text{Modelled Yaw Angle} = A.Cos\left(2\pi ft - p\right) \qquad [20]$$

where A = yaw angle modelled amplitude, f = FFT peak frequency, t = sub-time and p = FFT peak phase and where the yaw angle modelled amplitude $A = \frac{2}{n} A_{FFT}$ and where n = number of data samples (16,384).

An example of such a result is given in Figure 204, where the sinusoidal response with differing amplitude and phase changes can be seen along the trace. Visually the comparison shows a poor correlation from the original yaw against time trace against that generated by the FFT process.

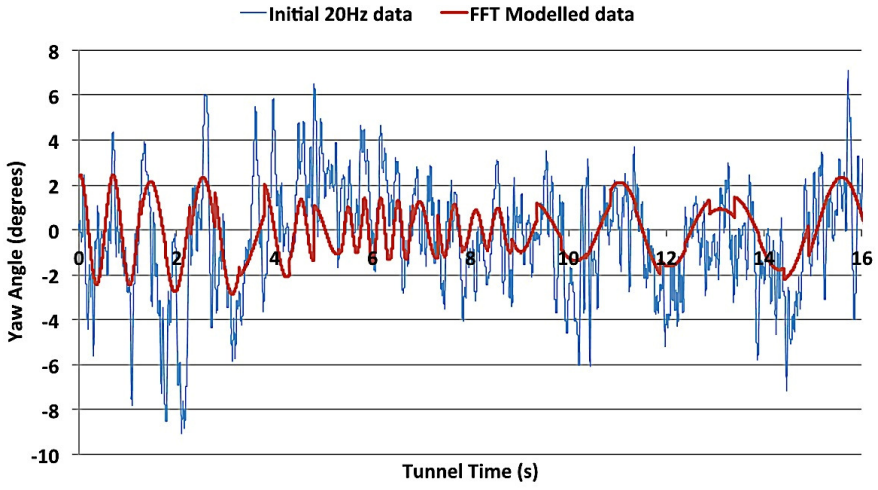


Figure 204 - FFT modelled yaw angle trace and 20Hz sampled on-road trace, using a 0.1Hz minimum search frequency

### 7.6.3 Comparison of methods for generating TGS yaw against time profile

With two approaches to generate the TGS input control profile considered, it was necessary to analytically compare each approach's ability to replicate the original on-road yaw against time profile. To compare the range of options available the standard error was evaluated for both the initial input trace and then the modelled trace, as:

$$\text{Standard Deviation of On-road Yaw} = \sqrt{\frac{\sum Yaw^2}{n}} \quad \text{and} \qquad [21]$$

$$\text{Modelled Standard Error} = \sqrt{\frac{\sum (\text{Simulated Yaw} - \text{Raw Yaw})^2}{n}} \qquad [22]$$

Finally the RMS standard error is then evaluated simply as given by:

$$\text{Total RMS Standard Error} = \frac{\text{On-Road (Raw) Standard Deviation}}{\text{Modelled Standard Error}} \qquad [23]$$

The time against yaw profiles tested were the on-road raw trace, the 20Hz resampled trace (after the 10Hz low-pass filter) and the peak yaw inflexions for a range of search frequencies. After the full analysis was completed, the results were as presented in Table 10. The cases are titled as the input file (20Hz sampled, on-road raw results or inflexion results) and the minimum search frequency used. The 'RMS initial standard error' is the input profile standard deviation into the FFT algorithm, and the 'RMS modeller standard error' is the output profile standard deviation, and the 'RMS standard error' is the difference between these two (analysed data point-wise).

The results are then ranked in terms of minimum RMS standard error. The orange highlighted row is the inflexions result from the raw result, this being the lowest rank that is practical by using a time against position method. The green highlighted results are the best frequency and phase based results (using the inflexions case), then the blue is the best method from the raw road results and the yellow row is the best using the 20Hz data input file.

The final three rows of the table compare the accuracy of yaw against time profile after each of the initial signal processing stages (i.e. without any FFT algorithm modelling).

Table 10 - FFT modelled yaw angle results

| Case | RMS Initial Std. Deviation (degs) | RMS Modeller Std. Deviation (degs) | RMS Std. Error (degs) | Rank |
|---|---|---|---|---|
| 20Hz @ 0.1Hz: | 2.53 | 2.22 | 0.88 | 8 |
| 20Hz @ 0.5Hz: | 2.53 | 2.32 | 0.92 | 10 |
| 20Hz @ 1.0Hz: | 2.53 | 2.31 | 0.92 | 9 |
| 20Hz @ 3.0Hz: | 2.53 | 2.48 | 0.98 | 13 |
| 20Hz @ 5.0Hz: | 2.53 | 2.49 | 0.98 | 15 |
| | | | | |
| Raw @ 0.1Hz: | 2.65 | 2.31 | 0.87 | 7 |
| Raw @ 0.5Hz: | 2.65 | 2.45 | 0.92 | 11 |
| Raw @ 1.0Hz: | 2.65 | 2.45 | 0.92 | 12 |
| Raw @ 3.0Hz: | 2.65 | 2.60 | 0.98 | 14 |
| Raw @ 5.0Hz: | 2.65 | 2.61 | 0.98 | 16 |
| | | | | |
| Inflexions @ 0.1Hz: | 2.59 | 1.95 | 0.75 | 4 |
| Inflexions @ 0.5Hz: | 2.59 | 2.11 | 0.81 | 5 |
| Inflexions @ 1.0Hz: | 2.59 | 2.17 | 0.84 | 6 |
| Inflexions @ 3.0Hz: | 2.59 | 2.57 | 0.99 | 17 |
| Inflexions @ 5.0Hz: | 2.59 | 2.59 | 1.00 | 18 |
| | | | | |
| 20Hz from Raw: | 2.65 | 0.79 | 0.30 | 1 |
| Inflexions from Raw: | 2.65 | 1.86 | 0.70 | 3 |
| Inflexions from 20Hz: | 2.53 | 1.68 | 0.67 | 2 |
| | | | | |
| *All deviations and error values are in yaw angle degrees* | | | | |

The results therefore show that the best method to reproduce the on-road yaw recording is to use the inflexion based input file as a aerofoil angle against time approach, rather than using an FFT frequency and phase based method, as this approach generates a lower standard error than all of the FFT derived profiles.

Finally, in order to confirm that the FFT windowing used (2.0-second windows with 0.5-second intervals) was optimum, and that the windowing was not limiting the assessment, a comparison was made of a variety of window and interval permutations within the constraints detailed earlier. The case used was the 20Hz sampled yaw against time profile with a 0.1Hz minimum search frequency, with the results shown in Table 11.

The results show that minor improvements could have been made from the datum result (the green row), corresponding to a reduction of -0.03° in RMS standard error. Such an improvement on the best frequency and phase-based result would take the inflexions RMS standard error result using a 0.1Hz minimum search frequency from 0.75Hz to 0.72Hz, which is still above the yaw against time result, which has an RMS standard error of 0.70Hz. Therefore the approach used and the conclusions made remained valid.

Table 11 - FFT frequency and phase method with varying window and interval sizes

| Period | Window Size (n samples) | RMS Modeller Std. Deviation (degs) | RMS Std. Error (degs) | Rank |
|---|---|---|---|---|
| 256 | 1024 | 2.53 | 2.25 | 7 |
| 256 | 2048 | 2.53 | 2.19 | 3 |
| 256 | 4096 | 2.53 | 2.32 | 8 |
| 512 | 1024 | 2.53 | 2.24 | 5 |
| 512 | 2048 | 2.53 | 2.22 | 4 |
| 512 | 4096 | 2.53 | 2.36 | 9 |
| 1024 | 1024 | 2.53 | 2.18 | 2 |
| 1024 | 2048 | 2.53 | 2.24 | 6 |
| 1024 | 4096 | 2.53 | 2.55 | 11 |
| 2048 | 2048 | 2.53 | 2.14 | 1 |
| 2048 | 4096 | 2.53 | 2.49 | 10 |

*All deviations and errors are in yaw angle degrees*

From these multiple stages of analysis, the method that offers the most accurate conversion process from an on-road yaw profile to a TGS yaw profile is by undertaking a process of resampling the on-road data trace and selecting the main inflexion peaks from the trace. As this profile is a set of yaw against time measurements, the direct arbitrary method of driving the aerofoils from peak-to-peak yaw angles between points of time (i.e. with the motors kept in phase) is the more suited method of the two proposed. Therefore, the final variable to consider in determining the inputs in the TGS yaw against time profile is the motor frequency (i.e. crank rotational rate), which defines the time period between yaw peaks.

## 7.7 Determination of Motor Frequency for Arbitrary Aerofoil Motion

In order to oscillate the aerofoils between yaw peaks in a relatively linear and smooth motion (as would occur in the on-road environment) within a set time period, it is necessary to determine the correct rotational rate of the motor cranks. The derivation of the target velocity is split into three stages of a motor's motion, initial acceleration, constant speed and final retardation. The initial acceleration occurs between time $t_o$ to $t_1$, moving the motor crank from angle $\theta_0$ to $\theta_1$, then constant speed between time $t_1$ to $t_2$ when the motor crank is moving at constant velocity from angle $\theta_1$ to $\theta_2$, and then finally a retardation period between time $t_2$ to $t_3$ where the aerofoil slows to stationary from angle $\theta_2$ to $\theta_3$. The equations governing the motion during these periods are those of standard displacement through velocity and acceleration, with the maximum velocity of the aerofoils being, v, and the acceleration rate being, a:

$$\theta_2 = \theta_1 + v(t_2 - t_1) \text{ and } \theta_3 = \theta_2 + \frac{a(t_3 - t_2)^2}{2}, \text{ where } t_3 - t_2 = \frac{v}{a} \quad [24]$$

$$\text{By simplification and substitution} \Rightarrow \theta_3 = \theta_0 + \frac{v^2}{a} + v\left(t_3 - \frac{2v}{a}\right) \quad [25]$$

$$\Rightarrow 0 = (\theta_0 - \theta_3) - \frac{v^2}{a} + vt_3, \text{ where } t_0 = 0 \quad [26]$$

$$\text{Solving the quadratic} \Rightarrow v = \frac{t_3 \pm \sqrt{t_3^2 + 4/a(\theta_0 - \theta_3)}}{(2/a)} \quad [27]$$

For an arbitrary set of inputs, the results are plotted in Figure 205, showing three clear stages of motor crank motion between illustrative times and angles.

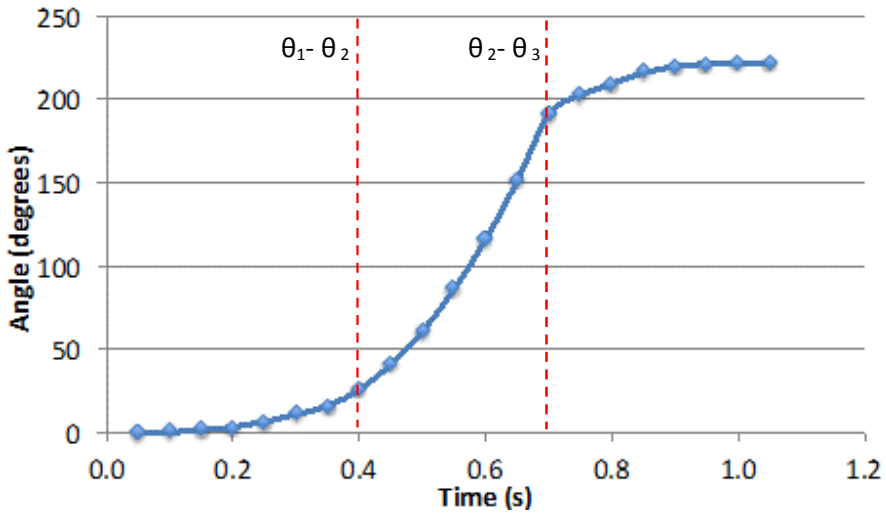


Figure 205 - Typical motor motion showing stages of constant acceleration and constant velocity

Therefore by evaluating the target velocity, the motor driving frequency can be set. Hence the arbitrary TGS test case can use the evaluated frequency, the target yaw angle determined from the inflexions yaw profile and no phase adjustments between the motors, for its complete set of control parameters.

## 7.8 Conclusion

This chapter has covered the theoretical operation of the TGS system and the development of a TGS arbitrary case file from raw on-road yaw measurements. An initial overview was made of the concepts

that affect the operation of the dual motor drive, noting the need to ensure that the aerofoils accurately follow the correct yaw paths without exceeding the target yaw angle as the aerofoils move between set points, all within the constraints of the TGS control software. A direct arbitrary control method was proposed where the aerofoils are simply driven within one $180^{o}$ arc of the motors. This method requires the assignment of a very high acceleration rate and a variable frequency to set the time period between yaw peaks. Additionally a process was presented where frequency and phase adjustments could be used to create an arbitrary TGS case whilst keeping the motors running continuously in one direction of rotation. The process by which the shutter actuation triggers could be determined was also presented.

As the flow yaw angle generated is less than that of the aerofoil's angle, a scalar between the on-road yaw and aerofoil angle was demonstrated. Consideration was then made to the appropriate analysis of the on-road data measurements to determine whether to use either the spectral properties of the on-road flow or simply just the peak flow angles recorded to configure the TGS motion. In order to prepare the on-road recorded results for such a comparison, the data was filtered through a 10Hz low-pass filter and then down-sampled at 20Hz. The filtered trace was then compared to the on-road results from the resultant traces using both spectral (i.e. FFT based on frequency and amplitude) and direct (i.e. moving the aerofoils to the major inflexion points of a trace) approaches, using a variety of evaluation sampling windows. Finally a derivation of motor crank target velocity was presented, which was used to determine the driving frequency of the motor cranks. From these assessments, the inflexions yaw angle input approach proved to be the best, which will be used with the direct arbitrary control method to generate the input file for the TGS yaw profile.

# 8. Wind Tunnel TGS Commissioning Tests

This chapter presents a comprehensive study of the TGS's parameters that were found to significantly affect flow uniformity and yaw generation. A series of tests are undertaken to commission the wind tunnel and then studies to understand the parameters affecting yaw and pitch generation. The test map for the commission study is as shown in Figure 206.

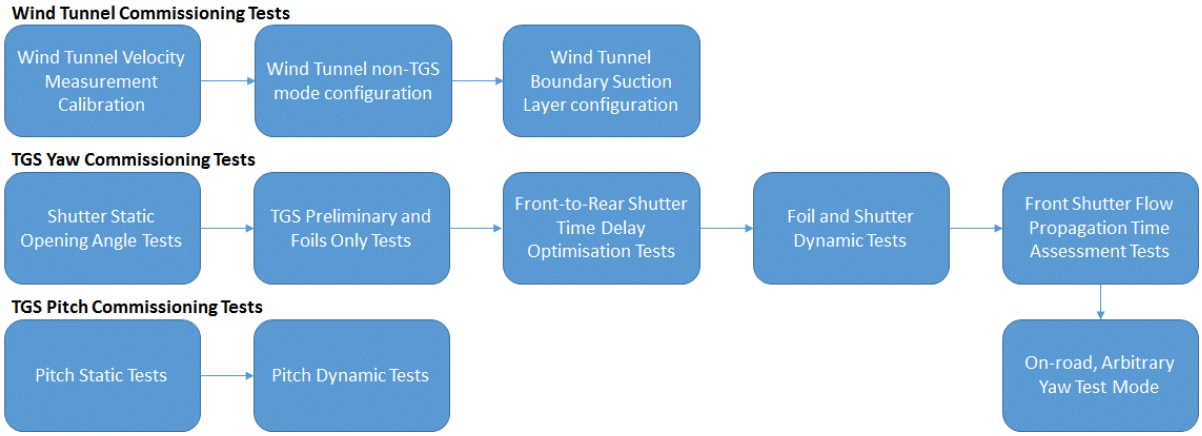


Figure 206 - Wind tunnel and TGS commissioning study test map

## 8.1 Tunnel Commissioning Tests

The installation of the turbulence generation system and the simultaneous power upgrade of the 2m wind tunnel at Durham University meant that the nominal aerodynamic characteristics of the wind tunnel had changed, requiring a series of preliminary tests. These covered:

- Velocity measurement via a calibration of a Plenum based flow velocity measurement system.
- Static pressure gradient assessment to determine the nominal TGS aerofoil angles for operating the tunnel in a static, non-TGS mode.
- Boundary suction layer fan to tunnel flow rate calibration

These tests were conducted in unison. A pitot-static tube was located at turntable-centre (the static pressure tap located at X = +1800, Y = 0, Z = 250mm from boundary layer suction splitter plate leading edge), and 5 static pressure lollipop tappings were located on the tunnel floor in a row along Y = 0mm (and hence Z = 0mm). The central tapping was located at X = +1800mm, with the others being located at $\Delta X$±500 and ±1000mm. Finally, the plenum method nozzle calibration for wind tunnel velocity measurement was set-up with a ring of 4 static pressure taps placed around the tunnel nozzle inlet's walls, before the contraction (and just after the inlet bellmouth), located in the middle of the ±Y and ±Z

walls. Two additional static pressure taps were located at extreme ±Y locations at the highest height possible on the front wall panel of the plenum. This location placed the 2 plenum tappings well out of the transient flow effects that could be generated by the TGS and, by having two tappings, averaged out any potential lateral flow effects during TGS operation. This offered more reliable velocity measurement system where the tunnel mass flow could vary with shutter motion.

The wind tunnel was run at speeds of 5, 10, 15, 20 and 25ms$^{-1}$, and at each velocity set-point the boundary layer suction fans were varied to generate horizontal flow over the boundary layer suction plate leading edge as shown in Figure 207 (determined using a wool tuft flown from a location of X = +50, Y = 0, Z = 50mm). Once flow was correctly established, pressure readings were taken of the pitot-static, floor lollipops, plenum and nozzle tappings.

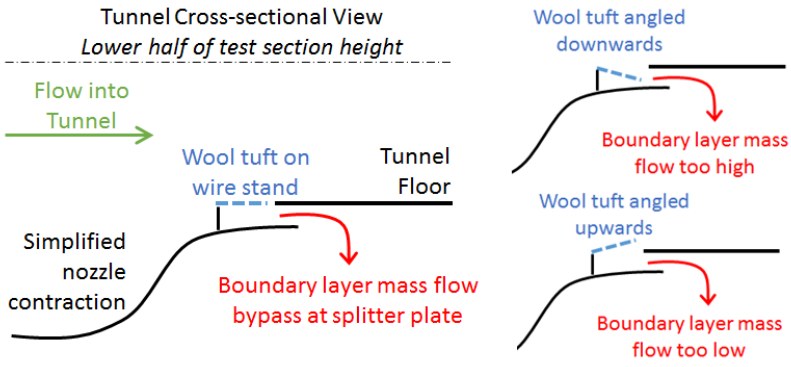


Figure 207 - Boundary layer fan calibration set-up using wool tufts

These measurements were recorded in unison with the percentage demand of power of the pair of main tunnel fans and the boundary layer fan, recorded at 1,000Hz with a resolution of 4,096 readings and repeated for 50 sets. The test was conducted with the trailing edge of the TGS aerofoils being set as were the trailing edge of the plenum inlet nozzle before TGS installation, giving a width of Y = 1750mm.

The graph presented in Figure 208 shows the tunnel's boundary layer profile in both rolling road and fixed ground configurations.

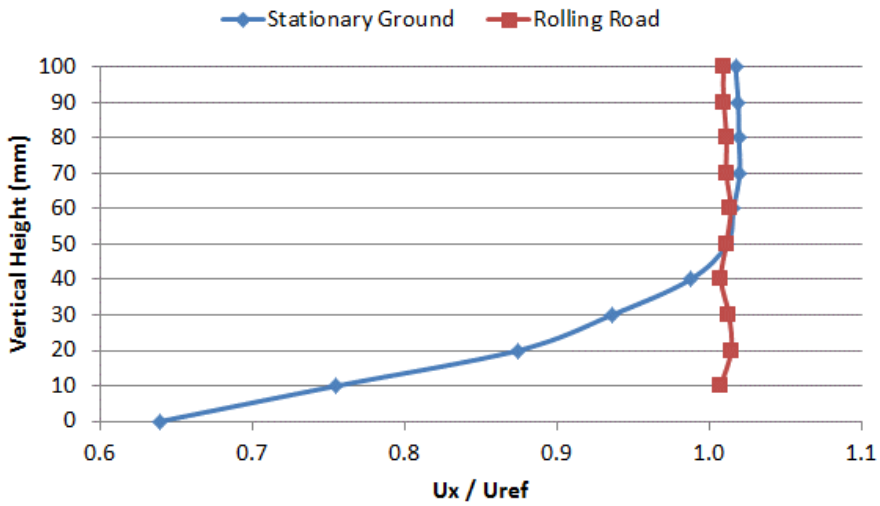


Figure 208 - Boundary layer velocity profile

Figure 209 shows the longitudinal static pressure gradient along the working section, found to have a difference of less than 2% per metre.

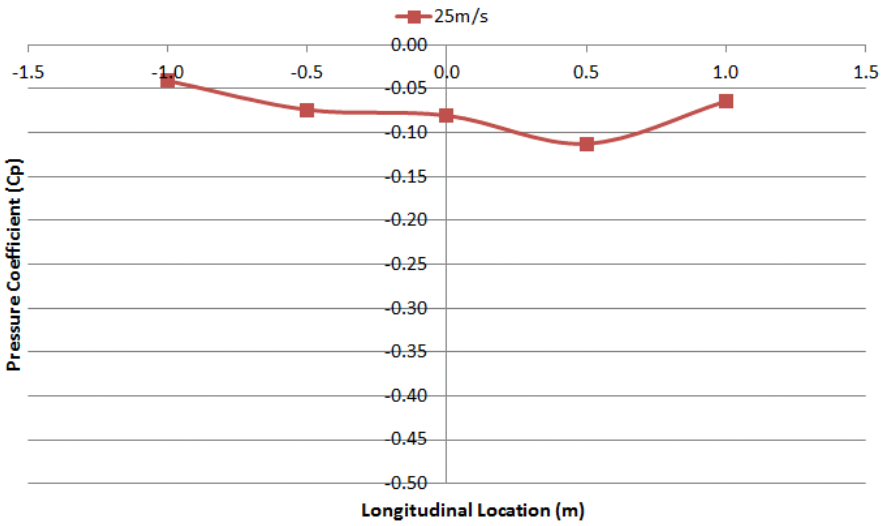


Figure 209 - Tunnel static pressure gradient against X-location

A new system was calibrated to measure tunnel velocity by recording the pressure difference between the static pressure tappings installed in the nozzle and those installed in the plenum. This pressure difference was then correlated to a pitot - static tube in the freestream flow through the working section of the tunnel. In Figure 210 the pressure difference between the nozzle set of 4 static pressure tappings to the plenum set of 2 static pressure tappings is shown against dynamic pressure measured from the pitot - static tube. The resultant pressure ratio is also shown, given in Reynolds number per metre. The TGS was set in the 'non-TGS' configuration, giving the normal nozzle contraction ratio.

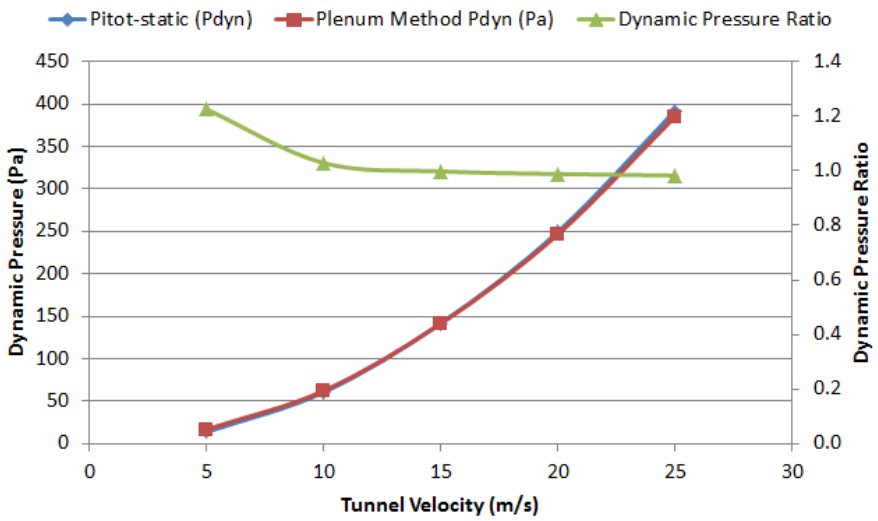


Figure 210 - Wind tunnel nozzle calibration measurements

Finally, it was necessary to align the two motors that both act on each aerofoil, by measuring the aerofoil trailing edge displacement from rotating only one of each of the pair of motors through 180°. This gave motor crank phase corrections to the left aerofoil of -7°, -4° and to the right aerofoil of +1°, -4° (motor crank to aerofoil angle calibration is included in the Appendix, p.258).

## 8.2 Shutter Open Angles - Static Tests

### 8.2.1 General Test Approach

The TGS contains a wide range of devices, each of which needs to be operated with respect to one another, and as such the commissioning test plan needed to assess all potential permutations and optimisations of the system. The key metric is to maximise flow uniformity whilst achieving high peak yaw angles. The approach was to first determine the optimum angle that the shutters should open to, and then assess the aerofoils angles at which each shutter should open using static yaw tests, and then to establish these results as a datum configuration for the harmonic, dynamic test work. The parameters being assessed were:

- The angle that the shutters open to
- The aerofoil angles at which each shutter open and close, based on static aerofoil tests
- The aerofoil angles at which each shutter open and close based on dynamic aerofoil tests (i.e. factoring in a range of aerofoil oscillation frequencies, front-to-rear shutter phases and additional inlet flow acceleration times)

TGS tests were conducted at 25ms$^{-1}$ tunnel velocity, with 5-Hole probe measurements taken at 9-locations for 4.0s at 1,024Hz through 250Hz filters, this timing window being the same from the quasi-steady frequency analysis undertaken earlier in this thesis. Measurement locations were the extents of a typical 35% scale model, which is TTC ±350mm in the Y-axis and ±650mm in the X-axis, all recorded at mid-model height (275mm). Aerofoil increments were 2$^{o}$ with a full measurement sweep taken at each location, giving 20 measurement aerofoil incidence angles. When these locations are denoted in graphs, they are referred to by figurative names, these being Front Left, Front Middle and Front Right, Mid Left, Turntable Centre, Mid Right, Rear Left, Rear Mid and Rear Right. In this vein, based upon the coordinate system used throughout this thesis, the front of the wind tunnel is X-, the rear is X+, and when facing the nozzle, the right hand side is Y+ and the left hand side is Y-, as illustrated in Figure 211.

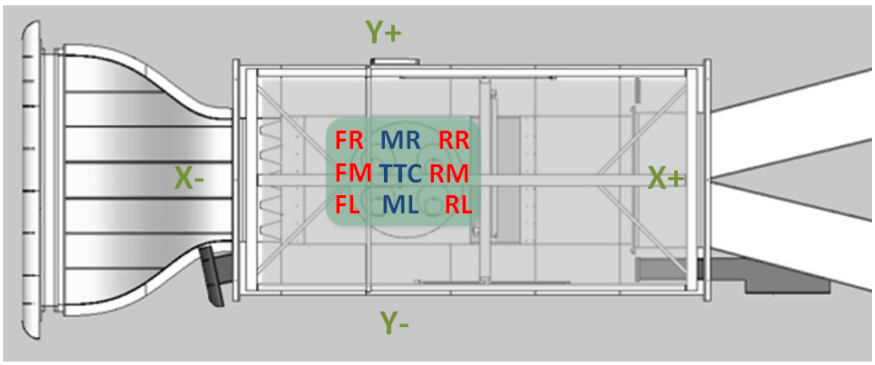


Figure 211 - Definition of measurement location names in the 2m wind tunnel

Additionally, throughout this chapter the recorded yaw and standard deviation measurements are averaged between locations. Collections of the length-wise sets can be seen in Figure 212, where the red labels are a front set of three, the blue labels are the mid set of three and the green labels are the rear locations in a set of three. In Figure 213 width-wise sets are shown, with the red labels being the three Y+ locations, the blue labels being the three mid locations and the green labels being the three Y- locations in a set.

When shown in results, the side-to-side (width-wise) comparisons are denoted as Y+-Y-, and front-to-rear (length-wise) comparisons as FR-RR.

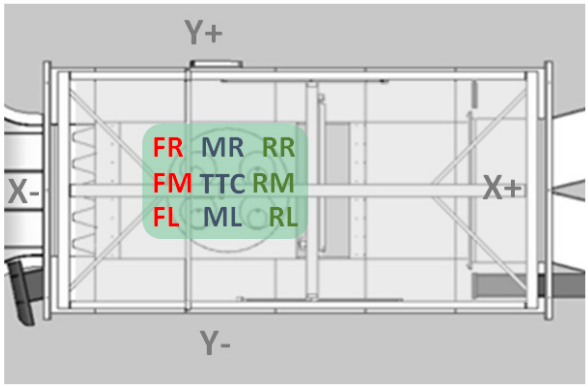


Figure 212 - Measurement locations when averaged as length-wise sets

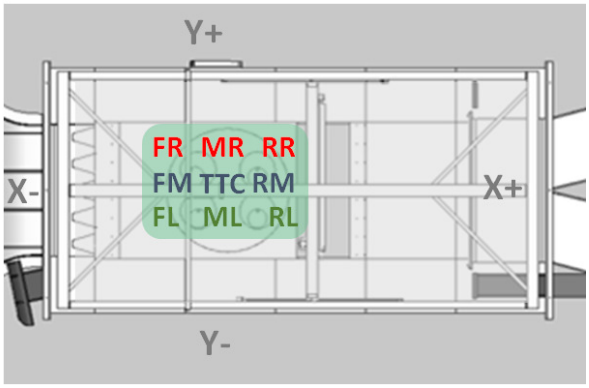


Figure 213 - Measurement locations when averaged as width-wise sets

It should also be reiterated that in many of the graphs presented in the static and dynamic TGS tests, lines are drawn between points, but are for clarity purposes only and should only be considered as illustrative. Also, when a variation between data points is significant (i.e. more than one standard deviation) a regressed curve would imply a linear or otherwise behaviour between points that would not be valid, as a physical change to the system (i.e. a shutter opening) may have occurred.

### 8.2.2 Repeatability Analysis

In order to assess the repeatability of flow measurements, a repeatability test was completed. The test used a logging window of 4.0s with 10 sets of data recorded at each measurement location in order to make set-to-set comparisons. The standard deviation at each of the 9 locations was always less than 0.1°, with a 95% confidence interval of ±0.1°, showing a highly level of repeatability in measurement. This of course requires correct probe traverse alignment and at the beginning of each test run the probe alignment was assessed through taking multiple measurements with the probe in its normal orientation and inverted. Where a shift correction was required, this was applied and is shown in the corresponding results.

### 8.2.3 Probe Design and Configuration

In the commissioning study, two probes were used, one being made of acrylic and the latter being a laser sintered metal model as in Figure 214, an improved design that became available between tests. During the static angle tests a single metal probe arm was used, with the acrylic probe. However, during the initial dynamic tests it was evident that the probe arm was flexing and therefore a stiff, carbon probe stem was used to prevent deflection in yawed flow. For all of the dynamic (i.e. time-variant) measurements a Transfer Function correction was applied to all probe

measurements (as shown in Figure 96), with the resultant correction spectrum and the probe calibration for the laser sintered probe (given as an example) both available in the Appendix (p.263).

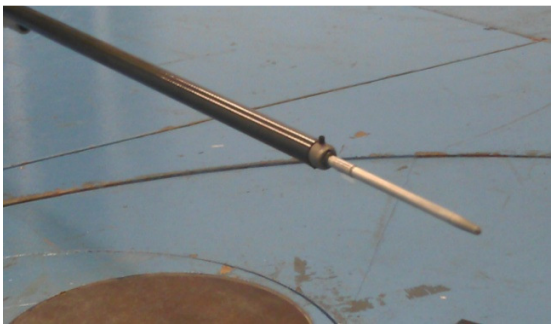

Figure 214 - Laser sintered probe with carbon fibre arm

### 8.2.4 Shutter Static Open-To Angle Tests

The shutters can have their open angle controlled by adjusting a setscrew on a milled-slide that controls the position of a rubber stop, against which the shutters rest when open. Two choices became significant with consideration for optimising the turning of the flow as it enters and exhausts from the test section. At the front of the working section, the consideration was that at peak angles the aerofoils are attempting to turn the flow 15°, so this is the peak angle that the shutters should be angled to, in order to aid this vane turning effect. The other option is that when the shutters first open they open to mid-aerofoil incidence of around 8°, which would generally be closer to the average aerofoil incidence angle in a test cycle. These therefore became the two potential test options for the front shutters. The same assessment was required for the rear shutters. Therefore 2 x 2 = 4 tests were required for the front and rear shutter open-to angles of 8° and 15°.

Measurements taken (yaw average, standard deviation, front-to-rear and side-to-side comparisons of flow yaw) were averaged over the entire range of shutter open angles and split into 2 categories for this process. The first averaged for every 2° angle increment and the second used the extreme angles (±12° and ±15°) to generate 4 'extreme angle result' metrics. At these extreme angles the shutters were set to all be open, and therefore results for these aerofoil angles can be considered independently of how many shutters should be open. The full results are available in the Appendix, p.259.

Graphical results of the test are shown Figure 215, with the shutters closed condition (i.e. datum) additionally plotted. It is observed that the angle of the shutters makes a nominal variation against the

other configurations. Error bars of 95% confidence are plotted, but due to their extreme tightness, are barely shown.

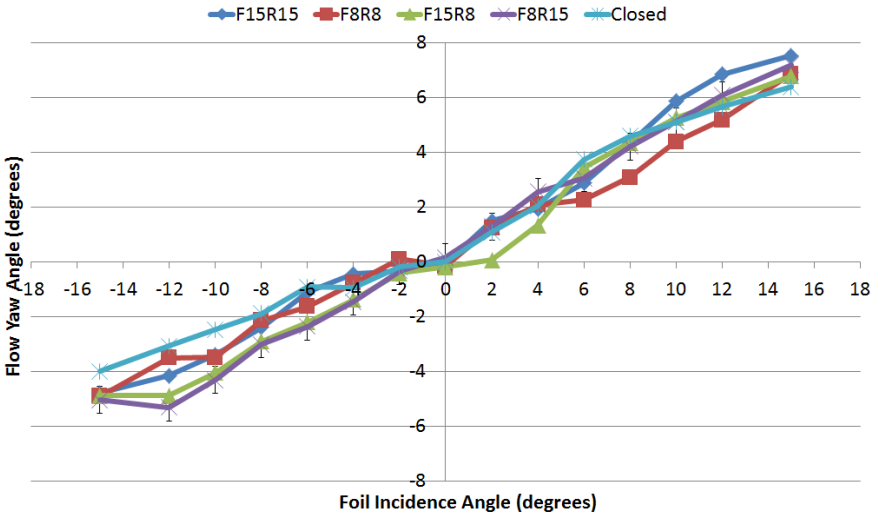


Figure 215 - Average flow yaw angle for aerofoil incidence

Figure 216 shows the standard deviations of yaw angle over the 9 measurements taken at each location. The error bars plotted are comparable to the measurement variability and there is systematic variance evident between all of the cases. Note that for this chapter's results presentation, the flow yaw angle standard deviation is frequently presented. The standard deviation represents the spatial yaw variation in the test section and not the unsteady, transient variation of yaw angle in time.

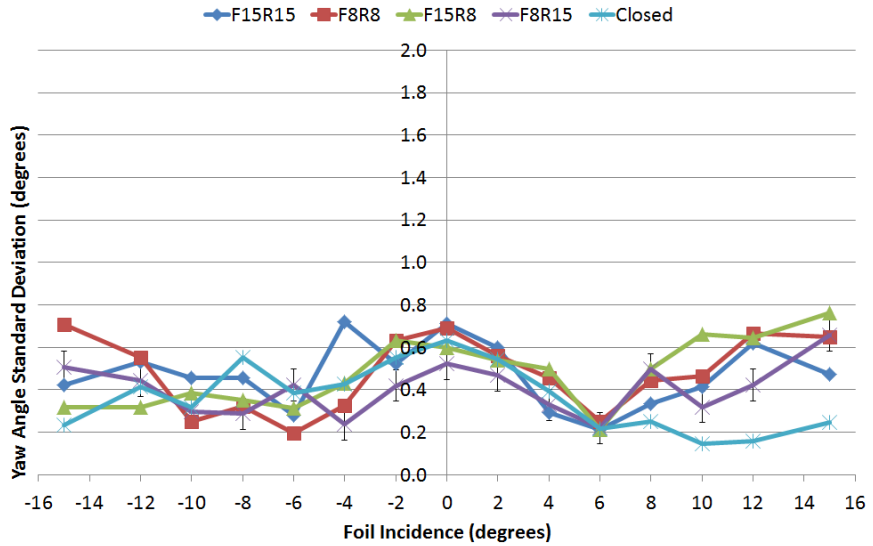


Figure 216 - Standard deviation of yaw angle for each configuration

Figure 217 shows the difference in yaw angle between the front and rear measurements. It is noted that the variation seems to dip at positive yaw flow angles rather than negative angles. The results show that a notable variance exists, but no clear systematic variation with shutter open angle.

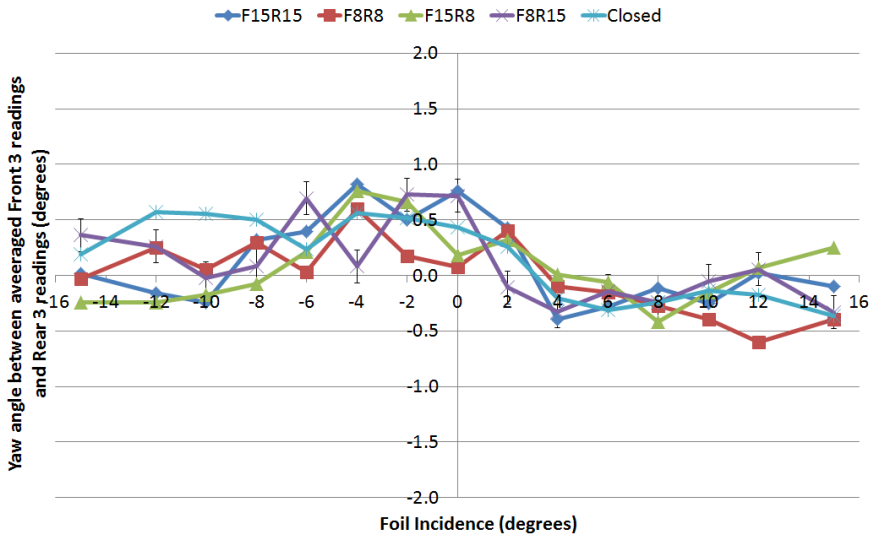


Figure 217 - Front-to-rear (FR-RR) flow yaw angle difference

Figure 218 shows the difference between the Y+ averaged 3 readings and the Y- set of 3 readings (i.e. Y+-Y-). There is clearly a systematic variance with aerofoil angle. At the extreme yaw angles the side-to-side difference is negative at approximately -1.0°, yet at near zero aerofoil angle the side-to-side difference is positive at approximately +1.5°. However, there is no clear variation with shutter open angle.

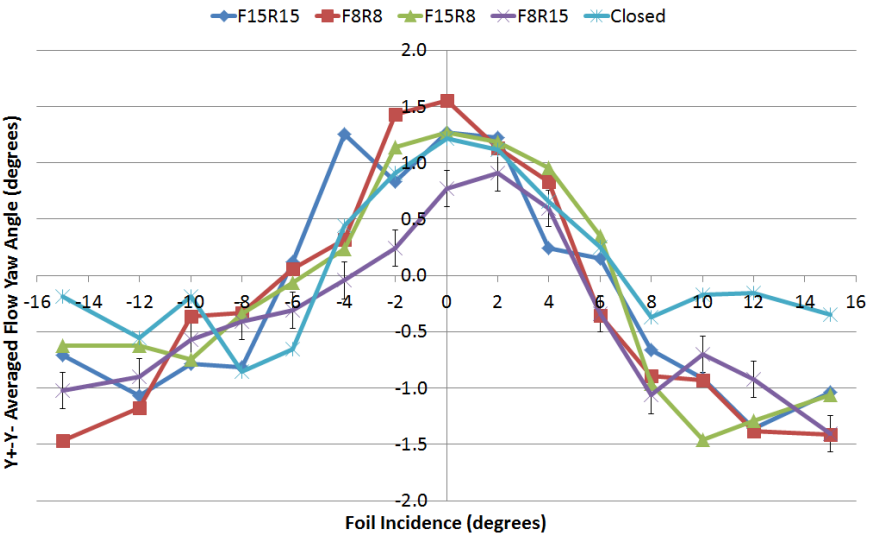


Figure 218 - Side-to-side (Y+-Y-) averaged flow yaw angle

In order to compare the findings, the results were then ranked amongst each of the four configurations, shown in Table 12. The titles denote the angles at which the front and rear shutters opened to.

Table 12 - Ranks of the results from each shutter open angle configuration test

| RANKS | *F15R15* | *F8R8* | *F15R8* | *F8R15* |
|---|---|---|---|---|
| **Mod. Avg** | 3 | 4 | 2 | 1 |
| **Avg. Std Dev.** | 3 | 2 | 4 | 1 |
| **Avg FR-RR** | 4 | 1 | 2 | 3 |
| **Avg. Y+-Y-** | 3 | 2 | 1 | 4 |
| **Ext. Avg.** | 2 | 4 | 3 | 1 |
| **Ext. Std. Dev.** | 2 | 4 | 3 | 1 |
| **Ext. FR-RR** | 1 | 4 | 2 | 3 |
| **Ext. Y+-Y-** | 2 | 4 | 1 | 3 |

| RANKS | F8: | F15: | R8: | R15: |
|---|---|---|---|---|
| **Mod. Avg** | 3 | 2 | 4 | 1 |
| **Avg. Std Dev.** | 1 | 4 | 3 | 2 |
| **Avg FR-RR** | 2 | 3 | 1 | 4 |
| **Avg. Y+-Y-** | 3 | 2 | 1 | 4 |
| **Ext. Avg.** | 3 | 2 | 4 | 1 |
| **Ext. Std. Dev.** | 3 | 2 | 4 | 1 |
| **Ext. FR-RR** | 4 | 1 | 3 | 2 |
| **Ext. Y+-Y-** | 4 | 1 | 3 | 2 |

To further compare the results, the rankings were averaged in terms of whether they assess flow peak angle (i.e. yaw average results) or flow uniformity (i.e. standard deviation, FR-RR and Y+-Y- results) to fairly weight the results, as shown in Table 13. The results show that front shutters set at 8° and the rear shutters set at 15° (result F8R15) offered the best flow compromise.

Table 13 - Final results from shutter open-to angles test

| | *F15R15* | *F8R8* | *F15R8* | *F8R15* |
|---|---|---|---|---|
| **Angle (degrees):** | 2.5 | 4 | 2.5 | 1 |
| **Uniformity:** | 2.5 | 2.8 | 2.2 | 2.5 |
| ***Average:*** | *2.5* | *3.4* | *2.3* | *1.8* |

| | F8: | F15: | R8: | R15: |
|---|---|---|---|---|
| **Angle (degrees):** | 3 | 2 | 4 | 1 |
| **Uniformity:** | 2.8 | 2.2 | 2.5 | 2.5 |
| ***Average:*** | *2.9* | *2.1* | *3.3* | *1.8* |

### 8.2.5 Shutter Opening-At Angle Tests

With the shutter open angles determined of 8° front and 15° rear, it was then possible to consider the correct shutter actuation options. A nominal condition was found by evaluating the lateral shutter

locations in the Y-axis and the X-axis distance between the front and rear shutters. Straightforward trigonometry was then used to evaluate the lateral location that the air flow would propagate to, for each aerofoil angle. These gave the results in Table 28, in the Appendix, on p.260. This set-up of shutter opening angles was denoted the 'nominal' shutter opening angles.

Using the nominal calculated shutter opening angles, this gave the test plan as given in Table 14, showing the nominal shutter opening angles and then the two additional test batches that would test opening more or fewer shutters (with the greyed areas being where no other iterations seemed to practically be viable). Of course the shutters were only opened on the appropriate side to maximise flow yaw, depending upon the aerofoils' angle, and no shutters are open at 0° of aerofoil incidence.

**Table 14 - Nominal shutter opening angles and additional tests - numbers in shaded cells are the number of shutters open**

| Foil angle (degrees) | Nominal Front | Nominal Rear | | Test1-Front | Test1-Rear | Test2-Front | Test2-Rear |
|---|---|---|---|---|---|---|---|
| 15 | 5 | 4 | | 4 | 3 | | |
| 12 | 5 | 4 | | 4 | 3 | | |
| 10 | 4 | 4 | | 5 | 4 | 3 | 3 |
| 8 | 2 | 3 | | 3 | 4 | 1 | 2 |
| 6 | 1 | 2 | | 2 | 3 | 0 | 1 |
| 4 | 0 | 0 | | 1 | 1 | 2 | 2 |
| 2 | 0 | 0 | | 1 | 1 | 2 | 2 |
| 0 | 0 | 0 | | | | | |
| -2 | 0 | 0 | | 1 | 1 | 2 | 2 |
| -4 | 0 | 0 | | 1 | 1 | 2 | 2 |
| -6 | 1 | 2 | | 2 | 3 | 0 | 1 |
| -8 | 2 | 3 | | 3 | 4 | 1 | 2 |
| -10 | 4 | 4 | | 5 | 4 | 3 | 3 |
| -12 | 5 | 4 | | 4 | 3 | 4 | 4 |
| -15 | 5 | 4 | | 4 | 3 | 4 | 4 |
| | | | | | | | |
| | | More Open than Nominal | | | Less Open than Nominal | | |

The tests were then conducted and the results are given in Table 29, in the Appendix, on p.260. The results show the achieved flow yaw for the batches of shutter configuration tests, at the range of aerofoil incidence angles.

From these range of tests a best shutter opening configuration was found (denoted the 'optimum' set-up), which was slightly different to the nominal set-up. Figure 219 to Figure 222 are the average yaw results for all of the tests, including what were determined to be the optimum results (which are discussed later). All results have 95% confidence error bars plotted (though are barely shown on most of the plots). Figure 219 shows the variation in yaw angle for the variety of configurations tested. It can be seen that the average flow yaw variation between shutter tests (at the same aerofoil angle) is only nominal, and that the generated yaw is essentially symmetric about 0° of aerofoil angle. The nominal (blue) trace and the pink trace (optimised set-up) seem to be almost identical, and though the

additional yaw deviation for the −2 shutters (orange) and −1 shutter (green) suggest that the optimised set-up should have offered greater yaw at negative incidence angles, the optimised run shows little improvement over the nominal configuration. The pink bars in the background of each graph illustrate the number of shutters open at each yaw angle.

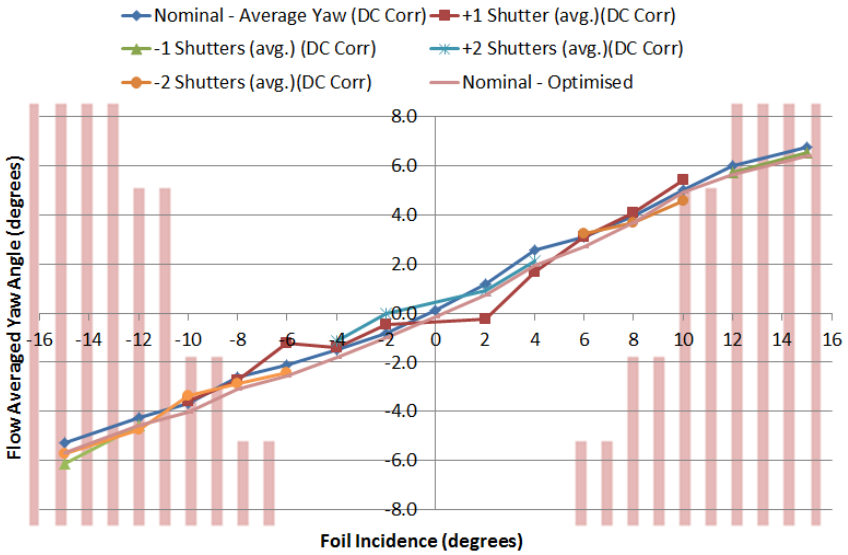


Figure 219 - Average yaw for all test cases

Figure 220 shows the variation in flow standard deviation, averaged over the 9 recording locations. It can be seen that there is a systematic increase in flow deviation with aerofoil incidence, showing increased flow instability at higher yaw angles. Standard deviation is always less than 0.9°, with a nominal measure of around 0.4° of standard deviation at zero incidence, suggesting acceptable yaw consistency over the aerofoil angle range.

The optimised trace does show a generally lower standard deviation than the nominal run, though the difference is not significant.

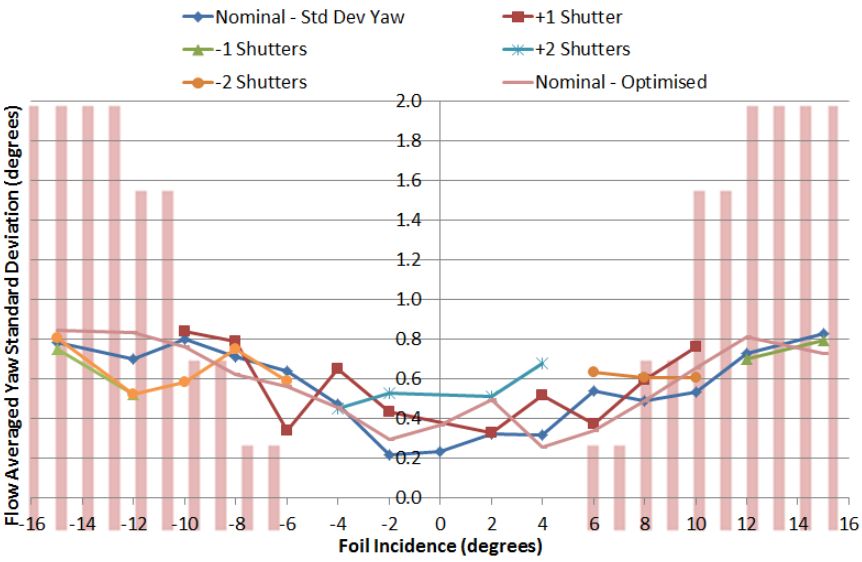


Figure 220 - Flow averaged yaw standard deviation

Figure 221 represents the variation between front and rear yaw angle across the yaw range. The most notable point is that the optimised and nominal results show very similar trends, with the optimised result showing slightly negative yaw (rear greater than front yaw) bias, whereas the nominal run presents slightly front yaw bias results. Either way, the variation is not too dissimilar between the results and suggests good flow uniformity throughout the test section of less than 0.5° of yaw variation over the 1.5m of axial length measurement region.

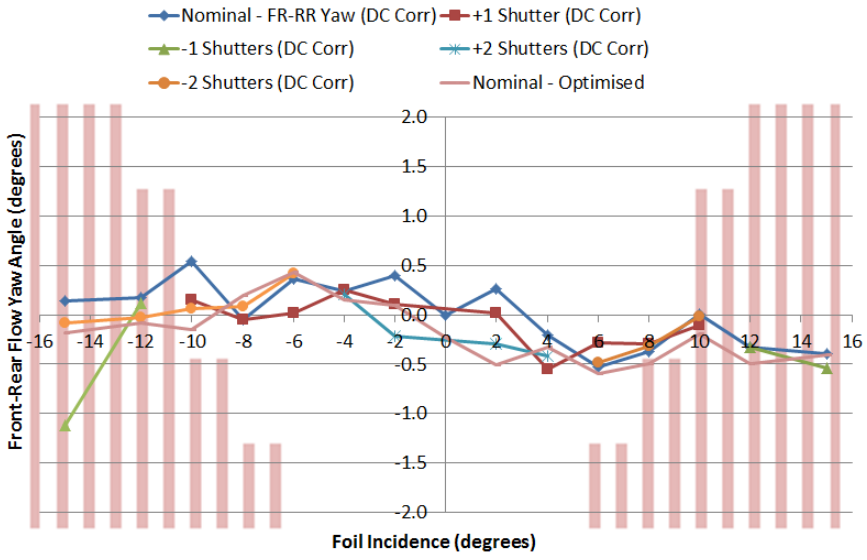


Figure 221 - Front-to-rear average flow yaw angle

Figure 222 represents the side-to-side yaw variation, with a clear systematic bias to Y+ at near zero aerofoil incidence and Y- bias at more extreme aerofoil incidence angles.

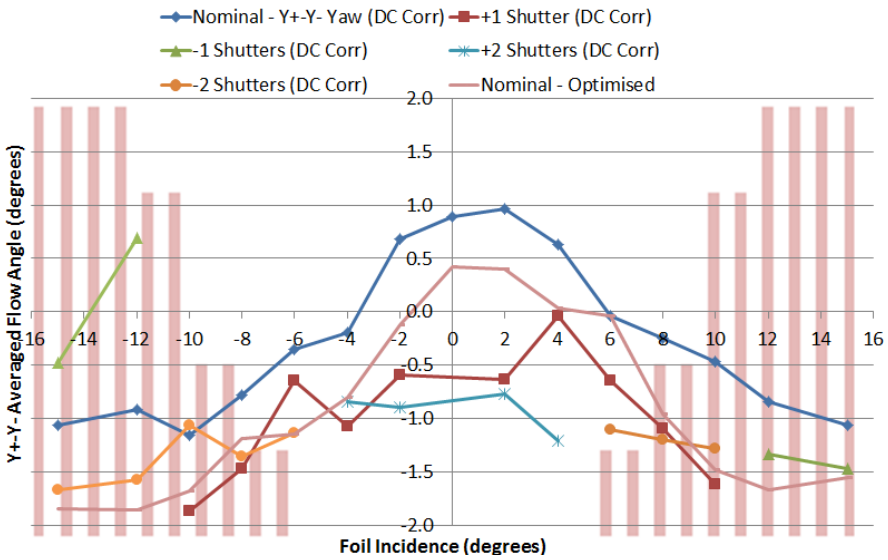


Figure 222 - Side-to-side averaged flow yaw angle

Table 15 therefore displays the best configurations from the original test map, determined by the set-up that generated the greatest yaw angle without compromising the front-to-rear or side-to-side uniformity and without increasing flow instability. The optimum results, however, required an asymmetric configuration that opens the shutters differently at positive and negative aerofoil yaw angles.

This is counter-intuitive and did not offer any significant benefit over the logical, 'nominal' configuration. Therefore, the nominal results were deemed the best configuration, especially as they require symmetrical shutter operation ensuring improved flow uniformity in the dynamic test cases.

Table 15 - Optimum results for all tests - numbers show ranking of configuration test result

| Foil angle (degrees) | Nominal Front | Nominal Rear | | Test1-Front | Test1-Rear | | Test2-Front | Test2-Rear |
|---|---|---|---|---|---|---|---|---|
| 15 | 5 | 4 | | 4 | 3 | | | |
| 12 | 5 | 4 | | 4 | 3 | | | |
| 10 | 4 | 4 | | 5 | 4 | | 3 | 3 |
| 8 | 2 | 3 | | 3 | 4 | | 1 | 2 |
| 6 | 1 | 2 | | 2 | 3 | | 0 | 1 |
| 4 | 0 | 0 | | 1 | 1 | | 2 | 2 |
| 2 | 0 | 0 | | 1 | 1 | | 2 | 2 |
| 0 | 0 | 0 | | | | | | |
| -2 | 0 | 0 | | 1 | 1 | | 2 | 2 |
| -4 | 0 | 0 | | 1 | 1 | | 2 | 2 |
| -6 | 1 | 2 | | 2 | 3 | | 0 | 1 |
| -8 | 2 | 3 | | 3 | 4 | | 1 | 2 |
| -10 | 4 | 4 | | 5 | 4 | | 3 | 3 |
| -12 | 5 | 4 | | 4 | 3 | | 4 | 4 |
| -15 | 5 | 4 | | 4 | 3 | | 4 | 4 |
| | | | | | | | | |
| | | | Best Results | | | | | |

From the tests results, the final aerofoil angles at which the shutters open, as per the nominal configuration, were determined as in Table 16, converted into motor crank angles (required for the TGS software). The raw aerofoil angles are shown in Table 28, in the Appendix, on p.260.

Table 16 - Static test results; Final shutter opening angles based on motor crank position

**Front Shutters**

| | Shutter No. | Angle (degrees) |
|---|---|---|
| *Positive* | 1 | 208 |
| | 2 | 215 |
| | 3 | 217 |
| | 4 | 222 |
| | 5 | 334 |

| | Shutter No. | Angle (degrees) |
|---|---|---|
| *Negative:* | 6 | 26 |
| | 7 | 28 |
| | 8 | 33 |
| | 9 | 37 |
| | 10 | 42 |

**Rear Shutters**

| | Shutter No. | Angle (degrees) |
|---|---|---|
| *Positive* | 11 | 20 |
| | 12 | 26 |
| | 13 | 29 |
| | 14 | 33 |

| | Shutter No. | Angle (degrees) |
|---|---|---|
| *Negative:* | 15 | 200 |
| | 16 | 208 |
| | 17 | 216 |
| | 18 | 219 |

*Positive angles: Shutters 6-10 and 11-14 open*

*Negative Angles: Shutter 1-5 and 15-18 open*

## 8.3 Initial Dynamic Aerofoil Oscillation and Shutter Actuation Tests

### 8.3.1 Dynamic Test Set-up

Dynamic TGS commissioning tests were also undertaken using the harmonic mode of the device at a range of frequencies, as specified in Table 17. Frequencies were chosen to be equidistant on the log scale and yet capture the full frequency range, from the peak frequency of the TGS down to the quasi-steady limit at tunnel scale and speed.

Table 17 - Dynamic test frequencies

| Frequency (Hz): | 0.5 | 1.0 | 2.0 | 4.0 | 9.0 |
|---|---|---|---|---|---|
| Log. Frequency: | -0.30 | 0.00 | 0.30 | 0.60 | 0.95 |
| Log Frequency Delta: | -0.60 | -0.30 | 0.00 | 0.30 | 0.65 |

Dynamic results were processed in a similar fashion to the static results with average peak yaw, standard deviation and side-to-side variation shown. Front-to-rear comparisons are made through assessment of the yaw against time period traces shown. Results were generated using ensemble averaging, aligned by aerofoil yaw, which returns one aerofoil oscillation trace consisting of numerous aerofoil oscillation recordings. The peak-to-peak yaw (or pitch) result was evaluated from the maximum and minimum yaw angles reported from the ensemble averaged yaw results. To avoid spurious peak angle results, the reported peak angle needed to occur for more than 20 readings at 1,024Hz. The standard deviation, as earlier, is the standard deviation of the peak yaw angles from all of the measurement locations. The side-to-side average yaw is similarly evaluated from the yaw maximum to minimum range result for each of the 3 respective measurement locations (e.g. average of the left hand side 3 yaw range measurements minus the average of the right hand side 3 yaw range measurements). When plotted, these results are shown as the time-averaged result over the test run (which, due to time alignment, is always an integer number of periods).

Of course, as a yaw wave propagates down the test section over a period of time, the yaw at the front of the test section would not, for the same instantaneous moment, be expected to be the same as at the rear of the test section. However, the peak angle and deviation over an aerofoil oscillation cycle would be expected to be equal (i.e. achieve the same peak yaw, just at a different time). Hence, where front-to-rear comparisons are noted, they are based upon this concept.

A set of dynamic tests were conducted to assess the effect of changing a variety of parameters to the system's operation. The main factors considered were:

1. The aerofoil angle at which the shutters open and the sequence of opening
2. The aerofoil angle at which the shutters close and the sequence of closing
3. The air flow time delay between the front and rear shutters

### 8.3.2 Preliminary Dynamic Test Results

The consideration of the sequence of shutter actuation assessed the following options, with earlier and later being relative to the phasing of the shutters to the lateral yaw aerofoils:

1. Open all shutters at the nominal angles found from the static tests.

2. Open the shutters earlier (i.e. in advance, pre-fire) than the static angle tests, to make potential consideration for the time required to accelerate the air flow in the TGS inlet ducts.
3. Open the shutters later than the static angle tests to make potential consideration for the time required for the aerofoils to turn the air flow (i.e. to open once the main flow has yawed).
4. To open all of the shutters in the cascading format suggested by the static test results, or all at once.

With the same respective considerations for the closing of the shutters.

The test format used a datum condition, which was the nominal set-up from the static shutter tests. Tests were aligned based upon master axis angle (when the aerofoils passed $0^{o}$, using a TTL signal) and were ensemble averaged over an 8-second recording window at a 1,024Hz logging frequency.

The preliminary set of tests were completed with varying shutter opening and closing sequences, with the results shown in Table 30, in the Appendix, on p.260. The cases are titled as to how the cascading opening or closing of the shutters was set relative to the datum condition (essentially a set of tests to vary the shutter opening and closing sequence and timings). The 'open all the shutters initially' case (i.e. open all the shutters once the foiled was not at $0^{o}$) showed the largest yaw angle range, however as this case would cause problems in an arbitrary mode, and would create problematic flow asymmetry at lower frequencies, it was not an ideal option. Ultimately the preliminary tests showed that a more analytical approach would need to be taken to find an improvement in shutter sequencing from the nominal set-up, but provided experience in to the analysis of the TGS's operation.

## 8.4 Aerofoils Only Test

In order to gain a further understanding and datum condition for the dynamic tests, a set of tests were conducted using the aerofoils only, with no shutter operation, with the traces presented in Figure 223 to Figure 228. Very good flow uniformity was found at lower peak angles of yaw. It is also evident that at the high frequencies, 4Hz and above, though the traces are clearly correctly time aligned by a TTL signal, the yaw is less consistent around the vehicle's measurement area due to there being multiple yaw wavelengths in the test section at any one time (e.g. at 9Hz, covering a time period of 230ms, there are 2.1 yaw periods in the 5.5m test section). Figure 228 additionally shows 2 periods at frequencies of 0.5, 2.0 and 9.0Hz in order to show the variation of yaw at turntable-centre over the frequency range. The consistency of the yaw traces for all of the 9 measurement locations shows good yaw consistency both longitudinally and laterally in the test section.

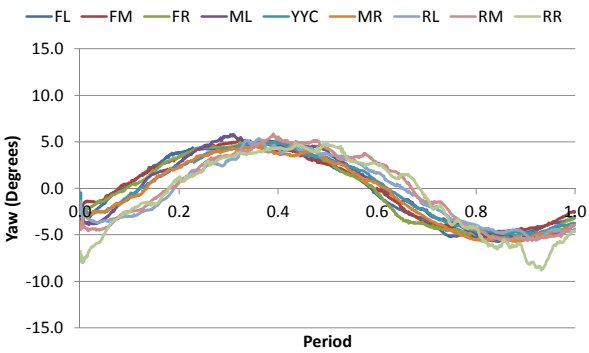


Figure 223 - Aerofoils only - 0.5Hz

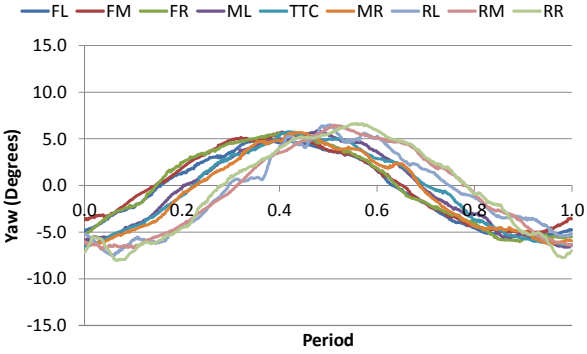


Figure 224 - Aerofoils only - 1.0Hz

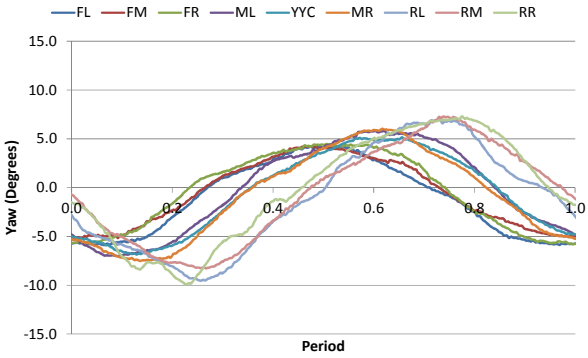


Figure 225 - Aerofoils only - 2.0Hz

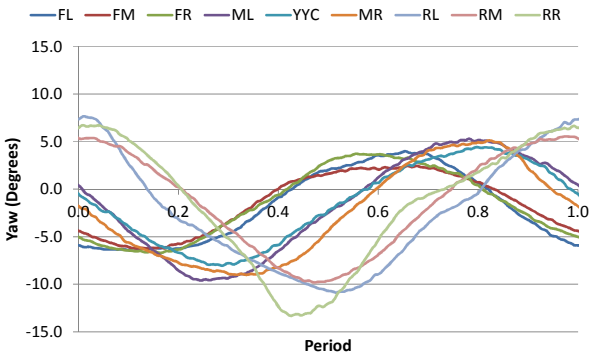


Figure 226 - Aerofoils only - 4.0Hz

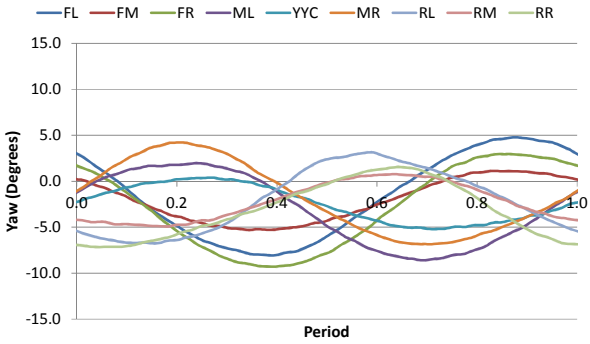


Figure 227 - Aerofoils only - 9.0Hz

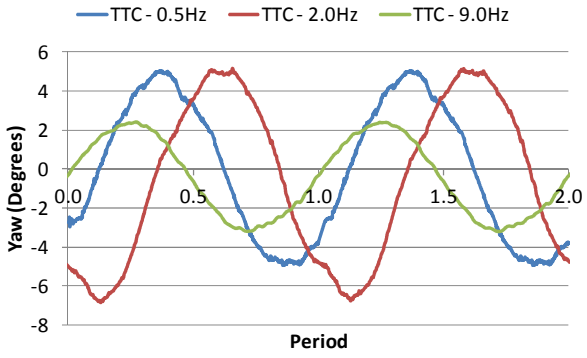


Figure 228 - 2 Periods at 0.5, 2.0 and 9.0Hz

Cross-correlation was also undertaken between the mid-front, TTC and mid-rear 5-hole probe locations to see the time delay between them at 4Hz, given in Figure 229. Note the increasing phase-shift between the front, middle and rear measurement locations, as would be expected. The cross-correlation (τ) peak occurs at a time interval that correctly correlates with the test-section velocity and distance between measurement locations.

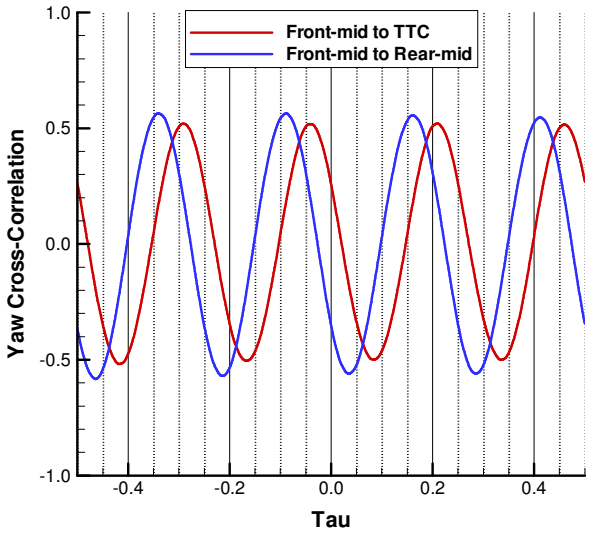


Figure 229 - Cross-correlation showing the time delay between the front-mid and TTC and rear-mid probe location at 4Hz

Analysing the aerofoils only tests in greater detail, Figure 230 to Figure 232 show the standard test metrics. The average peak yaw is relatively consistent at all frequencies, but drops off at 9Hz, which is suggesting that the momentum of the flow, as well the decay rate of the yaw angle with propagation distance, becomes significant at higher frequencies. This is also evident by the notable increase in average yaw angle deviation with frequency (Figure 232).

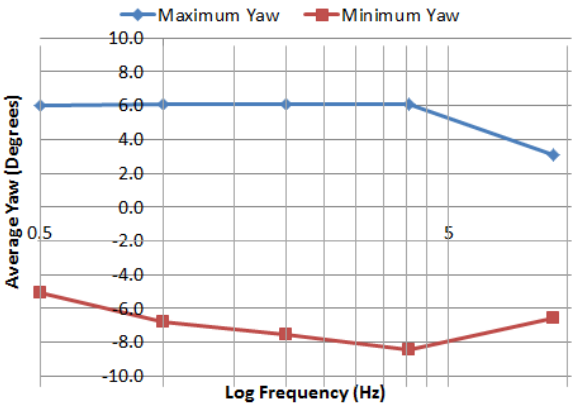


Figure 230 - Average peak flow yaw of against oscillation frequency

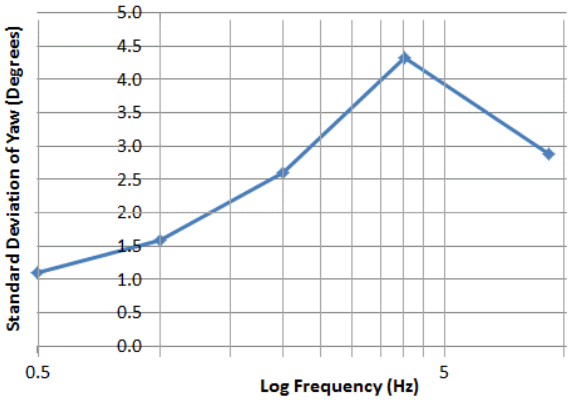


Figure 231 - Standard deviation of averaged yaw against oscillation frequency

Side-to-side variations, shown in Figure 232, show a degree of frequency sensitivity, but are close to typical readings from earlier shutter tests and are small relative to total yaw angle deviations, suggesting good lateral yaw consistency.

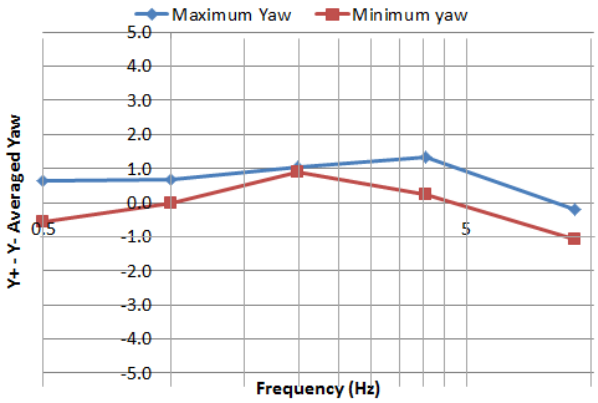


Figure 232 - Side-to-side averaged yaw difference against oscillation frequency

## 8.5 Shutter Opening and Time Delay Tests

### 8.5.1 Front to Rear Shutter Actuation Phasing by Time Delay and Sequencing

A study was completed into the effects of varying the sequence at which the shutters open and close and the time delay between the front and rear shutters from an experimental (as opposed to theoretical) set of tests. Ten tests were undertaken. The first 5 tests used the shutter opening profile from the static test results (i.e. the nominal configuration) with the shutters all closing at once as the aerofoils passed 0° incidence. The second set of 5 tests had the shutters cascading open and close. The cascade was set such that the shutters would open inner to outer, then close outer to inner, so the outer shutter was open for the shortest period and the inner shutter the longest. Each of the 5 tests were conducted at 2Hz, but with the time delay between the front and rear shutters varying in terms of phase, as given in Table 18. The time delay is based upon the test-section freestream longitudinal velocity and longitudinal distance between the inlet and outlet TGS shutter units.

Table 18 - Time delay phasing in terms of motor crank phasing

| **Time delay phases:** | | |
|---|---|---|
| 90 | 273 | ms |
| 45 | 245 | ms |
| 20 | 230 | ms |
| 0 | 218 | ms |
| -20 | 206 | ms |
| -45 | 191 | ms |
| -90 | 164 | ms |

The datum condition was at 2Hz oscillation rate with a 218ms time delay between the front to rear shutters, with data logging at 1,024Hz for 8-seconds and 250Hz low-pass filters in use. Readings were all time-aligned by a TTL generated from an optical pick-up on the motor crank, with the results ensemble averaged.

For the results from the cascade open only tests, shown in Table 30 in the Appendix, p.261, the focus was to assess the peak angle of the rear three readings to see whether the yaw peaks are greater than the upstream results in the same graph. A difference would suggest poor rear shutter timing as the flow has to turn significantly to enter the main collector rather than return via the rear TGS ducts. In this manner, the 218ms and 230ms result were of the greatest interest, with the rear-right yaw peak being slightly lower at 230ms, but interestingly the rear-left peaking lower in yaw in the 218ms trace. It is also of interest to note how similar the yaw traces are at all locations showing consistent yaw propagation. From the results of the cascade open only tests, it was evident that closing all of the shutters at once caused a sudden and large change in the yaw angle in the flow at the rear of the section, which was not ideal. Therefore the tests of the shutters cascading open and close are only presented in detail.

### 8.5.2 Cascade Open and Close Results

Moving to a test configuration where the shutters cascade open and close, the same time delay tests were undertaken and are shown in Figure 233 to Figure 237. These results show a general shift in time relative to the 'cascade open only' results as the sudden pulse caused by the shutters all closing at once is no longer occurring. The results still show a good yaw consistency, with the 218ms result presenting a generally smoother yaw trace than the other time delay tests.

It is of interest to see a double peak in the rear-left result suggesting that the shutters are opening just in time, and that potentially having them open for longer could offer an improved yaw trace at the rear, which would be of value if a larger test vehicle model was used. Again, the yaw consistency both longitudinally and laterally throughout the test section is evident from the similar yaw traces.

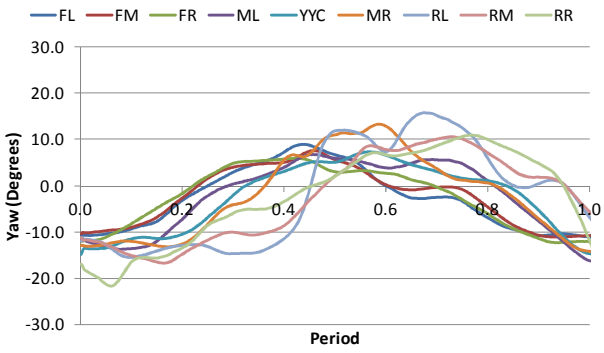


Figure 233 - 2.0Hz - Cascade open and close - 164ms

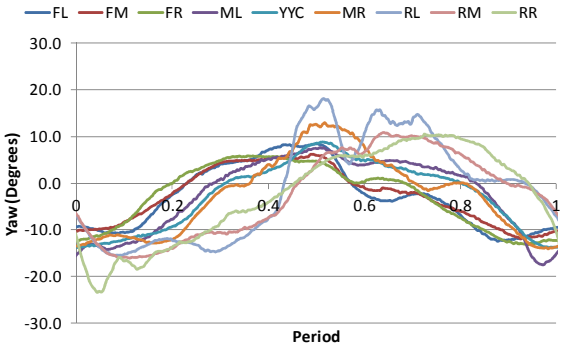


Figure 234 - 2.0Hz - Cascade open and close - 206ms

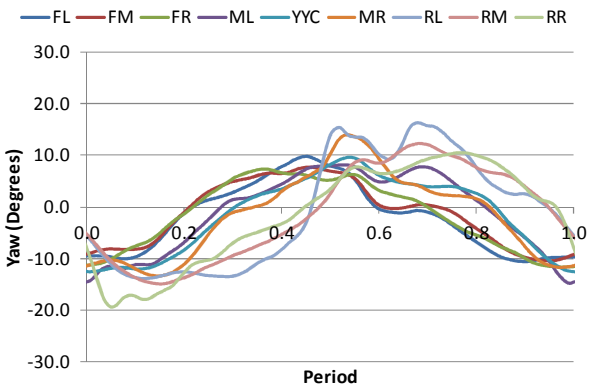


Figure 235 - 2.0Hz - Cascade open and close - 218ms

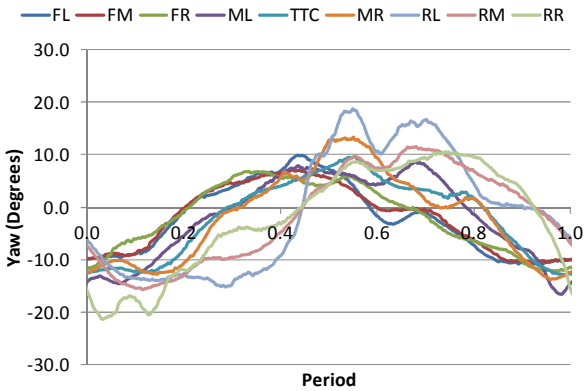


Figure 236 - 2.0Hz - Cascade open and close - 230ms

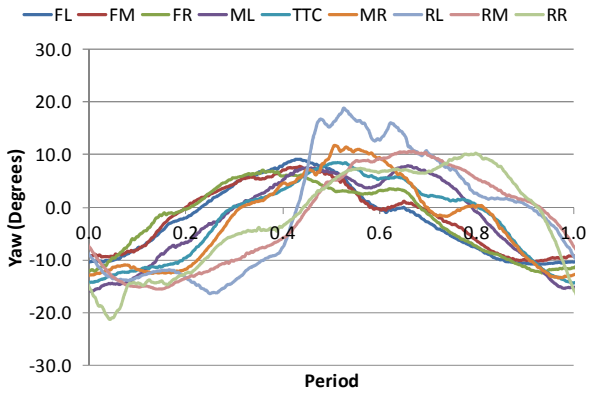


Figure 237 - 2.0Hz - Cascade open and close - 273ms

Figure 238 summaries the time delay tests for TTC average yaw measurements. The average peak yaw angles are very similar for the range of time delays. However, in the side-to-side variation, shown in Figure 239, the 218ms result clearly shows the smallest total variation between side-to-side measurements, suggesting the optimum time delay.

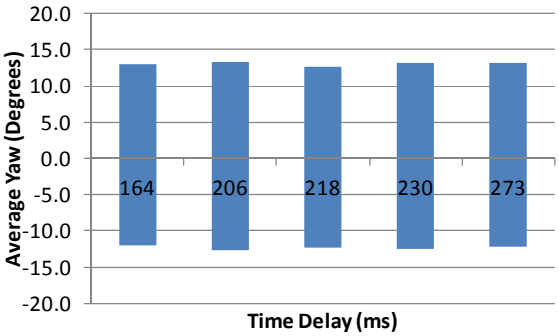


Figure 238 - Cascade open and close - peak yaw angle at TTC

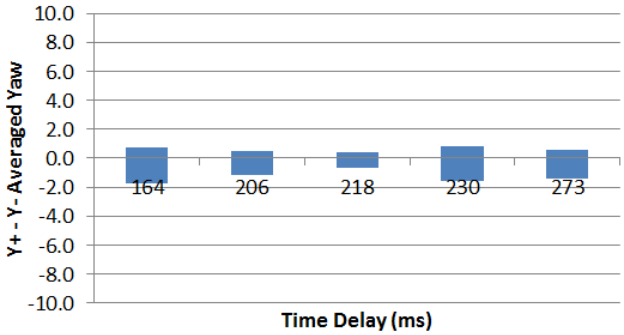


Figure 239 - Cascade open and close - side-to-side difference

## 8.6 Nominal Aerofoil and Shutter Test Run

The nominal test configuration was then tested at 0.5, 1.0 and 2.0Hz with the 218ms time delay between the front and rear shutters. Since the lower frequencies show the more notable effects of shutter timing, not performing higher frequency tests was not a significant limitation. It can be seen in Figure 240 to Figure 242 that higher yaw angles result than from the aerofoils only run, though the traces are not as clearly sinusoidal as the aerofoils only test runs.

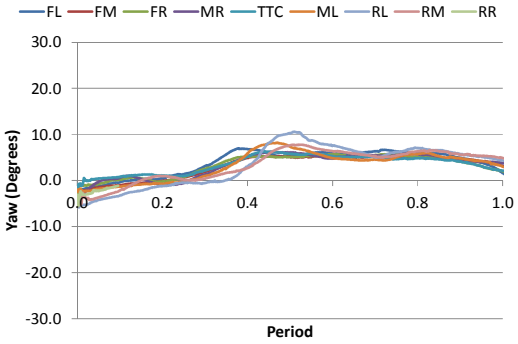


Figure 240 - 0.5Hz nominal aerofoil and shutter test

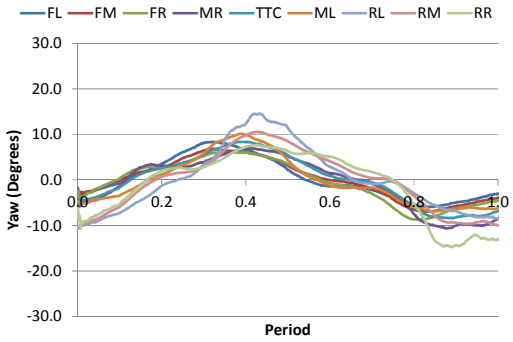


Figure 241 - 1.0Hz nominal aerofoil and shutter test

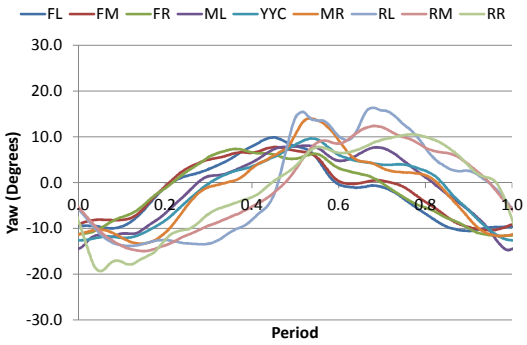


Figure 242 - 2.0Hz nominal aerofoil and shutter test

Figure 243 to Figure 245 show the variation in average yaw, standard deviation of average yaw and side-to-side variation by frequency. It can be seen, as previously, that peak yaw increases with frequency up to 2Hz and equally that standard deviation increases with frequency. However, yaw peak angles are greater than the aerofoils only test, showing an improvement in the TGS operation.

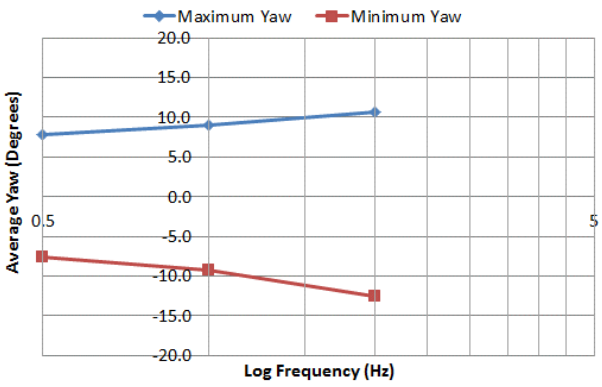


Figure 243 - Average peak yaw

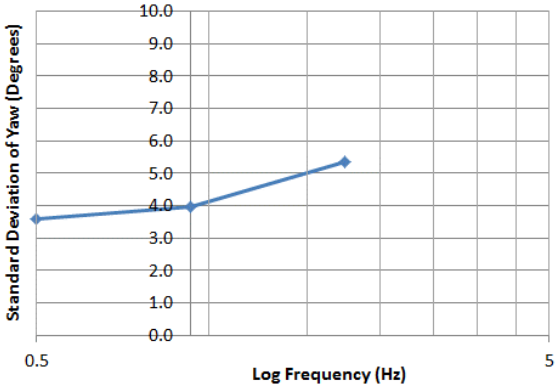


Figure 244 - Standard deviation of averaged yaw

Side-to-side comparison results, shown in Figure 245, are of a similar order of difference to the aerofoils only result.

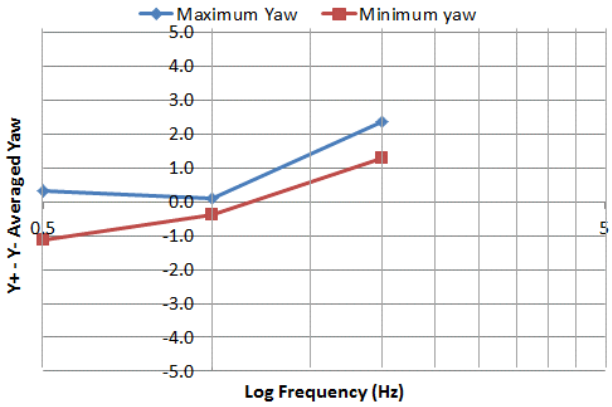


Figure 245 - Average side-to-side yaw difference

Tests were additionally run using the experimentally derived shutter configuration results from the static tests (denoted the 'optimum' results in the static shutter test section) at 0.5, 1.0 and 2.0Hz. Again large peak yaw angles were generated, greater than in the aerofoils only scenario. However a double yaw peak was evident in the rear-left measurement at 2Hz, suggesting that the rear shutters may not be open for a sufficiently long period at intermediate oscillation rates. Average yaw was comparable to the aerofoils only test, but with a similar standard deviation and side-to-side variation remaining consistent. However, the configuration did not show any notable improvements over the nominal set-up and was therefore not investigated further.

## 8.7 Shutter Impulse Propagation Assessment

Earlier tests have shown the challenge involved in comparing TGS set-up tests side-by-side, and as such it became relevant to assess the required shutter operation more analytically than simply through

numerous comparative tests. Ignoring the shutters initially, flow yaw in the test section propagates at axial flow velocity down the test section. Therefore a straightforward cross-correlation between aerofoil angle (time aligned from the TGS PLC) to each of the 5-Hole probe measurement locations would yield the yaw propagation time down the test section, as given in Table 19 and Figure 246. Tau (τ) indicates the time difference between two correlated signals, and the amplitude represents the level of correlation. The tau values are nominally greater than predicted (i.e. axial velocity is around 25.6ms$^{-1}$, so the entire test section should be traversed in 218ms) but the difference is mainly due to the time taken for the PLC command to be implemented, that is to say that the trigger to yaw time is being measured as opposed to yaw at nozzle to yaw at 5-hole probe location time.

**Table 19- Trigger of aerofoil oscillation to 5H-Probe measurement time delays, by cross-correlation**

| FL | FM | FR | MR | TTC | ML | RL | RM | RR |
|---|---|---|---|---|---|---|---|---|
| 0.109 | 0.112 | 0.111 | 0.161 | 0.153 | 0.163 | 0.221 | 0.228 | 0.218 |

| Front Average: 0.111 s | Middle Average: 0.159 s | Rear Average: 0.222 s |
|---|---|---|

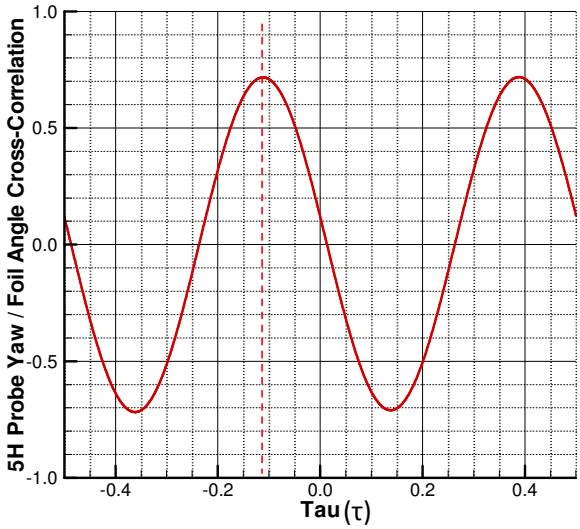


**Figure 246 - Aerofoil angle to probe cross-correlation for Front-Right (FR) (Location 2)**

With this propagation time known, there is the question of the propagation time of the shutter flow. When the shutters of a front inlet duct open all at once, the time taken for the flow to accelerate can be determined analytically, giving the time required for the added flow to reached freestream velocity:

$$\text{so } a = \frac{P_{DYN}}{\rho A} \text{ and } t = \sqrt{\frac{U}{\frac{1}{2}a}} \Rightarrow t = \sqrt{\frac{U\rho A}{\frac{1}{2}P_{DYN}}} = 0.20s \quad [28]$$

Where time taken for flow to accelerate to freestream velocity (t) is in seconds, $P_{DYN}$≈ 500Pa, inlet area (A) = 6 x 0.06 x 1.12m = 0.336m$^2$, freestream velocity (v) = 25.6ms$^{-1}$ and air density (ρ) = 1.125kgm$^{-3}$.

This gives 0.20s as the time for the flow to reach freestream velocity, which of course is greater than the time taken for the flow already at freestream velocity to propagate. Additional to this (as seen with the aerofoil cross-correlation time) is a time delay for the TGS PLC to actuate the shutters. Therefore the shutters, in theory, need to be pre-fired by 0.20s to factor in this delay such that the flow from the shutters can have the necessary time to be at full velocity.

These parameters are summarised in Figure 247, where it can be seen that there is a delay in shutter movement from the PLC actuation signal, plus an additional delay for flow acceleration after the shutters open. The period of time for which a shutter is open should not be varied too greatly, otherwise the outer shutters would never be able to open at even moderate harmonic frequencies (as the out shutters open last and close first).

Effects for the rear TGS collectors (i.e. when they open and close) should, however, propagate upstream at the speed of sound (i.e. effectively instantly relative to freestream), which was supported by earlier tests showing that the exhaust shutters are already correctly timed.

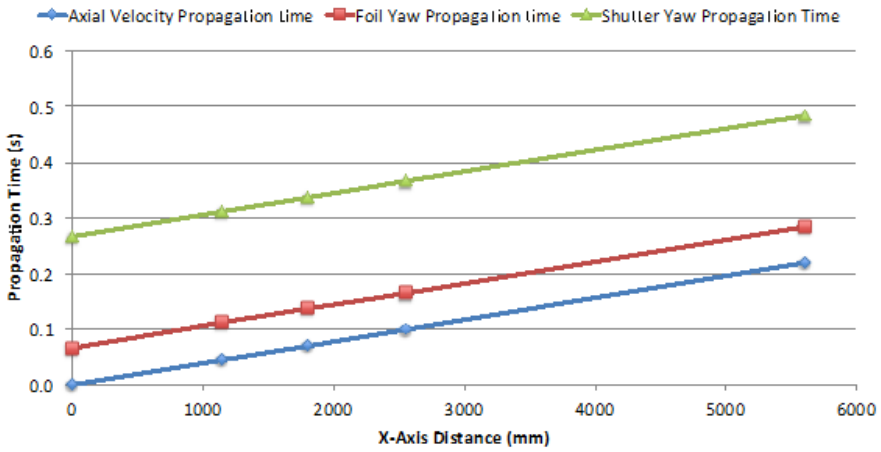


Figure 247 - Yaw propagation time against longitudinal location

There is a velocity rise time (i.e. acceleration overcoming the air momentum) for the inlet TGS ducts, and it was necessary to conduct a test to evaluate the correct shutter firing (and closing) time for both the front and rear shutter sets to verify the appropriate timings (though the rear shutters were expected to be set correctly). In order to do so, a test was undertaken with four actions (front shutters close, open, rear shutters close and then open) each spaced by 3.6s (sufficient time to allow for the fans to settle after a previous actuation). These actions were logged and time-aligned by a trigger signal, with the trigger signal and the time profile both shown in Figure 248.

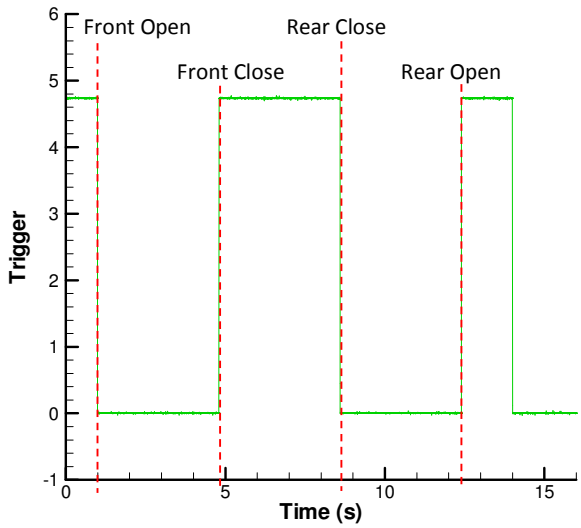


Figure 248 - Event sequencing - Front open (1.0s), Front close (4.8s), Rear close (8.6s) and Rear open (12.4s)

Additionally, in order to measure the flow acceleration characteristic, pitot-static tubes were placed at the downstream side of the front and rear shutters, as in Figure 249. The probes, being large, do exhibit some pressure measurement effects due to the stagnation and static tappings being

approximately 50mm apart, but otherwise offer a good insight into flow velocity. They were logged simultaneously with the trigger signals and the 5-hole probe. The two tests were conducted, with the first opening and closing all shutters and the second with just the middle shutter moving (with the other shutters open on the inner side, and closed on the outer, as correct with the nominal shutter opening angles). Flow velocity was consistent at 25.6ms$^{-1}$ and logged at 1,024Hz.

Figure 249 - Pitot-static tube mounting location on the downstream side of the front Y+ inlet duct

It was found that using axial velocity ($U_X$) for when the shutters open, and yaw for when the shutters close, as the metrics for propagation time was appropriate as these yielded the clearest result and are directly comparable. From opening and closing the rear shutters, rapid changes could be seen in axial velocity and yaw upstream of the rear shutters. However, as the pressure propagation effects are almost instant, and there is a relatively long time for the mass of air in the rear shutter ducts to accelerate or equally to be absorbed by the fans, the changes are not sufficiently clear to be seen on a time against pressure plot. This suggests that the timing of the rear shutters does not requires phasing adjustment, especially as the two batches of time delay tests completed earlier showed that the time delay of 218ms offered the optimum result in terms of a reduced standard deviation of flow yaw. Therefore only the front shutters, and specifically the test of opening and closing all of the shutters at once for the front of the test section measurements, are detailed.

The results from the 'opening all shutters' test can be seen in Figure 250, with the trigger signal at 0.0s (i.e. immediate, that is 0.0s after the data logger started recording, which is 1.0s into the TGS case file as shown in Figure 248). It can be seen that there is a clear lag between the trigger signal and the shutter actuating (around 0.08s) and then additionally a time delay of around 0.12s for the test section to show a drop in flow velocity due to the increased flow area, with a full flow acceleration time of around 0.20s, as predicted. It is therefore apparent that at frequencies above 2Hz, where the inner shutter is open for only around 0.20s, that the flow in the TGS side inlet ducts never reaches full velocity (which was around 23 - 24ms$^{-1}$ over the first few seconds of recording). Though the result suggests a notable velocity change in the test section, note that the pitot-static was extremely close to the shutter and that in normal operation all of the shutters would not actuate simultaneously. Therefore the dramatic velocity change is unique to this experiment and, as seen in earlier results, the shutter actuation aids yaw generation without significantly affecting test section velocity.

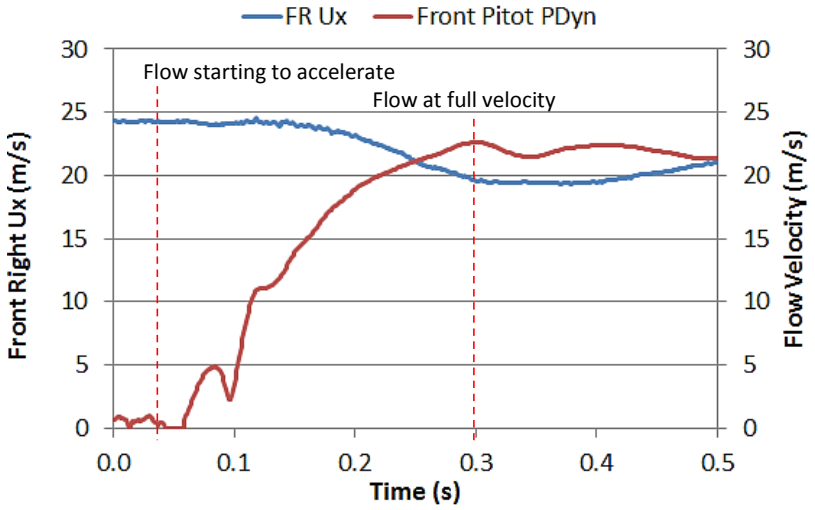


Figure 250 - Front Right 5-Hole probe measurement location longitudinal velocity and front pitot dynamic pressure for all shutters opening, triggered at t=0.0s

The closing front shutter test showed a response for the pitot-static tube as shown in Figure 251, where after approximately 0.08s the probe showed a rapid rise in dynamic pressure, and then after around 0.12s from trigger the 5-Hole probe showed a change in yaw angle. Clearly the closing of the shutters cause the flow to rapidly retard (under 0.04s). Again, the dramatic pressure changes are due to the shutters closing all at once, without the aerofoils oscillating, and therefore in normal operation the shutter motion does not cause such velocity perturbations.

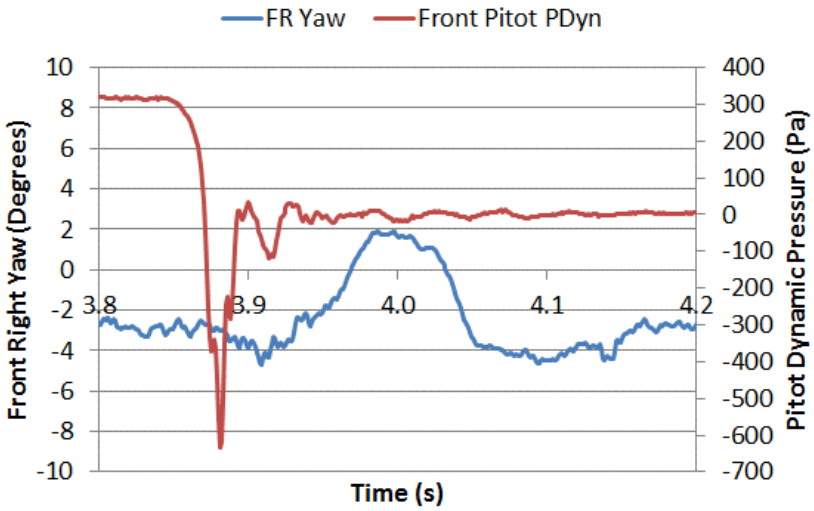


Figure 251 -Yaw trace with pitot-static dynamic pressure for closing all front-right shutters at once, triggered at t=3.8s

A cross-correlation of the 5-Hole probe $U_X$ with the shutter trigger signal is given in Figure 252, showing a peak at 0.15s The peak in τ correlates with the time taken for a shutter open trigger signal to cause a notable variation in the axial velocity and for that variation to propagate downstream (i.e. $\left(\Delta X / U_X\right)$.

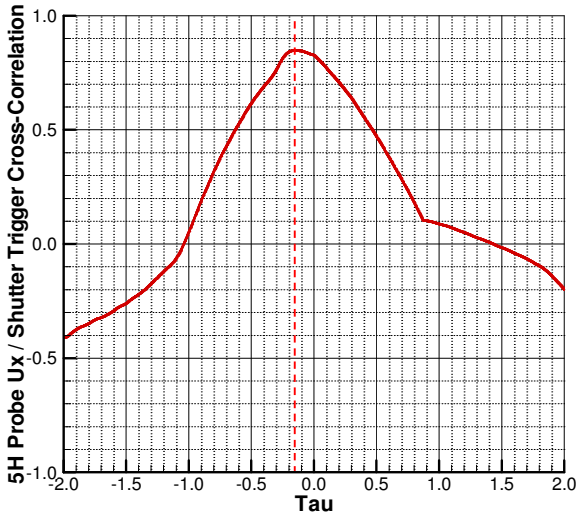


Figure 252 - 5-Hole probe to shutter trigger signal cross-correlation for the front-right shutter unit

Tau values for the three averaged lateral measurement locations are given in Table 20. The results are both realistic and increasing with downstream location. Since the actual peak of the cross-correlation curve is slightly flat, averaging offers the best interpretation of the actual time value.

Table 20 - Shutter closing to 5-Hole probe $U_X$ variation, averaged over width-wise sets

| | | | | | | | | |
|---|---|---|---|---|---|---|---|---|
| Front average: | 0.159 | s | Middle average: | 0.189 | s | Rear average: | 0.203 | s |

Additionally a cross-correlation was performed between the 5-Hole probe axial velocity and the front pitot-static dynamic pressure, shown in Table 21. The results show that the distribution is similar to Table 20 by axial position and that the times are notably less than the correlation against the trigger signal. The trigger signal to front pitot-static probe time of 0.09s by cross-correlation relates well to the early time graphs, showing 0.09s to be the typical PLC actuation time.

**Table 21 - Front Close - Front pitot $P_{DYN}$ to 5H-probe $U_X$**

| | | | | | | | | | |
|---|---|---|---|---|---|---|---|---|---|
| Front Average: | | 0.105 | s | Middle Average: | 0.137 | s | Rear Average: | 0.153 | s |
| | | | | | | | | | |
| | | | Trigger to Front Pitot: | | 0.085 | s | | | |

Finally, it is possible to determine the corresponding pre-fire advance required for the shutters, given in Table 22. The time of the flow propagation to the front three measurement locations was averaged, and was subtracted from the average trigger to probe propagation time, giving a pre-fire advance time of 0.048s.

**Table 22 - Determination of shutter opening pre-fire time**

| Location | Trigger to Foil Delay (s) | Trigger to Probe Motion (s) | Opening Pre-Fire Advance (s) |
|---|---|---|---|
| 0 | 0.109 | 0.159 | 0.050 |
| 1 | 0.112 | 0.159 | 0.047 |
| 2 | 0.111 | 0.159 | 0.048 |
| Average (s): | 0.111 | 0.159 | **0.048** |

For this time to be of value, it has to be converted into a pre-fire advance by motor crank angle for the TGS control software, as shown in Table 23. These results are frequency dependent, and are therefore of greatest value for harmonic tests.

**Table 23 - Evaluation of shutter opening pre-fire angle**

| Frequency (Hz) | Period (s) | Opening Pre-Fire Advance (degrees) |
|---|---|---|
| 0.5 | 2.0 | 9 |
| 1.0 | 1.0 | 17 |
| 2.0 | 0.5 | 35 |
| 4.0 | 0.3 | 70 |
| 9.0 | 0.1 | 157 |

## 8.8 Horizontal Aerofoil Tests

### 8.8.1 Static Horizontal Aerofoil Tests

Pitch control, that is variation in $U_Z$, was assessed through tests using the installed horizontal aerofoil. The horizontal aerofoil tests were undertaken in a very similar manner to lateral yaw flow tests. The first test was a static angle test, with pitch results shown in Figure 253 and yaw results in Figure 254 (to

determine if pitch flow effects the flow yaw). The pitch results, shown in Figure 253, show that pitch range is -0.2° to -4.0°, showing a nominal downwash when the aerofoil is level. The tunnel 'non-TGS' mode has the horizontal aerofoil set with a motor angle of 85°, giving a aerofoil incidence of +9°, which is actually when the aerofoil is level, confirming that the non-TGS mode configuration induces no additional pitch to the test section flow. Standard deviation of flow is consistent at all angles, with very consistent front-to-rear and side-to-side variation in pitch over the aerofoil incidence range, showing what would be a consistent pitch over the entire vehicle model.

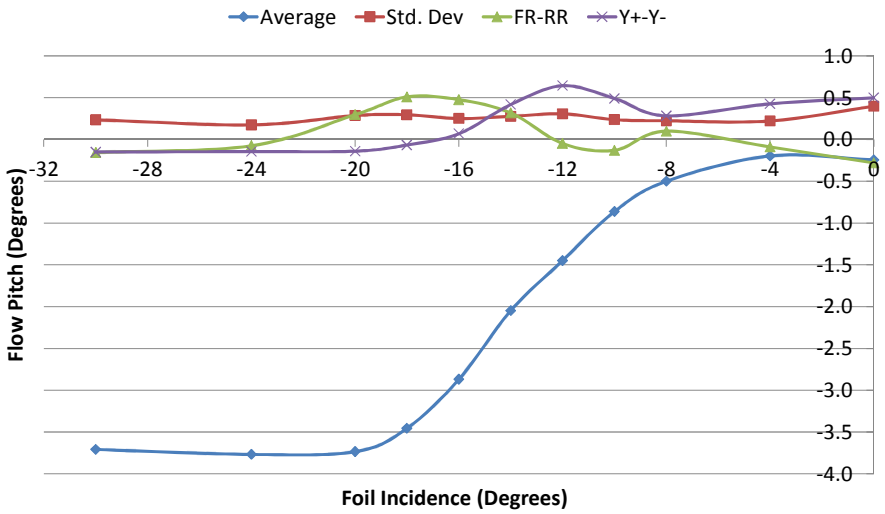


Figure 253 - Horizontal static tests - pitch results

Figure 254 presents the yaw results caused by the horizontal aerofoil incidence, which shows consistent average yaw variation and front-to-rear yaw. However, it is evident that the side-to-side yaw increases above −10° of incidence (which is causing the standard deviation to increase) due to recirculating flow regions occurring at the sides of the test section. Therefore if pitch tests are to be undertaken, the effect of these recirculation regions should be also considered (i.e. large pitch variations will corrupt expected yaw results).

The asymmetric nature of the plot is due to the aerofoil having only a few degrees of upwash pitch, and also that angling the aerofoil upwards creates a diffusion angle, where flow direction changes are less prominent.

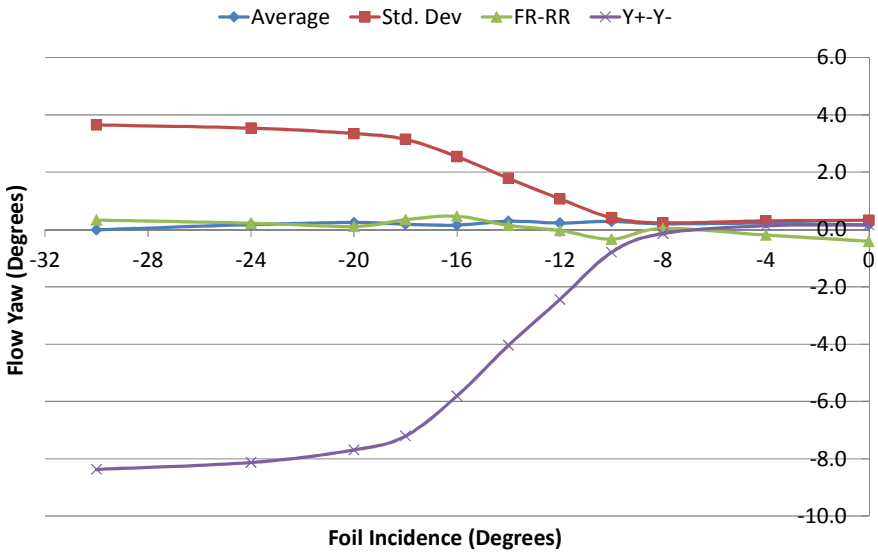


Figure 254 - Horizontal static tests - yaw results

### 8.8.2 Dynamic Horizontal Aerofoil Tests

Figure 255 to Figure 259 present the pitch traces at a range of 5 frequencies, with 6Hz being the maximum frequency that was thought to be sustainable for aerofoil operations at ±15° of incidence. Note that, as shown in the static test results, the aerofoil's mid oscillation pitch is at a downwash angle, hence the pitch will always tend to a downwash bias in harmonic testing mode (but can be controlled as desired in an arbitrary test mode). The results show consistent pitch generation up to 2Hz, and then a decrease in flow longitudinal pitch consistency at higher frequencies, as more pitch oscillation periods are in the test section. Pitch range was demonstrated to be consistent to aerofoil angles of −10° incidence, but interestingly the maximum pitch angle increases with frequency, with moments of up-wash occurring above 2Hz.

All traces show a lack of true sinusoidal behaviour as at high incidence angles little pitch is created, causing the 'flat top' that is shown in many of the traces, particularly evident at 1Hz.

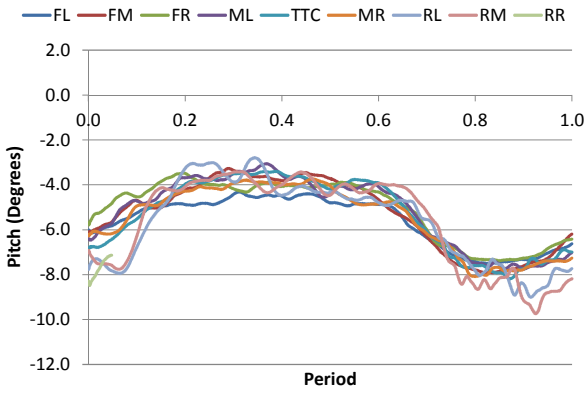


Figure 255 - Pitch results - 0.5Hz

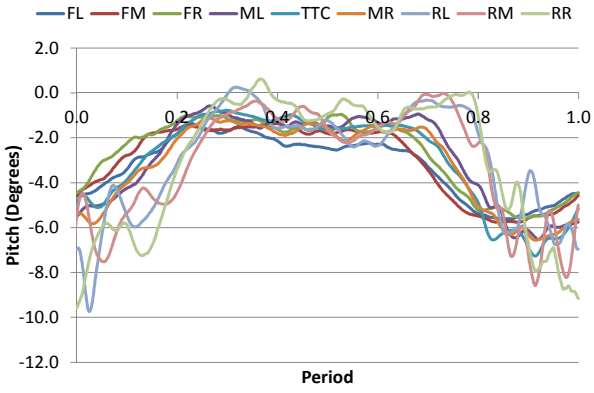


Figure 256 - Pitch results - 1.0Hz

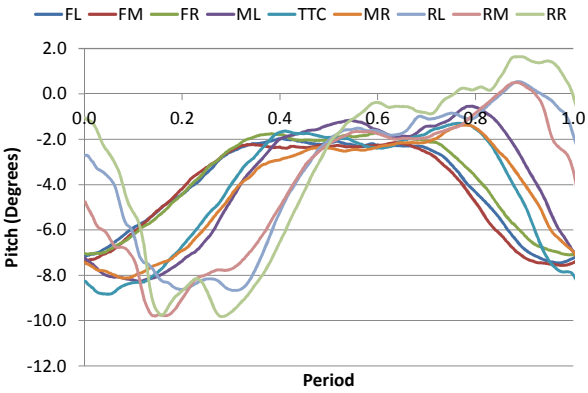


Figure 257 - Pitch results - 2.0Hz

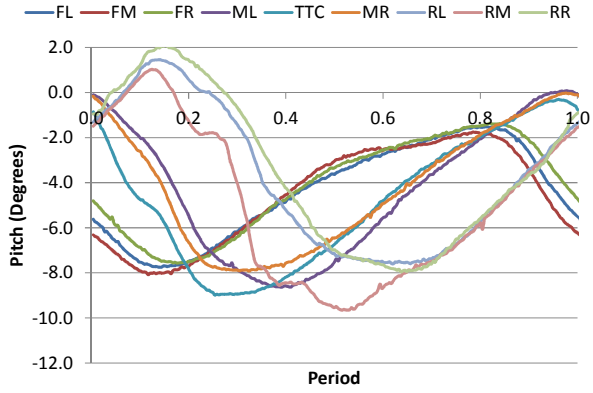


Figure 258 - Pitch results - 4.0Hz

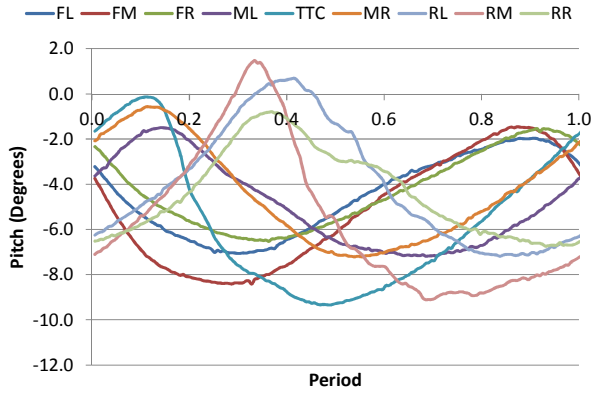


Figure 259 - Pitch results - 6.0Hz

Figure 260 and Figure 261 show pitch results grouped by both longitudinal and lateral location. The sets at the front, mid and rear of the test section show the pitch being relatively consistent, even at the vehicle rear, with angles up to -9° being common. Sets grouped by Y location show the expected time delay required for flow propagation, but otherwise good pitch consistency is seen down the test section.

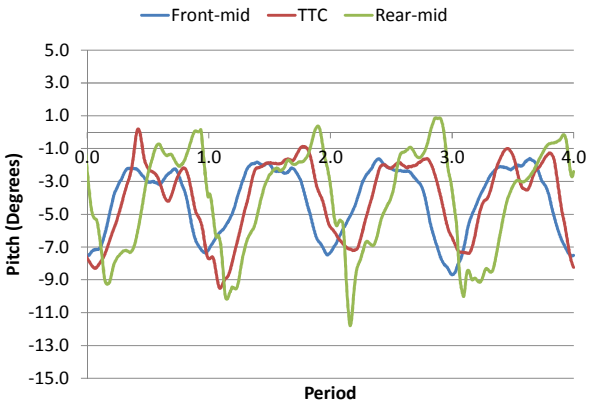


Figure 260 - Pitch Results - 2.0Hz - Mid X-axis Set

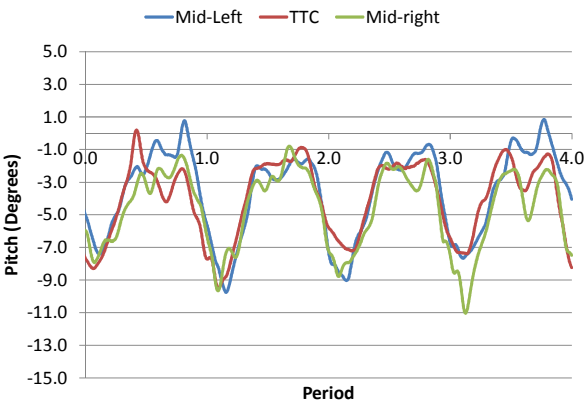


Figure 261 - Pitch Results - 2.0Hz - Mid Y-axis Set

Finally, Figure 262 shows the yaw variation at 2Hz for all measurement locations, with only one test frequency given to be indicative of all the frequencies, showing an increase in yaw at the side due to recirculating flow regions at the higher pitch angles.

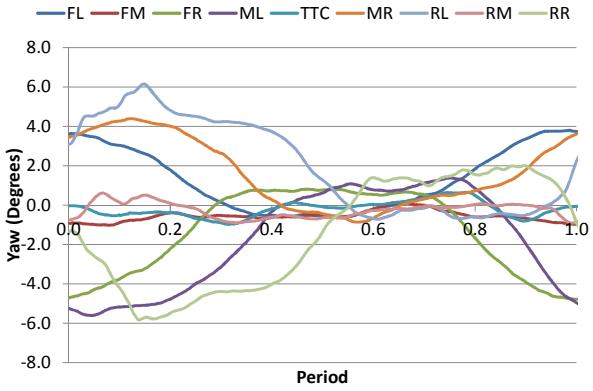


Figure 262 - Yaw result from pitch oscillations - 2.0Hz

Figure 263 to Figure 265 compare the results of average pitch, deviation and side-to-side flow consistency. It can be seen that a slight negative average pitch (i.e. downwash) is seen when the aerofoil is oscillating in a harmonic mode, showing notable pitched flow at all frequencies. The results also confirm that in the non-TGS mode, the aerofoil can be set at an angle to cause no downwash.

The standard deviation results show, however, a decrease in deviation with frequency, suggesting that at low frequencies flow instability increases, most likely occurring at higher pitch angles.

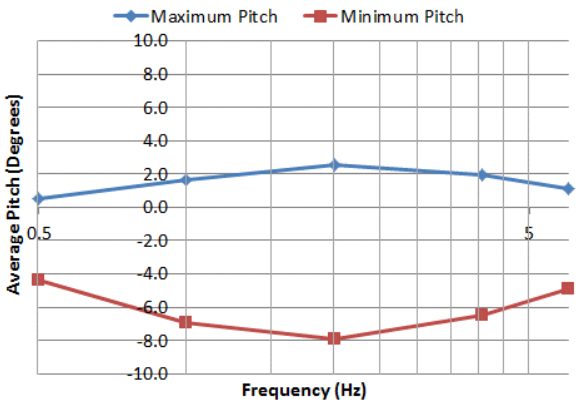


Figure 263 - Average pitch flow angle

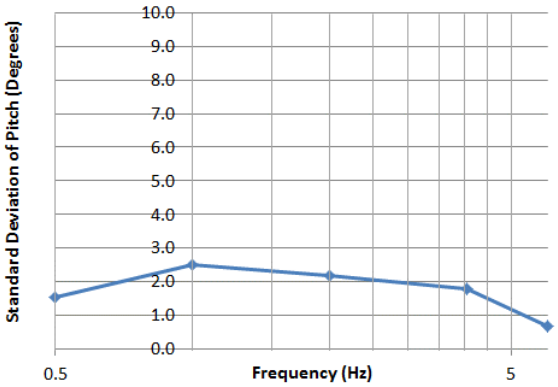


Figure 264 - Standard deviation of pitch

Figure 265 shows the side-to-side pitch variation, which shows a much tighter spread with the +0.5° step-shift likely being due to the variation in reverse pitch flow at the extreme sides of the tunnel as the aerofoil passes through its lower incidence peak.

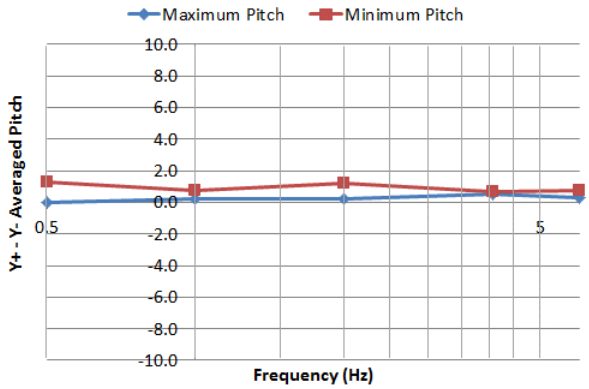


Figure 265 - Difference in side-to-side pitch

## 8.9 Arbitrary Flow Measurements

As a test of the TGS device's capability, the development of an arbitrary trace representative from the on-road measurements was completed. This trace was the on-road data, selected as a 32-second case in Chapter 4, which was processed in Chapter 7 to become an 'inflexions' trace. This yaw profile was then programmed into the TGS's PLC as motor crank angles, which is directly comparable to the measured on-road yaw. The TGS motor acceleration value was set to 14,500deg.s$^{-2}$.

The resultant aerofoil motion was recorded by a rotary Hall sensor, with the result of a wind-on and wind-off test shown in Figure 266. Firstly, it can be seen that the reproduction of the demand trace is very accurate and secondly that the wind has no shown effect on the operation of the aerofoils.

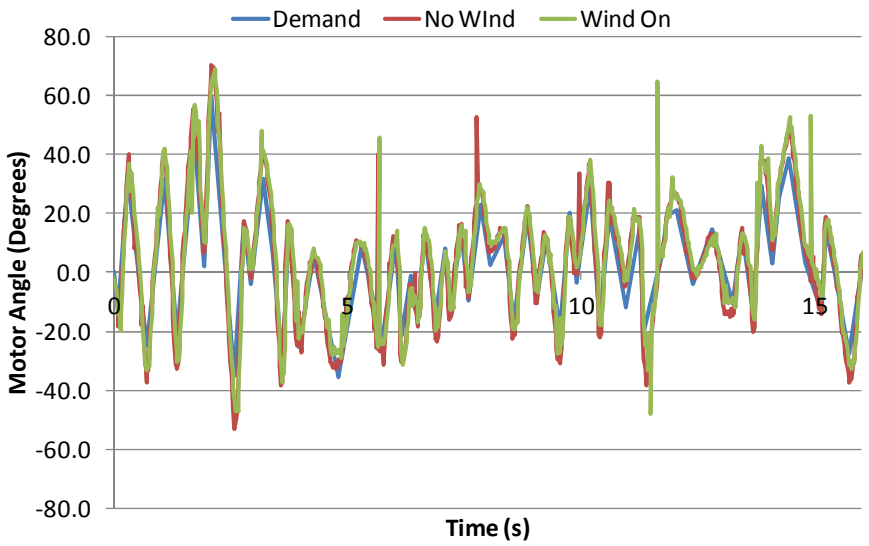


Figure 266 - TGS arbitrary trace with wind on and off against input motor crank angle demand trace

The arbitrary motion trace, given in Figure 267, is a mechanical test comparing the demand trace to the motor movement, showing a high accuracy of motion reproduction.

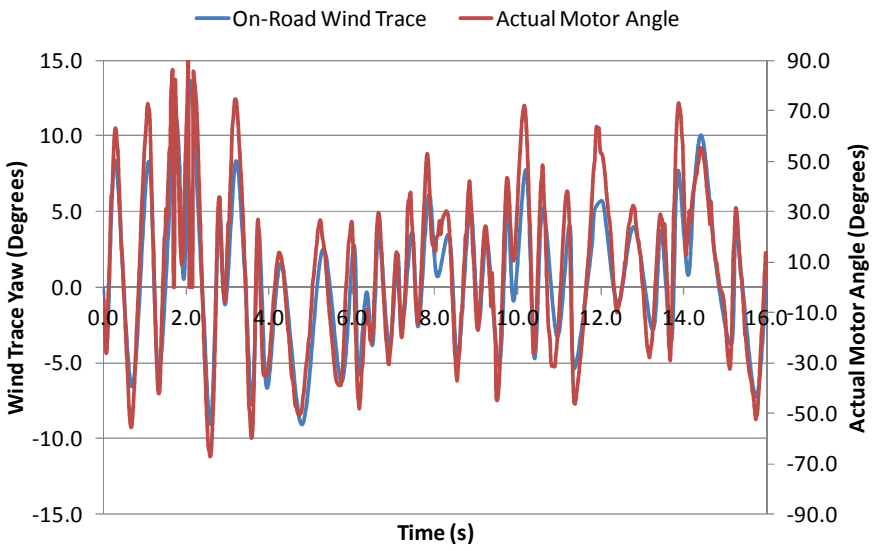


Figure 267 - On-road trace (motor demand) against aerofoil motor crank angle

Significantly, Figure 268 shows a comparison between the aerofoil movement and the recorded aerodynamic yaw at turntable centre. It can be seen that there is a strong correlation between the aerofoil angle (given in terms of motor crank angle) and the flow yaw at TTC.

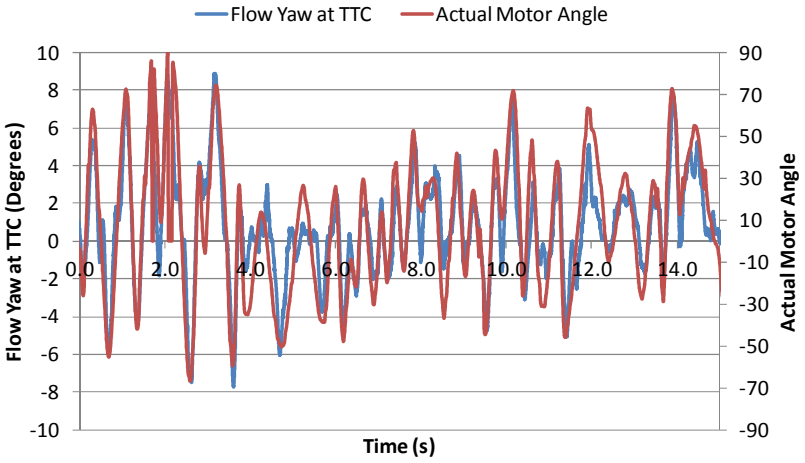


Figure 268 - Flow yaw at TTC against motor crank actual angle

The key result is that shown in Figure 269, where the TGS generated flow yaw angle is compared to the recorded on-road trace. A strong correlation is shown, with the TGS able to accurately recreate the example on-road flow condition. The generation of this accurate flow yaw is indicative that the on-road raw data conversion process, the control methodology and the shutter actuation configuration and timing settings are all well optimised.

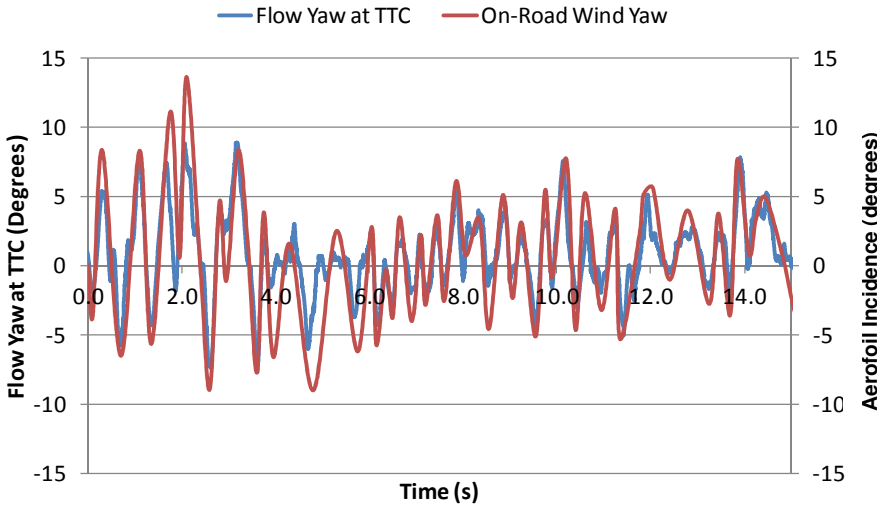


Figure 269 - TGS generated and on-road yaw comparison

Finally, it was of interest to see whether there would be peak angle attenuation if the shutters were left closed throughout the arbitrary trace. The result of this is given in Figure 270, which shows, as expected, that with the shutters always closed the peak yaw angles could not be reproduced as compared to having the shutters active. This shows, as seen in the earlier CFD studies and

commissioning tests, that the additional inlets and outlets are invaluable in generating higher peak yaw angles than with aerofoils only operations.

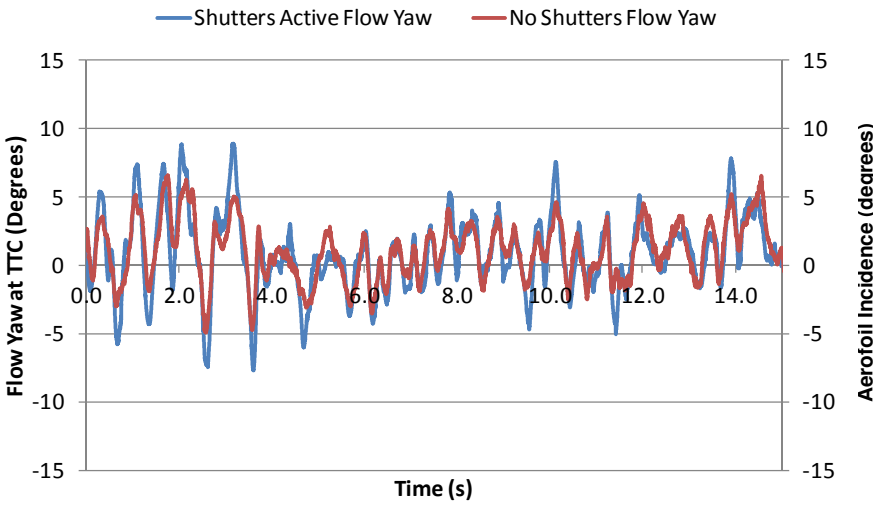


Figure 270 - Arbitrary trace flow yaw with shutters active against shutters always closed

## 8.10 Conclusions

This chapter has presented a comprehensive process to the commissioning of the TGS system at Durham University. Initially the open angles that the shutters open to were investigated to determine the effect of varying the shutter open position angle. The angle affects the inlet and outlet flow angles, with a set-up of the front shutters at 8° and the rear shutters at 15° found to be optimum.

A static assessment was completed of the shutter opening sequence at each respective yaw angle, with a nominal set-up proposed using the trigonometrically calculated yaw angles against those found through experimental derivation. It was shown that though the experimental method suggested a potentially optimum solution, such a set-up would have induced some asymmetry to the tunnel's air flow, and that on balance the nominal set-up did prove to be very good. The study then assessed the system in a dynamic mode, determining at which angles the shutters should open when the aerofoils are oscillating in a sinusoidal manner. The results were compared alongside tests when only the aerofoils operated, and using the angles found in the static tests proved to offer a good aerodynamic flow uniformity and peak yaw angle over a test vehicle's footprint.

In order to further optimise the timings of the front and rear shutters, the commissioning study experimentally evaluated the flow propagation times between shutter and aerofoil yaw operations. This was in order to produce an experimentally derived time delay between the aerofoil motion and

the front shutter and rear shutter actuations. Tests were conducted to evaluate the flow characteristics in the TGS inlet and exhaust ducts and it was found that the flow acceleration time was around 0.20s for a freestream flow rate of 25.6ms$^{-1}$. Closing the shutters all at once caused a significant pulsation to run through the tunnel and was therefore concluded to be worth avoiding. Test section flow yaw amplitude was not significantly affected by use of the rear shutters, notably as pressure effects propagated upstream at the speed of sound. The results of these tests was a TGS system that could achieve harmonically induced yaw angles up to ±10$^{o}$ with flow uniformity under 1$^{o}$ for the side-to-side variation over a vehicle's footprint in the test section, operating up to 9Hz.

The horizontal aerofoil was assessed for its pitch generation capability. The initial -5$^{o}$ of aerofoil incidence had nominal pitch effects, but thereafter pitch downwash of -4$^{o}$ could be generated, though the resultant up-wash in the lateral shear flow regions did cause side-to-side flow variations. Finally, the arbitrary test mode was developed, using the inflexions trace generated earlier in this thesis. A highly accurate replication of the on-road trace was generated, which was shown to work with the shutters active to achieve the on-road yaw profile. Ultimately, the TGS commissioning was successfully completed, offering a system that can achieve harmonic frequencies up to 9Hz, generating up to ±10$^{o}$ of peak flow yaw, variable pitch flow conditions as well as being able to replicate real world on-road flow environments within the 2m wind tunnel at realistic vehicle speeds.

# 9. Rover 200 Model Wind Tunnel Testing

As a final stage in the assessment of the effects of transient aerodynamics on passenger cars, the TGS was run with a 40% scale model under arbitrary and harmonic wind conditions. Results in earlier chapters showed that the quasi-steady simulation technique was accurate at low turbulence frequencies, but was unable to accurately predict pressure fluctuations at intermediate turbulence frequencies, where there is still significant energy in the on-road environment. Through running the TGS at these intermediate frequencies (i.e. 1 - 10Hz), the TGS's capability to replicate a vehicle's response to the on-road transient flow conditions was evaluated. The results presented show that running the TGS in an arbitrary mode is required if true on-road characteristics are to be modelled correctly in a wind tunnel.

## 9.1 Preparation of the Rover 200 40% scale model

In order to compare the effect of on-road wind conditions to the TGS simulated wind conditions, an existing 40% scale model of the Rover 200 R3 road car (produced by MG-Rover) was modified to add 9 sideglass pressure tappings, located identically as in the on-road study. Tubing between the tappings and the pressure transducer were much shorter than for the on-road test, and hence the frequency response of the tappings was notably improved.

Preparation of the model required the initially solid model to have its passenger sideglass region hollowed out and a new Rapid-Prototyped (RP) sideglass shell inserted. The new RP sideglass panel included pressure tappings, which were produced from 1.0mm inner-diameter hypodermic tubing. The RP sideglass (CAD images given in Figure 271) was designed using geometry data recorded from a Baumer laser-distance measuring device with a 0.1mm axial resolution, fitted to a 3-axis traverse. Data was recorded at a 1mm resolution along an Y-Z grid that followed the contour of the window seal (and 10mm Y-Z grid mesh for the remainder of the window area). This grid measurements were meshed in Solidworks before being exported as an STL for rapid-prototyping.

The laser measuring device and the traverse can be seen in Figure 272, and the final product in Figure 273.

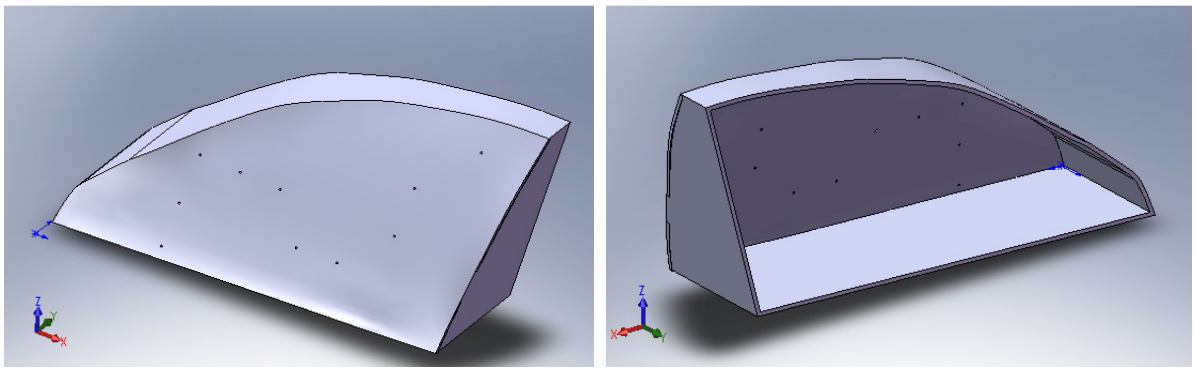

Figure 271 - CAD images of the RP Rover 200 sideglass shell

Figure 272 - Laser distance measuring device, Baumer, 30–130mm range, on 3-axis traverse

Figure 273 - Rover 200 model with sideglass tappings

## 9.2 Turntable 6-Component Balance Calibration

The wind tunnel was placed into 'fixed ground' configuration for the Rover 200 tests, in which a turntable with a 6-component balance becomes the mounting platform for test vehicles. The turntable underwent an overhaul before installation and had 6 new load cells installed, and therefore required a new calibration. The resultant loading profile is shown in the Appendix, Figure 336 to Figure 341, with notice made of the low force hysteresis as the balance was loaded and then unloaded. This calibration is used for all force measurements presented in this chapter, with a repeatability found to be better than ±0.002 on drag coefficient and ±0.003 on lift coefficient.

## 9.3 Rover 200 Wind Tunnel Test Setup

The Rover 200 model was placed into Durham University's 2m wind tunnel (Figure 274), mounted on to the turntable, with the 5-Hole probe located above the roof, in the same position as with the full-scale vehicle used for the on-road tests. Sideglass tapping locations mirrored those used on the full-scale car (with details as in Table 24 and numbering as in Figure 275).

Figure 274 - Rover 200 40% model in Durham University's 2m wind tunnel

Table 24 - Wind tunnel model specification

| | |
|---|---|
| **Model:** | Rover 200 (R3) |
| **Scale:** | 40% |
| **Frontal Area:** | 0.308m$^2$ |
| **Height:** | 555mm |
| **Length:** | 1588mm |
| **Width:** | 568mm |
| **Wheel base length:** | 1000mm |
| **Wheel base width:** | 547mm |
| **Ride height to sills:** | 88mm |

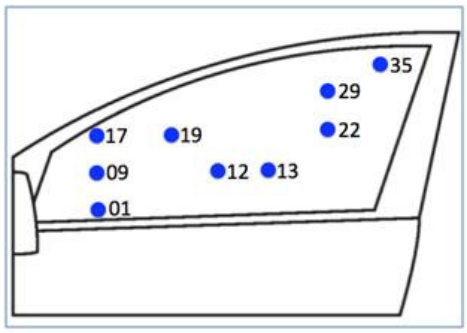


Figure 275 - Rover 200 tapping arrangement and model details

All pressure and balance data were recorded at 1,024Hz for 16,384 samples, giving 16-seconds of flow data. Where periodic TGS driving frequencies were used, force and yaw ensemble averages were taken, with each test performed twice, the first to log the sideglass tappings and the second for the 6-component force balance, with the 5-Hole probe being recorded in both tests. Transient results were processed with a transfer function correction for frequency response and forces non-dimensionalised by dynamic pressure and frontal area (as given in Table 24). Drag and sideforce corrections were not applied to the forces, and as such the coefficients are vehicle (and hence balance) aligned through both TGS and turntable induced yaw, as shown in Figure 276.

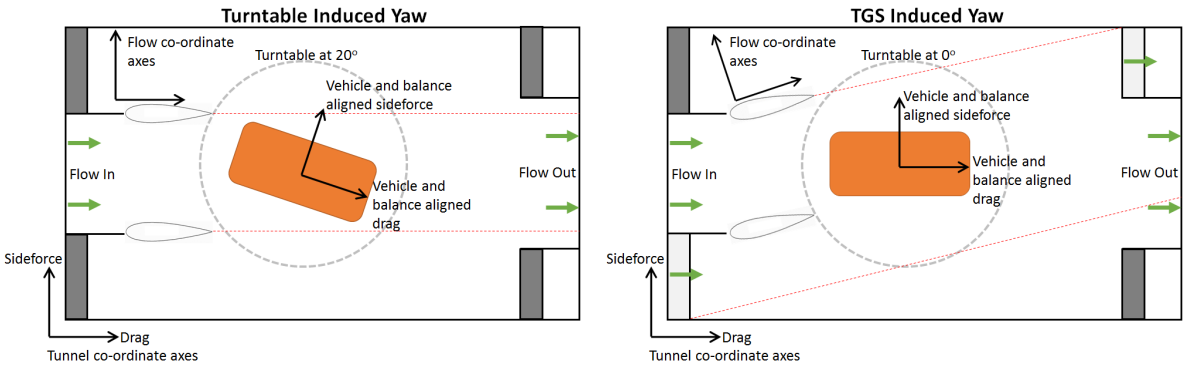


Figure 276 - Vehicle aligned forces during Turntable and TGS induced yaw (illustrative scale)

## 9.4 Test Approach

The following tests were performed on the Rover 200 model, with the balance, sideglass tappings and 5-Hole roof probe recorded for all cases:

- Steady turntable yaw angle.
- Steady TGS yaw angle.
- Harmonic excitation at 0.5, 1.0, 2.0, 4.0 and 9.0Hz.
- Arbitrary trace (taken from the Rover 200 on-road study).

## 9.5 Results - Steady-state Measurements

Steady-state measurements were performed using both the turntable and TGS induced yawed flow over the Rover model. When yawed flow propagates over a vehicle, flow is accelerated as it passes over the front windscreen (correspondingly increasing dynamic pressure over the roof relative to freestream). Yaw angles can, therefore, be corrupted if the lateral flow velocity component accelerates differently than the axial flow velocity component, which occurs most at larger yaw angles.

Figure 277 shows the increase in probe longitudinal velocity by turntable yaw angle. As this 'stretch' in yaw causes probe reported yaw angles to be greater than the actual freestream yaw angle, when roof probe yaw angles are plotted alongside turntable yaw angles, the roof probe yaw angles need to be adjusted by the relevant factor (proportionate to yaw angle). This adjustment has significance when the roof probe yaw angle is interpolated from the turntable yaw angle to determine the simulated sideglass pressures. Therefore the pressure against yaw calibration file had the turntable yaw adjusted by this 'roof probe yaw stretch factor' to ensure that the reported simulation results were accurate. The Rover 200 model underwent a turntable sweep through ±30°, recording both force balance and sideglass tappings, using steps between 1.0° and 2.5°. In Figure 278 the resultant pressure coefficient against yaw trace is shown, with a greater pressure sensitivity evident for tappings close to the A-pillar.

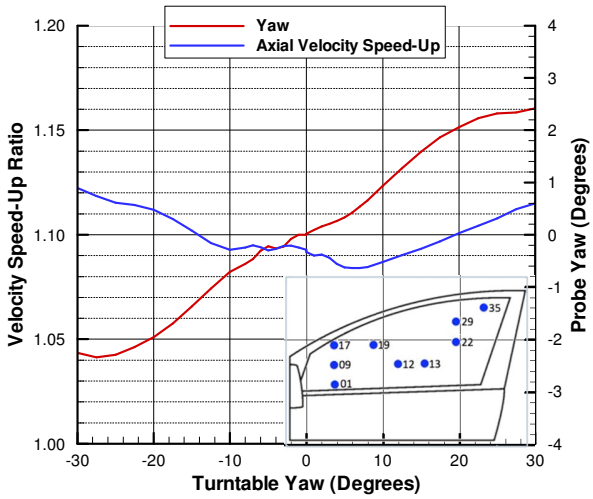


Figure 277 - Velocity speed-up and yaw error for roof probe on the 40% Rover model

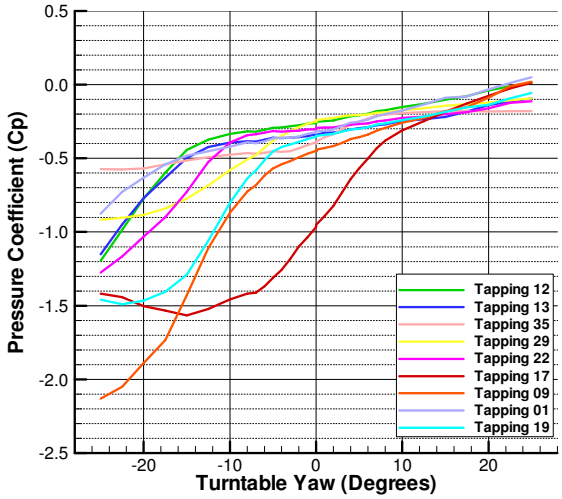


Figure 278 - Sideglass pressure coefficient against turntable yaw for the 40% Rover model

The measured force readings are given in Figure 279, showing a zero yaw drag coefficient of 0.36 (reported as 0.4 by MG-Rover (1996)), lift coefficient of 0.18, with side and yawing moment coefficients having realistic values and a linear sensitivity to yaw, for relatively small angles of yaw.

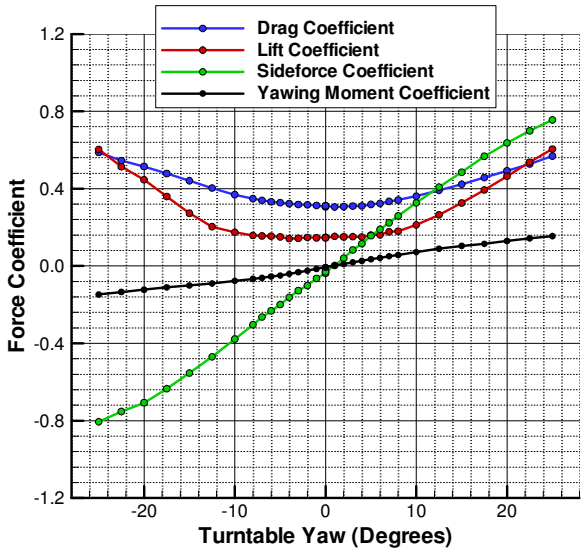


Figure 279 - Force and moment coefficients from a turntable yaw sweep of the Rover 40% model

Figure 280 to Figure 282 show pressure coefficient against yaw angle results for both turntable and TGS induced steady yaw angles, with the TGS angle being referenced by the achieved flow yaw angle from earlier TGS commissioning tests. Two key results are evident, firstly that the correlation between TGS and turntable flow yaw is good, showing that TGS yaw provides a flow that is comparable to that created by turntable yaw. Secondly, that in the yaw angle range of ±7° of steady flow, in both the turntable and TGS yaw pressure profiles, many of the sideglass tappings show a low degree of sensitivity (i.e. pressure variation against yaw angle).

This low sensitivity would impact on the effectiveness of the transient quasi-steady simulation technique for yaw permutations within such a yaw range.

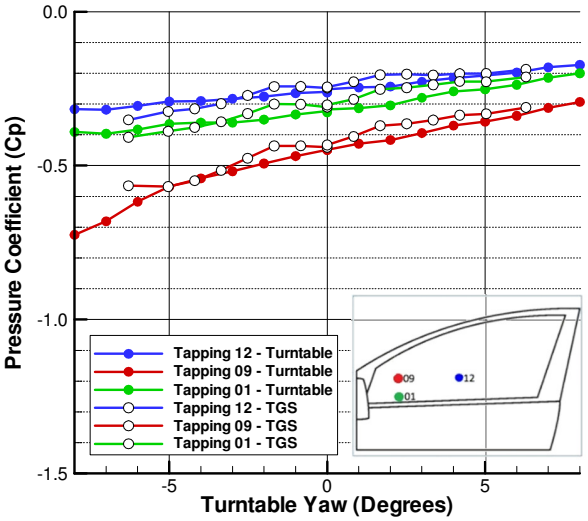


Figure 280 - Sideglass pressure coefficient results for both turntable and TGS induced yaw, tappings 01, 09 and 12

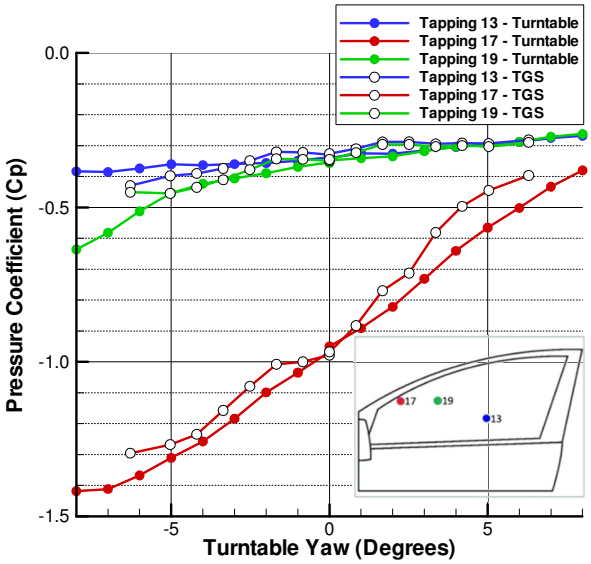


Figure 281 - Sideglass pressure coefficient results for both turntable and TGS induced yaw, tappings 13, 17 and 19

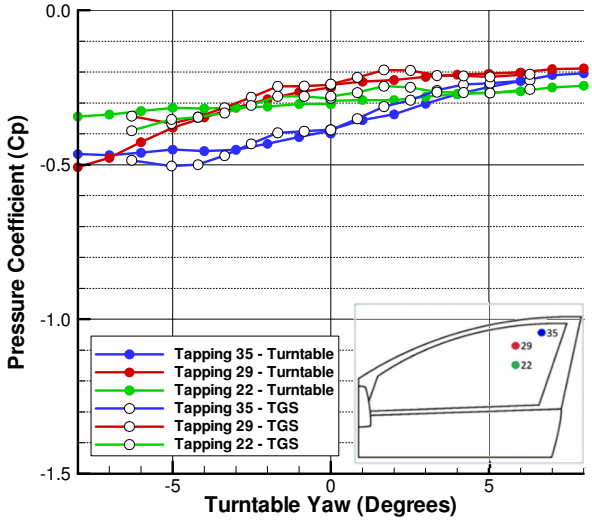


Figure 282 - Sideglass pressure coefficient results for both turntable and TGS induced yaw, tappings 22, 29 and 35

Figure 283 and Figure 284 also demonstrate a strong correlation between force and moment coefficients against both turntable and TGS induced yaw. TGS and turntable yaw are well correlated, with the sideforce showing a significant yaw interaction.

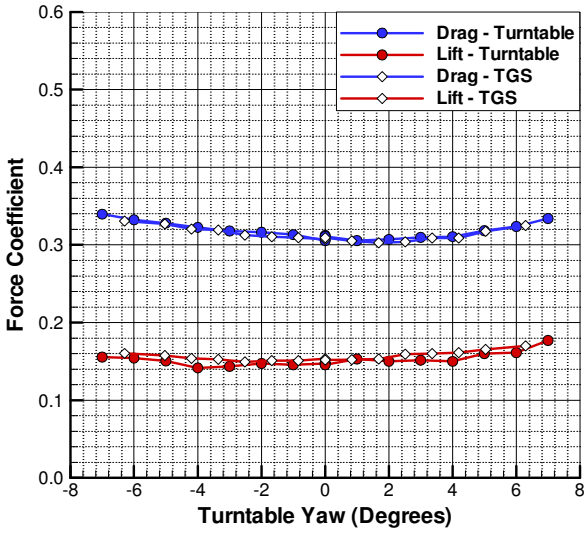


Figure 283 - Drag and lift force coefficient results for both turntable and TGS induced yaw

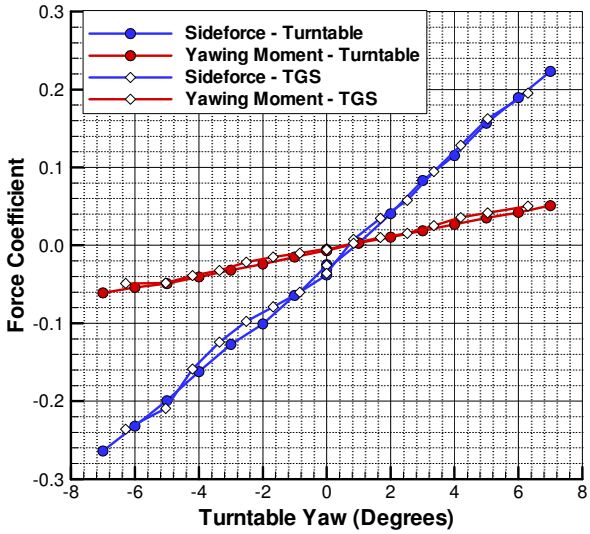


Figure 284 - Sideforce and yawing moment coefficient results for both turntable and TGS induced yaw

## 9.6 Harmonic Excitation Results

### 9.6.1 Sideglass Pressures

The TGS was run in its harmonic mode at 0.5, 1.0, 2.0, 4.0 and 9.0Hz, as in the TGS commissioning study, again with sideglass and balance measurements recorded for a 16-second window at 1,024Hz. Data recordings were time aligned by a trigger off the aerofoil incidence angle and the yaw and force results ensemble averaged where appropriate. It was noted that additional higher frequency artefacts were shown in the component forces, which are attributed to the natural frequency of the turntable balance. By auto-correlation, it was found that the natural frequency of the drag component was 4.8Hz, lift was 16.1Hz and sideforce was 6.3Hz.

Figure 285 to Figure 293 show the measured and simulated (i.e. result using a lookup based upon the pressure coefficient against yaw trace from the steady yaw angle test) sideglass pressure coefficient for tappings 17 (A-pillar region), 09 (mirror wake region, though mirrors not fitted) and 35 (A-pillar/hybrid region) at 0.5, 1.0 and 4.0Hz. All of the tappings show a strong correlation between measured and simulated pressures up to intermediate frequencies (i.e. 2Hz).

Deviation of the simulated result from the recorded trace increases at the higher frequencies, even though a high frequency yaw variation, which is most likely the vortex shedding frequency, remains consistent between the TGS driving frequencies. The higher frequency variations in sideglass pressure that were measured are not evident in the simulated traces, due to the small gradient on the pressure

coefficient against yaw calibration seen earlier in Figure 280 to Figure 282. An example of this can be seen when a significant, but short, yaw variation is seen, for example around 0.12s in Figure 293, evident in the recorded trace but not so in the simulation trace, suggesting that the simulation technique supresses reported pressure fluctuations from such yaw perturbations.

As the frequency increases above 1.0Hz, the accuracy of the simulation can be seen to decrease, with the simulated pressure coefficients often being under-predicted against the recorded readings, relative to the average result. However the general trends are still followed and the simulation technique remains of value at the higher frequencies.

The results therefore show that the TGS system gives an accurate representation of the vehicle's response over a wider frequency range than the quasi-steady simulation technique, offering insight in to vehicle pressure fluctuations at relatively high excitation frequencies.

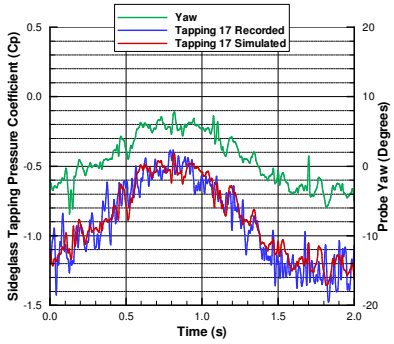


Figure 285 - Tapping 17, harmonic 0.5Hz

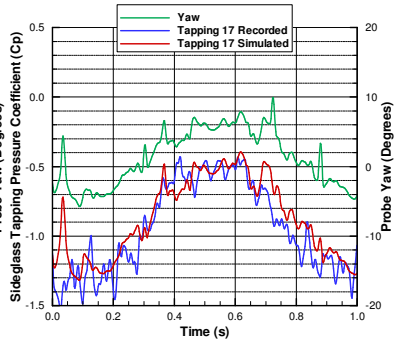


Figure 286 - Tapping 17, harmonic 1.0Hz

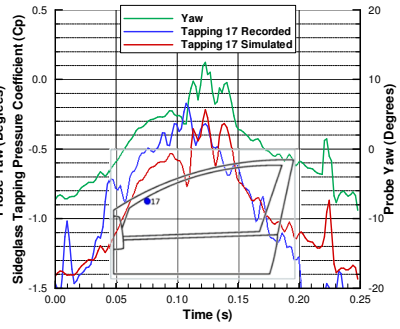


Figure 287 - Tapping 17, harmonic 4.0Hz

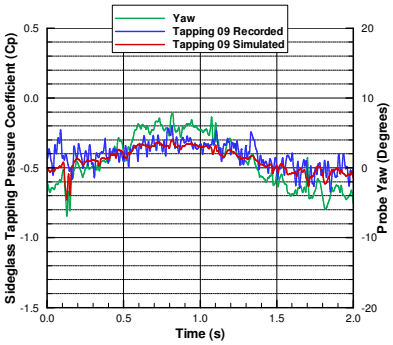


Figure 288 - Tapping 09, harmonic 0.5Hz

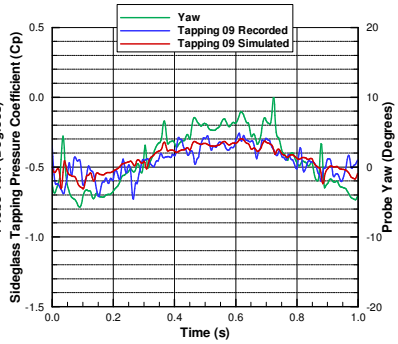


Figure 289 - Tapping 09, harmonic 1.0Hz

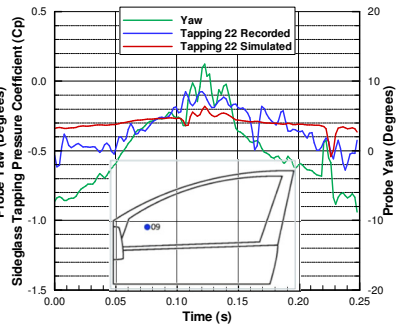


Figure 290 - Tapping 09, harmonic 4.0Hz

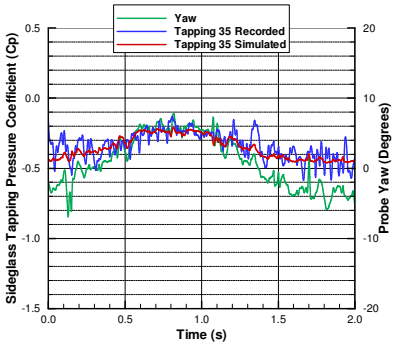


Figure 291 - Tapping 35, harmonic 0.5Hz

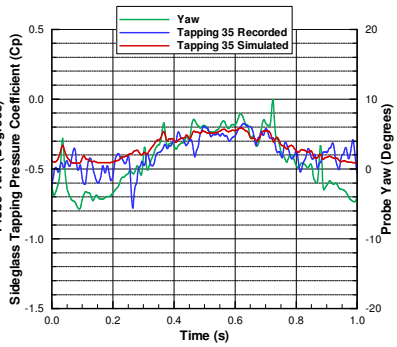


Figure 292 - Tapping 35, harmonic 1.0Hz

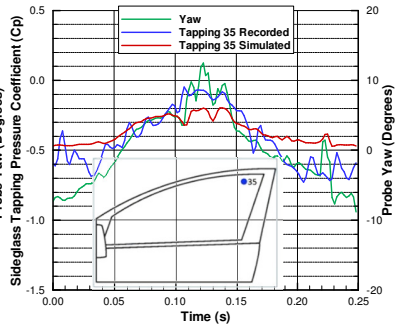


Figure 293 - Tapping 35, harmonic 4.0Hz

## 9.6.2 Forces - Sideforce

Figure 294 to Figure 296 show the recorded against simulated sideforce for the range of frequencies tested. It can be seen that, visually, the quasi-steady simulation technique is a good method of prediction. A resonance is shown in the results from the turntable balance's natural frequency, and is shown in the results from all axes. The results demonstrate that the simulation method, being yaw derived, does not report the natural frequency of the turntable and its balance. Correlation between measured and simulated can be seen to be accurate at high frequencies, even with a highly unsteady yaw angle, with a consistent yaw angle and sideforce range being generated at all frequencies.

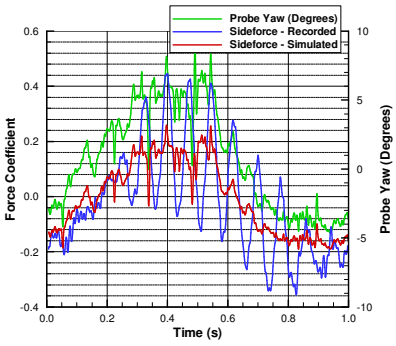


Figure 294 - Sideforce, harmonic 0.5Hz

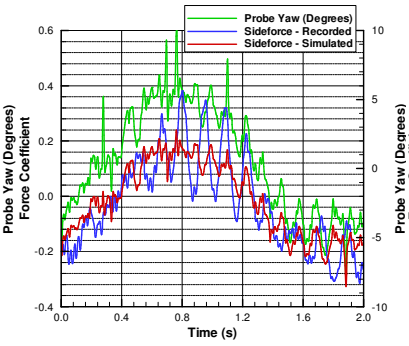


Figure 295 - Sideforce, harmonic 1.0Hz

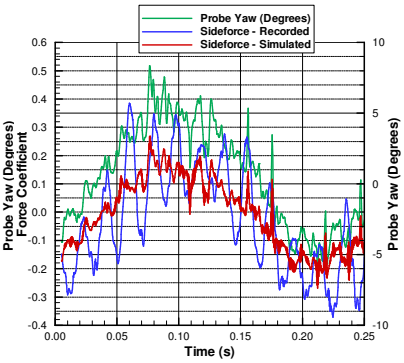


Figure 296 - Sideforce, harmonic 4.0Hz

## 9.6.3 Forces - Yawing Moment

Figure 297 to Figure 299 present the yawing moment coefficient for both measured and simulated results. The yawing moment is accurately simulated through TGS excitation and responds to a similar range of force coefficient at all frequencies. The natural frequency of the balance is not shown in the simulated result, and the lower frequency variations are accurately simulated.

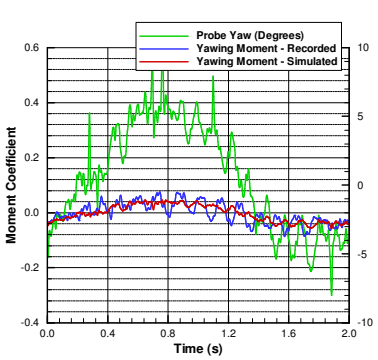


Figure 297 - Yawing moment, harmonic 0.5Hz

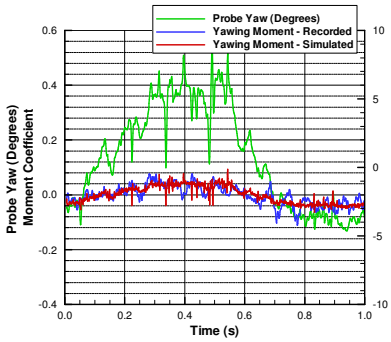


Figure 298 - Yawing moment, harmonic 1.0Hz

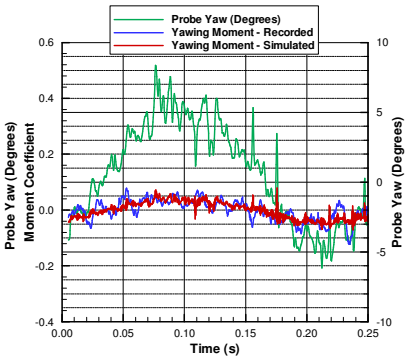


Figure 299 - Yawing moment, harmonic 4.0Hz

## 9.7 Arbitrary Excitation Results

Using the sample yaw trace taken from the on-road study of the Rover 200, which was accurately simulated during the TGS commissioning tests, the model's response was recorded under the same yaw flow against time profile, with sideglass pressure measurements shown in Figure 300 to Figure 303. It can be seen that, though the timescale is large, the simulation technique has captured the major pressure fluctuations over the model, with realistic sideforce and yawing moment traces being generated. Pressures at tapping 09 (Figure 300) show extremely good simulation correlation, being in a region without a mirror, but also have some significant unsteady components. The yaw trace plotted is that of the roof probe, with no time alignment required between sideglass and roof results due to their close longitudinal location.

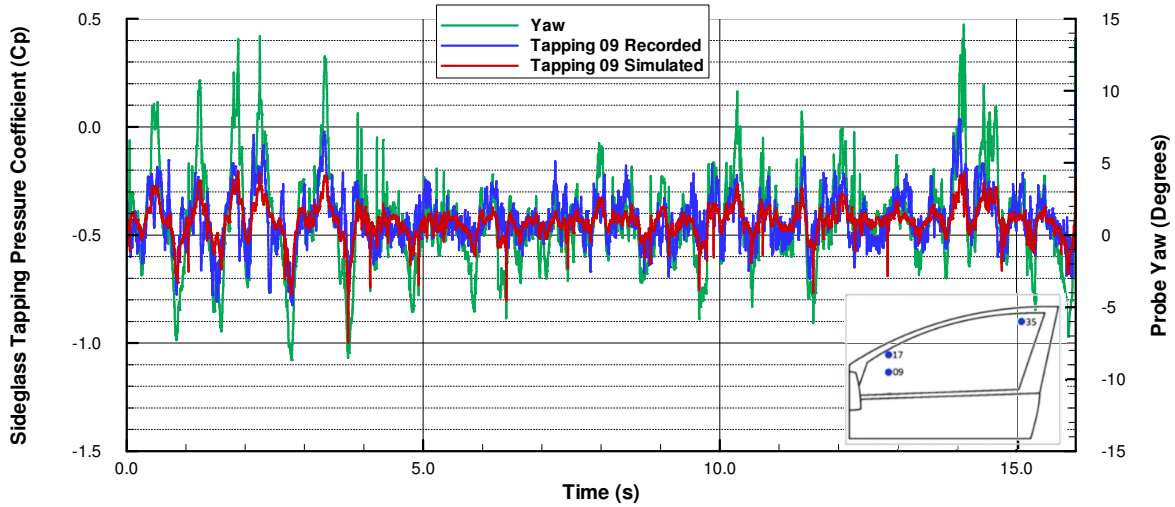


Figure 300 - Arbitrary trace, tapping 09

Tapping 17, Figure 301, in the A-pillar wake region, shows a general reduction in pressure coefficient, due to its highly sensitive pressure coefficient against yaw characteristics. Simulation is qualitatively accurate and the resultant pressure profiles, both measured and simulated, are a good presentation of the recorded roof probe yaw angle.

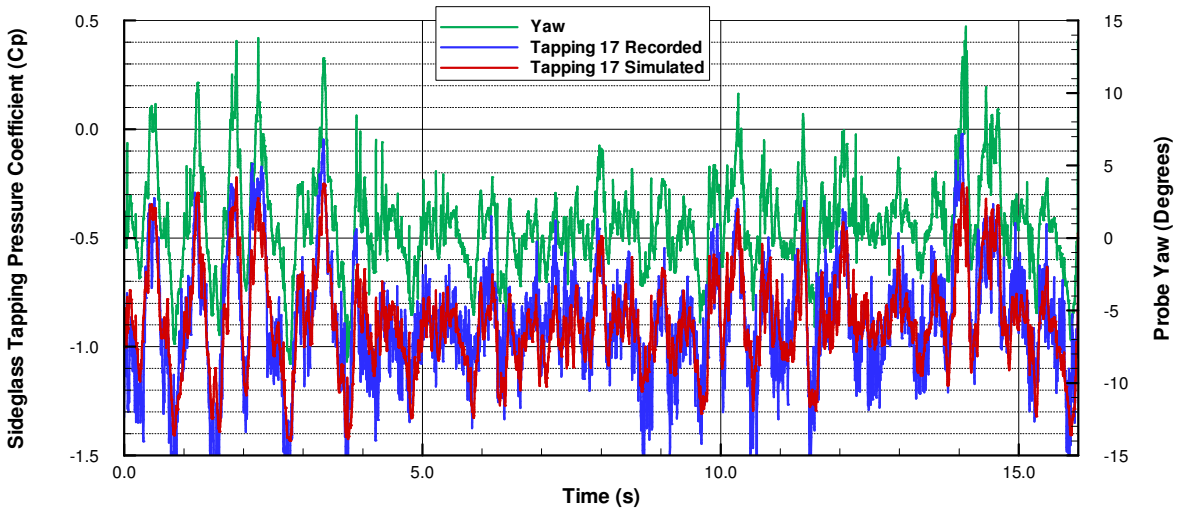


Figure 301 - Arbitrary trace, tapping 17

Tapping 35, Figure 302, at the far downstream location of the sideglass, again shows accurate simulation with a less sensitive pressure coefficient against yaw characteristic for the test case time period.

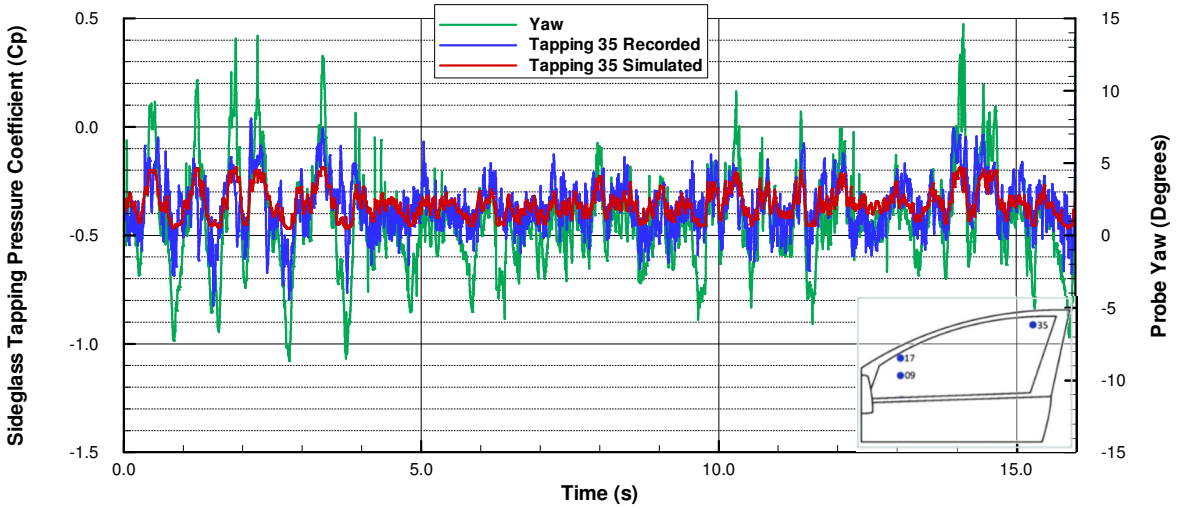


Figure 302 - Arbitrary trace, tapping 35

Sideforce coefficient is presented in Figure 303, with the simulation result showing a smaller deviation range than that measured. This has been presented in earlier results, and suggests that dynamic TGS

driving frequencies cause greater forces than the steady-state calibration would predict (though this was not especially evident for the periodic excitation).

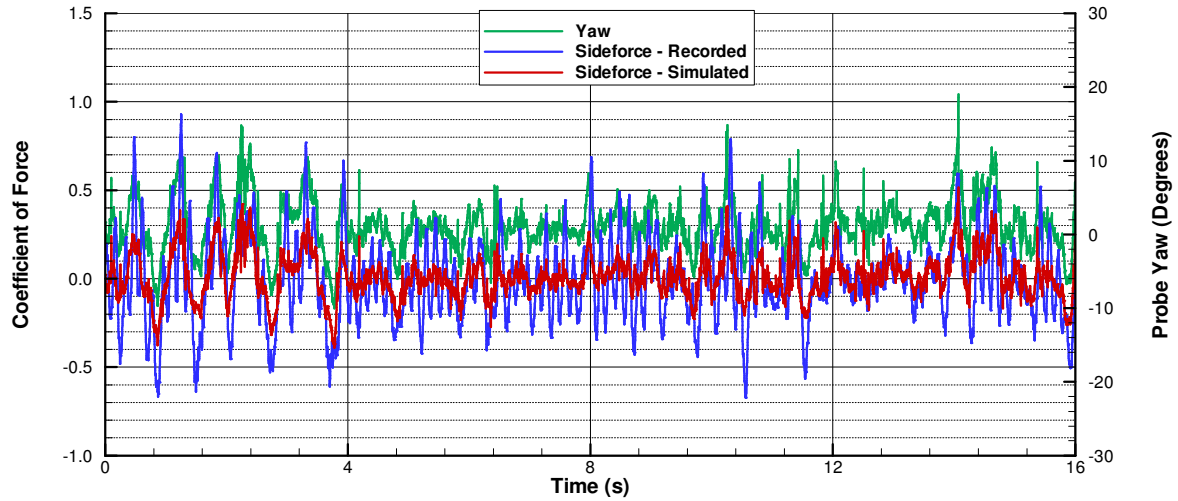


Figure 303 - Arbitrary trace - sideforce coefficient

Finally yawing moment coefficient is shown in Figure 304, again with a reduction in force range seen for the simulated case, suggesting a greater force against yaw sensitivity for dynamic test cases, when compared to the steady-state turntable calibration. Again, qualitatively, the measured and simulated forces do correlate, with a consistent magnitude and response to the roof probe measured yaw angle.

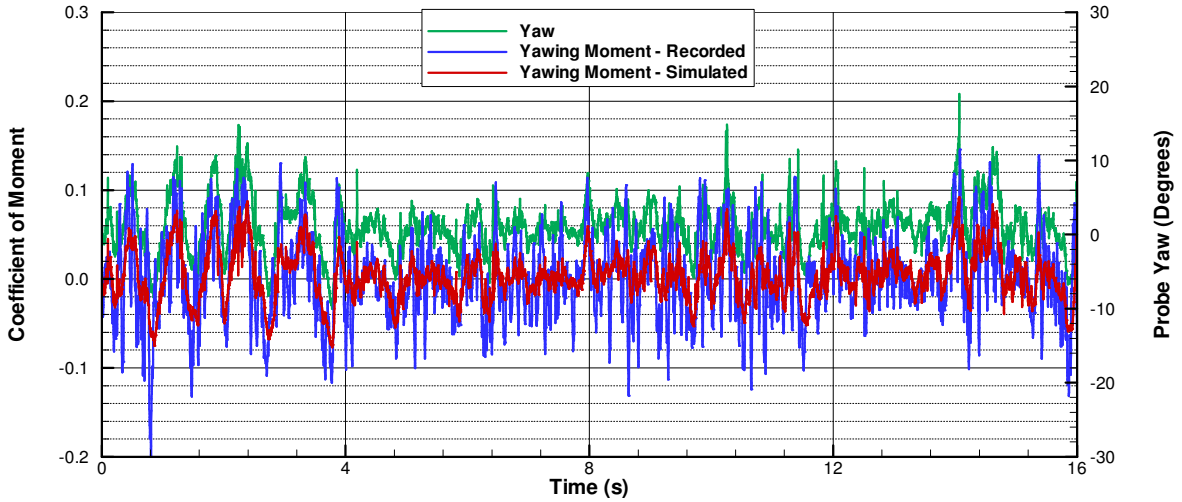


Figure 304 - Arbitrary trace - yawing moment coefficient

## 9.8 Standard Deviation of Measured and Simulated Pressure Coefficient from Arbitrary TGS Excitation

Standard deviation analysis of the recorded pressure measurements against the deviation of the simulated results was performed in order to identify the frequency range over which the simulation technique represents the measured pressures. This is because at higher frequencies the on-road flow yaw energy reduces and the flow can become dominated by self-excited turbulence. Pressures were logged for 16-seconds at 1,024Hz. Due to the scaling in length scale and wind-speed between the on-road frequencies, the frequency bands are increased by a factor of 2.06, and therefore 'tunnel time' is reduced by a factor of 2.06 from 'full-scale time', in order for fair comparisons to be made. The arbitrary trace was divided into 2-second samples, by dividing by 2.06 from 4-seconds that was used on-road. 15 time history samples of the arbitrary trace were evaluated for standard deviation within each frequency band, and for all sideglass tappings. These standard deviation clusters of data points within each frequency band can be fitted with a linear regressed curve (i.e. $Y = aX + b$), where the slope, a, of the curve represents the admittance between the measured and simulated result, and the intercept, b, of the linear regression represents the self-excited component of the air flow pressure fluctuations.

Additionally on each plot there are individual points at the simulated pressure deviation = 0Pa location, representing the steady-state self-excitedness. These were evaluated by finding the probability density of yaw from the arbitrary case (which sums to unity), which is then rescaled onto the same yaw base as the turntable yaw measurements. Then for each yaw angle from the turntable results, each tapping's standard deviation within every frequency band is evaluated. Finally, the frequency band standard deviation at each turntable recorded yaw angle is then multiplied by the probability density for the respective case (e.g. arbitrary), which is then summated for all of the turntable yaw angles.

As such, the evaluated steady-state self-excitedness for each tapping, per frequency band, is the product sum of the pressure coefficient standard deviation and the probability density of that yaw occurring in the case, summated for all yaw angles, as summarised in Figure 305.

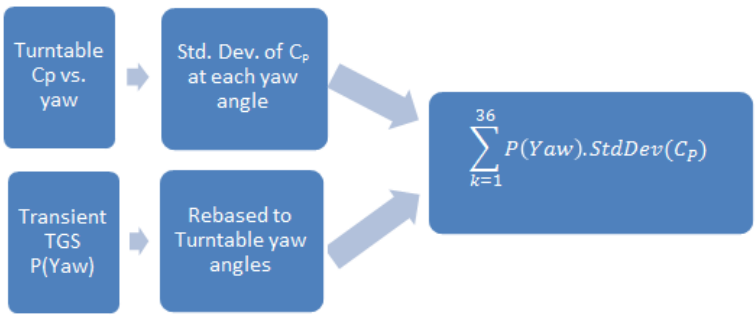


Figure 305 - Evaluation of steady-state self-excitedness

As seen for the on-road data analysis, a clustering of data points around the 45° line shows accurate simulation of the sideglass pressure coefficient (or forces) using a turntable (i.e. steady) calibration and the roof probe recorded flow yaw angle (Figure 132). If a data point is below this line, it suggests greater unsteadiness for the simulated results as opposed to the measured, which can be considered to be either a pressure variation suppressed by the transient flow environment or as an artefact of the flow propagation time between the sideglass and roof probe (especially at higher frequencies, when yaw wavelengths are shorter). Data points above the line signify greater unsteadiness for the recorded pressure measurements rather than those simulated (i.e. greater than unity yaw sensitivity).

Increased unsteadiness is common at higher frequency bands and is considered representative of 'self-excited' turbulence. This turbulence is generated by small-scale vehicle geometry, from which the pressure fluctuations can average-out for steady-state (i.e. turntable) readings, but do not for the transient measurements.

As a general trend from the on-road study, low frequency bands should have data points clustering around the 45° line (i.e. measured = simulated), as the simulation results are a good representation of the steady-state results. At intermediate frequency bands the data point clustering moves to the bottom left of the plot, as the pressure standard deviation reduces and the self-excited turbulence is still small. At the higher frequency bands, the data point cluster remains near to the left-hand side of the plot, as the simulation technique cannot resolve high frequency pressure fluctuations. The data point cluster then gradually moves in the increasing Y-axis direction with frequency, as the recorded pressure measurements start to have significant components of self-excited turbulence. Of course values cannot (and were not) less than zero.

Figure 306 to Figure 314 show the sideglass pressure coefficient standard deviation for 2-second time histories, ordered by flow region type (as defined in the on-road study, Figure 94).

Tapping 01 and 09 (Figure 306 and Figure 307) represent what would be the mirror-wake region. At lower frequencies, the overall pressure standard deviation is relatively small, with clear yaw dependency in the pressure measurements up to 11.6Hz. Above 11.6Hz the simulation is less able to accurately predict sideglass pressures, which in comparison to the scaled frequencies is at a similar range to that for the on-road model, though differences are less apparent due to fewer data points. The steady-state result (plotted at simulated pressure deviation = 0Pa) is often the majority component of the pressure deviations, and therefore is significant in the variation of measured pressure. Note that for tapping 09 the admittance is around unity for the initial three frequency bands, whereas the on-road admittance reduces at comparatively lower frequencies. This is most likely due to the lack of sideglass mirrors on the Rover model, and as such the flow is much more stable and predictable for small downstream distances from the model's A-pillar.

Tapping 17, 25 and 35 (Figure 308 to Figure 310) demonstrate pressure variations in the A-pillar region. Tapping 17 (Figure 308) the tapping closest to the A-pillar where the A-pillar is most angled (i.e. greatest flow wake), shows the greatest pressure variations at low frequencies, representative of vortices shedding from the A-pillar. For all three tappings, as the frequency increases, the clustering of data points moves towards the bottom left (i.e. reduction in pressure variation) and then move upwards showing the inability of the simulation to accurately predict the sideglass pressures at these frequencies. It should be noted that the frequency band of 115.8 - 366.2Hz is a very high frequency band for turbulence and could be expected to have a greater measured component than it does. However, it should also be remembered that the -6dB, 250Hz hardware filters would be suppressing spectral energy at this level.

Tappings 12, 13, 22 and 29, (Figure 311 to Figure 314) are all in the hybrid region. Pressure variations are lower than when near the A-pillar, with the tight clustering of data points showing that the flow is much more stable than when further upstream. Admittance roll-off is now slightly earlier, around 3Hz, showing that both stable and unstable flow regions can also show poor simulation prediction at relatively low frequencies (where typically a road vehicle would have wipers and mirrors affecting both A-pillar and sideglass flow). Again data point clustering is relatively tight and all clusters show slightly greater pressure deviation than the corresponding steady-state result.

It has been seen in several cases that the clustering of the steady-state points is very close to, if not sometimes slightly lower than, the measured pressure coefficient standard deviation. Though it is theoretically possible that in the dynamic case the pressure deviations are less variant than in the

steady-state turntable yaw, this effect would only really be valid at specific yaw angles where the tapping happens to be in a barely separated flow (which would report an instantaneous admittance near to zero). Of greatest probability is that when a cluster is just below the steady-state result this is an artefact of the distance between the roof probe and sideglass at what are often the intermediate frequencies where the length scale is approximately the length of the model.

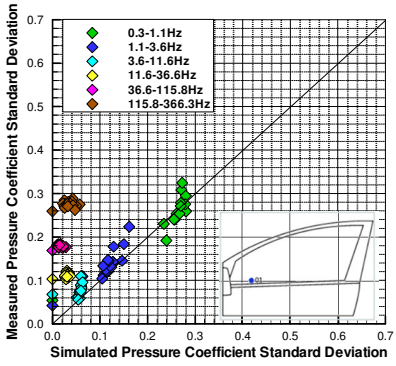


Figure 306 - Standard deviation of pressure, tapping 01 (Mirror)

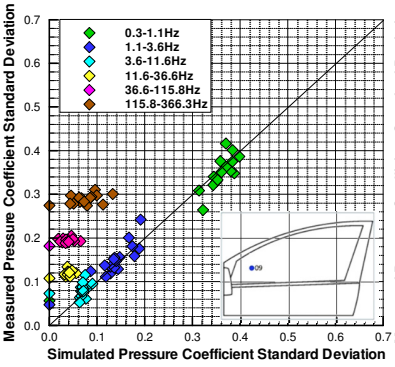


Figure 307 - Standard deviation of pressure, tapping 09 (Mirror)

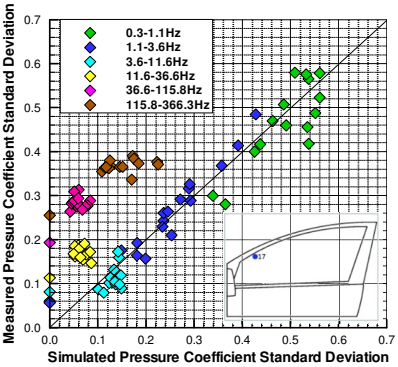


Figure 308 - Standard deviation of pressure, tapping 17 (A-Pillar)

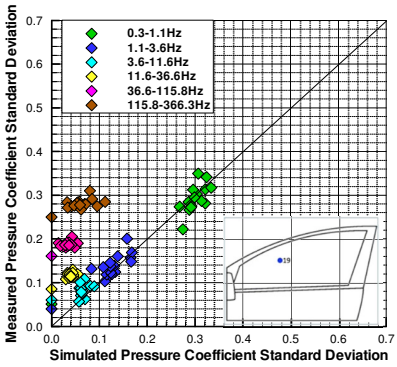


Figure 309 - Standard deviation of pressure, tapping 19 (A-Pillar)

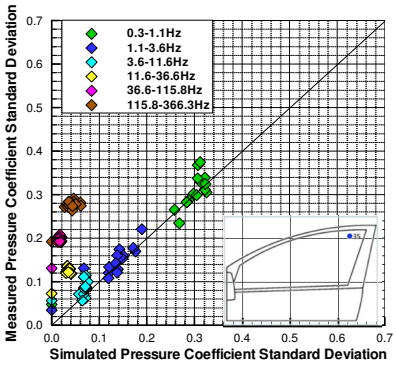


Figure 310 - Standard deviation of pressure, tapping 35 (A-Pillar)

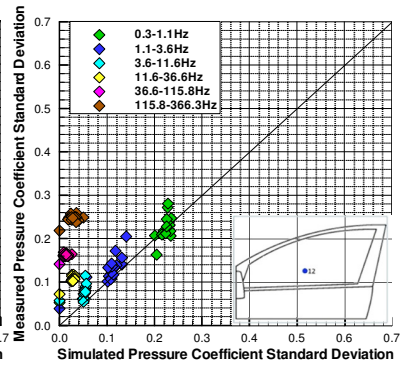


Figure 311 - Standard deviation of pressure, tapping 12 (Hybrid)

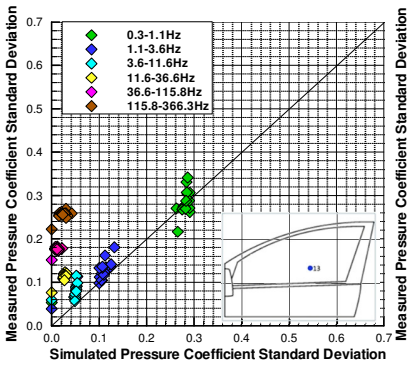


Figure 312 - Standard deviation of pressure, tapping 13 (Hybrid)

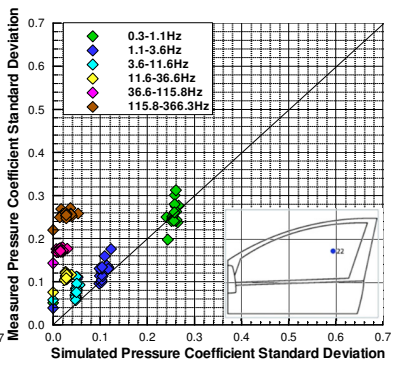


Figure 313 - Standard deviation of pressure, tapping 22 (Hybrid)

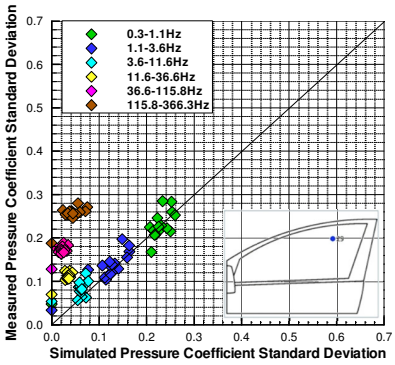


Figure 314 - Standard deviation of pressure, tapping 29 (Hybrid)

Therefore the approach of assessing the vehicle's response using the TGS arbitrary excitation mode has shown greater vehicle response detail than from results of the quasi-steady simulation technique, particularly at the higher frequency bands. The pressure fluctuations seen at the higher frequency bands are comparable to those found in the on-road environment, showing that the TGS is able to replicate a vehicle's response to equivalent on-road flow conditions.

Figure 315 and Figure 316 compare the simulation of sideforce and yawing moment with the measured results. For the sideforce readings, the results show less frequency dependence with non-unity admittance noticeable at even low frequencies. It is not surprising to see the 3.6 – 11.6Hz frequency band having such high force deviations, as this is the frequency at which the turntable balance had natural frequencies adding additional spectral energy into the force measurements. Yawing moment deviations are notably smaller in size, with good simulation up to 11.6Hz, and then a similar trend of admittance roll-off at higher frequencies. It should be noted that these results show significant frequency dependence and that by 36.0Hz the results demonstrate that the simulation is unable to predict the measured readings. This is due to the high frequency pressure variations seen by the probe having very little spectral energy and therefore do not have the momentum and force to move the vehicle and hence are not detected by the balance.

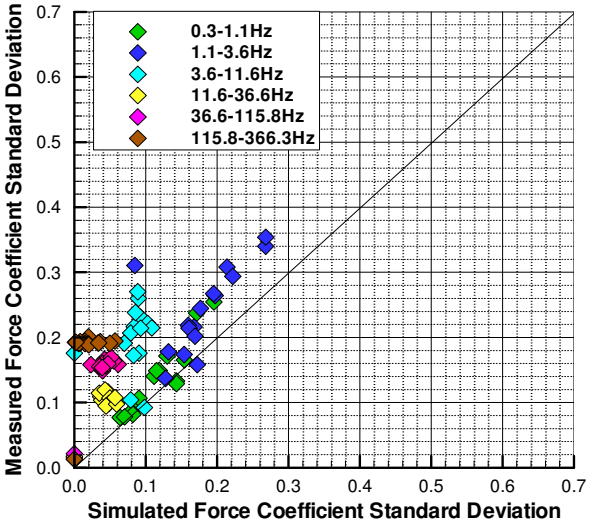


Figure 315 - Standard deviation of sideforce

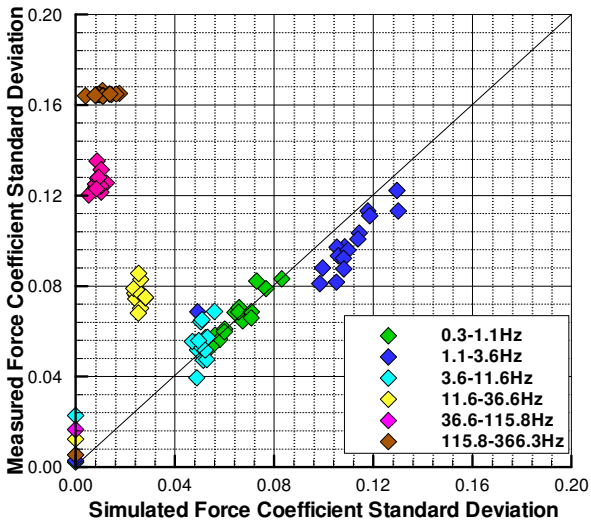


Figure 316 - Standard deviation of yawing moment

Similar plots were inspected for the harmonic cases but are summarised by the admittance and self-excitedness plots in the following section.

## 9.9 Correlation of Standard Deviation of Pressure Coefficient Studies

### 9.9.1 Admittance Results

The arbitrary case standard deviation of pressure coefficient results were then regressed for a linear curve fit, offering a slope (representing admittance) and an intercept (representing self-excited unsteadiness) for each frequency band of each sideglass tapping. The admittance demonstrates the turbulence variation of the incoming flow and corresponding pressure changes that are therefore yaw dependent. Correspondingly, the self-excited pressure unsteadiness is therefore part of the vehicle response. The harmonic driving frequency data points shown on each of the admittance and self-excitedness graphs were produced by evaluating the standard deviation of pressure coefficient, at each tapping, by each frequency band, for their entire 16-seconds. For each of the harmonic frequencies the steady-state point was evaluated as described earlier, but using the probability density function of yaw from the respective frequency case. The standard deviation of measured over simulated pressure coefficient for the entire harmonic case sample was used, as the dominant frequency in the harmonic cases was the TGS aerofoil oscillation frequency, and had the 2-second time samples been used, which were used for the arbitrary case, this approach would result in numerous points being all aligned vertically on a measured against simulated standard deviation plot.

Therefore the use of the ratio of the standard deviation for the entire sample to find the harmonic admittance allows a similar and fair comparison. Furthermore, the 5 data points from the harmonic

cases shown are from the 5 test driving frequencies, as each harmonic frequency band was only evaluated for pressure coefficient standard deviation centred on the aerofoil oscillation driving frequency, effectively applying a notch filter (i.e. non-overlapping low and high pass filter) to each harmonic test case. Frequency bandwidth was set to be consistent, in terms of log frequency, between each harmonic case. Finally the data point of each harmonic frequency test case are plotted at the TGS driving frequency (which is the mid-point of the respective notch filter frequency range).

For the arbitrary result, the intercept (representing self-excitedness) is a result different from the 'steady-state' standard deviation value previously shown (which is based upon the probability of yaw derived from a tapping's entire steady-state recorded time history). The self-excitedness (i.e. intercept) data point was plotted on the arbitrary standard deviation results (Figure 306 to Figure 316) at the axis location corresponding to the simulated pressure standard deviation = 0Pa. The result shown in the arbitrary self-excitedness plots is the true regression intercept from the standard deviation frequency band data clusters.

The harmonic driving frequency case slopes were found by a simple two point regression of this intercept with the ratio of measured to simulated pressure coefficient standard deviation, and as such were evaluated as shown (note the sum of standard deviations by converting them to variances initially in the numerator of the equation):

$$\text{Harmonic Slope (Admittance)} = \frac{\sqrt{(\text{Measured } C_P \text{ Std Dev})^2 - (\text{Steady State } C_P \text{ Std Dev})^2}}{\text{Simulated } C_P \text{ Std Dev}} \quad [29]$$

Finally, as the on-road data samples are also plotted on each chart, frequency was converted into reduced frequency using the following equation, effectively 2π of Strouhal number:

$$\text{Frequency(f)} \rightarrow \text{Reduced Frequency } (\omega_R) : \omega_R = \frac{2\pi f l}{u} \quad [30]$$

where u = test velocity ($ms^{-1}$) and l = test vehicle length (m).

This gave a frequency to reduced frequency conversion scalar of k = 0.390 for the Rover model and k = 0.797 for the full-scale vehicle, in order to compare the results from vehicles of different scales, recorded at different test velocities.

For the admittance (Figure 317 to Figure 327) and self-excitedness (Figure 328 to Figure 329) graphs, it was expected that at low frequencies a slope of near to unity would be reported, as the quasi-steady simulation accurate predicts the measured sideglass pressures. At intermediate frequencies the slope

would start to deviate from unity, and at higher frequencies the slope becomes unreliable as the simulation technique is unable to accurately predict sideglass pressures (though ideally would go to zero). On-road measurements (Chapter 4) have simply been aligned by reduced frequency for the on-road vehicle scale and test speed.

Figure 317 and Figure 318 show the admittance results for tapping 01 and 09, in what would be the mirror wake region. At lower frequencies, tapping 01 shows larger admittances than the on-road results, with tapping 09 showing more correlated admittances. At higher frequencies, where the on-road trace shows a rapid increase in admittance, the arbitrary results tend to zero, which when reviewed alongside the standard deviation results is a consequence of the curve fit process to such a tight cluster of data. Additionally, the lack of mirrors in the tunnel model would cause notable flow differences through yaw sweeps. The harmonic results, however, show poor correlation with the on-road results, suggesting that driving at one dominant frequency does not produce the full pressure variation that would be seen for a more aperiodic and variant flow. This suggests that though the induced yaw angle is varying in a smooth manner, the sideglass pressures actually still significantly fluctuate due to increased flow unsteadiness at higher yaw angles.

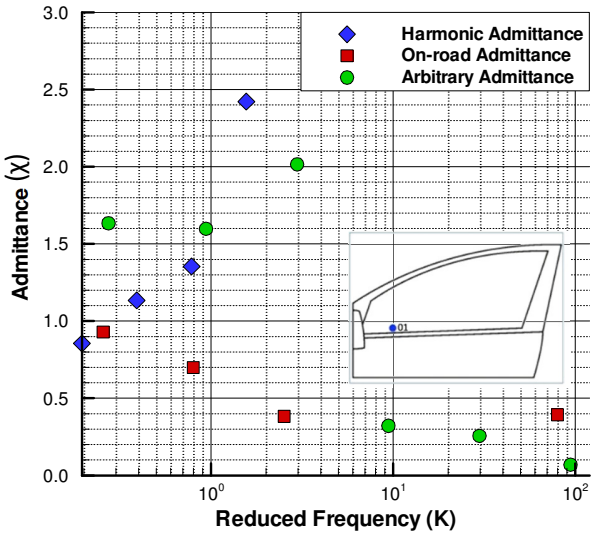


Figure 317 - Admittance for tapping 01 (Mirror)

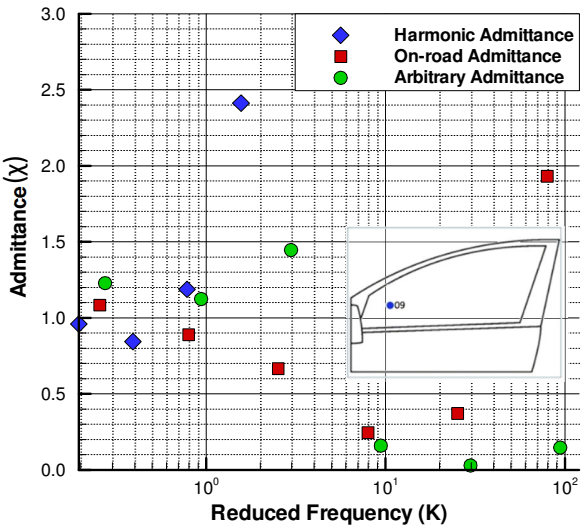


Figure 318 - Admittance for tapping 09 (Mirror)

Figure 319 to Figure 321 show the admittance results for tapping 17, 19 and 35, all located in the A-pillar region. Tapping 17 and 35 show near to unity arbitrary and harmonic admittances at low frequencies, whereas tapping 19 shows slightly greater arbitrary admittances at low frequencies. All of the 3 tappings show a rapid decrease in arbitrary admittance at higher frequencies, but are, in general,

correlated with the on-road results. Harmonic correlation with the on-road and arbitrary trace is poor above 2Hz, with points only correlating at low frequencies.

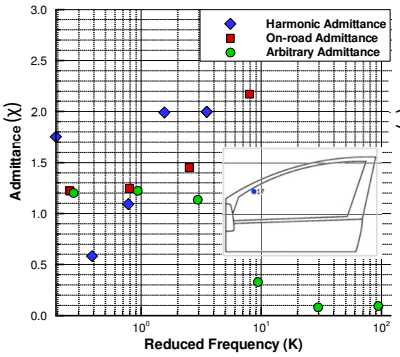


Figure 319 - Admittance for tapping 17 (A-Pillar)

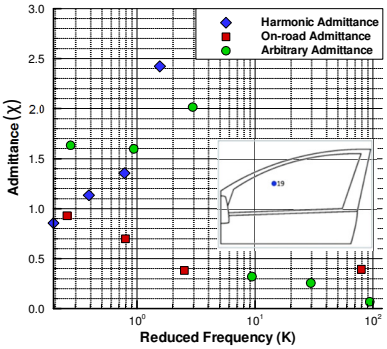


Figure 320 - Admittance for tapping 19 (A-Pillar)

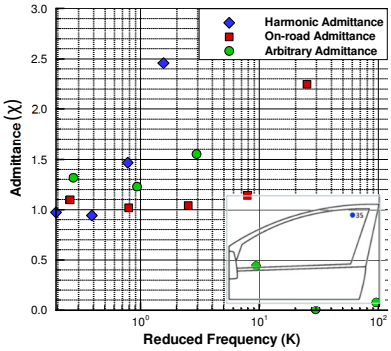


Figure 321 - Admittance for tapping 35 (A-Pillar)

Figure 322 to Figure 325 present tapping 12, 13, 22 and 29, tappings all in the hybrid flow region. Generally arbitrary admittances are much higher than unity, even at low frequencies, except for tapping 29 which is physically higher and more rearward than the other tappings, therefore potentially experiencing more A-pillar flow interaction. Harmonic admittances are near to unity at around 0.5Hz, but thereafter rapidly increase showing a poor correlation with the on-road results.

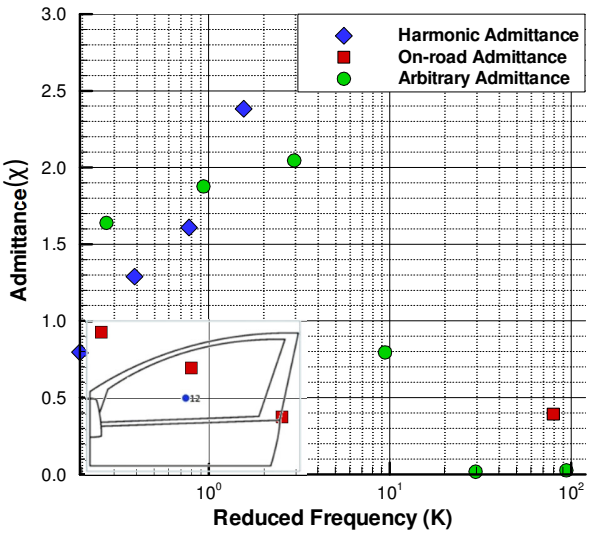


Figure 322 - Admittance for tapping 12 (Hybrid)

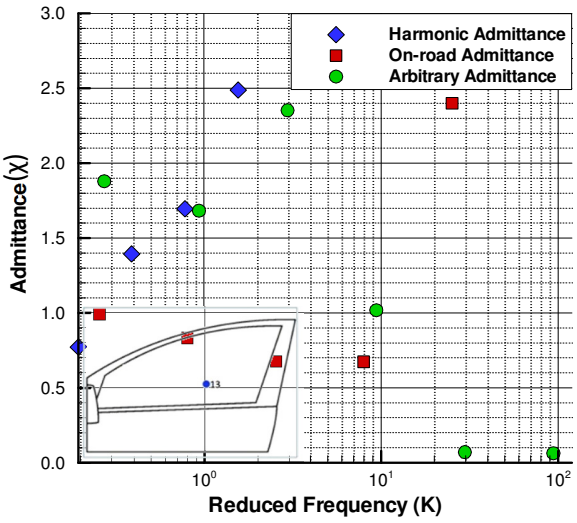


Figure 323 - Admittance for tapping 13 (Hybrid)

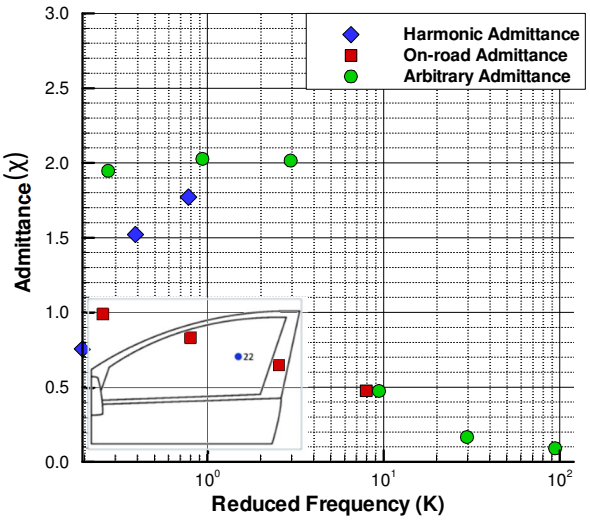


Figure 324 - Admittance for tapping 22 (Hybrid)

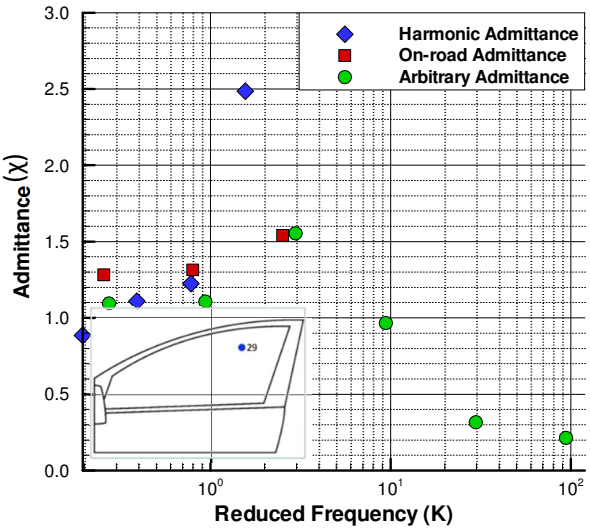


Figure 325 - Admittance for tapping 29 (Hybrid)

Figure 326 and Figure 327 display the admittance results for only the harmonic and arbitrary case, there is not a result for the on-road data set. Sideforce is reasonably accurately simulated by the harmonic case at lower frequencies, but not so above 4Hz, with the arbitrary result again tending to zero at higher frequencies due to the tight clustering of standard deviation data points. A similar result is seen for the yawing moment, with poor harmonic case correlation at even intermediate frequencies, and again a trend to zero as frequency increases. It is of interest to note that even though more deviation was seen at the 3.6 – 11.6Hz (tunnel scale frequency) in the standard deviation clusters, due to natural frequencies of the balance, these additional spectral energy components have not notably corrupted the admittances at a similar frequency band as admittances close to unity are still being reported.

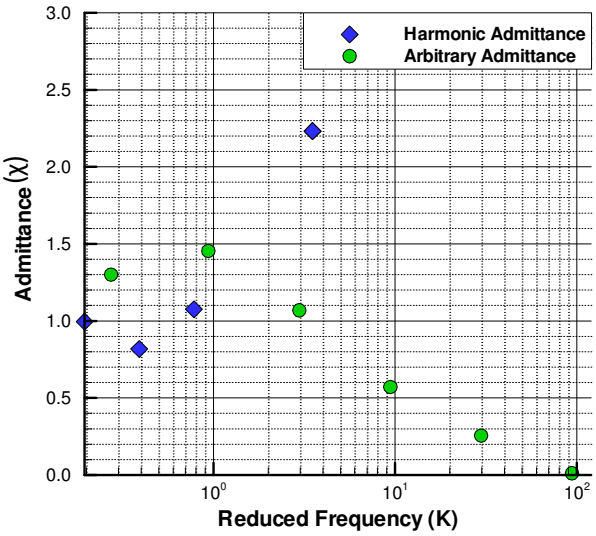


Figure 326 - Admittance for sideforce

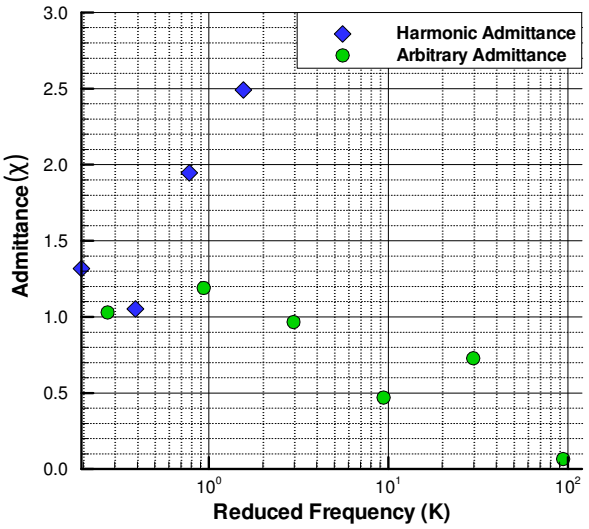


Figure 327 - Admittance for yawing moment

The results show that the arbitrary induced yaw study generated results better correlated with the on-road results, but with harmonic induced yaw studies showing a poor correlation. It can also be seen that for many of the results the TGS generated admittance results do not align with the on-road equivalent measurements, even though the pressure standard deviation plots showed a stronger correlation. This is due to the arbitrary trace having very few data plots for the curve regression process, relative to the on-road results (the arbitrary trace having 8 data points, the harmonic results having only two, against ≈2,200 data points for curve fitting for the on-road results). Therefore, though the approach has been shown to be valid, the accuracy of the curve fitting for admittance evaluation is improved with more data points. More data points could be gained through either running the arbitrary case numerous times or through running numerous arbitrary cases recorded from the on-road study.

### 9.9.2 Self-Excitedness Results

Finally, it is of interest to consider the self-excitedness results, which for the on-road and arbitrary case are the intercept of the linear regression of standard deviation data points, and for the harmonic case are the steady-state values (i.e. the product sum of P(Yaw) with frequency band pressure coefficient standard deviation). These values report the level of unsteadiness (that is pressure coefficient deviation) that would be expected with no additional yaw frequencies, be they the TGS aerofoils or on-road wind. Such self-excited unsteadiness are artefacts of the geometry of the vehicle as opposed to spectral energy components in the air flow (though in reality any background turbulence in the air does have an effect, but which can be considered to be small in the tunnel and yet notable on-road).

Figure 328 and Figure 329 show tappings 17 and 12, in the A-pillar and hybrid regions of air flow, respectively. Only two tappings are shown as an illustration of the self-excitedness order of magnitudes, rather than a detailed report. There is a good correlation between the on-road and arbitrary levels of self-excitedness, but it is clear that the harmonic induced yaw tests are unable to create representative levels of self-excitedness. However, the self-excitedness values are low at the lower frequency levels and are seen to increase as frequency increases. It should also be noted that the self-excited turbulence is greater for the model than for the full-scale study.

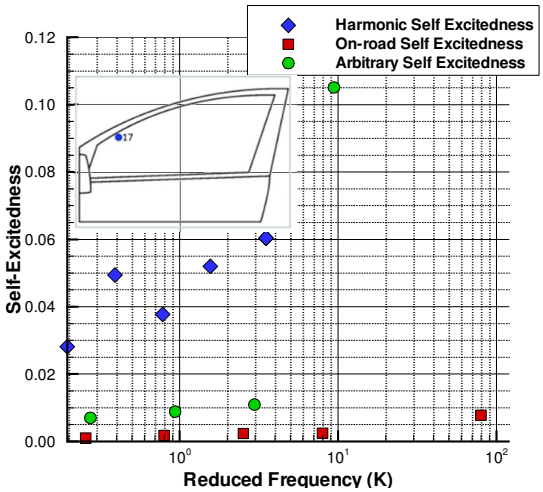


Figure 328 - Sideglass pressure self-excitedness for tapping 17 (A-Pillar)

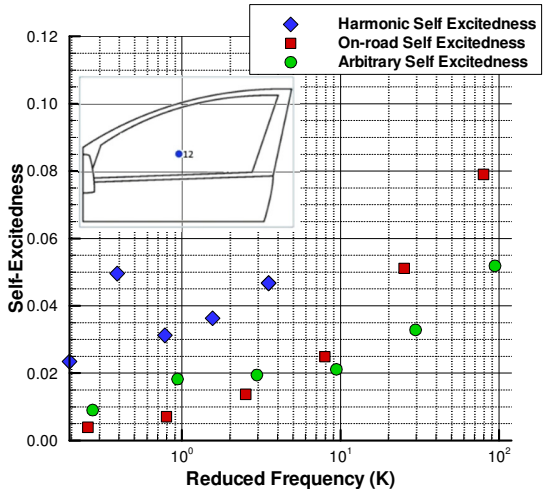


Figure 329 - Sideglass pressure self-excitedness for tapping 12 (Hybrid)

## 9.10 Rover 200 Model Test Conclusions

A Rover 200 40% scale model was tested in the wind tunnel with the roof probe, 9-sideglass static pressure tappings and 6-component force measurements being recorded. A range of static test yaw angles using the TGS and turntable were performed, as well as harmonic and arbitrary excitation tests.

Initial tests showed that the sideglass pressure results between the TGS and turntable induced yaw were highly correlated, as well as quantifying yaw dependent flow effects that a roof probe experiences. The steady-state results were used to generate a pressure and force against yaw angle profile for sideglass pressures and vehicle forces, which was used as the input into the quasi-steady simulation process. A method was presented to determine a steady-state, by frequency band, deviation of pressure and force from the probability density of yaw and the frequency band standard deviation, evaluated for each turntable yaw angle. These processes resulted in a set of standard deviation of pressure and force coefficients graphs shown for all relevant pressures and forces.

The standard deviation of pressure and force measurement results showed large pressure standard deviations at the lower frequency bands, notably sub-4Hz tunnel scale (that is around K = 2 reduced frequency). A strong measured to predicted pressure correlation was seen up to the 3.6Hz (K = 2) frequency band. Pressure deviations then decreased at the intermediate frequencies between K = 2 – 10 reduced frequency, and then increased again at higher frequencies, with poor simulation correlation at higher frequencies. Steady-state pressure deviation results were shown to be close to the measured results and as such the self-excited, that is the non-frequency driven pressure deviations, made a significant component of the reported pressure deviations. Sideforce was accurately simulated up to K = 2, and yawing moment up to K = 5, but was poor thereafter.

Admittance plots, derived from the linear regression of the deviation clusters, were generated for the on-road, harmonic and arbitrary cases. Tight data point clusters were seen in the standard deviation results and this became evident in the admittance results due to the admittance tending to zero at higher frequencies, where the more dispersed on-road results had admittances varying more widely at higher frequencies. However, the curve regression process was seen to be sensitive in reporting admittances where few data points exist (i.e. for the arbitrary test measurements).

The harmonic case results often poorly predicted the arbitrary or on-road case tests, suggesting that generating single-frequency, periodic waveforms does not generate the same pressure and force variations that the full on-road spectrum creates. However, the harmonic results, considering the kurtosis in their spectral energy relative to the on-road spectral energy, were able to generate results in line with the on-road and arbitrary results, albeit without consistency. Correlations were seen between the on-road and model pressure results, offering confidence that the admittance method is able to capture the true flow frequency dependent characteristics. Sideforce and yaw arbitrary results were valid up to 4Hz tunnel-scale (K = 2) when compared to the harmonic results, but the correlation decreased with frequency. Finally, self-excited turbulence results were presented, with the arbitrary and on-road results tending to agree, but with the model showing higher levels of self-excited unsteadiness.

Therefore, the use of the harmonic case, considering its spectral limitations, still offered an insight into the pressure and force frequency dependent deviations. However, the arbitrary case, considering how much shorter the time history was in comparison to the vast on-road data collection (32-seconds against 8,800-seconds) gave a notable insight for a greatly reduced test duration. In summary:

- Large pressure standard deviations are noted at the sub-4Hz tunnel scales (K < 2).

- A strong ‘measured to predicted’ pressure correlation was seen to exist up to the 3.6Hz frequency band (K = 2).
- Standard deviation of pressures reduces at the intermediate frequencies between K = 2 – 10 reduced frequency, and then increases at higher frequencies, with poor simulation correlation at the higher frequencies.
- Sideforce and yaw arbitrary results were valid up to 4Hz tunnel-scale (K = 2) when compared to the harmonic results, but the correlation was poor at higher frequencies.
- In a direct assessment between the harmonic and arbitrary test modes, the arbitrary test mode was found to be more representative of the physical, real-world environment than by operating the TGS at one discrete frequency.

Therefore a quasi-steady approach (i.e. turntable) is only able to predict transient flow effects in stable flow regions for a road passenger vehicle up to the frequencies where self-excited turbulence becomes significant. For unstable flow regions, such as in the mirror wake or A-pillar flow, transient flow effects become poorly predicted above around 2Hz (K = 1). For transient flow effects in such regions above K = 1, the use of a TGS in an arbitrary mode can more accurately simulate a vehicle’s response. At frequencies above 10Hz (K = 5) self-excited turbulence becomes significant and needs to be quantified and factored into an analysis approach.

# 10. Conclusions

The on-road environment was shown to have significant energy in the 0.1 - 10Hz range (reduced frequency K = 0.1 - 10 for a vehicle driving at highway speeds). An active, lift-based, TGS was created able to generate harmonic and arbitrary yaw variations of up to ±10$^{o}$ across the frequency range of greatest importance: K = 0.3 - 5 (0.3 - 5Hz full-scale at 32ms$^{-1}$, up to 10Hz model-scale). At lower frequencies quasi-steady approaches are sufficient and at higher frequencies both on-road energy and vehicle response are reduced.

## 10.1 On-road Environment

### 10.1.1 Velocity Components

On-road turbulence experienced by a road vehicle is a combination of velocity non-uniformity in space, which a vehicle perceives temporally, and also unsteadiness in the atmospheric boundary layer and due to other vehicles. The wind velocity may be constant at specific locations, but as the vehicle translates through a domain, it experiences varying flow velocities (i.e. varying crosswind) in terms of time. In addition, air flow can have induced unsteadiness due to roadside furniture and unsteady wakes of other vehicles.

Sources presented, as well as the on-road study, showed that variations in lateral flow velocities are the most significant, causing notable variations in vehicle drag, sideforce and yawing moment. These lateral variations are readily characterised by the yaw angle, and sideglass pressure variations were shown to correlate strongly with yaw variations. Longitudinal flow velocity variations occur to almost the same intensity as lateral velocity variations, but longitudinal velocity variation effects can be handled adequately as variations in dynamic pressure. The intensity of vertical velocity variations was shown to be approximately 60% of that of longitudinal and lateral velocity variations.

### 10.1.2 Yaw Range

Sources reviewed correlated well with the on-road study. Yaw angles ranged between ±20$^{o}$, but with the vast majority within ±6$^{o}$. Correspondingly, the turbulence intensity range was 0.5 - 15%, but with the majority below 8%.

### 10.1.3 Unsteady Time and Length Scales

From the literature and the on-road study, a broad range of on-road flow conditions has been shown to exist, especially in terms of time and length scales. The majority of the energy in the on-road yaw

spectrum was found to exist in the 0.1 - 10Hz range. Above 10Hz the spectral energy was seen to roll-off significantly, decreasing by more than an order of magnitude by 100Hz. Turbulent length scales can be used to summarise the flow spectrum, and turbulent length scales from 1 - 15m were found to be typical, but care is needed as the method of calculation can influence the result. A strong negative correlation was found between length scale and intensity, with shorter length scales occurring simultaneously with high intensities. The length scale of vertical velocity variations was found to be typically 30% of that of longitudinal and lateral velocity variations.

## 10.2 Vehicle Response

### 10.2.1 Assessment of Vehicle Response

Conventional transfer function or admittance approaches can be corrupted by the presence of uncorrelated sources (e.g.: self-excited unsteadiness). In many cases the level of self-excited unsteadiness was significant when compared with that correlated with onset flow unsteadiness. Therefore an assessment approach needs to make consideration for the self-excited unsteadiness. The approach used in this thesis has combined a quasi-steady prediction and a regression of multiple short-duration (4-second) measurements to separate self-excited unsteadiness and unsteadiness correlated with yaw. Additionally the influence of steady yaw on self-excited unsteadiness has been assessed using the recorded probability of yaw function multiplied by the corresponding flow unsteadiness for each yaw angle.

### 10.2.2 Quasi-Steady Boundary

The reduced frequency, K, is a fundamental parameter in considering vehicle aerodynamic response. When comparing spectra between the on-road and the wind tunnel domains, reporting of frequencies in terms of reduced frequency allows differences in test velocities and scale to be readily assessed. A vehicle's response to external unsteadiness was observed. The use of a roof mounted probe was shown to be a good method to record time-aligned yaw. Comparisons were made between measured unsteady surface pressures (on-road and wind tunnel) and forces (wind tunnel) and a quasi-steady simulation based on either steady-state tunnel or unsteady road measurements. The simulation process used the roof-probe recorded yaw to predict sideglass pressures or vehicle forces, and the comparison with unsteady measurements demonstrated the frequency range that could be treated as quasi-steady.

The 2D CFD study, considering forces on a simple body, indicated a quasi-steady reduced frequency threshold around K = 0.3 for drag and sideforce. Similarly, the on-road study confirmed that below K = 0.3 sideglass pressure fluctuations behaved in a quasi-steady way, while for K > 5 admittance always deviated from unity. Additionally, in the 2D CFD study, unsteady effects were found to be largely independent of Reynolds number, including for near-inviscid conditions. This indicates that the sources of non-quasi-steady response are not viscous in origin.

### 10.2.3 Local Admittance Effects

The on-road study showed that different regions on the vehicle (sideglass) exhibited different responses in terms of admittance and quasi-steady boundary.

Via the on-road study, the A-pillar region showed consistent admittances greater than unity at frequencies in the region of K = 3. This region was also shown to have a high steady-state sensitivity to yaw, which, with its greater than unity admittance, demonstrates that the region's unsteady response to yaw is even more extreme. The simulated sideglass pressures in this region were less accurate at lower frequency bands due to the aerodynamically less stable nature of this region.

In the mirror wake region the yaw to sideglass pressure admittance was generally below unity, with an admittance roll-off beginning by K = 1. Pressure variations were found to be less yaw dependent than in other sideglass regions, with significant levels of self-excited unsteadiness at higher frequencies (typically K > 5).

### 10.2.4 Non-Linear Effects

The 2D CFD study showed that increasing yaw amplitude or combining multiple frequency components did not have a summative impact on the time-averaged drag and sideforce. This effect was also seen in the wind tunnel study, with individual harmonic TGS driving frequencies indicating a different vehicle response to that found through the TGS arbitrary mode or on-road study. Care therefore needs to be taken in trying to describe vehicle response to transient conditions using linear concepts such as transfer or admittance function, as non-linearity exists in the underlying physics. Using a multiple frequency approach, such as the arbitrary mode, was seen to provide better agreement with the on-road measurements.

## 10.3 Wind tunnel Simulation of On-road Unsteadiness

### 10.3.1 Significant Frequency Region

A key question in the potential simulation of an unsteady incoming flow is the range of frequencies to generate. As discussed, most of the energy on-road is in the 0.1 - 10Hz range (K = 0.1 - 10 for a vehicle driving at highway speeds). For the lowest frequencies (K < 0.3) a quasi-steady approach (e.g.: turntable yaw) will be sufficient. At higher frequencies the energy present on-road reduces and the vehicle response to on-set unsteadiness also reduces; these two factors together making higher frequencies progressively less important. Hence the target frequency band of greatest importance for a simulation device is approximately K = 0.3 - 5 (0.3 - 5Hz full-scale). In this region the on-road energy is significant and the vehicle aerodynamic response is notable, but is not fully understood and will depend on aerodynamic geometry. Additionally, this frequency range encompasses typical vehicle suspension Eigen-frequencies (≈ 1Hz) and the noise modulation, syllable, frequencies at which humans are most sensitive (≈ 4Hz).

### 10.3.2 Turbulence Generation Devices

Sources reviewed showed a variety of drag, lift and thrust systems for generating turbulence in wind tunnels. Static grids, either square or fractal in configuration or plate or rod in shape all generated turbulence length scales which were short in comparison to on-road turbulence length scales of greatest interest. Active drag systems, such as the Pininfarina vane system or oscillating horizontal bars, can generate some longer length scales but the devices' wakes also contain higher frequency components that cannot be regulated. Therefore a lift based device, using oscillating aerofoils, was selected. Sources reviewed also showed the advantage of generating longitudinal turbulence, such as through varying tunnel blockage and bypass flows, and that the ability to induce pitch flows would allow the generation of comparable on-road tri-axis turbulence.

A 2D and 3D CFD TGS design study was completed, showing at 10Hz and ±9° of aerofoil angle, flow yaw angles of up to ±6° could be generated, with an acceptable flow uniformity throughout the test section. The studies showed the advantage of having additional inlet and outlets, controlled by shutter panels. The shutters ensured that even under extreme yaw, the jet shear layer did not interact with the test model and that higher peak yaw angles and improved flow uniformity could be generated. The TGS CFD studies showed that generating higher frequency turbulence (i.e. >10Hz) caused flow uniformity issues, and therefore the TGS design focussed on larger peak aerofoil angles (i.e. ±15°) at 10Hz as opposed to higher aerofoil oscillation rates.

Finally, dynamic CFD simulations showed a ratio between aerofoil angle and flow peak yaw angle of 1.0 : 0.7, and consequently a scalar between the on-road yaw and aerofoil angle was utilised.

### 10.3.3 Turbulence Generation Capability

A TGS system was installed and commissioned at Durham University with twin lateral yaw aerofoils and one horizontal aerofoil imposing pitch, operating up to 10Hz at ±15$^{o}$ incidence. Its twin motor configuration allows real-time aerofoil amplitude and frequency adjustments. Solenoid operated shutter units at the test section inlet and outlet operate in a coordinated unison with the aerofoils, with the shutter open-to angles and opening sequence optimised to create good flow uniformity and peak yaw angles over a test vehicle's plan view. For harmonic test studies, an experimentally derived time delay between the aerofoil motion and the front shutter actuation was found, with an inlet flow acceleration time of 0.20s for a freestream flow rate of 25.6ms$^{-1}$.

A commissioning study demonstrated harmonically induced yaw angles up to ±10$^{o}$ yaw with flow uniformity better than 1$^{o}$ for the side-to-side variation over a vehicle's footprint in the test section. Pitch downwash of -4$^{o}$ could be generated, though the resultant up-wash in the lateral shear flow regions did cause side-to-side flow variations. A highly accurate replication of the on-road trace, denoted the arbitrary trace, was generated, demonstrating the ability to replicate real world on-road flow environments within the 2m wind tunnel at realistic vehicle speeds.

### 10.3.4 Turbulence Generation Approaches

A scaling of time scale between on-road and the wind tunnel is required to achieve the required reduced frequency, accounting for flow velocity and model scale-size differences. On-road yaw measurements were shown to be prepared for TGS simulation and it was found that recreating the prominent yaw peaks from on-road yaw time histories offered the most accurate flow recreation method.

The wind tunnel test study showed that the harmonic case results often poorly predicted the on-road results, suggesting that generating single-frequency, periodic waveforms does not generate the same response that the full on-road spectrum creates. However the arbitrary case test, replicating on-road conditions, gave a notable insight for a greatly reduced test duration in comparison to the vast on-road data collection (32-seconds against 8,800-seconds).

## 10.4 Further Work

The results of the research from this thesis indicate a few areas of interest that would be the proposed onward direction for further work:

- The harmonic test modes all generate a probability density function of a sine function. The sine function has a PDF where the majority of the foil displacement is at the higher angles of yaw displacement, whereas the on-road yaw PDF shows that yaw angles are centred on $0^{o}$ of yaw. One area where the harmonic tests cases could be improved is modifying the harmonic periodic tests to run with a yaw PDF matching the on-road yaw PDF (i.e. less time at higher yaw angles and more time in a cycle at the lower yaw angles).
- The on-road study in this thesis indicated non-symmetric roof probe velocity speed-up over the measured yaw range. This behaviour was proposed to be due to headwinds and tailwinds, though could be due to a Reynolds number effect. Tests conducted reviewing roof probe speed-up over a range of yaw angles at differing test speeds would give further insight into this systematic variance.
- The development of a test case with both an on-road representative spectrum and PDF that accounts for factors such as headwinds and tailwinds and at differing test speeds.
- Develop a facility to measure unsteady forces with a higher fidelity and frequency response than those shown in this thesis. The issue of the measured forces at a similar frequency as the natural frequency of the balance and pressure effects occurring at the upper end of the measurement sampling rate limit could be alleviate by such a facility.
- Undertake further investigations into where on a vehicle and in what environments and flow conditions unsteady effects are important. For example the effect on a vehicle response's through varying vehicle geometry, driving speed and aspect ratio.

## References


Aynsley, R. M., W. Melbourne and B. J. Vickery (1977). "*Architectural Aerodyanmics*." London, Applied Science.

Baker, C. J., S. Dalley, T. Johnson, M. Brown, A. Gaylard, A. Quinn and N. G. Wright (2000). "*Measurements of the slipstream and wake of a model lorry*." Proc. 3rd MIRA International Vehicle Aerodynamics Conference Vehicle Aerodynamics 2000.

Basu, R. I. (1986). "*Aerodynamic forces on structures of circular cross-section. Part 2. The influence of turbulence and three-dimensional effects*." Journal of Wind Engineering and Industrial Aerodynamics 24: 33-59.

Batchelor, G. K. and A. A. Townsend (1948). "*Decay of isotropic turbulence in the initial period*." Proc. Roy. Soc. London 193(539-558).

Bearman, P. W. and T. Morel (1983). "*Effect of Free Stream Turbulence on the Flow Around Bluff Bodies*." Progress in the Aerospace Sciences Vol. 20: p.97-122.

Bearman, P. W. and S. P. Mullarkey (1994). "*Aerodynamic Forces on Road Vehicles due to Steady Side Winds and Gusts*." RAeS Conference Proceedings: p.1-12.

Bienkiewicz, B., J. E. Cermak and J. A. Peterka (1983). "*Active Modeling of Large Scale Turbulence*." Journal of Wind Engineering and Industrial Aerodynamics Vol. 13: p.465-475.

Bischof, G. (2008). "*On-Road Investigation of a Vehicle's Response to Longitudinal Gusts*." SAE Int'l. Journal of Passenger Cars - Aerodynamics SP2151(2008-01-0472): p.113-120.

Buckley, F., C. Marks and W. Walston (1976). "*Analysis of Coast-Down Data to Assess Aerodynamic Drag Reduction on Full-Scale Tractor-Trailer Trucks in Windy Environments*." SAE Int'l. Journal of Passenger Cars - Aerodynamics 760850: 10.4271/760850.

Carlino, G., D. Cardano and A. Cogotti (2007). "*A new technique to measure the aerodynamic response of passenger cars by a continuous flow yawing*." SAE Int'l. Journal of Passenger Cars - Aerodynamics 2007-01-0902.

Carr, G. W. (1994). "*Vehicle Stability studies with a cross-wind generator*."

Cekli, H. E. and W. van de Water (2009). "*Response of periodically modulated turbulence*." Advances in Turbulence XII 132: 237.

Cogotti, A. (2003). "*Generation of Controlled Level of Turbulence in the Pininfarina Wind Tunnel for the Measurement of Unsteady Aerodynamics and Aero Acoustics* " SAE Int'l. Journal of Passenger Cars - Aerodynamics SP1786(2003-01-0430): p.87-96.

Cogotti, A. (2004). "*Update on the Pininfarina TGS and its Effects on the Car Aerodynamics and Aero Acoustics* " SAE Int'l. Journal of Passenger Cars - Aerodynamics SP1874(2004-01-0807): p.265-279.

Cogotti, A. (2005). "*Transient behaviour of vehicles at Pininfarina test facility*." SAE Vehicle Aerodynamic Studies SP1931(2005-01-1455).

Coleman, S. A. and C. J. Baker (1993). "*The reduction of accident risk for high sided road vehicles in cross winds*." Journal of Wind Engineering and Industrial Aerodynamics 44(1-3): 2685-2695.

Coleman, S. A. and C. J. Baker (1994). "*An experimental study of the aerodynamic behaviour of high sided lorries in cross winds*." Journal of Wind Engineering and Industrial Aerodynamics 53(3): 401-429.

Cooper, K. R. (1989). "*An Active turbulence generator for the wind tunnel simulation of the large-scale turbulence required for section-model bridge testing*." Proceedings Canada-Japan Workshop on Bridge Aerodynamics, Ottawa.

Cooper, K. R. and W. F. Campbell (1981). "*An examination of the effects of wind turbulence on the aerodynamic drag of vehicles*." Journal of Wind Engineering and Industrial Aerodynamics 9.

Corin, R. J., L. He and R. G. Dominy (2008). "*A CFD Investigation into the Transient Aerodynamic Forces on Overtaking Road Vehicles*." Journal of Wind Engineering and Industrial Aerodyanmics 96: p.1390-1411.

Corrsin, S. and G. Comte-Bellot (1966). "*The Use of a Contraction to Improve the Isotropy of Grid-Generated Turbulence*." Journal of Fluid Mechanics 25.4: 657-682.

Davenport, A. G. (1961). "*The spectrum of horizontal gustiness near the ground in high winds*." Journal of the Royal Meteorological Society 87(194-211).

Devinant, P., T. Laverne and J. Hureau (2002). "*Experimental study of wind turbine airfoil aerodynamics in high turbulence*." Journal of Wind Engineering and Industrial Aerodynamics Vol: 90: p.689-701.

Docton, M. (1996). "*The Simulation of Transient Crosswinds on Passenger Vehicles*." Durham University PhD Thesis.

Dryden, H. and G. B. Schubauer (1936). "*Effect of turbulence on the drag of flat plates*." NACA Tech. Rept. 546.

ESDU74030 (1974). "*Characteristics of Atmospheric Turbulence near the Ground - Part 1*." ESDU(74030): 15.

ESDU85020 (1985). "*Characteristics of Atmospheric Turbulence near the Ground - Part 2*." ESDU(A9232): p.1-20.

Gad-el-Hak, M. and S. Corrson (1974). "*Measurements of the Nearly Isotropic Turbulence Behind a Uniform Jet Grid*." Journal of Fluid Mechanics Vol. 62(1): p.115-143.

Garry, K. and K. R. Cooper (1986). "*Comparison of quasi-static and dynamic wind tunnel measurements of simplified tractor-trailer models*." Journal of Wind Engineering and Industrial Aerodynamics 22: 9.

Garry, K. P. (1982). "*Wind tunnel techniques for reducing commercial vehicle aerodynamic drag*." PhD Thesis, Cranfield Institute of Technology.

Gaylard, A., M. Beckett, J. Gargoloff and B. Duncan (2010). "*CFD based modelling of flow conditions capable of inducing hood flutter*." SAE Int'l. Journal of Passenger Cars - Aerodynamics SP2269(2010-01-1011): p.307-329.

Gilhaus, A. and V. Renn (1986). "*Drag and Driving-Stability Related Aerodynamic Forces and Their Inter-dependence. Results of Measurements on 3/8-Scale Basic Car Shapes*." SAE Int'l. Journal of Passenger Cars - Aerodynamics 860211(10.4271/860211).

Gilhome, B. and J. Saunders (2002). "*The Effect of Turbulence on Peak and Average Pressures on a Car Door*." SAE Int'l. Journal of Passenger Cars - Aerodynamics SP1667 (2002-01-0253).

Holdsworth, R. (2005). "*Simulation of Atmospheric Turbulence for Wind Tunnel Testing of Road Vehicles*." Durham University Masters Thesis: p.1-48.

Hopkins, A. (2007). "*Analysis of Ground Atmospheric Turbulence* " Durham University Masters Thesis: p.1-50.

Howell, J. (1995). "*Experiences with the MIRA X-wind generator*." Aerodynamics Special Interst Group, MIRA.

Howell, J., C. Sherwin and M. Passmore (2002). "*Aerodynamic Drag of a Compact SUV as Measured On-Road and in the Wind Tunnel*." SAE Int'l. Journal of Passenger Cars - Aerodynamics SP1667 (2002-01-0529).

Huang, R. F. and H. W. Lee (1999). "*Effects of Freestream Turbulence on Wing-Surface Flow and Aerodynamic Performance*." Journal of Aircraft Vol. 36(Issue 6): p.965-972.

Hunt, J. C. R., H. Kawai, S. R. Ramsey, G. Pedrizetti and R. J. Perkins (1992). "*A review of velocity and pressure fluctuations in turbulent flows around bluff bodies*." Advances in Turbulence XII 35.

Hurst, D. J. and J. C. Vassilicos (2007). "*Scalings and decay of fractal-generated turbulence*." Physics of Fluids 19.

Iyengar, A. K. and C. Farell (2001). "*Experimental Issues in Atmospheric Boundary Layer Simulations: Roughness Length and Integral Length Scale Determination*." Journal of Wind Engineering and Industrial Aerodynamics Vol. 89: p.1059-1080.

Jancauskas, E. D. (1983). "*The Cross-Wind Excitation of Bluff Structures and the Incident Turbulence Mechanism*." Monash University PhD Thesis.

Kang, J. C., H. Kawai, S. R. Ramsey, G. Pedrizetti and R. J. Perkins (1990). "*A review of velocity and pressure fluctuations in turbulent flowas around bluff bodies*." Journal of Wind Engineering and Industrial Aerodynamics Vol. 35: p.49-85.

Knebel, P., A. Kittel and J. Peinke (2010). "*Atmospheric Wind Field Conditions Generated by Active Grids*." Experiments in Fluids Vol. 51(Issue 2): p.471-481.

Kobayashi, H. and A. Hatanaka (1992). "*Active Generation of wind gust in a 2-D wind tunnel*." Journal of Wind Engineering and Industrial Aerodynamics Vol. 41: p.959-970.

Lawson, A., R. G. Dominy and D. B. Sims-Williams (2007). "*A comparison between on-road and wind tunnel surface pressure measurements on a mid-sized hatchback*." SAE Int'l. Journal of Passenger Cars - Aerodynamics SP2166(2007-01-0898): p.173-183.

Lawson, A., D. B. Sims-Williams and R. G. Dominy (2007). "*Rover 200 MIRA Wind Tunnel Data*." Private Communication.

Lawson, A., D. B. Sims-Williams and R. G. Dominy (2008). "*Effects of On-Road Turbulence on Vehicle Surface Pressures in the A-Pillar region*." SAE Int'l. Journal of Passenger Cars - Aerodynamics SP2151(2008-01-0474): p.139-147.

Lawson, A., D. B. Sims-Williams and R. G. Dominy (2008). "*Rover 200 MIRA Wind Tunnel Data*." Private Communication.

Lindener, N., H. Miehling, A. Cogotti, F. Cogotti and M. Maffei (2007). "*Aeroacoustic measurements in turbulent flow on the road and in the wind tunnel*." SAE Int'l. Journal of Passenger Cars - Aerodynamics SP(2007-01-1551).

Ling, S. C. and C. A. Wang (1972). "*Decay of Isotropic Turbulence Generated by a Mechanically Agitated Grid*." Physics of Fluids Vol. 15(Issue 1363): p.1-7.

Liu, H. T. (1992). "*Atmospheric Turbulence and Gust on the Performance on a Worthmann Wing at Low Reynolds Numbers*." Journal of Aircraft Vol. 29(Issue 4): p.532-539.

Macklin, R., K. Garry and J. Howell (1997). "*Assessing the Effects of Shear and Turbulence During the Dynamic Testing of the Crosswind Sensitivity of Road Vehicles*." SAE Int'l. Journal of Passenger Cars - Aerodynamics SP1232(970135): p.29-42.

Makita, H. and K. Sassa (1991). "*Active turbulence generation in a laboratory wind tunnel*." Advances in Turbulence Vol. 3.

Mala, G. M. and D. Li (1999). "*Flow characteristics of fluids*." Int Journal Heat Fluid Flow 20: 142-148.

Mankowski, O. A., D. B. Sims-Williams and D. R.G. (2013). "*A Wind Tunnel Simulation Facility for On-Road Transients*." SAE Int'l. Journal of Passenger Cars - Aerodynamics 2014-01-0587.

Melbourne, W. H. (1993). "*Turbulence and the Leading Edge Phenomenon*." Journal of Wind Engineering and Industrial Aerodynamics 49(45-64).

MG-Rover (1996). "*Rover 200 R3 Performance Specifications*." Private Communication.

Mish, P. F. (2001). "*Mean Loading Effects on the Surface Pressure Fluctuations on an Airfoil in Turbulence*." Virginia Polytechnic Institute and State University PhD Thesis.

Mullarkey, S. (1990). "*Aerodynamics Stability of Road Vehicles in Side Winds and Gusts*." PhD Thesis, Imperial College, Univeristy of London.

Nagata, K., H. Suzuki, Y. Sakai, T. Hayase and T. Kubo (2008). "*Direct numerical simulation of turbulent mixing in grid-generated turbulence*." Royal Academy of Sciences.

Neff, D. E. and R. N. Meroney (1985). "*Measurement in a Wind Tunnel of the Modification of Mean Wind and Turbulence Characteristics Due to Induction Effects Near Wind Turbine Rotors*." Fluid Mechanics and Wind Engineering Program(CER85-86DEN-RNM10).

Newnham, P. and M. Passmore (2006). "*On the Optimisation of Road Vehicle Leading Edge Radius in Varying Levels of Freestream Turbulence*." SAE Int'l. Journal of Passenger Cars - Aerodynamics SP2017(2006-01-1029).

Newnham, P. and M. Passmore (2008). "*The Effect of Raised Freestream Turbulence on the Flow Around Leading Edge Radii*." SAE Int'l. Journal of Passenger Cars - Aerodynamics SP2151(2008-01-0473): p.121-134.

Nguyen, T., J. Saunders and S. Watkins (1997). "*The Sideways Dynamic Force on Passenger Cars in Turbulent Winds*." SAE Int'l. Journal of Passenger Cars - Aerodynamics SP1232(970405): p.157-172.

Nishi, A. and H. Miyahi (1995). "*Computer controlled wind tunnel for wind engineering applications*." Journal of Wind Engineering and Industrial Aerodynamics Vol. 54-55: p.493-504.

Oettle, N. R. and D. B. Sims-Williams (2012). "*The Effects of Unsteady On-Road Flow Conditions on Cabin Noise*." PhD Thesis, Durham University.

Oettle, N. R., D. B. Sims-Williams, R. G. Dominy, C. J. E. Darlington, C. M. Freeman and P. F. Tindall (2010). "*The Effects of Unsteady On-Road Flow Conditions on Cabin Noise*." SAE Int'l. Journal of Passenger Cars - Aerodynamics SP2269(2010-01-0289).

Ozono, S., A. Nishi and H. Mygaghi (2006). "*Turbulence generated by a wind tunnel of multi-fan type in uniformly active and quasi-grid modes*." Journal of Wind Engineering and Industrial Aerodynamics Vol. 94(Issue 4): p. 225-240.

Passmore, M., S. Richardson and A. Imam (2001). "*An Experimental Study of Unsteady Vehicle Aerodynamics*." Proc. of the iMechE Part D Journal of Automobile Engineering 215.

Pearce, W. and C. J. Baker (1998). "*Measurements of the unsteady crosswind forces and moments on ground vehicles*." MIRA Conference on Vehicle Aerodynamics, Birmingham.

Ryan, A. (2000). *The Simulation of Transient Cross-Wind Gusts and Their Aerodynamic Influence on Passenger Cars*, Durham University. PhD.

Sacre, C., J. P. Flori and P. Duchene-Marullaz (1987). "*Preliminary Study of Turbulence in Complex Terrain for Wind Turbine Setting Up*." Second Contractors' Meeting 23-24: 187-192.

Sarkar, P. and F. Henn (2002). "*Design and testing of Iowa State University's AABL (Atmospheric Boundary Layer) Wind and Gust Tunnel*." Iowa State University Paper: p.1-18.

Sato, H. and S. T. (1974). "*Laboratory Simulation of Atmospheric Turbulence: Generation of Arbitrary velocity Distribution and Model experiment of Flow Around Mt. Fuji*." Advances in Geophysics 18B: p.241-251.

Saunders, G. H. (1974). "*Mutual Aerodynamic Interference Effects for Multiple Bodies of Revolution and Distorted Bodies of Revolution*." Auburn University.

Saunders, J. and R. Mansour (2000). "*On road and wind tunnel turbulence and its measurement using a four-hole dynamic probe ahead of several cars*." SAE Int'l. Journal of Passenger Cars - Aerodynamics SP1600(2000-01-0350).

Saunders, J. and S. Wordley (2006). "*A review of measurement of ambient Turbulence with respect to Ground Vehicles* " SAE Int'l. Journal of Passenger Cars - Aerodynamics SP1991(2006-01-1028): p.273-282.

Saunders, J. W., S. Watkins and P. H. Hoffmann (1987). "*Wind tunnel modelling of commercial vehicle drag reducing devices*." SAE Int'l. Journal of Passenger Cars - Aerodynamics(870717).

Schröck, D., W. Krantz, N. Widdecke and J. Wiedemann (2011). "*Unsteady Aerodynamic Properties of a Vehicle Model and Their Effect on Driver and Vehicle under Side Wind Conditions*." SAE Int'l. Journal of Passenger Cars - Aerodynamics SP(2011-01-0154).

Schröck, D., N. Widdecke and J. Wiedemann (2009). "*Aerodynamic Response of a Vehicle Model to Turbulent Wind*." 7th FKFS Conference, Stuttgart.

Simmons, L. F. G. and C. Salter (1934). "*Experimental investigation and analysis of velocity variations in turbulent flow*." Proc. Roy. Soc. London A145: 212-234.

Sims-Williams, D. B. (2001). "*Self-Excited aerodynamic unsteadiness associated with passenger cars*." Durham University PhD Thesis.

Sims-Williams, D. B. (2002). "*The design of a new wind tunnel for vehicle aerodynamics research*." Mira 4th Conference.

Sims-Williams, D. B. (2010). "*Cross-Winds and Transients: Reality, Simulation and Effects*." SAE Int'l. Journal of Passenger Cars - Aerodynamics Vol. 4(2011-01-0172): p.172-183.

Sims-Williams, D. B. (2011). "*Cross winds and transients: reality, simulation and effects*." SAE Int'l. Journal of Passenger Cars - Aerodynamics SP(2011-01-0172).

Sims-Williams, D. B. (2012). "*Durham Software for Wind Tunnels User Manual*." Internal Document.

Sims-Williams, D. B. and R. G. Dominy (1998). "*Experimental Investigation into Unsteadiness and Instability in Passenger Car Aerodynamics*." SAE Int'l. Journal of Passenger Cars - Aerodynamics SP1318(980391).

Sluman, T. J., H. R. E. van Maanen and G. Ooms (1980). "*Atmospheric boundary layer simulation in a wind tunnel, using air injection*." App Sci 36: 289-307.

Spalart, P. R. and S. R. Allmaras (1992). "*A One-Equation Turbulence Model for Aerodynamic Flows*." AIAA Paper 92-0439.

Stack, J. (1931). "*Tests in the Variable Density Wind Tunnel to Investigate the Effects of Scale and Turbulence on Airfoil Characteristics*." NACA Langley Memorial Aeronautical Laboratory NACA-TN-364.

Swalwell , K. (2005). "*The Effect of Turbulence on Stall of Horizontal Axis Wind Turbines*." Monash University PhD Thesis: p.1-315.

Teunissen, H. W. (1980). "*Structure of mean wind and turbulence in the planetary boundary layer over rural terrain*." Boundary-Layer Meteorology Vol. 19(Issue 2): p.187-221.

Theissen, P., J. Wojciak and K. Heuler (2010). "*Experimental Investigation of Unsteady Vehicle Aerodynamics under Time-Dependent Flow Condition*." SAE Int'l. Journal of Passenger Cars - Aerodynamics SP2305(2011-01-0177).

Vickery, B. J. (1966). "*Fluctuating lift and drag on a long cylinder of square cross-section in a smooth and in a turbulent stream*." Journal of Fluid Mechanics 25: 481-494.

Wasco, M. (2003). "*Wind tunnel simulation of on-road turbulence using an oscillating, upstream pendulum*." RMIT, Melbourne Masters Thesis.

Watkins, S. (2007). "*The unsteady wind environment of Road Vehicles Part 2: Effects on vehicle development and simulation of turbulence*." Vehicle Aerodynamics 2007 SP2066(SAE Paper 2007-01-1237): 15.

Watkins, S. (1990). "*Wind Tunnel Modeling of vehicles Aerodynamics: Turbulent effects on Commercial Vehicle Drag*." RMIT University PhD Thesis: p.1-300.

Watkins, S., M. Riegel and J. Wiedemann (2001). "*The Effect of Turbulence on Wind Noise*." FKFS/Stuttgart University.

Watkins, S. and J. Saunders (1998). "*A Review of the Wind Conditions Experienced by a Moving Vehicle*." SAE Int'l. Journal of Passenger Cars - Aerodynamics SP1318(981182).

Watkins, S., J. W. Saunders and P. H. Hoffmann (1995). "*Turbulence experienced by moving vehicles. Part I. Introduction and turbulence intensity*." Journal of Wind Engineering and Industrial Aerodynamics 57: 17.

Wordley, S. and J. Saunders (2009). "*On-Road Turbulence: Part 2*." SAE Int'l. Journal of Passenger Cars - Aerodynamics SP2226(2009-01-0002): p.232-261.

Wyngaard, J. C. and S. F. Clifford (1977). "*Taylor's Hypothesis and High-Frequency Turbulence Spectra*." Journal of Atmospheric Sciences 34(922-929).

# Appendix 1. TGS Commissioning Results and Configuration

## 1.1 TGS Aerofoil to Motor Angle Conversions

| Lateral Foils | | | Horizontal Foils | |
|---|---|---|---|---|
| Foil Angle | Motor Angle | | Foil Angle | Motor Angle |
| 0 | 0 | | 0 | 0 |
| 1 | 4 | | 1 | 4 |
| 2 | 8 | | 2 | 8 |
| 3 | 12 | | 3 | 12 |
| 4 | 16 | | 4 | 16 |
| 5 | 20 | | 5 | 20 |
| 6 | 24 | | 6 | 24 |
| 7 | 28 | | 7 | 28 |
| 8 | 33 | | 8 | 33 |
| 9 | 37 | | 9 | 37 |
| 10 | 42 | | 10 | 42 |
| 11 | 47 | | 11 | 47 |
| 12 | 53 | | 12 | 53 |
| 13 | 60 | | 13 | 60 |
| 14 | 69 | | 14 | 69 |
| 15 | 90 | | 15 | 90 |
| -1 | 356 | | -1 | 356 |
| -2 | 352 | | -2 | 352 |
| -3 | 348 | | -3 | 348 |
| -4 | 344 | | -4 | 344 |
| -5 | 340 | | -5 | 340 |
| -6 | 336 | | -6 | 336 |
| -7 | 332 | | -7 | 332 |
| -8 | 327 | | -8 | 327 |
| -9 | 323 | | -9 | 323 |
| -10 | 318 | | -10 | 318 |
| -11 | 313 | | -11 | 313 |
| -12 | 307 | | -12 | 307 |
| -13 | 300 | | -13 | 300 |
| -14 | 291 | | -14 | 291 |
| -15 | 270 | | -15 | 270 |
| | | | | |
| | | | With a Phase Shift of 180 degrees | |

Figure 330 - Aerofoil to motor angle conversions

## 1.2 TGS Commissioning Test Results

### 1.2.1 Shutter Open-to Test Results

**Table 25- Results from the static shutter tests to determine optimum shutter open-to angle (from p.219)**

| | | 15 | 12 | 10 | 8 | 6 | 4 | 2 | 0 | -2 | -4 | -6 | -8 | -10 | -12 | -15 | Mod. Avg | Extremity Mod Avg. |
|---|---|---|---|---|---|---|---|---|---|---|---|---|---|---|---|---|---|---|
| Average | *F15R15* | 7.536 | 6.853 | 5.87 | 4.34 | 2.877 | 1.934 | 1.500 | -0.048 | -0.326 | -0.440 | -1.117 | -2.393 | -3.397 | -4.167 | -4.792 | 3.396 | 5.837 |
| Std. Dev | *F15R15* | 0.472 | 0.619 | 0.41 | 0.33 | 0.214 | 0.292 | 0.599 | 0.711 | 0.522 | 0.720 | 0.282 | 0.458 | 0.454 | 0.532 | 0.422 | 0.473 | 0.497 |
| FR-RR | *F15R15* | -0.101 | 0.019 | -0.247 | -0.117 | -0.279 | -0.398 | 0.429 | 0.756 | 0.501 | 0.817 | 0.398 | 0.323 | -0.245 | -0.161 | 0.012 | 0.121 | 0.013 |
| Y+-Y- | *F15R15* | -1.040 | -1.361 | -0.917 | -0.662 | 0.153 | 0.242 | 1.222 | 1.268 | 0.832 | 1.255 | 0.119 | -0.818 | -0.785 | -1.067 | -0.709 | 0.111 | 0.749 |

| | | 15 | 12 | 10 | 8 | 6 | 4 | 2 | 0 | -2 | -4 | -6 | -8 | -10 | -12 | -15 | Mod. Avg | Extremity Mod Avg. |
|---|---|---|---|---|---|---|---|---|---|---|---|---|---|---|---|---|---|---|
| Average | *F8R8* | 7.362 | 5.686 | 4.878 | 3.586 | 2.756 | 2.589 | 1.744 | 0.337 | 0.590 | -0.279 | -1.141 | -1.637 | -2.990 | -3.005 | -4.402 | 2.962 | 5.113 |
| Std. Dev | *F8R8* | 0.647 | 0.666 | 0.464 | 0.445 | 0.252 | 0.454 | 0.562 | 0.690 | 0.633 | 0.325 | 0.196 | 0.324 | 0.250 | 0.552 | 0.708 | 0.461 | 0.620 |
| FR-RR | *F8R8* | -0.396 | -0.600 | -0.393 | -0.274 | -0.149 | -0.096 | 0.403 | 0.078 | 0.175 | 0.602 | 0.028 | 0.297 | 0.054 | 0.253 | -0.027 | 0.001 | 0.255 |
| Y+-Y- | *F8R8* | -1.412 | -1.382 | -0.933 | -0.893 | -0.354 | 0.836 | 1.134 | 1.554 | 1.435 | 0.321 | 0.060 | -0.332 | -0.365 | -1.173 | -1.463 | 0.107 | 1.038 |

| | | 15 | 12 | 10 | 8 | 6 | 4 | 2 | 0 | -2 | -4 | -6 | -8 | -10 | -12 | -15 | Mod. Avg | Extremity Mod Avg. |
|---|---|---|---|---|---|---|---|---|---|---|---|---|---|---|---|---|---|---|
| Average | *F15R8* | 7.532 | 6.590 | 6.005 | 5.110 | 4.201 | 2.080 | 0.807 | 0.562 | 0.331 | -0.630 | -1.454 | -2.152 | -3.296 | -4.134 | -4.134 | 3.414 | 5.597 |
| Std. Dev | *F15R8* | 0.762 | 0.644 | 0.662 | 0.499 | 0.214 | 0.496 | 0.541 | 0.600 | 0.632 | 0.431 | 0.314 | 0.352 | 0.384 | 0.317 | 0.317 | 0.489 | 0.553 |
| FR-RR | *F15R8* | 0.250 | 0.065 | -0.150 | -0.414 | -0.062 | 0.011 | 0.321 | 0.185 | 0.663 | 0.758 | 0.216 | -0.079 | -0.178 | -0.245 | -0.245 | 0.096 | 0.041 |
| Y+-Y- | *F15R8* | -1.060 | -1.292 | -1.457 | -0.961 | 0.349 | 0.953 | 1.188 | 1.272 | 1.138 | 0.232 | -0.066 | -0.340 | -0.744 | -0.622 | -0.622 | 0.101 | 0.718 |

| | | 15 | 12 | 10 | 8 | 6 | 4 | 2 | 0 | -2 | -4 | -6 | -8 | -10 | -12 | -15 | Mod. Avg | Extremity Mod Avg. |
|---|---|---|---|---|---|---|---|---|---|---|---|---|---|---|---|---|---|---|
| Average | *F8R15* | 8.199 | 7.077 | 6.118 | 5.205 | 4.044 | 3.558 | 2.292 | 1.162 | 0.662 | -0.462 | -1.366 | -2.012 | -3.313 | -4.320 | -4.051 | 3.668 | 5.912 |
| Std. Dev | *F8R15* | 0.656 | 0.421 | 0.319 | 0.496 | 0.219 | 0.329 | 0.469 | 0.521 | 0.419 | 0.236 | 0.421 | 0.287 | 0.296 | 0.441 | 0.506 | 0.395 | 0.495 |
| FR-RR | *F8R15* | -0.333 | 0.054 | -0.053 | -0.244 | -0.143 | -0.323 | -0.109 | 0.716 | 0.728 | 0.081 | 0.694 | 0.087 | -0.024 | 0.260 | 0.363 | 0.099 | 0.046 |
| Y+-Y- | *F8R15* | -1.406 | -0.923 | -0.700 | -1.064 | -0.338 | 0.595 | 0.908 | 0.771 | 0.242 | -0.044 | -0.308 | -0.405 | -0.574 | -0.897 | -1.021 | 0.296 | 0.764 |

| | | 15 | 12 | 10 | 8 | 6 | 4 | 2 | 0 | -2 | -4 | -6 | -8 | -10 | -12 | -15 | Mod. Avg | Extremity Mod Avg. |
|---|---|---|---|---|---|---|---|---|---|---|---|---|---|---|---|---|---|---|
| Average | *Closed* | 6.880 | 6.150 | 5.603 | 5.088 | 4.241 | 2.540 | 1.586 | 0.503 | 0.314 | -0.453 | -0.422 | -1.386 | -1.971 | -2.584 | -3.501 | 3.006 | 4.779 |
| Std. Dev | *Closed* | 0.246 | 0.158 | 0.145 | 0.249 | 0.217 | 0.393 | 0.543 | 0.630 | 0.551 | 0.428 | 0.385 | 0.552 | 0.316 | 0.414 | 0.235 | 0.373 | 0.253 |
| FR-RR | *Closed* | -0.368 | -0.174 | -0.136 | -0.247 | -0.308 | -0.201 | 0.261 | 0.434 | 0.517 | 0.564 | 0.239 | 0.502 | 0.553 | 0.572 | 0.187 | 0.158 | 0.049 |
| Y+-Y- | *Closed* | -0.345 | -0.156 | -0.170 | -0.367 | 0.251 | 0.656 | 1.113 | 1.216 | 0.911 | 0.441 | -0.653 | -0.855 | -0.187 | -0.558 | -0.189 | 0.093 | 0.149 |

| Averages | *F8R15* | | |
|---|---|---|---|
| Set | -10 | 0 | 10 |
| 1 | -1.796 | 1.218 | 5.574 |
| 2 | -1.647 | 1.286 | 5.509 |
| 3 | -1.731 | 1.267 | 5.530 |
| 4 | -1.683 | 1.221 | 5.614 |
| 5 | -1.742 | 1.259 | 5.553 |
| 6 | -1.734 | 1.215 | 5.578 |
| 7 | -1.732 | 1.311 | 5.528 |
| 8 | -1.788 | 1.333 | 5.486 |
| 9 | -1.776 | 1.357 | 5.594 |
| 10 | -1.710 | 1.278 | 5.504 |
| Std. Dev: | 0.047 | 0.049 | 0.042 |
| Avg Std Dev: | 0.046 | | |

| Std Devs | *F8R15* | | |
|---|---|---|---|
| Set | -10 | 0 | 10 |
| 1 | 0.629 | 0.470 | 0.392 |
| 2 | 0.491 | 0.449 | 0.380 |
| 3 | 0.656 | 0.521 | 0.439 |
| 4 | 0.660 | 0.344 | 0.514 |
| 5 | 0.582 | 0.414 | 0.558 |
| 6 | 0.722 | 0.363 | 0.525 |
| 7 | 0.666 | 0.359 | 0.487 |
| 8 | 0.619 | 0.410 | 0.349 |
| 9 | 0.505 | 0.375 | 0.466 |
| 10 | 0.476 | 0.519 | 0.367 |
| Std. Dev: | 0.084 | 0.065 | 0.073 |
| Avg Std Dev: | 0.074 | | |

| FR-RR | *F8R15* | | |
|---|---|---|---|
| Set | -10 | 0 | 10 |
| 1 | 0.277 | 0.352 | -0.139 |
| 2 | -0.055 | 0.334 | 0.011 |
| 3 | 0.387 | 0.355 | 0.107 |
| 4 | 0.356 | 0.202 | -0.204 |
| 5 | 0.022 | 0.335 | 0.170 |
| 6 | -0.030 | 0.198 | -0.299 |
| 7 | -0.060 | 0.304 | -0.064 |
| 8 | 0.123 | -0.004 | -0.069 |
| 9 | 0.231 | 0.085 | -0.188 |
| 10 | 0.231 | 0.138 | -0.197 |
| Std. Dev: | 0.171 | 0.126 | 0.148 |
| Avg Std Dev: | 0.149 | | |

| Y+-Y- | *F8R15* | | |
|---|---|---|---|
| Set | -10 | 0 | 10 |
| 1 | -1.249 | 0.733 | -0.829 |
| 2 | -1.027 | 0.845 | -0.747 |
| 3 | -1.322 | 1.021 | -0.886 |
| 4 | -1.409 | 0.618 | -1.099 |
| 5 | -1.279 | 0.766 | -1.117 |
| 6 | -1.459 | 0.778 | -1.127 |
| 7 | -1.116 | 0.724 | -1.067 |
| 8 | -1.319 | 0.856 | -0.723 |
| 9 | -1.003 | 0.782 | -0.984 |
| 10 | -0.912 | 1.087 | -0.795 |
| Std. Dev: | 0.184 | 0.140 | 0.160 |
| Avg Std Dev: | 0.162 | | |

**Table 26 - Summary of results by rankings from the static shutter tests to determine optimum shutter open-to angle (from p.219)**

| Metrics | Mod. Avg | Avg. Std Dev. | Avg FR-RR | Avg. Y+-Y- | Ext. Avg. | Ext. Std. Dev. | Ext. FR-RR | Ext. Y+-Y- |
|---|---|---|---|---|---|---|---|---|
| F8: | 3.315 | 0.428 | 0.050 | 0.202 | 5.513 | 0.558 | 0.151 | 0.901 |
| F15: | 3.405 | 0.481 | 0.108 | 0.106 | 5.717 | 0.525 | 0.027 | 0.734 |
| R8: | 3.188 | 0.475 | 0.049 | 0.104 | 5.355 | 0.587 | 0.148 | 0.878 |
| R15: | 3.532 | 0.434 | 0.110 | 0.204 | 5.874 | 0.496 | 0.029 | 0.757 |
| Closed: | 3.006 | 0.373 | 0.158 | 0.093 | 4.779 | 0.253 | 0.049 | 0.149 |
| **Ranks** | | | | | | | | |
| F8: | 3 | 2 | 2 | 4 | 3 | 4 | 5 | 5 |
| F15: | 2 | 5 | 3 | 3 | 2 | 3 | 1 | 2 |
| R8: | 4 | 4 | 1 | 2 | 4 | 5 | 4 | 4 |
| R15: | 1 | 3 | 4 | 5 | 1 | 2 | 2 | 3 |
| Closed: | 5 | 1 | 5 | 1 | 5 | 1 | 3 | 1 |
| | 0 | 1 | 1 | 1 | 0 | 1 | 1 | 1 |
| | High=Good | Low=Good | Low=Good | Low=Good | High=Good | Low=Good | Low=Good | Low=Good |

**Table 27 - Compilation of results from the static shutter open-to angle tests (from p.219)**

| | F15R15 | F8R8 | F15R8 | F8R15 | Closed | Assesses |
|---|---|---|---|---|---|---|
| Mod Avg. | 3 | 5 | 2 | 1 | 4 | Angle |
| Avg. Std Dev. | 4 | 3 | 5 | 2 | 1 | Uniformity |
| Avg FR-RR | 4 | 1 | 2 | 3 | 5 | Uniformity |
| Avg. Y+-Y- | 4 | 3 | 2 | 5 | 1 | Uniformity |
| Ext.Mod. Avg. | 5.8 | 5.1 | 5.6 | 5.9 | 4.8 | Angle |
| Ext. Std. Dev. | | | | | | Uniformity |
| Ext. FR-RR | 0 | 0.3 | 0 | 0 | 0 | Uniformity |
| Ext. Y+-Y- | 0.7 | 1 | 0.7 | 0.8 | 0.1 | Uniformity |

**Table 28 - Shutter nominal opening angles**

| | FRONT RIGHT | | | | | FRONT LEFT | | | | | REAR RIGHT | | | | REAR LEFT | | | |
|---|---|---|---|---|---|---|---|---|---|---|---|---|---|---|---|---|---|---|
| Shutter no.: | 1 | 2 | 3 | 4 | 5 | 6 | 7 | 8 | 9 | 10 | 11 | 12 | 13 | 14 | 15 | 16 | 17 | 18 |
| Foil x-dist. (m): | 0 | 0 | 0 | 0 | 0 | 0 | 0 | 0 | 0 | 0 | 5.6 | 5.6 | 5.6 | 5.6 | 5.6 | 5.6 | 5.6 | 5.6 |
| Foil y-dist. To centre (m): | 0.28 | 0.34 | 0.40 | 0.46 | 0.52 | -0.28 | -0.34 | -0.40 | -0.46 | -0.52 | 0.22 | 0.28 | 0.34 | 0.40 | -0.22 | -0.28 | -0.34 | -0.40 |
| Nominal Yaw Open Angle: | 2.87 | 3.48 | 4.10 | 4.72 | 5.34 | 2.87 | 3.48 | 4.10 | 4.72 | 5.34 | 2.25 | 2.87 | 3.48 | 4.10 | 2.25 | 2.87 | 3.48 | 4.10 |
| Flow Angle (degrees): | 5.73 | 6.97 | 8.20 | 9.43 | 10.67 | 5.73 | 6.97 | 8.20 | 9.43 | 10.67 | 4.50 | 5.73 | 6.97 | 8.20 | 4.50 | 5.73 | 6.97 | 8.20 |
| Motor Angle (degrees): | 203 | 208 | 213 | 219 | 226 | 23 | 28 | 33 | 39 | 46 | 198 | 203 | 208 | 213 | 18 | 23 | 28 | 33 |

**Table 29 - Resultant flow yaw based upon shutter opening configuration detailed in Table 14**

| Nominal | | 15 | 12 | 10 | 8 | 6 | 4 | 2 | 0 | -2 | -4 | -6 | -8 | -10 | -12 | -15 |
|---|---|---|---|---|---|---|---|---|---|---|---|---|---|---|---|---|
| Average (degrees) | F8R15 | 6.46 | 5.73 | 4.73 | 3.66 | 2.82 | 2.29 | 0.89 | -0.17 | -1.10 | -1.77 | -2.38 | -2.88 | -3.95 | -4.52 | -5.58 |
| Std. Dev (degrees) | F8R15 | 0.83 | 0.73 | 0.54 | 0.49 | 0.54 | 0.32 | 0.32 | 0.23 | 0.22 | 0.47 | 0.64 | 0.71 | 0.80 | 0.70 | 0.78 |
| FR-RR (degrees) | F8R15 | -0.39 | -0.33 | 0.01 | -0.37 | -0.53 | -0.21 | 0.27 | 0.00 | 0.40 | 0.24 | 0.37 | -0.05 | 0.54 | 0.17 | 0.14 |
| Y+-Y- (degrees) | F8R15 | -1.07 | -0.84 | -0.47 | -0.25 | -0.04 | 0.63 | 0.96 | 0.89 | 0.68 | -0.20 | -0.35 | -0.78 | -1.15 | -0.91 | -1.06 |
| | | | | | | | | | | | | | | | | |
| Batch 1 | | 15 | 12 | 10 | 8 | 6 | 4 | 2 | | -2 | -4 | -6 | -8 | -10 | -12 | -15 |
| Average (degrees) | F8R15 | 6.27 | 5.46 | 5.16 | 3.79 | 2.83 | 1.41 | -0.53 | #N/A | -0.75 | -1.69 | -1.51 | -3.02 | -3.85 | -4.84 | -6.40 |
| Std. Dev (degrees) | F8R15 | 0.79 | 0.70 | 0.76 | 0.60 | 0.37 | 0.52 | 0.33 | #N/A | 0.43 | 0.65 | 0.34 | 0.79 | 0.84 | 0.52 | 0.75 |
| FR-RR (degrees) | F8R15 | -0.79 | -0.58 | -0.36 | -0.55 | -0.54 | -0.81 | -0.24 | #N/A | -0.15 | -0.01 | -0.24 | -0.31 | -0.11 | -0.13 | -1.38 |
| Y+-Y- (degrees) | F8R15 | -1.47 | -1.33 | -1.62 | -1.09 | -0.64 | -0.04 | -0.63 | #N/A | -0.99 | -1.07 | -0.64 | -1.47 | -1.86 | 0.70 | -0.47 |
| | | | | | | | | | | | | | | | | |
| Batch 2 | | | | 10 | 8 | 6 | 4 | 2 | | -2 | -4 | -6 | -8 | -10 | -12 | -15 |
| Average (degrees) | F8R15 | | | 4.31 | 3.42 | 2.95 | 1.83 | 0.65 | #N/A | -0.28 | -1.40 | -2.71 | -3.17 | -3.63 | -5.04 | -6.01 |
| Std. Dev (degrees) | F8R15 | | | 0.60 | 0.60 | 0.63 | 0.68 | 0.51 | #N/A | 0.53 | 0.45 | 0.59 | 0.75 | 0.58 | 0.52 | 0.80 |
| FR-RR (degrees) | F8R15 | | | -0.28 | -0.57 | -0.74 | -0.67 | -0.54 | #N/A | -0.47 | -0.04 | 0.16 | -0.17 | -0.19 | -0.29 | -0.34 |
| Y+-Y- (degrees) | F8R15 | | | -1.28 | -1.20 | -1.10 | -1.21 | -0.77 | #N/A | -0.89 | -0.84 | -1.14 | -1.36 | -1.06 | -1.57 | -1.67 |
| | | | | | | | | | | | | | | | | |
| Optimum | | 15 | 12 | 10 | 8 | 6 | 4 | 2 | 0 | -2 | -4 | -6 | -8 | -10 | -12 | -15 |
| Average (degrees) | F8R15 | 6.54 | 5.75 | 5.07 | 3.82 | 2.82 | 2.08 | 0.86 | -0.02 | -0.86 | -1.66 | -2.45 | -2.97 | -3.92 | -4.44 | -5.54 |
| Std. Dev (degrees) | F8R15 | 0.42 | 0.49 | 0.41 | 0.23 | 0.37 | 0.33 | 0.61 | 0.52 | 0.39 | 0.37 | 0.43 | 0.45 | 0.51 | 0.58 | 0.56 |
| FR-RR (degrees) | F8R15 | -0.40 | -0.50 | -0.20 | -0.49 | -0.60 | -0.32 | -0.50 | -0.23 | 0.09 | 0.15 | 0.43 | 0.19 | -0.15 | -0.08 | -0.18 |
| Y+-Y- (degrees) | F8R15 | -1.55 | -1.67 | -1.48 | -0.96 | -0.04 | 0.03 | 0.40 | 0.43 | -0.12 | -0.80 | -1.14 | -1.18 | -1.68 | -1.86 | -1.84 |
| All results are in yaw angle (degrees) | | | | | | | | | | | | | | | | |

## 1.2.2 Preliminary Dynamic Test Results

**Table 30 - Preliminary test results**

| | Nominal Cascade | | Cascade - open initial | | Cascade - open mid | | Cascade - open immediaely | | Cascade - open -10deg | |
|---|---|---|---|---|---|---|---|---|---|---|
| | Mid Point | Range | Mid Point | Range | Mid Point | Range | Mid Point | Range | Mid Point | Range |
| Average: | 1.28 | 25.22 | 1.62 | 25.77 | 2.74 | 25.26 | 0.93 | 24.53 | 1.23 | 24.31 |
| Std Dev: | 4.02 | 8.45 | 3.65 | 7.90 | 3.95 | 7.92 | 3.49 | 7.18 | 2.54 | 6.92 |
| Y+-Y-: | 6.43 | -2.26 | 6.30 | 0.00 | 7.19 | 1.11 | 6.28 | -1.89 | 4.57 | -1.81 |

minus = open early
plus = open late

| | Cascade - open +10deg | | Cascade - close -10deg | | Cascade - close +10deg | | Cascade - close -20deg | |
|---|---|---|---|---|---|---|---|---|
| | Mid Point | Range | Mid Point | Range | Mid Point | Range | Mid Point | Range |
| Average: | 1.34 | 25.07 | 1.90 | 25.12 | 0.38 | 25.10 | 1.16 | 23.58 |
| Std Dev: | 4.03 | 8.63 | 3.45 | 6.67 | 3.24 | 7.29 | 2.59 | 6.98 |
| Y+-Y-: | 7.81 | -0.59 | 6.54 | -1.00 | 5.93 | -0.30 | 5.43 | 1.30 |

minus = open early
plus = open late

### 1.2.3 Cascade Open Only Dynamic Test Results

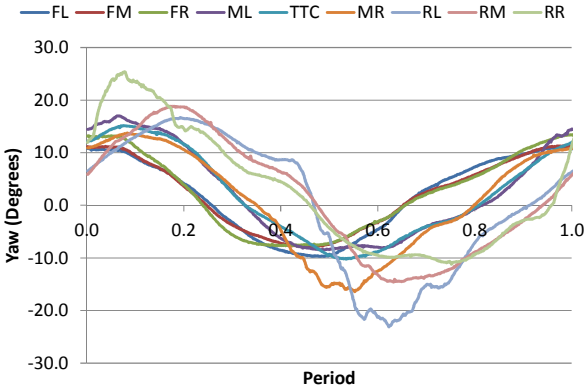


Figure 331 - Average yaw against period - 164ms delay

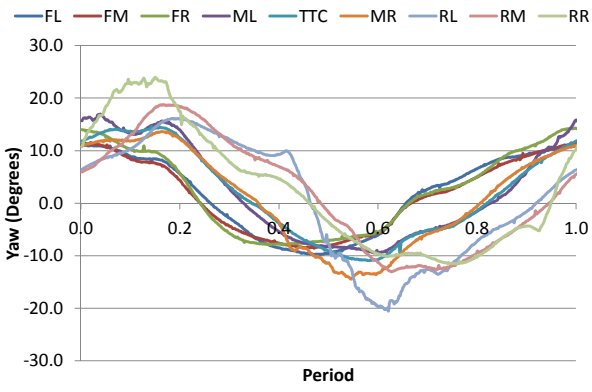


Figure 332 - Average yaw against period - 218ms delay

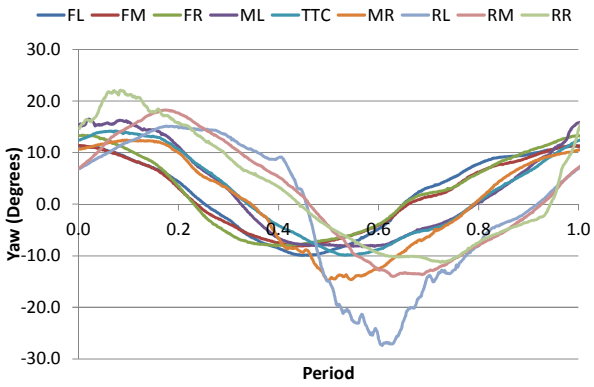


Figure 333 - Average yaw against period - 273ms delay

## 1.3 TGS Commissioning Probe Transfer Function Correction

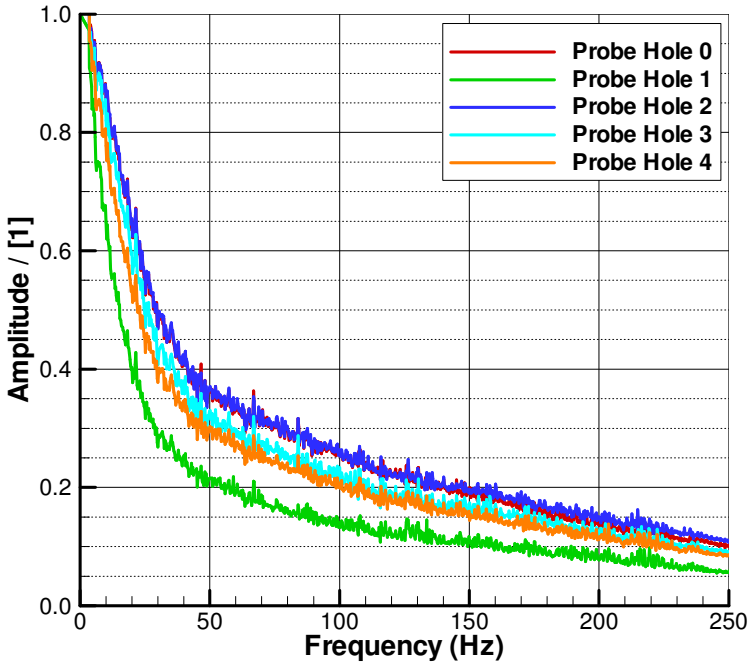


Figure 334 - TGS commissioning probe TF correction (applied to all probe set-ups during transient measurements)

## 1.4 TGS Commissioning Probe Calibration

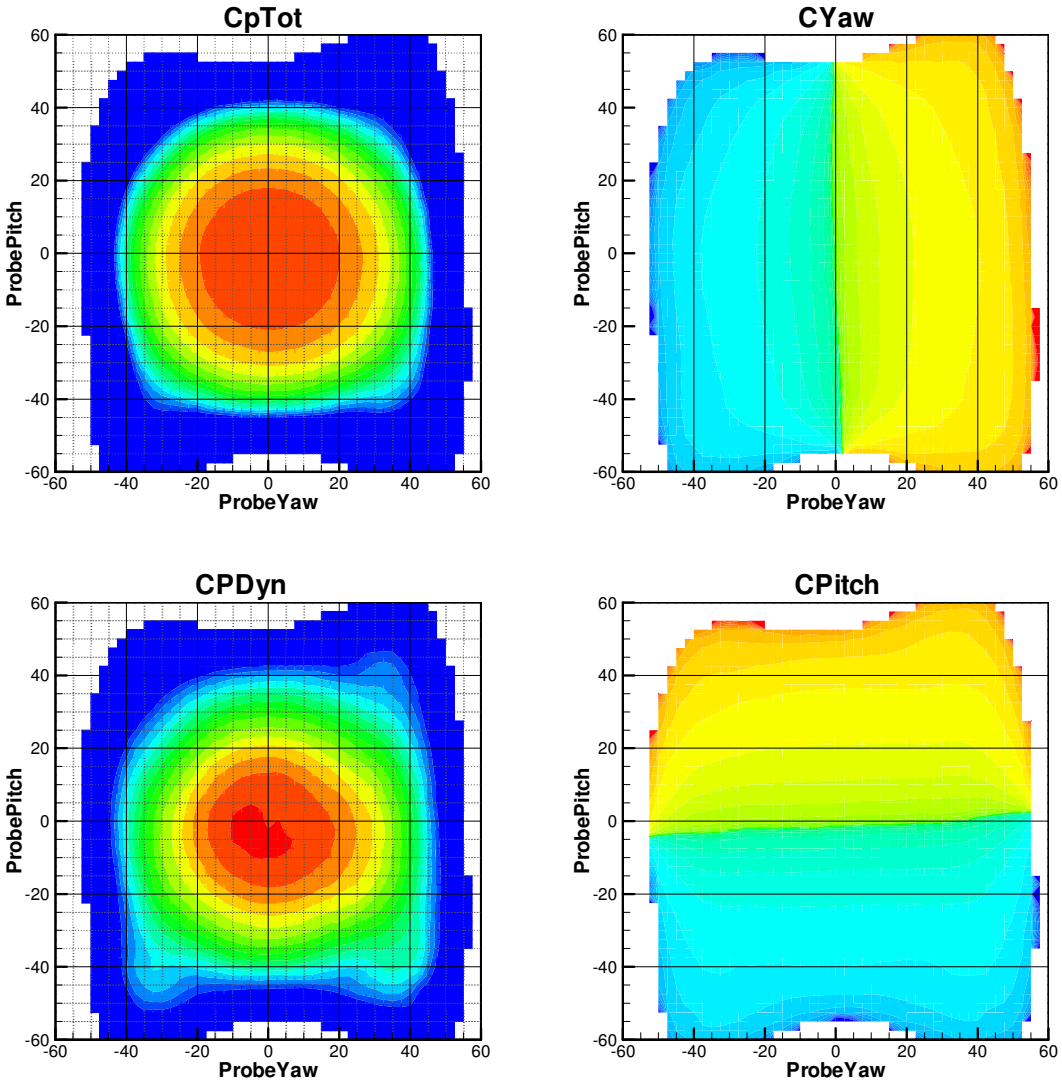


Figure 335 - Laser sintered probe pitch and yaw calibration results

## 1.5 Wind Tunnel Turntable Balance Calibration Results

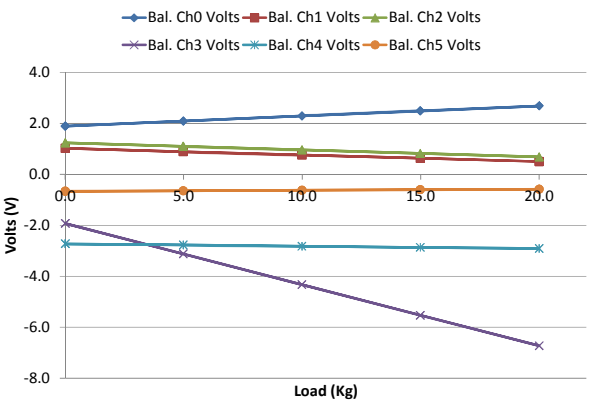


Figure 336 - Balance calibration - Drag

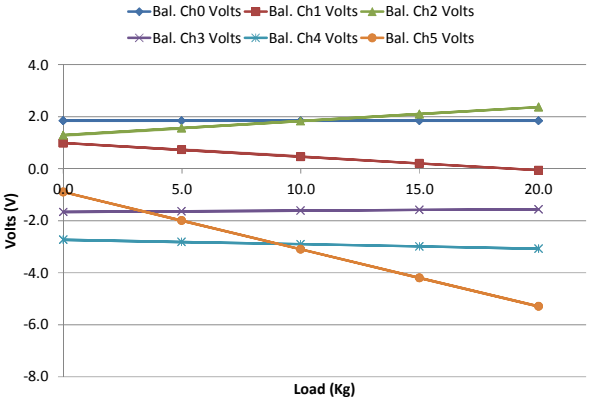


Figure 337 - Balance calibration - Yaw

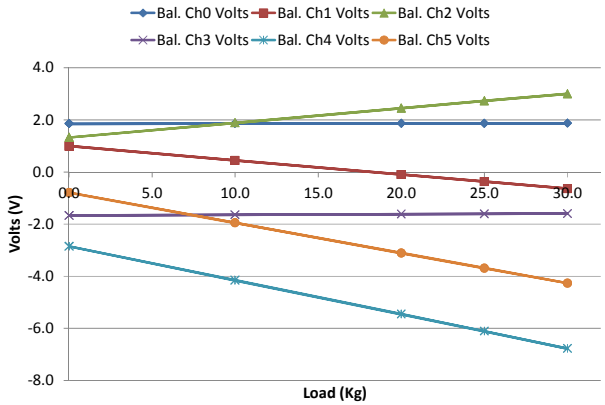


Figure 338 - Balance calibration - Sideforce

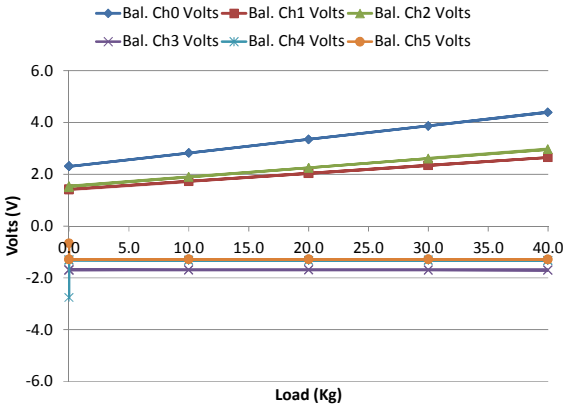


Figure 339 - Balance calibration - Lift

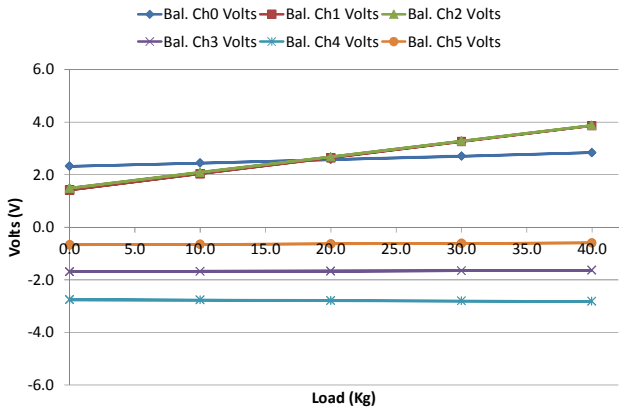


Figure 340 - Balance calibration - Pitch

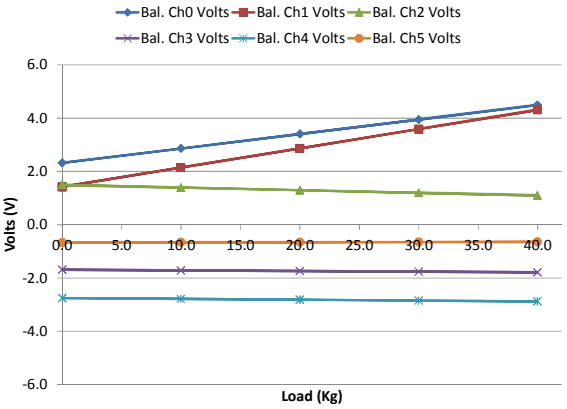


Figure 341 - Balance calibration - Roll

# Appendix 2. TGS Specification supplied to Labman Automation

## 2.1 Background

Durham University wishes to install a turbulence generation system into its 2m$^2$ wind tunnel in order to undertake wind tunnel tests with controlled dynamic yaw-like wind characteristics. This specification is for the tender to design, build, install and commission the system in full. It is believed that vehicle design with consideration for transient wind conditions will yield greater efficiencies and improved vehicle performance, and this system will be state-of-the-art in such research. Durham University's School of Engineering and Computing Sciences has undertaken an aerodynamic design of the turbulence generation system which is to be retrofitted to its current wind tunnel, and this specification outlines that design. The 2m wind tunnel at Durham University is a $^3/_4$ open jet tunnel with a total length of approximately 20m. The inlet nozzle has a contraction ratio of approximately 4:1, excluding bellmouth. The 5.5m long test section jet has a cross sectional area of 2m$^2$ (aspect ratio 1.5:1) and the tunnel operates at up to 30m/s. At the end of the test section the collector directs the flow into two main diffusers which feed into a fan chamber with two fans. These exhaust vertically via two exhaust diffusers.

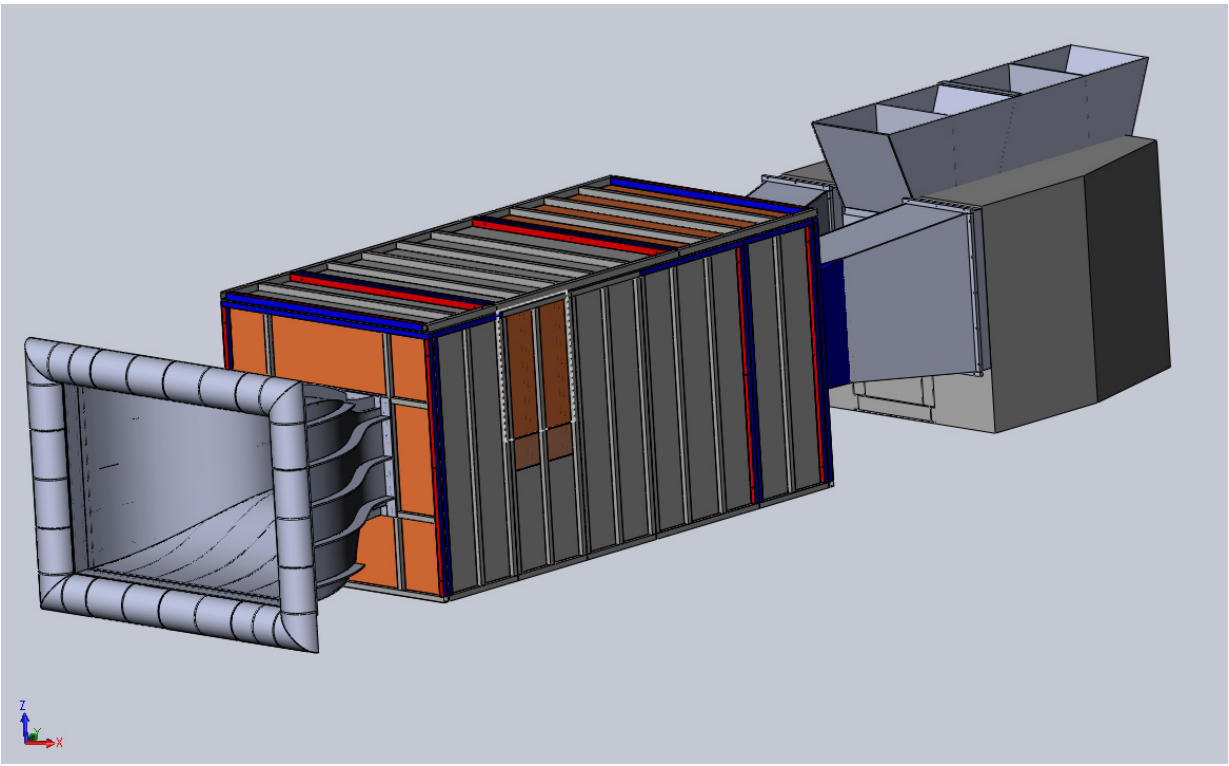

Figure 342 - General overview image of the wind tunnel

## 2.2 Tunnel Description

In Section 4 and Appendix C several images and drawings are included of the layout and shape of the tunnel, with the location of the new components. The system is to be retro-fitted to the tunnel and hence consideration for packaging and modifications to the tunnel are implicit. Note also that the tunnel can alternate between fixed and moving ground, and as such has a rolling road that sits under the test chamber floor. CAD (Solidworks / IGES) for the wind tunnel will be provided following tender award.

## 2.3 Project Outline

The turbulence generation system will consist of a variety of components. The characteristics of 'real world' wind are tri-axis, and as such the TGS design is to generate variant wave forms in all three axes, though in order of priority, lateral (yaw angle, y-velocity), longitudinal and then vertical scales are, respectively, of the greatest importance. This section qualitatively explains the design. The key design parameters are specified later in the electro-mechanical section and are the values to be most closely followed. All of the aerodynamic design has been completed and the tender is only for the mechanical design (and subsequent build, install and commission). It can be assumed that any aerodynamic assessments can or would be completed at no cost.

### 2.3.1 Component List

The following components will need to be installed (and includes their respective item labels for where they are discussed further in this specification).

| | | |
|---|---|---|
| A – 2x Front ducts | B – 2x set of Front Splitters | C – 2x set of Front shutters |
| D – 2x Main aerofoils | E – 1x Horizontal aerofoil | F – 2x set of Rear Shutters |
| G – 2x set of Rear Splitters | H – 2x set of Blow-in valves | I – 2x set of Diffuser shutters |
| J – 2x Rear ducts | | |

### 2.3.2 Front and Rear Duct, Splitters, Shutters and Front Main Foils (Lateral Flow Control)

Two NACA 0012, 0.60m chord, 1.14m in height aerofoils (Item D in Figure 343, Figure 344, Figure 345) are to be mounted vertically either side of the nozzle, with each oscillating in various modes, including sinusoidal and arbitrary programmable motion. In addition to these foils, additional inlet (item A) and exhaust vents (item J) are to be installed, mounted to the side of both the nozzle and collector, respectively. Each quadrant (i.e. 2-inlet side quadrants, 2-exhaust side quadrants) is to have 6-shutters

(items B & C and F & G), 0.10m in width, which will open corresponding to the main foils' incidence angle. These additional inlets are incorporated into the design such that the overall jet width, when viewed as a perpendicular y-axis (width) aligned slice, will be maintained even when the air flow is yawed (otherwise the effective jet width would decrease with flow yaw angle).

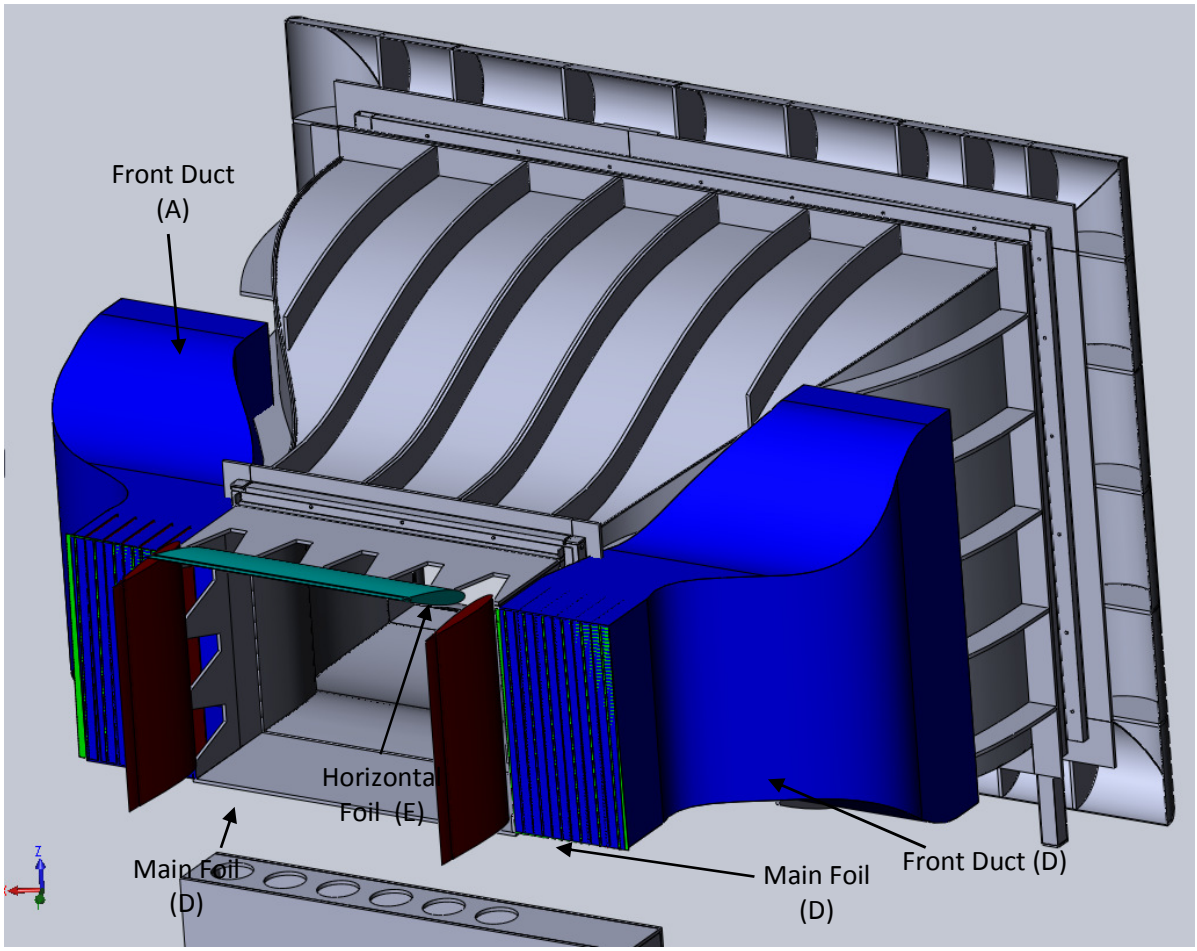


Figure 343 - Front turbulence generation system perspective

In Figure 343, items A (front ducting) is shown in blue, items B (splitters) are shown in red, items C (front shutters) are shown in bright green, items D (main foils) are shown in dark red and item E (horizontal foil) is in cyan.

In Figure 344, the front ducting on the left hand side of the image has been removed for clarity. Items B (splitters) are shown in red, items C (front shutters) are shown in bright green, items D (main foils) are shown in dark red and item E (horizontal foil) is in cyan.

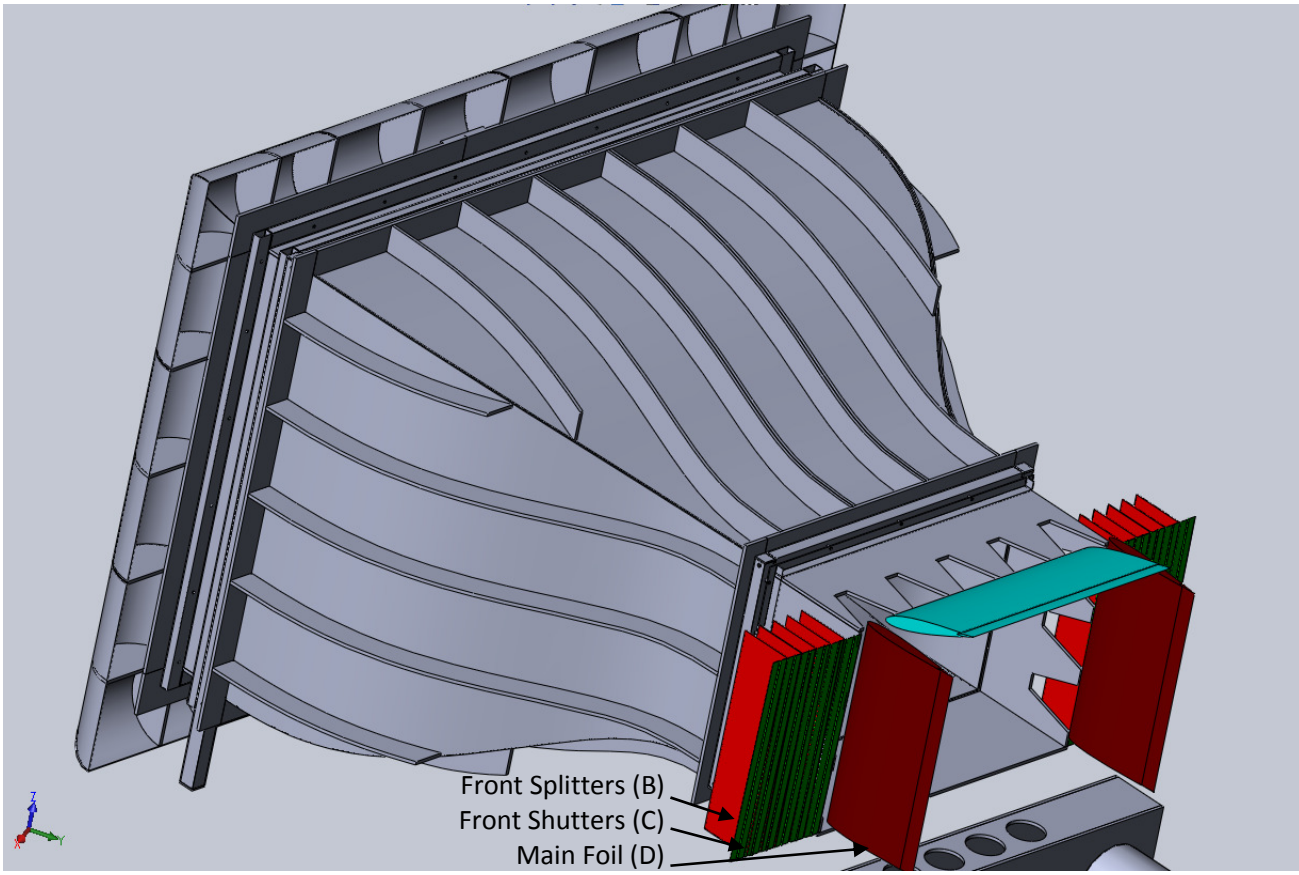


Figure 344 - Front perspective with inlet ducting removed for clarity

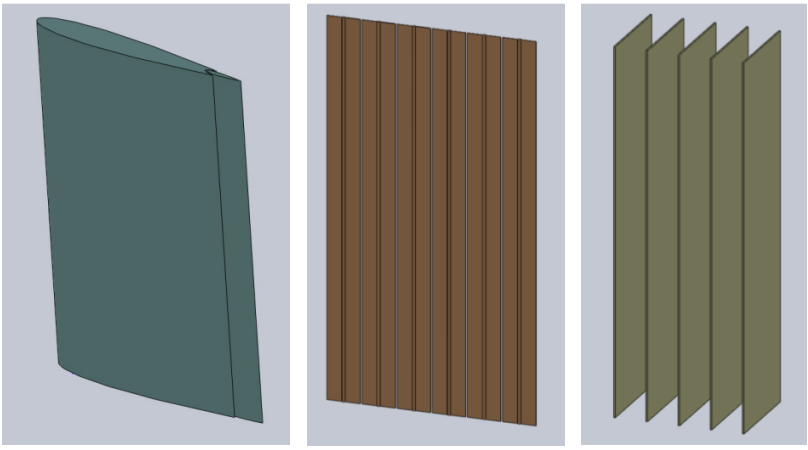

Figure 345 - Left, one of two main foils (item D and E), which has 2 segments - the main foil, and a second trailing foil, which flap quickly. Centre, a set of 6 shutters (item C, F and I), which pivot centrally, to rapidly vary airflow such to pass or to be stopped. Right, a set of splitters (item B and G) that simply separate the airflow as it approached the shutters. The splitters do not move.

To accommodate the transient yawed airflow at the downstream end of the test section new rear ducting (Items J in Figure 346, shown in blue) and rear shutters (items F, shown in bright green) are required. Inside the ducting splitters are required (Items G, partially shown in red behind the shutters in Figure 346).

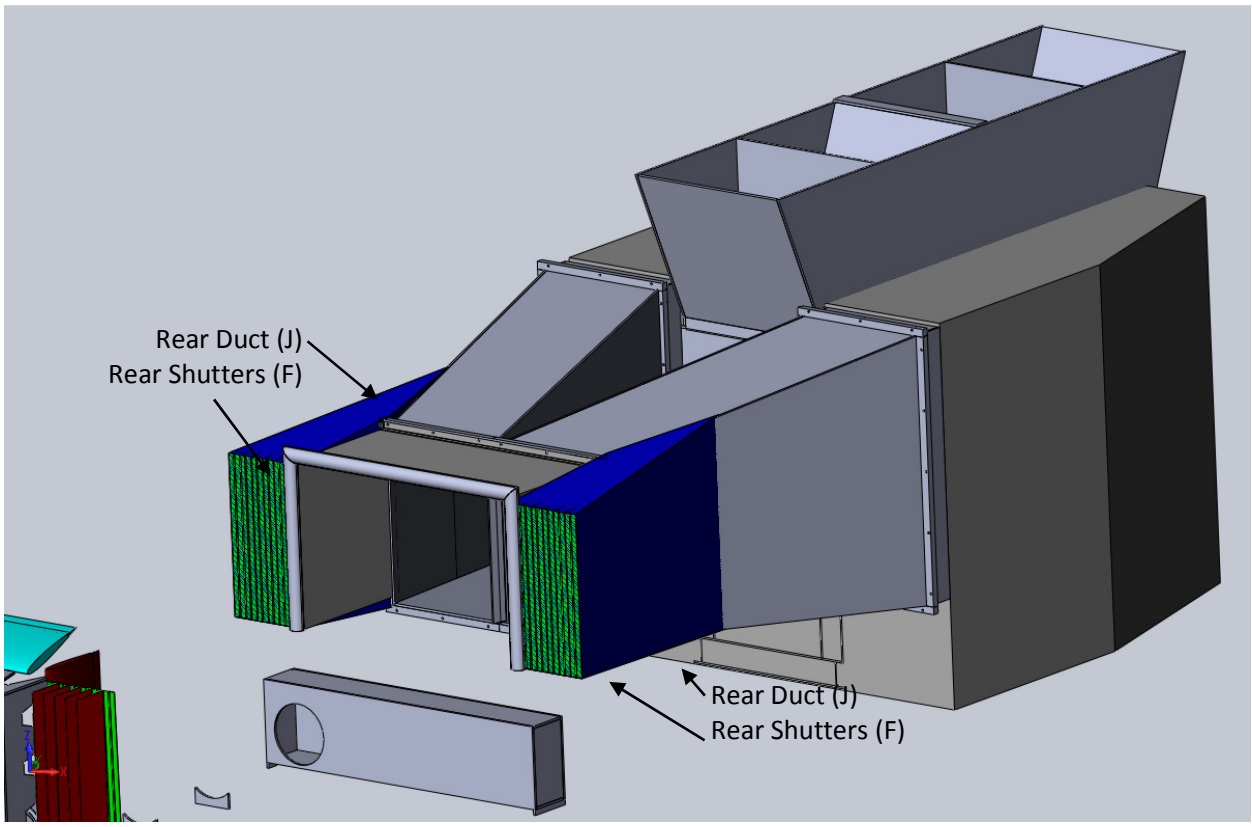


Figure 346 - Rear perspective of turbulence generation system in wind tunnel

In Figure 347, the rear ducting (items J) has been removed and items F (rear shutters) are shown in green and items G (rear splitters) are now more shown in dark red.

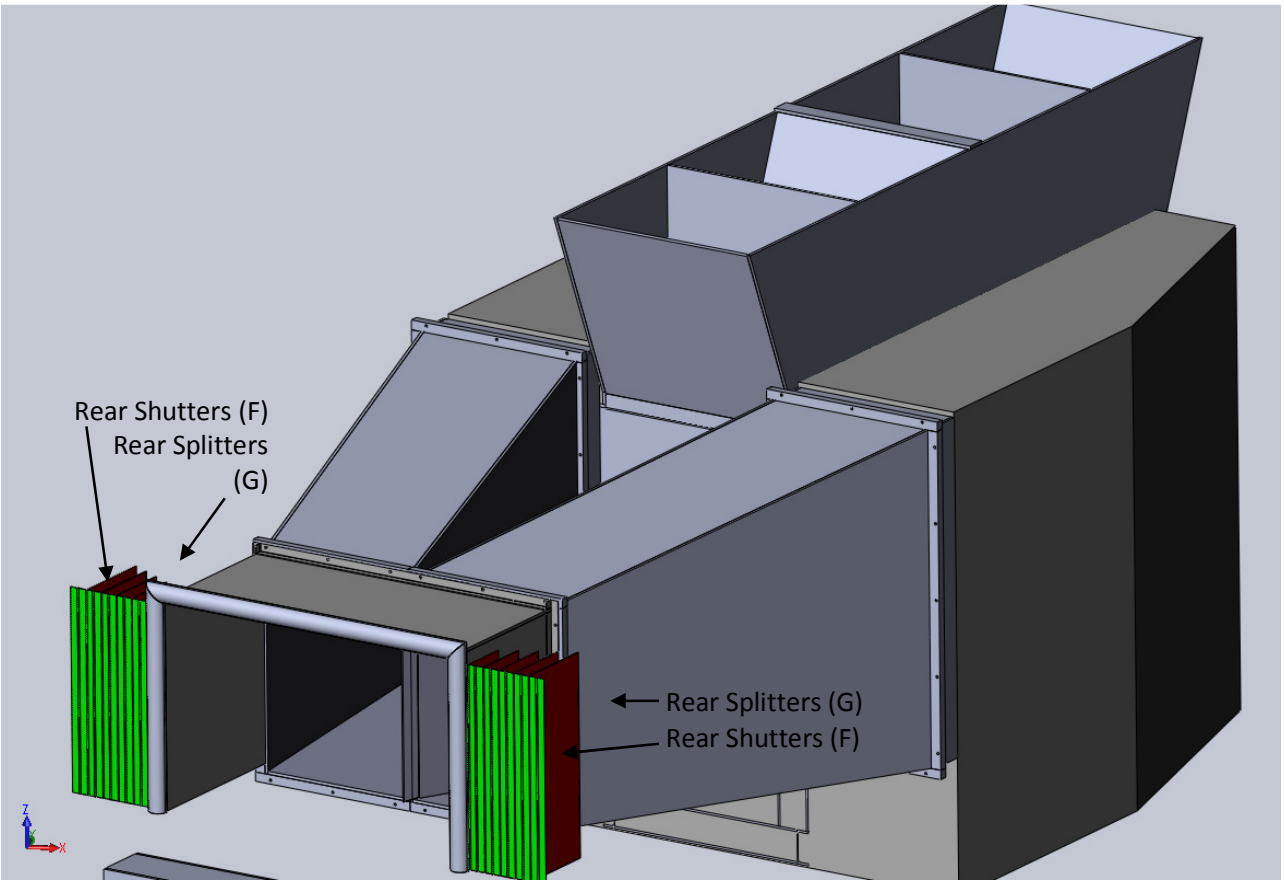


Figure 347 - Rear perspective of turbulence generation system in wind tunnel with ducting removed for clarity

### 2.3.3 Main Diffuser Shutters and Blow-in Valves (Longitudinal Flow Control)

In order to vary the longitudinal velocity, additional blockage shutters (item I) are to be installed in both of the main diffuser sections. These shutters, (4-shutters per diffuser side, 0.10m width each, 1.20m tall, not shown but very similar to the shutters in section 3.2), will each act independently to vary the main diffuser flow area by approximately 40%. This controlled blockage variation will correspondingly accelerate and retard the airflow as the shutters open and close. In order to avoid stalling the downstream fans as the flow is obstructed, downstream of these shutters are to be actuated 'blow-in' panels (item H), which open in co-ordination with the shutters to minimise the load variation from the fan (i.e. the air will blow-in from outside of the tunnel). Images of these items corrected located and orientated are included in Figure 348.

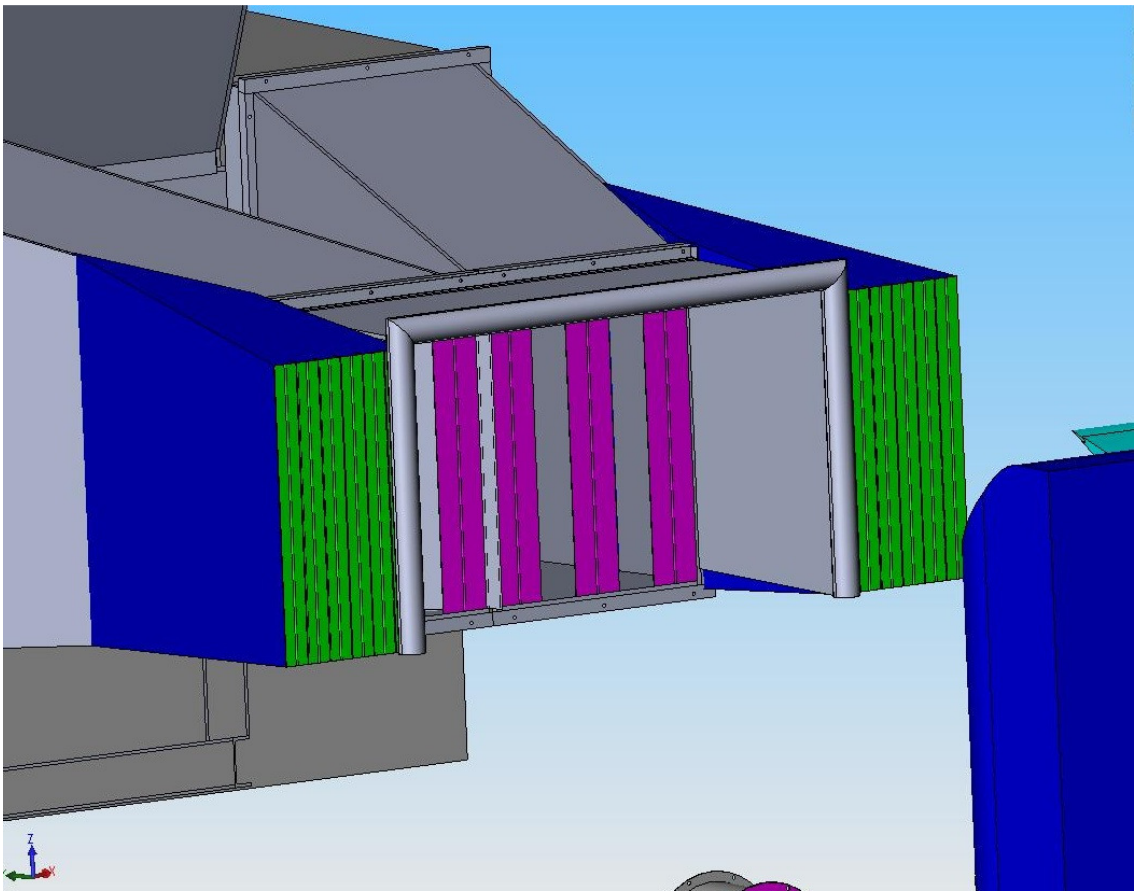

Figure 348 - Purple Item I showing the longitudinal shutters (dropped in other images for clarity)

In Figure 349, in bright pink, under the rear diffuser, item H, the Rear Duct blow-in valves can be seen. The main diffuser shutters (items I) and ducting (items J) are not shown; items F (rear shutters) are shown in green and items G (rear splitters) are shown in dark red.

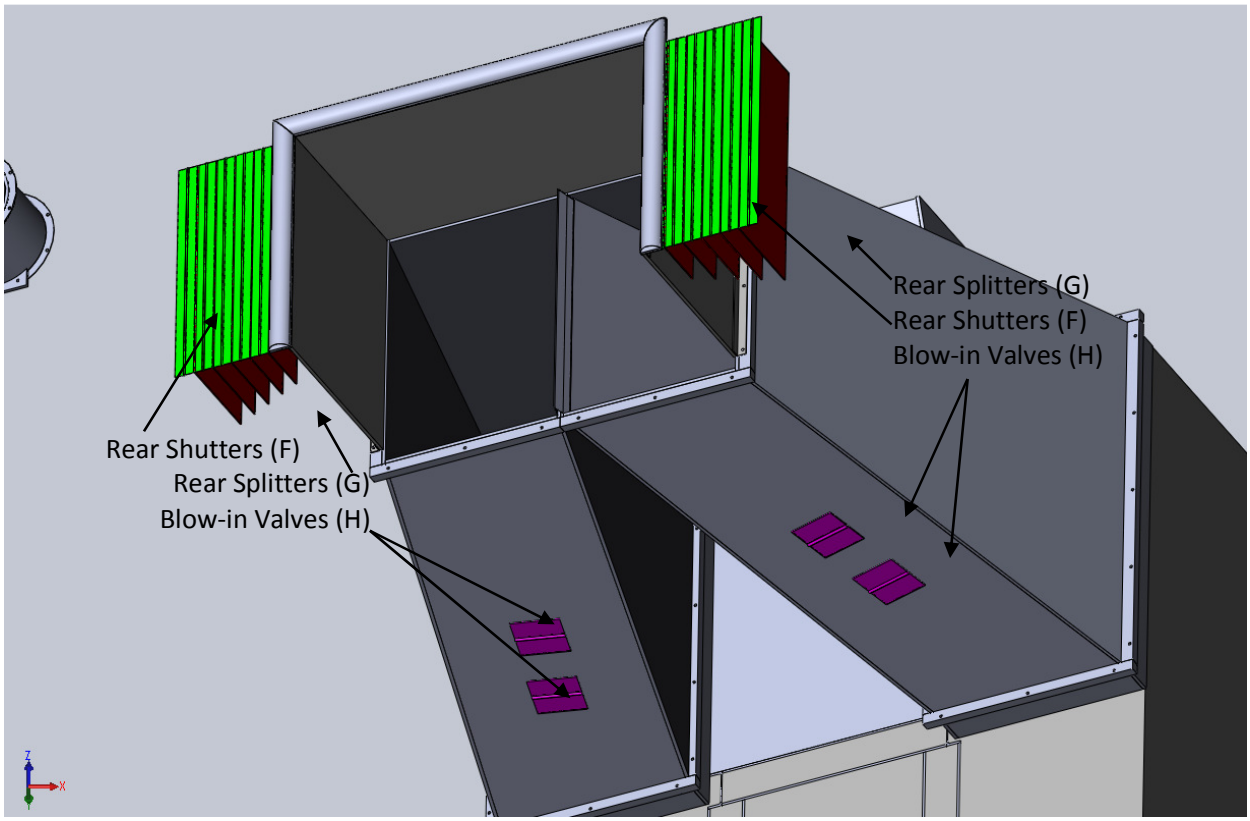


Figure 349 - Rear, underneath perspective, with rear ducting removed for clarity. The purple items are the blow-in flaps.

### 2.3.4 Horizontal Foil (Vertical Flow Control)

An aerofoil (item E) will be mounted horizontally across the top of the nozzle, NACA 0012 type with a chord of 0.40m, 1.40m length, able to oscillate up to around 10Hz to a peak angle range of 0 to -18°. Images of these items corrected located and orientated are included in and Figure 344.

### 2.3.5 Miscellaneous

Each movement of the devices will be controlled electronically through an open source C computer program (or similar, though c is preferred). Each movement (i.e. main left foil peak angle and oscillation frequency) will be expected to be able to be controlled in real-time. The program will also be expected to be fed a file that details all the motion parameters and then be able to execute that motion. The control system will be expected to have a feedback system from all device movements to validate fidelity of operation. The control system should monitor operation in real time and adequate failure protection modes should exist. Access to the test sections and space under the test section (where mechanical actuation can be housed) is already fully interlocked and the turbulence generation system can make use of the existing interlock arrangements.

The whole operation will be expected to be commissioned to this specification and it will be the ultimate responsibility of the supplier that the specification is met at commission. At the commissioning process the use and operation of the system should be expected to be explained, though no formal training is expected. The design and operation will also be expected to be under a warranty of 1-year that the specification will be maintained, and parts used should be selected in consideration to the ease of replacement and likelihood of failure for a 10-year operation life, operating at around 150-hours per annum. The TGS system should be designed for continuous operation of over 1-hour per session. Any cooling requirements or lubrication requirements must be considered.

The TGS should be able to be configured such that when not in use it has negligible impact on the standard flow operation of the wind tunnel. As such necessary drive-shafts and linkage mechanisms should be kept out of the flow as much as possible, or made aerodynamically insignificant (via shaping).

Parts should be chosen that are relatively standard, with the main consideration being ease of replacement should the particular part be discontinued. It is expected that all plans, part numbers and a general manual of operation will be included. A maintenance schedule should be supplied, but no onward maintenance commitments are essential as internal maintenance is expected, other than a 1-year parts and labour warranty. It would be ideal, though not essential, if a one-off 6-month service (i.e. to inspect that the unit is operating and being operated correctly) could be included in the quotation.

The dimensions given are accurate, but should be checked with any design made – different linkage, packing or mounting configurations could mean that the dimensions given are out of tolerance for correct operation.

It can be assumed that the specified operation parameters given in this specification will not cause any issues to the superstructure or currently installed systems in the wind tunnel (i.e. currently installed wind tunnel fans). If additional superstructure or mounting is felt required, this is possible.

### 2.3.6 Overview of Motion Generation

The turbulence generation system will be operated with arbitrary, yet programmable, motion. As such the combination of aerofoils, shutters and alike will, via the control system and its program, be programmed to undertake a variety of motions. However, it is understood that from a design perspective it is essential to have a guideline to the constraints of motion performance that will be

required. This constraint will be the operation of the aerofoils (and respective shutters, etc.) to be able to at least oscillate in a harmonic (i.e. sinusoidal) pattern at 10Hz, peak amplitude of +/-9°. Ideally the system will be able to operate up to 30Hz and/or +/-15°.

Under this constraint, it is therefore understood that the system may not (and likely will not) perform a continual harmonic output, and that the frequency and amplitude of oscillation will vary during operation, potentially quite frequently (i.e. within a second) but that the maximum frequency or amplitude will be 10Hz and +/-9° (or whatever greater that may be achieved in the design). It should also be understood that the operation may not be harmonic, in that a foil need to be programmed to extend to, say, -3°, then halt for 0.5s, then continue to -6°. However, as stipulated, the acceleration and peak amplitude demands will be limited to those corresponding to 10Hz and +/-9° (or whatever greater that may be achieved in the design). It is assumed that these operational constraints will be coded into the control system to ensure correct, safe and appropriate operation regardless of the requests made by the user input.

## 2.4 Vibration & Mounting

Tests have been undertaken to determine the vibration level and mechanical realism of the specification. A design with an inertia matched aerofoil was built and run up to 10Hz operating at +/- 9° in sinusoidal motion. The energy requirements were under 1kW and the vibration found to be safe and suitable for continual with the use of small fly-wheels and low weight, high second moment of area linkages. The addition of the second trailing foil is not expected to cause greater vibration issues.

## 2.5 Budget

A maximum £100,000 (exc. VAT) has been put aside for this project. This is to cover the design, construction, installation, delivery and commissioning of the complete system. 50% of the total figure will be paid upon delivery of the system. The next 40% will be paid upon commissioning of the system. 10% will then be paid 30-calendar days after the commissioning is complete for any snagging issues that may occur in the initial operation.

## 2.6 Electro-mechanical Specification

*Reminder of component identification labels (labelled upstream to downstream):*

| | | | |
|---|---|---|---|
| A - Front ducting | B - Front Splitters | C - Front shutters | D - Main Foils |
| E - Horizontal Foil | F - Rear Shutters | G - Rear Splitters | H – Blow-in Valves |

I - Diffuser shutters J - Rear Ducting

### 2.6.1 Main Lateral Foils – Item D

- Two aerofoils should be placed either side of the nozzle, mounted vertically, pivoting in the Z-axis, and each foil consisting of 2-sections, the main foil and the trailing foil.
- The main foils should be a NACA 0012 aerofoil, each having a 0.60m chord and 1.14m height (that is that the maximum thickness is 12% of chord, i.e. 0.072m).
- The main foils should oscillate in a sinusoidal manner at least to +/-9$^{o}$ at 10Hz, and ideally up to +/-15$^{o}$ at 30Hz. This is only a standard for the rate and range of motion. The foils will actually operate a variety of frequencies and ranges within these limits, including programmable arbitrary motion, but with the acceleration and range requirements within these constraints.
- Each main aerofoil should be independently controlled such that the phasing, frequency and peak angle of each foil can be set independently and all three of these varied during live operation.
- The main foils should have a second, trailing foil, in the general design of the CAD image in Figure 344 and Appendix A Figure 350 and Figure 351), with a chord of 0.10m, with the main and trailing foil together forming a NACA 0012 shape.
- The trailing foil should be able to oscillate up to +/-9$^{o}$ at 10Hz, and ideally up to +/-15$^{o}$ at 30Hz. The frequency of the trailing foil should be controlled and programmable, but the peak angle may (though ideally not) be fixed during operation. It must also be possible to operate the trailing foil in a programmable arbitrary motion.
- Each trailing foil should be able to be set and operate independently of the main foil.
- The foils should be designed to cope with an incoming airflow of 35m/s$^{-1}$.

### 2.6.2 Front Inlet Shutters – Item B and Item C

- The vertically mounted front shutters are to be 1.14m tall, 0.10m wide, 6 in number per side, located either side of the nozzle.
- They need to be able to be opened to a predetermined angle, and be able to operate at a higher frequency than the aerofoils to offer notable flow stop/start action.
- Ideally the shutter will open and close in a square-tooth pattern, as such achieving the closed or open position as quickly as possible, as such to have the greatest effect on airflow.
- The peak angle and frequency of operation should be programmable and each controlled independently.

- The shutters are to normally open in a sequence, starting from the shutter closet to the nozzle and then cascading outwards. This logic and the operation of the shutters should be controlled electronically and should be programmable.

- Upstream of each shutter, the sides of each shutter should have splitters to minimise spillage between shutters, in a way similar to that of the CAD images included in Figure 344). The splitters should have a length of no less than 0.30m in X-axis and be the full height of the shutters.

- The shutters should be designed to cope with an airflow of $35ms^{-1}$ and, when closed, achieve complete flow blockage (i.e. resist all airflow).

### 2.6.3 Rear Exhaust Shutters – Item F and Item G

- The operation of the rear shutters are identical to the front shutters, both in open-and-closed operation and sizing, except where otherwise stated.

- The height of the rear shutters is to be 1.20m, width of 0.10m per shutter with 6-number per side, either side of the collector.

- Downstream of each shutter, the sides of each shutter should have splitters to minimise spillage between each shutter, in a manner similar to that of the CAD images. The splitters should have a length of no less than 0.30m in X-axis and be the full height of the shutters. The rear shutter splitter plates may, and probably should, continue all the way aft to the main diffuser.

### 2.6.4 Longitudinal Operation – Item H and Item I

- The longitudinal flow control is maintained by varying the blockage of the airflow through the main diffuser. This is achieved using 4-shutters per diffuser side that can open and close to vary blockage.

- These shutters are to be mounted at the upstream end of the main diffuser and will each have width 0.10m, height 1.20m.

- The operation of the longitudinal shutters are identical to the front shutters, both in open-and-closed operation and sizing, except where otherwise stated.

- The peak angle, frequency and phasing of the shutters should be able to be controlled independently.

- Blow-in valves (effectively another actuated and programmable shutter) should be installed downstream of the blockage vanes in the main diffuser. The operation of the blow-in valves should be controlled and determined from the requested operation of the blockage vanes or by manual programmed control. The design (i.e. dimensions and location, etc.) of the blow-in values suggested is

only a guideline and may be varied, but the location at the bottom or top of the diffuser would be convenient.

### 2.6.5 Horizontal Foil – Item E

- Situated between the two lateral foils, a foil of NACA 0012 type, 0.40m chord, around 1.40m in width (or what is achievable depending on peak main foil angle), is to be located horizontally at the top of the nozzles.
- The horizontal foil is to be pivoted about roughly quarter chord or upstream of this point, pivoting in the Y-axis.
- The foil should be able to pivot from 0 to +18$^{o}$ incidence (i.e. downwash only) at 10Hz and ideally at 0 to +30$^{o}$ at 30Hz. This is only a standard for the rate and range of motion. The foils will actually operate a variety of frequencies and ranges within these limits, including arbitrarily programmable motion, but with the acceleration and range requirements within these constraints.
- The horizontal foil is not expected to have a second trailing foil section, though it ideally would. If it did, the trailing foil would operate at +/-9$^{o}$ at 10Hz and ideally at +/-15$^{o}$ at 30Hz, relative to the main horizontal foil.
- The aerofoil must operate in airflow up to 35ms$^{-1}$.
- The control system must ensure that the operation of the horizontal foil and the vertical foils cannot create a clash condition – though ideally this would be determined by the physical sizing of the components and range of motion limits.
- The operation of the horizontal foil should be controlled electronically, with phasing, peak angle and frequency variable.
- If a trailing foil is used, its frequency and phasing should be variable throughout operation. Its peak angle may be predetermined during operation, though would ideally be variable throughout. It should also be possible to operate the trailing foil in a programmable arbitrary motion.

### 2.6.6 Ducting – Item A and Item J

- The addition of front and rear shutters requires additional ducting. These must be made and installed within the physical constraints of the room and building design.
- The front ducting should use a contraction ratio of at least 1.5:1, with a honeycomb matrix (at least 0.10m length) near to the duct inlet.

- For the front inlet shutters, there will need to be two channels placed either side of the main tunnel inlet. These should follow a path similar to that of the CAD and fit within the building constraints, but otherwise their design is open and flexible.
- The top and bottom of the ducting for the front shutters should converge to meet at the top and bottom of the mechanical shutters. There should be no sudden jumps or blockages that would cause unnecessary flow disturbances (i.e. turbulence).
- As mentioned earlier, just upstream of the front shutters splitter plates of at least 0.30m in length and full channel/shutter height (at the meeting point, as per the previous point, this will be the same height) should be installed to ensure that flow cannot spill between shutters. These are fixed and do not move.
- Downstream of the rear shutters, ducting will need to exhaust the flow from the shutters into the main diffuser, and splitter plates of full height should ensure that flow from each shutter is constrained until it enters the main diffuser. This duct should diverge slightly to match the main diffuser area ratio where it meets the main diffuser.
- As the longitudinal shutters (controlling blockage) and the blow-in valves are to be installed in the main diffuser, the exhausting of the rear shutters should occur downstream of the blow-in valves.

### 2.6.7 Control and Monitor System *(No label)*

- The control system should preferably by written in C , be open-source, and govern the entire operation of all the systems in operation (2-main foils, 2-trailing foils, longitudinal shutters, blow-in flaps, horizontal foil (with or without trailing foil) and front and rear shutters).
- The control system should ensure that at no occasion do the foils clash or operate in a manner that is unsafe or could damage the other TGS equipment.
- The control system should have a safety cut-out if switches or limits are exceeded. Interlocks already exist for the tunnel and can be included in the design.
- The system should monitor the performance (i.e. frequency, angle and phasing) fidelity of the foils and all other systems and report these values. The control system should indicate when the TGS is operating correctly (i.e. at a high, tolerant, fidelity).
- The control system would desirably have inbuilt sinusoidal modes of operation and have program to control the operation of the foils either through command line or input files. The program should be able to control the frequency, phasing and peak angle (where applicable) of each device.
- The system should be able to read in a data file (of any format desired, but essentially a text file) which determines the operation of the entire system and any default (or assumed) parameters.

- The control system should undertake a logic check that the requested being made by the user are safe and within the design limits of the TGS and ensure no physical clash conditions occur.
- If the TGS requires cooling or lubrication control, within reason these should be monitored by the control system.
- The control system must ensure correct start-up and shut-down procedures are followed (i.e. soft start).

## 2.7 Essential and Desirable Requirements

In projects of this nature it is important to make clear what aspects of the specification are essential (i.e. a minimum), and where, if found possible by a design, a higher performance is found to be achievable, that that would be desirable and would score more greatly in this tender process. It should be assumed that if a design criterion is not discussed in this section, the specification of that aspect covered in the preceding chapter is an essential criterion.

*Reminder of component identification labels (labelled upstream to downstream):*

| | | | |
|---|---|---|---|
| A - Front ducting | B - Front Splitters | C - Front shutters | D - Main Foils |
| E - Horizontal Foil | F - Rear Shutters | G - Rear Splitters | H – Blow-in Valves |
| I - Diffuser shutters | J - Rear Ducting | | |

### 2.7.1 Main Lateral Foils – Item D

As indicated above, the lateral motion is the highest priority and desirable elements in this section are more important than those in other sections.

- Essential
    - For the main foils to be able to move in a sinusoidal oscillating motion with frequency and amplitude up to 10Hz and +/-9$^{o}$ respectively. Frequency, amplitude and phasing should be able to be variable while in motion.
    - For the main foils to be able to move in a programmed arbitrary motion.
    - For the trailing foils to be able to move in a sinusoidal oscillating motion with frequency and amplitude up to 10Hz and +/-9$^{o}$ respectively. Frequency and phasing should be able to be variable while in motion. Amplitude may require manual setting.
    - For the trailing foils to be able to move in a programmed arbitrary motion.
- Desirable

- For the main foils operating in sinusoidal oscillating motion to be able to achieve frequencies and/or amplitudes exceeding those above (e.g.: 30Hz and/or +/-15°).
- For the main foils to be able to move in a programmed arbitrary motion with high acceleration rates (ideally equivalent to those for sinusoidal oscillation at 10Hz and +/-9°).
- For the trailing foil amplitude in sinusoidal motion to be variable while in motion.
- For the trailing foils operating in sinusoidal oscillating motion to be able to achieve frequencies and/or amplitudes exceeding those above (e.g.: 30Hz and/or +/-15°).
- For the trailing foils to be able to move in a programmed arbitrary motion with high acceleration rates (ideally equivalent to those for sinusoidal oscillation at 10Hz and +/-9°).

### 2.7.2 Front Inlet Shutters – Item B and Item C

- Essential
  - Ideally the shutter will open and close in a rounded square-tooth pattern, that is be at its ultimate position for 60% of the cycle when the main foil is operating at 10 Hz.
  - The frequency should be programmable and controlled independently 'on-the-fly'. The peak angle may be set manually. Solenoids may be used to offer better open and closing times and hence compromise on the peak angle 'on-the-fly' adjustment.
- Desirable
  - Ideally the shutter will open and close in a square-tooth pattern, that is be at its ultimate position for 90% of the cycle.
  - The peak angle and frequency should be programmable and each controlled independently 'on-the-fly'.

### 2.7.3 Rear Exhaust Shutters – Item F and Item G

- As per section 6.2.

### 2.7.4 Longitudinal Operation – Item H and Item I

- As per section 6.2, the same shutter design can be used.

### 2.7.5 Horizontal Foil – Item E

- Essential

- For the horizontal foil to be able to move in a sinusoidal oscillating motion with frequency and amplitude up to 10Hz and 0 to +18° incidence (i.e. downwash only required). Frequency, amplitude and phasing should be able to be variable while in motion.
- For the horizontal foil to be able to move in a programmed arbitrary motion.

- Desirable
  - For the horizontal foil to include a trailing foil (as main foils).
  - For the horizontal foil operating in sinusoidal oscillating motion to be able to achieve frequencies and/or amplitudes exceeding those above (e.g.: 30Hz and/or 0 to +30°).
  - For the horizontal foil to be able to move in a programmed arbitrary motion with high acceleration rates (ideally equivalent to those for sinusoidal oscillation at 10Hz and 0 to +18 °).
  - For the trailing foil (if included) to be able to move in a sinusoidal oscillating motion with frequency and amplitude up to 10Hz and +/-9° respectively. Frequency and phasing should be able to be variable while in motion. Amplitude may require manual setting.
  - For the trailing foil (if included) to be able to move in a programmed arbitrary motion.

### 2.7.6 Ducting – Item A and Item J

- Essential
  - For ducting to be designed. Manufacture may be handed to Durham University to sub-contract and install. As such the build and installation cost of the ducting would be expected to be removed and deducted from the tender limit value of £100,000 (exc. VAT).
- Desirable
  - For ducting to be included within the tender price and built and installed by the tier one supplier or their subcontractor.

### 2.7.7 Control and Monitor System (No label)

- Essential
  - All the items specified in section 5.7.
- Desirable
  - For a more greatly developed graphical user interface that has certain built in modes than can be selected without the need to read in positional data.

## 2.8 Mechanical & Electrical Design

A CAD model of Durham University's 2m$^2$ wind tunnel will be supplied and may be used for geometry measurements. In this model will be the location and the major components, and it should be assumed that the size and location of the components cannot be altered without prior approval. Simple, but general changes are possible to the tunnel and space around the tunnel within reason. All components or designs used should be considerate to the aerodynamic nature of the wind tunnel and as such components should not inhibit the flow through the tunnel, or if they must, should be designed to be as aerodynamically streamlined as possible.

Vibration should principally not be transferred into the supporting (yellow) structure within the tunnel which is reserved for mounting instrumentation. Components that generate high torque or vibration should, mainly, be bolted to the concrete floor but may also be attached to the walls and floor of the wind tunnel.

The design should be completed within the specification as detailed. The choice of motors, electrical connections and systems, linkages and alike should be chosen by the supplier. Consideration should be carefully made to the frequencies and amplitudes of operation, and the need for low maintenance and ease or repair. Any stress, vibration or durability analysis or alike should be made by the supplier.

## 2.9 Manufacture

The components will need to be made accurately to the supplier's design and within all tolerances. The manufacture will be off the Durham University site for pre-fabrication and subsequent retro-fitting to the wind tunnel.

## 2.10 Installation & Commissioning

The components will need to be installed as a retro-fit to Durham University's wind tunnel. Pricing should include all installation, delivery, labour and tooling costs as well as finishes and time required to commission. Loading bays, floor space and overhead crane are all available for use in the laboratory at no cost during the allocated period of installation, within reason and the understanding that the laboratory will still be in use by students.

## 2.11 Control

The control system will need to be operated on a standard PC, and be ready and fully operational as and when the installation and commissioning occur. Correct operation of the control system will be part of the commissioning process.

## 2.12 Specification Appendix A – Potential Aerofoil Linkage Design

An example linkage system for aerofoil control system is proposed. This linkage system is only an example which has a good potential to achieve some key operating requirements:

- The variation of the frequency of each motor, when in phase, will control the foil oscillation frequency.
- The variation in phasing of each motor can control peak angle.
- The motors operate in a continuous rotational motion, reducing peak torque and power.
- Allows sinusoidal motion with controllable frequency amplitude and phase at large amplitudes and frequencies (not restricted by motor inertia).
- Allows arbitrary motion by programming one or both servo/ stepper motors accordingly (potentially with reduced amplitude / frequency compared with sinusoidal motion).

### 2.12.1 Main Foil

In Figure 350, the two motors (large white circles with arrows) rotate simultaneously. These are connected by rods to the rectangular bar in the middle right of the foil. This bar is pivoted in its centre, but only has this one-degree freedom of movement. This allows essentially 4 operating modes:

1- Operating both motors at the same constant speed but at different phase separations allows variable amplitude sinusoidal motion. This allows the largest foil accelerations (amplitude and angular velocities) as motor rotor inertia does not have to be accelerated.

2- Operating the two motors at different speeds allows two harmonics to be superposed.

3- Operating one motor at constant speed allows a large amplitude, high frequency, oscillation while the second motor can simultaneously provide a superposed programmed motion (not operating in full revolutions).

4- Operating both servo / stepper motors in an arbitrary motion allows any arbitrary motion for the foil, subject to the acceleration limits that can be achieved by the motors.

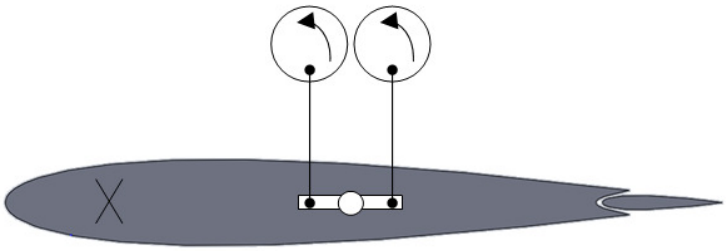

Figure 350 - Main foil potential linkage design

### 2.12.2 Trailing Foil

In Figure 351 the linkage for the main foil is omitted for clarity. The trailing foil is pivoted about the cross, and the linkage bar is simply driven by the rotation of the motor. The intention of the trailing foil is to facilitate higher frequency operation superposed on the main foil motion.

Figure 351 - Trailing foil potential linkage design

## 2.13 Specification Appendix B – Draft Model Drawings

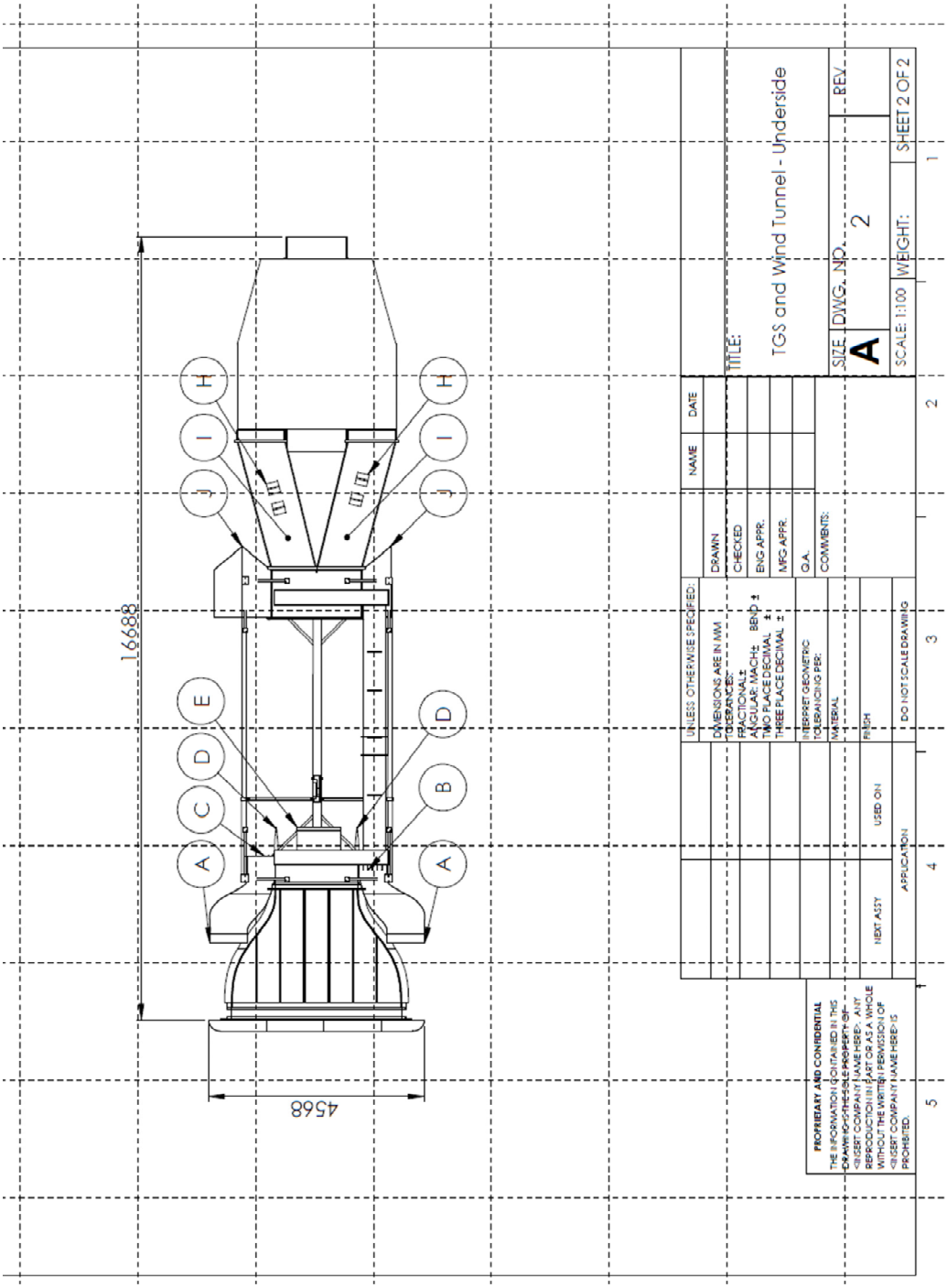

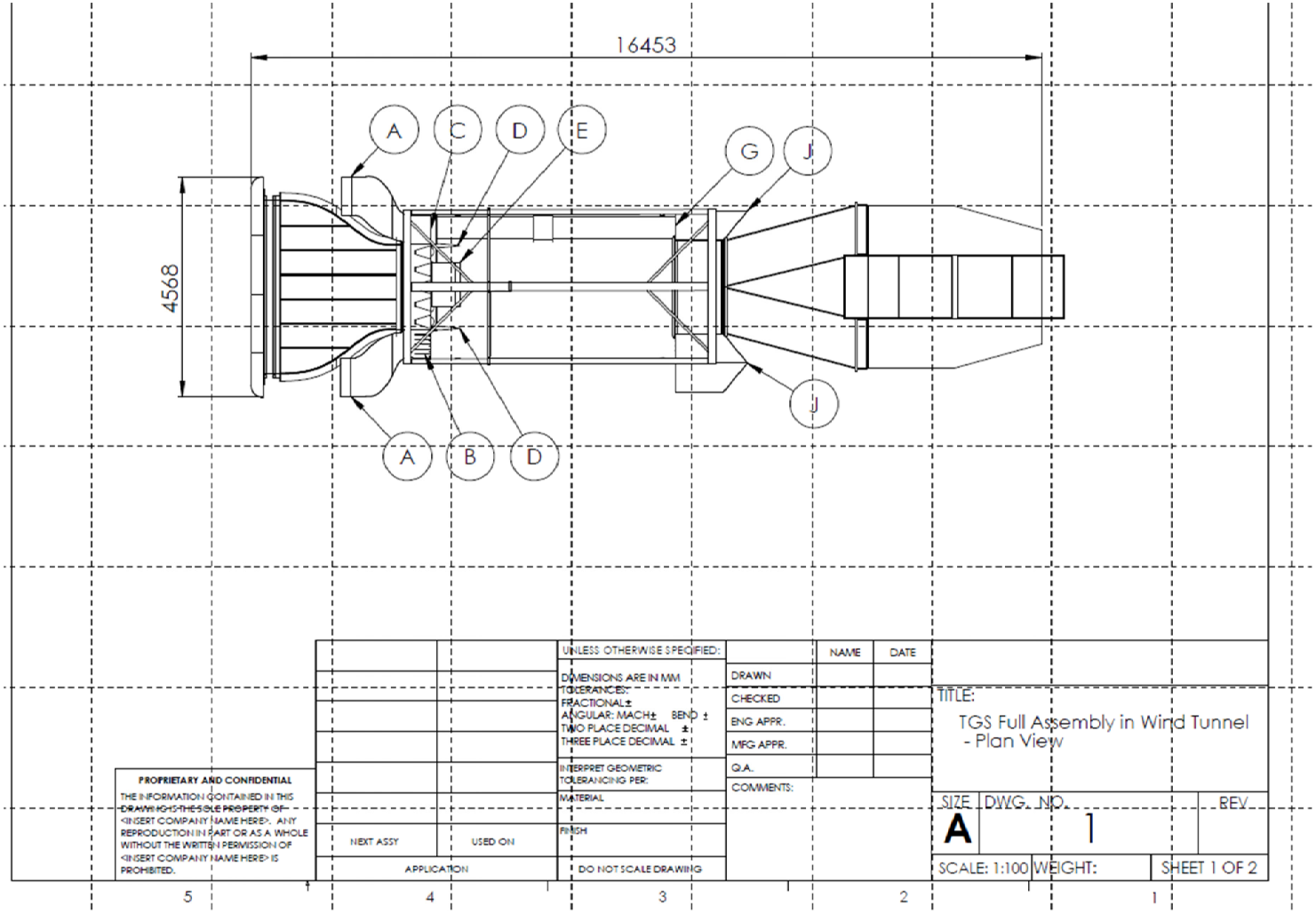
16453
4568
A
C
D
E
G
J
J
A
B
D
UNLESS OTHERWISE SPECIFIED:
DIMENSIONS ARE IN MM
TOLERANCES:
FRACTIONAL ±
ANGULAR: MACH ± BEND ±
TWO PLACE DECIMAL ±
THREE PLACE DECIMAL ±
INTERPRET GEOMETRIC TOLERANCING PER:
MATERIAL
FINISH
DO NOT SCALE DRAWING
NAME
DATE
DRAWN
CHECKED
ENG APPR.
MFG APPR.
Q.A.
COMMENTS:
NEXT ASSY
USED ON
APPLICATION
PROPRIETARY AND CONFIDENTIAL
THE INFORMATION CONTAINED IN THIS DRAWING IS THE SOLE PROPERTY OF <INSERT COMPANY NAME HERE>. ANY REPRODUCTION IN PART OR AS A WHOLE WITHOUT THE WRITTEN PERMISSION OF <INSERT COMPANY NAME HERE> IS PROHIBITED.
TITLE:
TGS Full Assembly in Wind Tunnel - Plan View
SIZE
A
DWG. NO.
1
REV
SCALE: 1:100
WEIGHT:
SHEET 1 OF 2
5
4
3
2
1